



PROCEEDINGS
of the
**Sixth International Conference
on the Ultrasonic Measurement and Imaging
of Tissue Elasticity[®]**

**Santa Fe, New Mexico, USA
November 2 – 5, 2007**

THE BALLAD OF KOKOPELLI

**A STRANGE LONELY FIGURE STARES OUT OF THE PAST
WHERE ENGRAVED BY AN ARTIST IN STONE
HELD FIRM BY THE SAND IN WHICH HE IS CAST,
THESE LAST THOUSAND YEARS QUITE ALONE.
COULD HE BE LISTENING, TRYING TO HEAR
MOCCASINS SCUFFING THE BUTTE?
BRINGING THE PEOPLE ONCE AGAIN NEAR
TO HEAR KOKOPELLI'S SWEET FLUTE?**

**HIS IMAGE INSCRIBED ON A THOUSAND ROCK FACES
FROM EAST TO THE GREAT WESTERN SEA;
FROM SONORA'S HOT SUN TO THE NORTH GLACIERS BASES,
PROCLAIMING THIS LOVED TUTELARY.
THOUGH POWERS POSSESSED AND METHODS EMPLOYED
ARE OFTEN IN OPEN DISPUTE;
ONE THING IS AGREED, THE PEOPLE DID LOVE
TO HEAR KOKOPELLI'S SWEET FLUTE.**

**THIS STICK FIGURE MAN, WITH A HUMP ON HIS BACK
SEEMED ALWAYS TO CAST A GOOD FEELING;
HIS MAGIC PERHAPS, TAKEN OUT OF HIS PACK
WOULD COMFORT THE SICK AND DO HEALING.
WHATEVER HIS TALENTS, THEY SURELY WERE GRAND,
A FACT NO ONE CARES TO REFUTE,
AS PEOPLE WOULD COME FROM AFAR IN THE LAND,
TO HEAR KOKOPELLI'S SWEET FLUTE.**



"If Kokopelli has lured you with his magical flute, it is time to listen to his song. This song is one of fertility. You are being asked to use your talents to create fertility in some area of your life. If things have been slow moving, Kokopelli's song is saying that whatever you intend to plant at this time will be very productive for you.

*Planting seeds for the future takes effort on your part, so now is the time to use your skill and resources to make use of the magic. If you have a project to begin or an idea to develop, the timing couldn't be better. Shift away from any old, limiting ideas and move forward. The time is now - the **POWER IS YOU!**"*

PROCEEDINGS

of the
Sixth International Conference
on the Ultrasonic Measurement and Imaging
of Tissue Elasticity[®]

Santa Fe, New Mexico, USA
November 2–5, 2007

Table of Contents

Foreword	3
Program	4
Conference–At–A–Glance	4
Program by Date and Time	5
Author Index	22
Classical Guitar Soloist Roberto Capocchi Concert	24
Abstracts	25
Session TUT: Tutorials	25
Session SIP-1: Signal and Image Processing – I	27
Session POS: Poster Session – Live Oral Summaries	33
Session MIP-1: Methods for Imaging Elastic Tissue Properties – I	63
Session INS-1: Instrumentation – I	71
Session CVE-1: Cardiovascular Elasticity – I	77
Session MMT-1: Mechanical Measurement Techniques for Tissues – I	82
Session FIP-1: Forward and Inverse Problems – I	86
Session CAA-1: Clinical and Animal Applications – I	91
Session MMT-2: Mechanical Measurement Techniques for Tissues – II	99
Session FIP-2: Forward and Inverse Problems – II	104
Session CVE-2: Cardiovascular Elasticity – II	108
Session SIP-2: Signal and Image Processing – II	113
Session INS-2: Instrumentation – II	117
Session CAA-2: Clinical and Animal Applications – II	121
Session MPT: Mechanical Properties of Tissues	129
Session MIP-2: Methods for Imaging Elastic Tissue Properties – II	136
Session SIP-3: Signal and Image Processing – III	144
Eldorado Conference Center Floor Plan	149
Santa Fe Map	150
Conference Evaluation and Questionnaire	151

QUESTIONS OR COMMENTS ARE WELCOME AT ANY TIME AT <elasticity.conference@uth.tmc.edu>

Copyright © 2007 International Conference on the Ultrasonic Measurement and Imaging of Tissue Elasticity[®] All Rights Reserved
Some abstracts may have been edited by the reviewers for clarity of presentation.

FOREWORD

Dear Conference Delegate:

Welcome to the 6th annual International Conference on the Ultrasonic Measurement and Imaging of Tissue Elasticity®.

This year we are continuing to experience growth in the number of abstracts accepted for presentation at the Conference. We are also seeing a steady increase in the number of clinical papers presented at the Conference, as well as the participation of more research groups from related disciplines and from industry and students (see bar graph). The international participation in this Conference is reflected by delegates from some 20 countries, including virtually all global entities engaged in research, development and practice in the field. We believe that this continually increasing level of participation bodes well for the future of the field.

Last year's Conference feedback was again unanimous in the desire for continuation of the tutorial series. We are pleased that Drs. Sean Kirkpatrick (USA) and Bill Svensson (UK) have agreed to present this year's exciting tutorials on the basic science and clinical progress and prospects of imaging the elastic properties of tissue. We are also continuing last year's popular format of the formal Poster Session, where each presenter has the opportunity to give a brief oral summary of his/her poster, and we thank Drs. Jeff Bamber (UK) and Ralph Sinkus (FR) for their enthusiastic leadership in conducting this event.

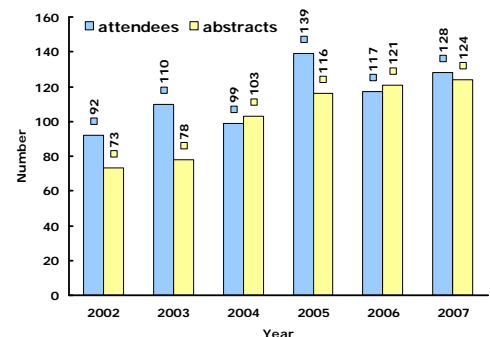
The Saturday evening Conference Dinner will conclude with a classical guitar concert performed by Dr. Roberto Capocchi, an accomplished guitar soloist. Dr. Capocchi will play a variety of classical guitar compositions by notable Latin American composers.

We would like to thank all the delegates, the reviewers and the session chairs for their continuing support of the Conference. Special thanks are in order to our enthusiastic support staff that has worked above and beyond. Ms Tammy Keidel (USA) of the Conference Secretariat's office has handled most of the Conference organizational duties, correspondence and budgets; Ms Karen Ophir (USA) volunteered to design the Conference's artwork, scientific program and publications, and to edit all abstracts in the Conference Proceedings; Ms Betsy Christiansen (USA) and Ms Liz Marshall (USA) have updated and greatly improved the Conference website. Yasin Jabir (USA) and Bill Shepherd (USA) were instrumental in setting up the Conference communications facilities.

The Conference is conducted under the joint auspices of the University of Rochester Center for Biomedical Ultrasound and the Ultrasonics Laboratory in the Department of Diagnostic and Interventional Imaging at the University of Texas Health Science Center Houston. These organizations have contributed in personnel, equipment and financial support. Most funding for the Conference is derived from registration fees, and with your continued support in abstract submissions and attendance, we are committed to improve and expand the Conference in the years to come. We appreciate your written and oral feedback that always helps us in planning for future Conferences.

We hope that you will enjoy this year's scientific and social programs as well as the Eldorado Hotel and the city of Santa Fe and beyond. Next year's Conference is planned for Hong Kong and will be hosted by Dr. Yongping Zheng (HK) of the Hong Kong Polytechnic University. The tentative Conference dates (October 28-31, 2008) are in close proximity to the IEEE-UFFC conference in Beijing, China.

J. Ophir and K.J. Parker
Conference Organizers
Santa Fe, New Mexico, November 2, 2007



CONFERENCE-AT-A-GLANCE

Sixth International Conference on the Ultrasonic Measurement and Imaging of Tissue Elasticity®
Eldorado Hotel and Spa – Santa Fe, New Mexico, USA November 2 – 5, 2007

Friday, November 2

9:00A – 11:30A	Set Up:	9:00A – 8:00P	Presentation & Exhibit Set Up	Anasazi South & Pavilion
9:00A – 8:00P			Registration Desk & Conference Office Open	Anasazi South Foyer
11:30A – 8:00P	Session EEX:		Equipment Exhibit (<i>during breaks</i>)	Pavilion
12:00P – 2:00P	Session TUT:		Tutorials	Anasazi South
2:00P – 2:30P			<i>Coffee Break</i>	Pavilion
2:30P – 4:00P	Session SIP-1:		Signal and Image Processing – I	Anasazi South
4:00P – 4:30P			<i>Recess</i>	
4:30P – 6:00P	Session POS:		Poster Session – Live Oral Summaries	Pavilion
6:00P – 8:00P			<i>Opening Dinner Reception</i>	Pavilion

Saturday, November 3

7:00A – 8:00A		7:00A – 10:30P	<i>Group Continental Breakfast</i>	Old House Dining Room
7:00A – 5:30P			Registration Desk & Conference Office Open	Anasazi South Foyer
8:00A – 5:30P	Session POS:		Posters	Pavilion
8:00A – 5:30P	Session EEX:		Equipment Exhibit	Pavilion
9:00A – 9:30A			<i>Tourist Information</i>	Pavilion
7:45A – 8:00A			Opening Remarks	Anasazi South
8:00A – 10:00A	Session MIP-1:		Methods for Imaging Elastic Tissue Properties – I	Anasazi South
10:00A – 10:30A			<i>Coffee Break</i>	Pavilion
10:30A – 12:00P	Session INS-1:		Instrumentation – I	Anasazi South
12:00P – 1:30P			<i>Group Lunch</i>	Old House Dining Room
1:30P – 2:45P	Session CVE-1:		Cardiovascular Elasticity – I	Anasazi South
2:45P – 3:45P	Session MMT-1:		Mechanical Measurement Techniques for Tissues – I	Anasazi South
3:45P – 4:15P			<i>Coffee Break</i>	Pavilion
4:15P – 5:30P	Session FIP-1:		Forward and Inverse Problems – I	Anasazi South
7:30P – 10:30P			<i>Conference Dinner & Concert with Soloist Roberto Capocchi</i>	Anasazi South

Sunday, November 4

7:00A – 8:00A		7:00A – 7:00P	<i>Group Continental Breakfast</i>	Old House Dining Room
7:00A – 6:00P			Registration Desk & Conference Office Open	Anasazi South Foyer
8:00A – 6:00P	Session POS:		Posters	Pavilion
8:00A – 6:00P	Session EEX:		Equipment Exhibit	Pavilion
8:00A – 10:00A	Session CAA-1:		Clinical and Animal Applications – I	Anasazi South
10:00A – 10:30A			<i>Coffee Break</i>	Pavilion
10:30A – 11:45A	Session MMT-2:		Mechanical Measurement Techniques for Tissues – II	Anasazi South
11:45A – 1:15P			<i>Group Lunch</i>	Old House Dining Room
1:15P – 2:15P	Session FIP-2:		Forward and Inverse Problems – II	Anasazi South
2:15P – 3:30P	Session CVE-2:		Cardiovascular Elasticity – II	Anasazi South
3:30P – 4:00P			<i>Coffee Break</i>	Pavilion
4:00P – 5:00P	Session SIP-2:		Signal and Image Processing – II	Anasazi South
5:00P – 6:00P	Session INS-2:		Instrumentation – II	Anasazi South
6:00P – 7:00P			<i>Group Photo</i>	To be announced

Monday, November 5

7:00A – 8:00A		7:00A – 10:00P	<i>Group Continental Breakfast</i>	Old House Dining Room
7:00A – 4:15P			Registration Desk & Conference Office Open	Anasazi South Foyer
8:00A – 4:15P	Session POS:		Posters	Pavilion
8:00A – 4:15P	Session EEX:		Equipment Exhibit	Pavilion
8:00A – 10:00A	Session CAA-2:		Clinical and Animal Applications – II	Anasazi South
10:00A – 10:30A			<i>Coffee Break</i>	Pavilion
10:30A – 12:15P	Session MPT:		Mechanical Properties of Tissues	Anasazi South
12:15P – 1:45P			<i>Group Lunch</i>	Old House Dining Room
1:45P – 3:45P	Session MIP-2:		Methods for Imaging Elastic Tissue Properties – II	Anasazi South
3:45P – 4:15P			<i>Coffee Break</i>	Pavilion
4:15P – 5:30P	Session SIP-3:		Signal and Image Processing – III	Anasazi South
7:00P – 10:00P			<i>Closing Dinner Reception (Proceedings Book Signing)</i>	Pavilion

PROGRAM

Sixth International Conference on the Ultrasonic Measurement and Imaging of Tissue Elasticity[©]

Santa Fe, New Mexico, USA

November 2–5, 2007

Friday, November 2

9:00A – 8:00P

9:00A – 11:30A Presentation & Exhibit Set Up

All Oral Presenters load presentations onto Conference computers (CD/jump drive) Anasazi South
Poster Presenters set up presentations Pavilion
Exhibitors set up exhibits Pavilion

9:00A – 8:00P

Registration Desk & Conference Office Open Anasazi South Foyer

11:00A – 12:00P 2:00P – 2:30P 4:00P – 4:30P 6:00P – 8:00P

Session EEX: Equipment Exhibit Pavilion

Friday 12:00P – 2:00P

Session TUT: Tutorials

Chair: KJ Parker, USA

Co-Chair: BS Garra, USA

Anasazi South
Page No.

12:00P – 12:45P

122 FROM PHYSICS TO PHYSIC – A HANDS ON APPROACH TO BREAST ELASTICITY IMAGING: 25
IS IT JUST SHEAR STRESS AND STRAIN?
WE Svensson^{1*}.
Charing Cross Hospital, London, England, UK.

12:45P – 1:00P Discussion

1:00P – 1:45P

123 OPTICAL ELASTOGRAPHY – HIGH RESOLUTION AT A COST. 26
SJ Kirkpatrick^{1*}.
¹Oregon Health & Science University, Beaverton, OR, USA.

1:45P – 2:00P Discussion

2:00P – 2:30P

COFFEE BREAK Pavilion

Friday 2:30P – 4:00P

Session SIP–1: Signal and Image Processing – I

Chair: E Brusseau, France

Co-Chair: K Hoyt, USA

Anasazi South
Page No.

2:30P – 2:45P

001 NORMALISATION IN FREEHAND STRAIN IMAGING. 27
GM Treece^{1*}, JE Lindop¹, AH Gee¹, RW Prager¹.
¹University of Cambridge, Cambridge, England, UK.

(Session SIP-1 continues on next page)

2:45P – 3:00P

- 007 AN IMPROVED STRAIN IMAGING METHOD WITH A NEW IMAGE QUALITY MEASURE. 28
MK Jeong^{1}, SJ Kwon¹, DG Hyun².*
¹Daejin University, Pocheon, Kyeonggi, KOREA; ²Medison, Gangnam-gu, Seoul, KOREA.

3:00P – 3:15P

- 003 COMPOUNDING AND DISPLAY OF PSEUDO-STRAIN DATA. 29
JE Lindop^{1}, GM Treece¹, AH Gee¹, RW Prager¹.*
¹University of Cambridge, Cambridge, England, UK.

3:15P – 3:30P

- 046 COMPOUNDING OF STRAIN IMAGES NON-INVASIVELY OBTAINED AT LARGE INSONIFICATION ANGLES. 30
HHG Hansen^{1}, RGP Lopata¹, CL de Korte¹.*
¹Radboud University Nijmegen Medical Center, Nijmegen, The NETHERLANDS.

3:30P – 3:45P

- 015 ITERATIVE DIRECT STRAIN ESTIMATION FOR HIFU LESION DETECTION. 31
CR Hazard^{1}, K Hiltawsky¹, F Lin¹, KW Rigby¹, M Seyed-Bolorforosh¹, KE Thomenius¹, AL Hall², ZC Wu², C Perrey³, B Castañeda⁴, K Hoyt⁴, KJ Parker⁴.*
¹GE Global Research, Niskayuna, NY, USA; ²GE Healthcare, Wauwatosa, WI, USA; ³GE Healthcare, Zipf, AUSTRIA; ⁴University of Rochester, Rochester, NY, USA.

3:45P – 4:00P

- 087 ACCUMULATED STRAIN AND SECANT MODULUS RECONSTRUCTIONS FOR *IN VIVO* BREAST TISSUE. 32
AM Sommer^{1}, TJ Hall¹, PE Barbone², AA Oberai³, S Goenzen³, J Jiang¹.*
¹University of Wisconsin-Madison, Madison, WI, USA; ²Boston University, Boston, MA, USA; ³Rensselaer Polytechnic Institute, Troy, NY, USA.

4:00P – 4:30P Recess**Friday 4:30P – 6:00P**

(Posters will be available for viewing and Coffee Break Discussion through Monday, November 5, 4:15P)

Session POS: Poster Session – Live Oral Summaries

Chair: JC Bamber, UK

Co-Chair: R Sinkus, France

Pavilion
Page No.

4:30P – 4:32P

- 004 STRAIN ESTIMATION BY NON-PARAMETRIC SURFACE REGRESSION. 33
JE Lindop^{1}, GM Treece¹, AH Gee¹, RW Prager¹.*
¹University of Cambridge, Cambridge, England, UK.

4:32P – 4:34P

- 021 CLOSED FORMS OF GAUSSIAN FUNCTIONS IN PRESENCE OF HEAT AROUND CURVILINEAR HOLES. 34
MA Abdou¹, SA Aseeri^{2}.*
¹Alexandria University, Alexandria, EGYPT; ²UQU University, Makkah, SAUDI ARABIA.

4:34P – 4:36P

- 022 MEASUREMENT OF THE NATURAL PULSATILE MOTION OF THE CEREBRAL TISSUE DUE TO CARDIAC CYCLES. 35
E Montagnon¹, JP Remeniéras¹, M Elkateb^{1}, F Tranquart², F Patat¹.*
¹Tours University, Tours, FRANCE; ²INSERM U619, CHU of Tours, Tours, FRANCE.

4:36P – 4:38P

- 030 REAL-TIME AXIAL SHEAR STRAIN ELASTOGRAPHY. 36
R Zahiri-Azar^{1}, A Thitai Kumar², J Ophir², SE Salcudean¹.*
¹The University of British Columbia, Vancouver, BC, CANADA; ²The University of Texas Health Science Center Houston, Houston, TX, USA.

4:38P – 4:40P

- 033 PROSTATE CANCER AND EXTRACAPSULAR EXTENSION (ECE): ASSESSMENT BY SONOELASTOGRAPHY IN COMPARISON WITH MRI – A PRELIMINARY STUDY. 37
L Pallwein¹, FH Aigner^{1}, E Pallwein¹, D zurNedden¹, F Frauscher¹.*
¹Medical University Innsbruck, Innsbruck, AUSTRIA.

4:40P – 4:42P

- 034 EARLY PROSTATE CANCER DETECTION: FINDINGS OF SONOELASTOGRAPHY IN COMPARISON TO ENDORECTAL MRI. 38
L Pallwein^{1}, FH Aigner¹, E Pallwein¹, D zurNedden¹, F Frauscher¹.*
¹Medical University Innsbruck, Innsbruck, AUSTRIA.

4:42P – 4:44P

- 037 EFFECT OF MECHANICAL SOURCE SIZE ON SHEAR MODULUS RECONSTRUCTION. 39
C Sumi^{1}, A Tanuma¹, T Itoh¹, D Takahashi¹.*
¹Sophia University, Chiyoda-ku, Tokyo, JAPAN.

4:44P – 4:46P

- 039 THERMAL PROPERTY RECONSTRUCTION – CASE OF STOPPING HEATING AND PERFUSION. 40
C Sumi^{1}, T Uchida¹, A Minami¹, T Ooba¹, K Inoue¹.*
¹Sophia University, Chiyoda-ku, Tokyo, JAPAN.

4:46P – 4:48P

- 040 PRELIMINARY STUDY ON HUMAN SKIN SHEAR MODULUS RECONSTRUCTION. 41
C Sumi^{1}, A Tanuma¹, T Itoh¹, D Takahashi¹, O Osana², M Sato².*
¹Sophia University, Chiyoda-ku, Tokyo, JAPAN; ²Kao Corporation, Tochigi, JAPAN.

4:48P – 4:50P

- 041 METHOD OF ELASTICITY MEASUREMENT OF BREAST CANCER BY UNIFORM PRESSURE COMPRESSION. 42
Y Hayakawa^{1}, K Ishida¹, K Ando¹, Y Amano¹, K Tsuji¹.*
¹Toin University of Yokohama, Yokohama, Kanagawa-ken, JAPAN.

4:50P – 4:52P

- 044 LIVER STIFFNESS MEASUREMENT (LSM) BY TRANSIENT ELASTOGRAPHY IN THE PREDICTION OF HEPATIC FIBROSIS IN NON-ALCOHOLIC STEATOHEPATITIS (NASH). 43
L Sandrin¹, V Miette^{1}, C Fournier¹.*
¹Echoscens, Paris, FRANCE.

4:52P – 4:54P

- 045 KALMAN FILTERING VERSUS LSQ AS STRAIN ESTIMATORS IN ELASTOGRAPHY. 44
D Sosa-Cabrera¹, J González-Fernández^{1}, L Gómez-Déniz¹, J Ruiz-Alzola^{1,2}.*
¹University of Las Palmas de Gran Canaria, Las Palmas de Gran Canaria, Canary Islands, SPAIN;
²Canary Islands Institute of Technology, Santa Lucía, Canary Islands, SPAIN.

4:54P – 4:56P

- 052 INVESTIGATING THE WAVE PROPERTIES IN TRANSIENT ELASTOGRAPHY USING AN FEM MODEL. 45
CJ Haw^{1}, H Burd², A Noble¹.*
^{1,2}University of Oxford, Oxford, England, UK.

4:56P – 4:58P

- 055 SONOELASTICITY IMAGING OF THE BREAST. 46
J Grajo^{1}, RG Barr¹.*
¹Radiology Consultants, Youngstown, Ohio, USA.

(Session POS continues on next page)

4:58P – 5:00P

- 058 TRANSIENT ACOUSTIC RADIATION FORCE ELASTOGRAPHY FOR HIFU APPLICATIONS. 47
GP Berry¹, JC Bamber^{1}, L Xu¹, Y Ma¹, I Rivens¹, GR ter Haar¹.*
¹Institute of Cancer Research, Sutton, Surrey, England, UK.

5:00P – 5:02P

- 060 DEVELOPMENT OF A MECHANICAL TESTING ASSAY FOR MODULUS ANALYSIS OF 48
 FIBROTIC MURINE LIVER.
SL Barnes^{1}, A Lyschik^{1,2,3}, JC Gore^{1,2,3}, MI Miga^{1,2,3}.*
¹Vanderbilt University, Nashville, TN, USA; ^{2,3}Vanderbilt University Medical Center, Nashville, TN, USA.

5:02P – 5:04P

- 064 THE EFFECT OF NONLINEARITY ON FOCUSED IMPULSIVE ACOUSTIC RADIATION FORCE 49
 EXCITATIONS.
GF Pinton¹, ML Palmeri^{1}, KR Nightingale¹, GE Trahey¹.*
¹Duke University, Durham, NC, USA.

5:04P – 5:06P

- 065 A REAL-TIME ARFI IMAGING SYSTEM ON A DIAGNOSTIC ULTRASOUND SCANNER. 50
JJ Dahl^{1}, GF Pinton¹, SJ Hsu¹, L Fan², GE Trahey¹.*
¹Duke University, Durham, NC, USA; ²Siemens Medical System USA, Inc., Issaquah, WA, USA.

5:06P – 5:08P

- 068 AN ELASTOGRAPHIC APPROACH FOR MEASURING DIASTOLIC FUNCTION. 51
MA Trimble¹, SJ Hsu^{1}, DB Adams¹, PS Douglas¹.*
¹Duke University, Durham, NC, USA.

5:08P – 5:10P

- 075 ELASTOGRAPHIC TRACKING OF *IN-VIVO* DISPLACEMENTS AND STRAINS DURING A CARDIAC 52
 CYCLE.
H Chen^{1,3}, T Varghese^{1}, PS Rahko², JA Zagzebski¹.*
^{1,2,3}University of Wisconsin-Madison, Madison, WI, USA.

5:10P – 5:12P

- 081 FEASIBILITY OF GELLED MINERAL OIL PHANTOM MATERIALS FOR ELASTOGRAPHY. 53
J González-Fernández^{1}, L Gómez-Déniz¹, J Ruiz-Alzola^{1,2}.*
¹University of Las Palmas de Gran Canaria, Las Palmas de Gran Canaria, Canary Islands, SPAIN;
²Canary Islands Institute of Technology, Santa Lucía, Canary Islands, SPAIN.

5:12P – 5:14P

- 088 RECONSTRUCTING SPATIALLY VARYING RAYLEIGH DAMPING PARAMETERS IN MAGNETIC 54
 RESONANCE ELASTOGRAPHY.
MDJ McGarry^{1}, N Naik¹, EEW Van Houten¹.*
¹University of Canterbury, Christchurch, Canterbury, NEW ZEALAND.

5:14P – 5:16P

- 094 ARTIFICIAL NEURAL NETWORK (ANN) INVERSE MODEL FOR THE ELASTIC PROPERTY 55
 PREDICTION OF INCLUSIONS.
PL Yen^{1}, DR Chen², CH Jen³.*
¹National Taipei University of Technology, Taipei, Taiwan; ²ChangHua Christian Hospital, ChangHua, Taiwan.; ³National Army Academy, Chung-Li, Taiwan,.

5:16P – 5:18P

- 104 IMPROVEMENT OF SPECKLE TRACKING IN ELASTICITY IMAGING USING PHASE ROTATION. 56
SW Huang^{1}, R Olafsson¹, C Jia¹, RS Witte¹, M O'Donnell², JM Rubin¹.*
¹University of Michigan, Ann Arbor, MI, USA; ²University of Washington, Seattle, WA, USA.

5:18P – 5:20P

110 SURFACE DISPLACEMENT–TRACTION MEASUREMENTS DO NOT UNIQUELY DETERMINE THE STIFFNESS AND DENSITY IN ANISOTROPIC ELASTIC MEDIA. 57
AL Mazzucato¹, LV Rachele^{2}.*
¹Penn State University, University Park, PA, USA; ²Rensselaer Polytechnic Institute, Troy, NY, USA.

5:20P – 5:22P

113 DEVELOPMENT OF A STRAIN IMAGING METHOD USING LUCAS–KANADE OPTICAL FLOW METHOD IN CONJUNCTION WITH EXPECTATION–MAXIMIZATION ALGORITHM. 58
YJ Zhou^{1}, YP Zheng¹.*
¹Hong Kong Polytechnic University, Hong Kong, CHINA.

5:22P – 5:24P

115 IMPROVING ELASTICITY IMAGING USING AN ADAPTIVE SMOOTHNESS PRIOR. 59
Y Zhang¹, RW Kramer¹, RG Barr^{2}.*
¹Youngstown State University, Youngstown, OH, USA; ²Southwoods Radiology Consultants Inc., Youngstown, OH, USA.

5:24P – 5:26P

120 TIME–REVERSAL OPERATION TO IMPROVE ESTIMATION PERFORMANCE OF LEFT VENTRICLE MOTION USING TAGGED MRI. 60
T Alrefae^{1,2}, M Bilgen^{2,3}.*
¹University of Kansas, Lawrence, KS, USA; ^{2,3}University of Kansas Medical Center, Kansas City, KS, USA.

5:26P – 5:28P

121 VISCOELASTIC CHARACTERIZATION OF THE TEMPORAL STRAIN BEHAVIOR OF BIOMIMETIC MATERIALS IN A CREEP TEST CONFIGURATION. 61
CI Flores¹, JJ Ammann¹.
¹Universidad de Santiago de Chile, Santiago, CHILE.

5:28P – 5:30P

125 SHEAR WAVE SPEED RECOVERY IN SONOELASTOGRAPHY USING CRAWLING WAVES. 62
A Thomas^{1}, J McLaughlin¹, D Renzi².*
¹Rensselaer Polytechnic Institute, Troy, NY, USA; ²Georgia Gwinnett College, Lawrenceville, GA, USA.

5:30P – 6:00P Discussion

Friday 6:00P – 8:00P

Opening Dinner Reception *Proceedings Book Signing* Pavilion
 After 8:00P *No Conference Activities*

Saturday, November 3 7:00A – 10:30P

7:00A – 8:00A
 GROUP CONTINENTAL BREAKFAST Old House Dining Room

7:00A – 5:30P
 Registration Desk & Conference Office Open Anasazi South Foyer

8:00A – 5:30P **Session POS: Posters** Pavilion
Session EEX: Equipment Exhibit Pavilion

9:00A – 9:30A *Tourist Information* Pavilion
Courtesy of the Santa Fe Convention and Visitors Bureau

Saturday 7:45A – 8:00A

OPENING REMARKS
KJ Parker, J Ophir Anasazi South

* indicates Presenter

Saturday 8:00A – 10:00A

Session MIP–1: Methods for Imaging Elastic Tissue Properties – I

Chair: *M Tanter, France*

Co-Chair: *MS Richards, USA*

Anasazi South

Page No.

8:00A – 8:15A

049 CORNEAL DISPLACEMENT MAPPING BY OPTICAL COHERENCE ELASTOGRAPHY. 63

WJ Dupps^{1}, MR Ford², AM Rollins².*

¹Cleveland Clinic, Cleveland, OH, USA; ²Case Western Reserve University, Cleveland, OH, USA.

8:15A – 8:30A

025 3D IMAGING OF RADIOFREQUENCY–ABLATED LESIONS USING THE SIEMENS C7F2 FOURSIGHT 4D ULTRASOUND TRANSDUCER FOR ELECTRODE DISPLACEMENT ELASTOGRAPHY. 64

S Bharat¹, TG Fisher¹, T Varghese^{1}, TJ Hall¹, J Jiang¹, EL Madsen¹, JA Zagzebski¹.*

¹University of Wisconsin – Madison, Madison, WI, USA.

8:30A – 8:45A

085 IMPORTANCE OF PRINCIPAL STRAIN ESTIMATION IN CLINICAL MYOCARDIAL ELASTOGRAPHY WITH VALIDATION AGAINST MRI TAGGING. 65

WN Lee^{1}, Z Qian², DN Metaxas², EE Konofagou^{1,3}.*

^{1,3}Columbia University, New York, NY, USA; ²Rutgers University, Piscataway, NJ, USA.

8:45A – 9:00A

002 FREEHAND STRAIN IMAGING WITH A 3D PROBE. 66

GM Treece^{1}, JE Lindop¹, AH Gee¹, RW Prager¹.*

¹University of Cambridge, Cambridge, England, UK.

9:00A – 9:15A

051 COMPARISON OF TISSUE VELOCITY AND STRAIN IN NORMAL BRAIN AND GLIAL TUMORS AS QUANTIFIED BY PROCESSING OF ULTRASOUND DATA. 67

T Selbekk^{1,2}, R Brekken^{1,2}, S Muller^{1,2}, F Lindseth^{1,2}, G Unsgaard^{2,3,4}.*

¹SINTEF Health Research, Trondheim, NORWAY; ²National Centre for 3D Ultrasound in Surgery, Trondheim, NORWAY; ³St. Olav Hospital, Trondheim University Hospital, Trondheim, NORWAY;

⁴The Norwegian University of Science and Technology, Trondheim, NORWAY.

9:15A – 9:30A

070 INTERFERENCE AND CHARACTERISTIC OF FLUID TISSUE IN ULTRASONIC ELASTICITY IMAGES. 68

L Fan^{1}, P Freiburger¹, C Lowery¹, A Milkowski¹.*

¹Siemens Medical Solutions, USA Inc., Issaquah, WA, USA.

9:30A – 9:45A

071 ELASTOGRAPHIC STUDY OF INJECTION. 69

A Baghani^{1}, R Rohling¹.*

¹University of British Columbia, Vancouver, BC, CANADA.

9:45A – 10:00A

083 REAL–TIME FEEDBACK OF CAVITATION INDUCED PHANTOM ABLATION USING THE SPECKLE TRACKING CORRELATION COEFFICIENT. 70

K Kim^{1}, TL Hall¹, CA Cain¹, JM Rubin².*

^{1,2}University of Michigan, Ann Arbor, MI, USA.

10:00A – 10:30A

COFFEE BREAK

Pavilion

Saturday 10:30A – 12:00P
Session INS–1: Instrumentation – I

Chair: V Egorov, USA

Co-Chair: K Kim, USA

Anasazi South
Page No.

10:30A – 10:45A

026 ULTRASONIC ELASTOGRAPHY AND PLANE STRAIN INVERSE ALGORITHMS FOR POLYMER GEL DOSIMETRY. 71

RA Crescenti¹, JC Bamber^{1}, AA Oberai², PE Barbone³, JP Richter², NL Bush¹, S Webb¹.*

¹Institute of Cancer Research, Sutton, Surrey, England, UK; ²Rensselaer Polytechnic Institute, Troy, NY, USA; ³Boston University, Boston, MA, USA.

10:45A – 11:00A

027 THEORETICAL VALIDATION OF SHEAR WAVE VELOCITY MEASUREMENT IN TRANSIENT ELASTOGRAPHY USING FIBROSCAN®. 72

L Sandrin^{1}.*

¹Echosens, Paris, FRANCE.

11:00A – 11:15A

042 SONOELASTOGRAPHY GUIDED BIOPSY FOR PROSTATE CANCER DETECTION. 73

B Castañeda^{1}, M Zhang², K Hoyt¹, D Pasternack³, L Baxter³, P Nigwekar³, A di Sant'Agnese³, J Joseph³, J Strang³, DJ Rubens³, KJ Parker¹*

^{1,2,3}University of Rochester, Rochester, NY, USA.

11:15A – 11:30A

050 SURFACE PRESSURE MEASUREMENTS IN ULTRASOUND STRAIN IMAGING. 74

LM Kiessel¹, TJ Hall^{1}, J Jiang¹.*

¹University of Wisconsin – Madison, Madison, WI, USA.

11:30A – 11:45A

069 MEASUREMENT OF ACOUSTIC RADIATION FORCE IMPULSE IMAGING SYSTEM RESOLUTION. 75

MG Menon^{1,2}, SA McAleavey^{1,2}.*

^{1,2}University of Rochester, Rochester, NY, USA.

11:45A – 12:00P

082 ULTRASONIC DETECTION OF CHANGES IN CORNEAL BIOMECHANICAL PROPERTIES ASSOCIATED WITH HYDRATION EFFECTS. 76

X He¹, J Liu^{1}.*

¹The Ohio State University, Columbus, OH, USA.

12:00P – 1:30P

GROUP LUNCH

Old House Dining Room

Saturday 1:30P – 2:45P

Session CVE–1: Cardiovascular Elasticity – I

Chair: CL de Korte, The Netherlands

Co-Chair: EE Konofagou, USA

Anasazi South
Page No.

1:30P – 1:45P

012 NON-INVASIVE VASCULAR ELASTOGRAPHY FOR CAROTID ARTERY CHARACTERIZATION: *IN VIVO* VALIDATION ON SUBJECTS WITHOUT PREVIOUS HISTORY OF CAROTID ATHEROSCLEROSIS. 77

RL Maurice^{1,2,3}, G Soulez³, MF Giroux³, G Cloutier^{1,2,3}.*

¹University of Montréal Hospital, Montréal, Québec, CANADA; ^{2,3}University of Montréal, Montréal, Québec, CANADA.

1:45P – 2:00P

047 4D CARDIAC STRAIN IMAGING IN THE HUMAN HEART: INITIAL *IN VIVO* RESULTS. 78

RGP Lopata^{1}, MM Nillesen¹, IH Gerrits¹, JM Thijssen¹, L Kapusta², CL de Korte¹.*

^{1,2}Radboud University Nijmegen Medical Center, Nijmegen, The NETHERLANDS.

(Session CVE–1 continues on next page)

2:00P – 2:15P

- 067 TRANSTHORACIC ACOUSTIC RADIATION FORCE IMPULSE IMAGING OF THE CARDIAC CYCLE. 79
SJ Hsu^{1}, DP Bradway¹, BJ Fahey¹, GE Trahey¹.*
¹Duke University, Durham, NC, USA.

2:15P – 2:30P

- 092 THE EFFECT OF FRAME RATE ON IMAGE QUALITY OF MYOCARDIAL ELASTOGRAPHY *IN-VIVO*. 80
J Luo^{1}, WN Lee¹, S Wang¹, EE Konofagou¹.*
¹Columbia University, New York, NY, USA.

2:30P – 2:45P

- 118 RELATIONSHIP BETWEEN CONTINUOUS HARMONIC PHASE AND DISCRETE 81
 HOMOGENEOUS STRAIN ANALYSIS METHODS AND BEYOND.
M Bilgen^{1,2}.*
^{1,2}University of Kansas Medical Center, Kansas City, KS, USA.

Saturday 2:45P – 3:45P**Session MMT–1: Mechanical Measurement Techniques for Tissues – I**Chair: *E Mazza, Switzerland*Co-Chair: *ML Palmeri, USA*Anasazi South
Page No.**2:45P – 3:00P**

- 020 MEASUREMENT OF THE HYPERELASTIC PROPERTIES OF TISSUE MIMICKING PHANTOMS. 82
JJ O'Hagan^{1}, A Samani^{1,2}.*
^{1,2}The University of Western Ontario, London, ON, CANADA.

3:00P – 3:15P

- 053 DAMPING ESTIMATION BASED ON A VISCOELASTIC MODEL OF SOFT TISSUE. 83
H Eskandari¹, SE Salcudean^{1}, R Rohling¹.*
¹University of British Columbia, Vancouver, BC, CANADA.

3:15P – 3:30P

- 076 MECHANICAL MUSCLE PROPERTIES: TRANSIENT ELASTOGRAPHY AND 3D ULTRASOUND 84
 ULTRAFAST IMAGING.
T Deffieux^{1}, JL Gennisson¹, J Bercoff², M Tanter¹, M Fink¹.*
¹Laboratoire Ondes et Acoustique, Paris, FRANCE; ²Supersonic Imaging, Aix-en-Provence, FRANCE.

3:30P – 3:45P

- 111 AN OCT-BASED AIR-JET INDENTATION SYSTEM FOR MEASURING MECHANICAL 85
 PROPERTIES OF SOFT TISSUES.
YP Huang^{1}, YP Zheng¹, SZ Wang¹.*
¹Hong Kong Polytechnic University, Hong Kong, CHINA.

3:45P – 4:15P

COFFEE BREAK

Pavilion

Saturday 4:15P – 5:30P**Session FIP–1: Forward and Inverse Problems – I**Chair: *J McLaughlin, USA*Co-Chair: *EEW Van Houten, New Zealand*Anasazi South
Page No.**4:15P – 4:30P**

- 105 FLUID-FLOW RELATED STRAIN RELAXATION IN SOFT TISSUES: AN INVERSE PROBLEM 86
 AND SOLUTION FOR THE MICROVASCULAR FILTRATION COEFFICIENT.
R Leiderman¹, GP Berry², JC Bamber², AA Oberai³, PE Barbone^{4}.*
¹Federal University of Rio de Janeiro, Rio de Janeiro, BRAZIL; ²Institute of Cancer Research, Sutton, Surrey, England, UK; ³Rensselaer Polytechnic Institute, Troy, NY, USA; ⁴Boston University, Boston, MA, USA.

4:30P – 4:45P

014 SIMULATION OF SHEAR WAVES PROPAGATION IN HETEROGENEOUS MEDIA USING A PSEUDO-SPECTRAL TIME DOMAIN METHOD. 87
C Bastard^{1,2}, JP Remeniéras¹, L Sandrin².*
¹Tours University, Tours, FRANCE; ²Echosens, Paris, FRANCE.

4:45P – 5:00P

124 DETECTABILITY OF THE SMALLEST POSSIBLE INCLUSION IN TIME HARMONIC ELASTOGRAPHY. 88
JR Yoon^{1}, J McLaughlin², AA Oberai².*
¹Clemson University, Clemson, SC, USA; ²Rensselaer Polytechnic Institute, Troy, NY, USA.

5:00P – 5:15P

035 RECONSTRUCTIVE ELASTOGRAPHY FOR FINITE-AMPLITUDE DEFORMATIONS. 89
W Khaled^{1}, A Arnold², S Reichling², OT Bruhns², H Ermert¹.*
^{1,2}Ruhr University Bochum, Bochum, GERMANY

5:15P – 5:30P

038 EFFECTIVENESS OF REGULARIZATION AND LATERAL MODULATION ON MULTIDIMENSIONAL SHEAR MODULUS RECONSTRUCTION IN DISPLACEMENT VECTOR MEASUREMENT. 90
C Sumi^{1}, A Tanuma¹, T Itoh¹, D Takahashi¹.*
¹Sophia University, Chiyoda-ku, Tokyo, JAPAN.

5:30P – 7:30P *No Conference Activities*

Saturday 7:30P – 10:30P
7:30P – 10:30P

Conference Dinner & Concert *Proceedings Book Signing*
Concert: *Classical Guitar selections performed by Soloist Roberto Capocchi*
 Anasazi South



Sunday, November 4 7:00A – 7:00P

7:00A – 8:00A

GROUP CONTINENTAL BREAKFAST Old House Dining Room

7:00A – 6:00P

Registration Desk & Conference Office Open Anasazi South Foyer

8:00A – 6:00P

Session POS: Posters Pavilion
Session EEX: Equipment Exhibit Pavilion

Sunday 8:00A – 10:00A

Session CAA-1: Clinical and Animal Applications – I

Chair: WE Svensson, UK Co-Chair: WJ Dupps, USA Anasazi South
 Page No.

8:00A – 8:15A

005 CHARACTERIZATION OF THE MECHANICAL BEHAVIOR OF HUMAN LIVER. 91
E Mazza^{1}, M Hollenstein¹.*
¹Swiss Federal Institute of Technology, Zurich, SWITZERLAND.

8:15A – 8:30A

008 BREAST LESION CHARACTERIZATION AND DIFFERENTIATION BY A MECHANICAL IMAGER: PRELIMINARY CLINICAL RESULTS. 92
V Egorov^{1}, S Airapetian¹, SB Pollak², A Sarvazyan¹.*
¹Artann Laboratories, Trenton, NJ, USA; ²Mercy Medical Center, Rockville Centre, NY, USA.

(Session CAA-1 continues on next page)

* indicates Presenter

8:30A – 8:45A

- 019 ULTRASOUND ELASTICITY IMAGING OF INTESTINAL FIBROSIS IN RATS. 93
JM Rubin^{1}, P Higgins², L Johnson², JC Joyce², C Jia³, K Kim³.*
^{1,2,3}University of Michigan, Ann Arbor, MI, USA.

8:45A – 9:00A

- 056 INITIAL RESULTS OF REAL-TIME ELASTICITY IMAGING IN THE EVALUATION OF BREAST LESIONS. 94
RG Barr^{1}, JR Grajo¹.*
¹Radiology Consultants, Youngstown, Ohio USA.

9:00A – 9:15A

- 059 ULTRASOUND ELASTOGRAPHY FOR THE NON-INVASIVE CHARACTERIZATION AND FOLLOW-UP OF ABDOMINAL AORTIC ANEURYSMS AFTER ENDOVASCULAR REPAIR. 95
J Fromageau^{1}, S Lerouge², RL Maurice¹, G Soulez³, G Cloutier¹.*
^{1,2}University of Montréal Hospital Research Center, Montréal, Québec, CANADA; ³University of Montréal Hospital, Montréal, Québec, CANADA.

9:15A – 9:30A

- 011 THE FEASIBILITY OF USING POROELASTOGRAPHIC TECHNIQUES FOR THE STUDY OF LYMPHEDEMA *IN VIVO*. 96
R Righetti^{1}, BS Garra², CM Chant², LM Mobbs², J Ophir¹, TA Krouskop³.*
¹The University of Texas Health Science Center at Houston, Houston, TX, USA; ²The University of Vermont College of Medicine, Burlington, VT, USA; ³Baylor College of Medicine, Houston, TX, USA.

9:30A – 9:45A

- 107 LEAST-SQUARES SPLINE FOR REDUCING TRACKING ERROR IN MUSCLE STRAIN IMAGING. 97
RS Witte^{1}, K Kim², SW Huang¹, BJ Martin¹, M O'Donnell².*
¹University of Michigan, Ann Arbor, MI, USA; ²University of Washington, Seattle, WA, USA.

9:45A – 10:00A

- 108 ELASTOGRAPHIC EVALUATION OF BREAST LESIONS: ADDITIONAL PERFORMANCE RESULTS FROM BLINDED READERS. 98
BS Garra^{1}, LM Mobbs², CM Chant¹, SC Harvey¹, J Ophir³.*
¹University of Vermont College of Medicine, Burlington, VT, USA; ²Fletcher Allen Health Care, Burlington, VT, USA; ³The University of Texas Health Science Center Houston, Houston, TX, USA.

10:00A – 10:30A

COFFEE BREAK

Pavilion

Sunday 10:30A – 11:45A**Session MMT-2: Mechanical Measurement Techniques for Tissues – II**

Chair: R Sinkus, France

Co-Chair: J Liu, USA

Anasazi South

Page No.

10:30A – 10:45A

- 112 DEVELOPMENT OF ULTRASOUND PLATFORM FOR THE EVALUATION OF THE PLANTAR SOFT TISSUE PROPERTIES. 99
JG Chen¹, YP Zheng^{1}, HY Ling¹, YP Huang¹.*
¹Hong Kong Polytechnic University, Hong Kong, CHINA.

10:45A – 11:00A

- 036 COMPARISON OF CONTRAST-TO-NOISE RATIOS OF AXIAL STRAIN AND SHEAR MODULUS RECONSTRUCTION BY AXIAL STRAIN RATIO. 100
C Sumi^{1}, A Tanuma¹, T Itoh¹, D Takahashi¹.*
¹Sophia University, Chiyoda-ku, Tokyo, JAPAN.

11:00A – 11:15A

- 078 3D ULTRASOUND ELASTOGRAPHY FOR BREAST CANCER DIAGNOSIS. 101
M Muller^{1}, JL Gennisson¹, T Deffieux¹, R Sinkus¹, P Annic¹, G Montaldo¹, M Tanter¹, M Fink¹.*
¹Laboratoire Ondes et Acoustique, Paris, FRANCE.

11:15A – 11:30A

- 117 SCANNING ACOUSTIC MICROSCOPY IMAGING OF CARIES AFFECTED DENTIN 102
 MICROMECHANICAL PROPERTIES.
O Marangos¹, A Misra¹, P Spencer¹, B Bohaty¹, Y Wang¹, M de Bruijn¹, MM Kalayeh¹, JL Katz^{1}.*
¹University of Missouri–Kansas City, Kansas City, MO, USA.

11:30A – 11:45A

- 013 SIMULTANEOUS US/MR MEASUREMENTS OF *IN VIVO* LOCAL HARMONIC MOTION. 103
L Curiel^{1}, Y Huang¹, R Chopra¹, K Hynynen¹.*
¹Sunnybrook Health Sciences Centre, Toronto, ON, CANADA.

11:45A – 1:15P

GROUP LUNCH

Old House Dining Room

Sunday 1:15P – 2:15P**Session FIP–2: Forward and Inverse Problems – II**Chair: *PE Barbone, USA*Co-Chair: *J Fehrenbach, France*Anasazi South
Page No.**1:15P – 1:30P**

- 103 ANISOTROPIC ELASTICITY IMAGING WITH APPLICATION TO ELASTICITY IMAGING OF BONE. 104
EF Morgan¹, AA Oberai^{2}, PE Barbone¹, A Nazarian³.*
¹Boston University, Boston, MA, USA; ²Rensselaer Polytechnic Institute, Troy, USA; ³Beth Israel
 Deaconess Medical Center, Boston, MA, USA.

1:30P – 1:45P

- 043 DIRECT LOCAL INVERSION OF WAVE EQUATION IN TRANSIENT ELASTOGRAPHY. 105
J Oudry^{1,2}, V Miette¹, R Willinger², L Sandrin¹.*
¹Echosens, Paris, FRANCE; ²Institut de Mécanique des Fluides et des Solides, Strasbourg, FRANCE.

1:45P – 2:00P

- 048 3D ANALYTICAL MODELING OF TRANSIENT AND HARMONIC PLANE SHEAR WAVE 106
 DIFFRACTION BY A SOFT CYLINDER FOR DYNAMIC VASCULAR ELASTOGRAPHY.
A Hadj Henni^{1}, C Schmitt¹, G Cloutier¹.*
¹University of Montréal Hospital Research Center, Montréal, Québec, CANADA.

2:00P – 2:15P

- 106 CHALLENGES IN QUANTITATIVE ELASTICITY IMAGING. 107
MS Richards¹, C Rivas², JP Richter³, S Goenzen³, RA Crescenti⁴, JC Bamber⁴, AA Oberai³, PE Barbone^{2}.*
¹University of Michigan, Ann Arbor, MI, USA; ²Boston University, Boston, MA, USA; ³Rensselaer
 Polytechnic Inst., Troy, NY, USA; ⁴Institute of Cancer Research, Sutton, Surrey, UK.

Sunday 2:15P – 3:30P**Session CVE–2: Cardiovascular Elasticity – II**Chair: *M Bilgen, USA*Co-Chair: *RL Maurice, Canada*Anasazi South
Page No.**2:15P – 2:30P**

- 119 A SIMPLE TIME-DEPENDENT MODEL OF LEFT VENTRICLE MOTION – IMPLEMENTATION 108
 USING TAGGED MRI.
T Alrefae^{1,2}, M Bilgen^{2,3}.*
¹University of Kansas, Lawrence, KS, USA; ^{2,3}University of Kansas Medical Center, Kansas City, KS, USA.

(Session CVE-2 continues on next page)

2:30P – 2:45P

- 093 PULSE WAVE IMAGING OF NORMAL AND ANEURISMAL ABDOMINAL AORTAS *IN VIVO*. 109
J Luo^{1*}, *K Fujikura*¹, *LS Tyrie*², *MD Tilson III*^{1,2}, *EE Konofagou*¹.
¹Columbia University, New York, NY, USA; ²St. Luke's-Roosevelt Hospital Center, New York, NY, USA.

2:45P – 3:00P

- 099 3D ELASTICITY IMAGING OF LV THROUGH SIMULATIONS AND PHANTOM EXPERIMENTS. 110
C Jia^{1*}, *P Yan*², *K Kim*¹, *TJ Koliass*¹, *JM Rubin*¹, *WF Weitzel*¹, *D Dione*², *AJ Sinusas*², *JS Duncan*²,
*M O'Donnell*³.
¹University of Michigan, Ann Arbor, MI, USA; ²Yale University, New Haven, CT, USA; ³University of Washington, Seattle, WA, USA.

3:00P – 3:15P

- 096 A COMPUTATIONAL STUDY OF REGIONAL ARTERIAL WALL – BLOOD FLOW INTERACTION WITH EXPERIMENTAL VALIDATION USING *IN VIVO* PULSE WAVE IMAGING. 111
IK Zervantonakis^{1*}, *J Luo*¹, *EE Konofagou*¹.
¹Columbia University, New York, NY, USA.

3:15P – 3:30P

- 016 *IN VIVO* ASSESSMENT OF ELASTICITY ALTERATIONS IN THE HUMAN HEART DURING THE CARDIAC CYCLE: SHEAR WAVE AMPLITUDE VARIATION MR ELASTOGRAPHY. 112
I Sack^{1*}, *J Rump*¹, *T Elgeti*¹, *A Samani*³, *J Braun*².
^{1,2}Charité Berlin, Berlin, GERMANY; ³University of Western Ontario, Ontario, CANADA.

3:30P – 4:00P

COFFEE BREAK

Pavilion

Sunday 4:00P – 5:00P**Session SIP–2: Signal and Image Processing – II**Chair: *SJ Kirkpatrick*, USACo-Chair: *GM Treece*, UKAnasazi South
Page No.**4:00P – 4:15P**

- 023 FAST AND ACCURATE LIVER MOTION ESTIMATION. 113
J Fehrenbach^{1*}, *D Melodelima*², *M Masmoudi*¹.
¹Institut de Mathematiques de Toulouse, Toulouse, FRANCE; ²Inserm U556, Lyon, FRANCE.

4:15P – 4:30P

- 028 INCREASING THE NUMBER OF VALID STRAIN ESTIMATES IN IVUS PALPOGRAPHY WITH MOTION COMPENSATION TECHNIQUES. 114
MG Danilouchkine^{1*}, *F Mastik*¹, *AFW van der Steen*^{1,2}.
¹Erasmus Medical Center, Rotterdam, The NETHERLANDS; ²Interuniversity Cardiology Institute of the Netherlands, Utrecht, The NETHERLANDS.

4:30P – 4:45P

- 032 REAL-TIME TISSUE DEFORMATION VISUALIZATION. 115
R Zahiri-Azar^{1*}, *O Goksel*¹, *SE Salcudean*¹.
¹The University of British Columbia, Vancouver, BC, CANADA.

4:45P – 5:00P

- 091 SPECKLE CHARACTERIZATION AND OUT-OF-PLANE MOTION ESTIMATION IN TISSUE. 116
H Rivaz^{1*}, *G Hager*¹, *R Zellars*², *G Fichtinger*^{1,3,4}, *E Boctor*⁴.
^{1,3}Johns Hopkins University, Baltimore, MD, USA; ^{2,4}Johns Hopkins Medical Institute, Baltimore, MD, USA.

Sunday 5:00P – 6:00P

Session INS-2: Instrumentation – II

Chair: *TJ Hall, USA*

Co-Chair: *Y Hayakawa, Japan*

Anasazi South

Page No.

5:00P – 5:15P

061 HEATING SIMULATION FOR VIBRO-ACOUSTOGRAPHY. 119

S Chen^{1}, JF Greenleaf¹, M Fatemi¹.*

¹Mayo Clinic College of Medicine, Rochester, MN, USA.

5:15P – 5:30P

095 MODALITY INDEPENDENT ELASTOGRAPHY: INITIAL RESULTS WITH A MURINE LIVER FIBROSIS MODEL. 118

MI Miga^{1,2,3}, JJ Ou¹, SL Barnes¹, A Lyschik^{2,3}, JC Gore^{1,2,3}.*

¹Vanderbilt University, Nashville, TN, USA; ²Vanderbilt University Medical Center, Nashville, TN, USA; ³Vanderbilt University Institute for Imaging Science, Nashville, TN, USA.

5:30P – 5:45P

114 A NEW REAL-TIME STRAIN IMAGING PROTOTYPE FOR RESEARCH: PRELIMINARY EXPERIMENTS. 117

R Souchon^{1}, D Melodelima¹, S Chesnais^{1,2}, M Oliveira de M Correia¹, A Chapelon¹, E Delabrousse¹, JY Chapelon¹.*

¹INSERM Unité 556, Lyon, FRANCE; ²Institut de Chirurgie Expérimentale (ICE), Centre Régional Léon Bérard, Lyon, FRANCE.

5:45P – 6:00P

116 MR IMAGING OF TRANSIENT SHEAR WAVES INDUCED BY RADIATION FORCE. 120

R Souchon^{1}, O Rouvière², O Beuf³, R Salomir¹, JY Chapelon¹.*

¹INSERM, Lyon, FRANCE; ²Hospices Civils de Lyon, Lyon, FRANCE; ³CNRS, INSA-Lyon, Lyon, FRANCE.

Sunday 6:00P – 7:00P

Group Photo

After 7:00P

No Conference Activities

To be announced

Monday, November 5

7:00A – 10:00P

7:00A – 8:00A

GROUP CONTINENTAL BREAKFAST

Old House Dining Room

7:00A – 4:15P

Registration Desk & Conference Office Open

Anasazi South Foyer

8:00A – 4:15P

Session POS: Posters

Pavilion

Session EEX: Equipment Exhibit

Pavilion

Monday 8:00A – 10:00A

Session CAA–2: Clinical and Animal Applications – II

Chair: *JM Rubin, USA*

Co-Chair: *L Pallwein, Austria*

Anasazi South

Page No.

8:00A – 8:15A

101 MAMMOGRAPHIC THROUGH-PADDLE ELASTOGRAPHY FOR IMPROVED BREAST LESION CHARACTERIZATION. 121

RC Booi¹, MA Roubidoux¹, MS Richards¹, JM Rubin^{1}, M O'Donnell², MM Helvie¹, AL Hall³, PL Carson¹.*

¹University of Michigan Health System, Ann Arbor, MI, USA; ²University of Washington, Seattle, WA, USA; ³General Electric Health Care, Milwaukee, WI, USA.

8:15A – 8:30A

054 QUANTIFICATION OF ORBICULAR MUSCLE CONTRACTION AND IDENTIFICATION OF SCAR TISSUE IN PATIENTS WITH A RECONSTRUCTED CLEFT LIP. 122

CL de Korte^{1}, N van Hees², RGP Lopata¹, G Weijers¹, C Katsaros², JM Thijssen¹.*

^{1,2}Radboud University Nijmegen Medical Center, Nijmegen, The NETHERLANDS.

(Session CAA–2 continues on next page)

* indicates Presenter

8:30A – 8:45A

009 *IN VIVO* VISUALIZATION OF ABDOMINAL MALIGNANCIES WITH ACOUSTIC RADIATION FORCE IMPULSE IMAGING. 123

BJ Fahey^{1*}, *RC Nelson*², *SJ Hsu*¹, *DP Bradway*¹, *DM Dumont*¹, *GE Trahey*^{1,2}.

¹Duke University, Durham, NC, USA; ²Duke University Medical Center, Durham, NC, USA.

8:45A – 9:00A

010 A FEASIBILITY STUDY OF CLINICAL RADIOFREQUENCY ABLATION ASSESSMENT WITH ACOUSTIC RADIATION FORCE IMPULSE IMAGING. 124

BJ Fahey^{1*}, *RC Nelson*², *SJ Hsu*¹, *DP Bradway*¹, *DM Dumont*¹, *GE Trahey*^{1,2}.

¹Duke University, Durham, NC, USA; ²Duke University Medical Center, Durham, NC, USA.

9:00A – 9:15A

073 VISUALIZATION OF INCLUSION-BACKGROUND BONDING USING AXIAL-SHEAR STRAIN ELASTOGRAPHY: PRELIMINARY *IN VIVO* IMAGES. 125

A Thitai Kumar^{1,2}, *J Ophir*^{1,2}, *CM Chant*³, *LM Mobbs*³, *BS Garra*^{3*}.

¹The University of Texas Health Science Center Houston, Houston, TX, USA; ² University of Houston, Houston, TX, USA; ³University of Vermont, Burlington, VT, USA.

9:15A – 9:30A

057 THE SPATIO-TEMPORAL STRAIN RESPONSE OF OEDEMATOUS AND NON-OEDEMATOUS TISSUE TO SUSTAINED COMPRESSION *IN VIVO*. 126

*GP Berry*¹, *JC Bamber*^{1*}, *PS Mortimer*¹, *NL Bush*¹, *NR Miller*¹, *PE Barbone*².

¹Institute of Cancer Research and Royal Marsden NHS Trust, Sutton, Surrey, UK;

²Boston University, Boston, MA, USA.

9:30A – 9:45A

084 QUANTITATIVE ASSESSMENT OF TISSUE SCAFFOLD DEGRADATION USING ULTRASOUND ELASTICITY IMAGING (UEI). 127

K Kim^{1*}, *CA Jeong*¹, *MS Richards*², *JM Rubin*², *SC Hollister*¹.

^{1,2}University of Michigan, Ann Arbor, MI, USA.

9:45A – 10:00A

109 BREAST ELASTICITY IMAGING AIDS PATIENT MANAGEMENT IN THE ONE STOP BREAST CLINIC. 128

WE Svensson^{1*}, *N Zaman*¹, *NK Barrett*¹, *G Ralleigh*¹, *K Satchithananda*¹, *S Comitis*¹, *V Gada*¹, *NR Wakeham*¹.

Charing Cross Hospital, London, England, UK.

10:00A – 10:30A

COFFEE BREAK

Pavilion

Monday 10:30A – 12:15P**Session MPT: Mechanical Properties of Tissues**

Chair: YP Zheng, China

Co-Chair: L Sandrin, France

Anasazi South

Page No.

10:30A – 10:45A

017 ON THE IMPACT OF VARYING VISCOELASTIC PARAMETERS ON IMPULSIVE ACOUSTIC RADIATION FORCE GENERATED SHEAR WAVES IN LIVER. 129

ML Palmeri^{1*}, *MH Wang*¹, *SJ Rosenzweig*¹, *KR Nightingale*¹.

¹Duke University, Durham, NC, USA.

10:45A – 11:00A

018 ACOUSTIC ENERGY BALANCE DURING DIAGNOSTIC AND THERAPEUTIC ULTRASOUND IMAGING. 130

ML Palmeri^{1*}, *RW Nightingale*¹, *KD Frinkley*¹, *GE Trahey*¹, *KR Nightingale*¹.

¹Duke University, Durham, NC, USA.

11:00A – 11:15A

- 077 ASSESSMENT OF NONLINEAR SHEAR ELASTIC MODULI IN INCOMPRESSIBLE SOFT MEDIA. 131
M Rénier¹, JL Gennisson^{1}, M Tanter¹, D Royer¹, M Fink¹.*
¹Laboratoire Ondes et Acoustique, Paris, FRANCE.

11:15A – 11:30A

- 079 THE SUPERSONIC SHEAR IMAGING AS A QUANTITATIVE TOOL FOR IMAGING *IN VIVO* LIVER STIFFNESS. 132
T Deffieux¹, M Muller¹, JL Gennisson¹, M Couade², J Bercoff², M Tanter^{1}, M Fink¹.*
¹Laboratoire Ondes et Acoustique, Paris, FRANCE; ²Supersonic Imagine, Aix-en-Provence, FRANCE.

11:30A – 11:45A

- 080 DIAGNOSTIC OF LIVER FIBROSIS IN RATS – COMPARISON BETWEEN SUPERSONIC SHEAR IMAGING AND MR ELASTOGRAPHY. 133
N Salameh¹, JL Gennisson², B Larrat¹, T Deffieux², M Tanter², R Sinkus^{2}, B van Beers¹, M Fink².*
¹Université Catholique de Louvain, Brussels, BELGIUM; ²Laboratoire Ondes et Acoustique, Paris, FRANCE.

11:45A – 12:00P

- 097 HIGH RESOLUTION MR-ELASTOGRAPHY: A UNIQUE TOOL TO STUDY THE RHEOLOGICAL PROPERTIES OF TISSUE *IN VIVO* AND THE ORIGIN OF ITS MULTISCALE BEHAVIOR. 134
B Larrat^{1}, N Salameh², M Tanter¹, M Fink¹, R Sinkus¹.*
¹Laboratoire Ondes et Acoustique, Paris, FRANCE; ²Clinique Universitaire Saint Luc, Brussels, BELGIUM.

12:00P – 12:15P

- 098 *IN-VIVO* APPLICATION OF MR-ELASTOGRAPHY TO AN AD MOUSE MODEL – ANISOTROPIC MECHANICAL PROPERTIES OF THE CORPUS CALLOSUM. 135
B Larrat^{1}, QC Chan^{2,3}, XF Yang³, G Li³, ES Yang^{2,3}, M Fink¹, R Sinkus¹.*
¹Laboratoire Ondes et Acoustique, ESPCI, CNRS UMR 7587, INSERM, Université Paris VII, Paris, FRANCE; ^{2,3}The University of Hong Kong, Hong Kong, CHINA.

12:15P – 1:45P

GROUP LUNCH

Old House Dining Room

Monday 1:45P – 3:45P**Session MIP-2: Methods for Imaging Elastic Tissue Properties – II**Chair: *JL Gennisson, France*Co-Chair: *AA Oberai, USA*Anasazi South
Page No.**1:45P – 2:00P**

- 072 A NOVEL *IN VIVO* QUANTITATIVE SONOELASTOGRAPHIC TECHNIQUE FOR INVESTIGATING THE ELASTICITY OF SKELETAL MUSCLE TISSUE. 136
K Hoyt^{1}, B Castañeda¹, T Kneezel¹, KJ Parker¹.*
¹University of Rochester, Rochester, NY, USA.

2:00P – 2:15P

- 090 TOWARD REAL-TIME 2D ULTRASOUND ELASTOGRAPHY USING GLOBAL OPTIMIZATION OF A REGULARIZED DISPLACEMENT FIELD. 137
H Rivaz^{1}, P Foroughi¹, E Boctor², R Zellars³, G Fichtinger^{1,2,4}, G Hager¹.*
^{1,4}Johns Hopkins University, Baltimore, MD, USA; ^{2,3}Johns Hopkins Medical Institute, Baltimore, MD, USA.

2:15P – 2:30P

- 031 REAL-TIME POROELASTOGRAPHY: A FEASIBILITY STUDY. 138
R Zahiri-Azar^{1}, R Righetti², J Ophir², SE Salcudean¹.*
¹The University of British Columbia, Vancouver, BC, CANADA; ²The University of Texas Health Science Center Houston, Houston, TX, USA.

(Session MIP-2 continues on next page)

2:30P – 2:45P

086 2D THEORETICAL ASSESSMENT OF THE AMPLITUDE-MODULATED HARMONIC MOTION 139
IMAGING (AM-HMI) AND EXPERIMENTAL VALIDATION.

C Maleke^{1}, J Luo¹, EE Konofagou¹.*

¹Columbia University, New York, NY, USA.

2:45P – 3:00P

089 DIGITAL IMAGE ELASTO-TOMOGRAPHY: IMAGING INTERNAL ELASTICITY THROUGH 140
EXTERNAL SURFACE MOTION MEASUREMENTS.

A Peters¹, JG Chase¹, EEW Van Houten^{1}.*

¹University of Canterbury, Christchurch, Canterbury, NEW ZEALAND.

3:00P – 3:15P

100 THREE DIMENSIONAL SHEAR ELASTIC MODULUS IMAGING FOR MAMMOGRAPHIC 141
SCREENING AND DIAGNOSIS.

MS Richards^{1}, JM Rubin¹, PE Barbone², AA Oberai³.*

¹University of Michigan Health System, Ann Arbor, MI, USA; ²Boston University, Boston, MA, USA;

³Rensselaer Polytechnic Institute, Troy, NY, USA.

3:15P – 3:30P

063 PERFORMANCE OF 3D DISPLACEMENT ESTIMATION USING A CURVILINEAR PROBE. 142

NR Miller¹, EJ Harris¹, PM Evans¹, RN Symonds-Tayler¹, JC Bamber^{1}.*

¹Institute of Cancer Research and Royal Marsden NHS Trust, Sutton, Surrey, England, UK.

3:30P – 3:45P

102 NONLINEAR ELASTICITY IMAGING OF BREAST TISSUE. 143

AA Oberai^{1}, S Goenzen¹, NH Gokhale², PE Barbone³ AM Sommer⁴, TJ Hall⁴, J Jiang⁴.*

¹Rensselaer Polytechnic Institute, Troy, NY, USA; ²Weidlinger Associates, New York, NY, USA;

³Boston University, Boston, MA, USA; ⁴University of Wisconsin-Madison, Madison, WI, USA.

3:45P – 4:15P

COFFEE BREAK

Pavilion

Monday 4:15P – 5:30P**Session SIP-3: Signal and Image Processing – III**

Chair: CR Hazard, USA

Co-Chair: C Sumi, Japan

Anasazi South

Page No.

4:15P – 4:30P

029 2D LOCALLY REGULARIZED DEFORMATION IMAGING DURING FREEHAND EXAMINATION: 144
INITIAL RESULTS.

E Brusseau^{1}, JF Déprez¹, F Duboeuf¹, O Basset¹.*

¹CREATIS UMR CNRS 5220 – INSERM U630, Villeurbanne, FRANCE.

4:30P – 4:45P

062 A NEW METHOD TO REDUCE THE COMPUTATION TIME OF FAST DISPLACEMENT 145
ESTIMATORS FOR ULTRASONIC STRAIN IMAGING.

A Eder^{1}, C Kargel¹.*

¹Bundeswehr University Munich, Neubiberg-Munich, GERMANY.

4:45P – 5:00P

066 CLUTTER REDUCTION METHODS FROM COMPRESSION OF TISSUE. 146

JJ Dahl^{1}, M Lediju¹, MJ Pihl¹, SJ Hsu¹, CM Gallippi², GE Trahey¹.*

¹Duke University, Durham, NC, USA; ²University of North Carolina, Chapel Hill, NC, USA.

5:00P – 5:15P

074 AN EDGE-PRESERVING RESTORATION PROCESS FOR ELASTOGRAM DENOISING. 147

D Auroux^{1}, R Souchon², J Fehrenbach¹.*

¹University Paul Sabatier Toulouse 3, Toulouse, FRANCE; ²INSERM-U556, Lyon, FRANCE.

5:15P – 5:30P

006 STRAIN TENSOR ELASTOGRAPHY BASED ON OPTICAL FLOW ESTIMATION OF DISPLACEMENT 148
FIELDS.

D Sosa-Cabrera^{1}, J González-Fernández¹, L Gómez-Déniz¹, J Ruiz-Alzola^{1,2}.*

¹University of Las Palmas de Gran Canaria, Las Palmas de Gran Canaria, Canary Islands, SPAIN;

²Canary Islands Institute of Technology, Santa Lucía, Canary Islands, SPAIN.

5:30P – 7:00P

No Conference Activities

Monday 7:00P – 10:00P

Closing Dinner Reception *Proceedings Book Signing*

Pavilion

Session EEX: Equipment Exhibit

Pavilion

Siemens Medical Solutions Ultrasound Group
Issaquah, WA, USA.

Ultrasonix Medical Corporation
Burnaby, BC, CANADA.

AUTHOR INDEX

AUTHOR	PAGE	AUTHOR	PAGE	AUTHOR	PAGE
Abdou, MA	34	Elgeti, T	112	Kapusta, L	78
Adams, DB	51	Elkateb, M	35	Kargel, C	145
Aigner, FH	37, 38	Ermert, H	89	Katsaros, C	122
Airapetian, S	92	Eskandari, H	83	Katz, JL	102
Alrefae, T	60, 108	Evans, PM	142	Khaled, W	89
Amano, Y	42	Fahey, BJ	79, 123, 124	Kiessel, LM	74
Ammann, JJ	61	Fan, L	50, 68	Kim, K	70, 93, 97, 110, 127
Ando, K	42	Fatemi, M	119	Kirkpatrick, SJ	26
Annic, P	101	Fehrenbach, J	113, 147	Kneezel, T	136
Arnold, A	89	Fichtinger, G	116, 137	Kolias, TJ	110
Aseeri, SA	34	Fink, M	84, 101, 131-135	Konofagou, EE	65, 80, 109, 111, 139
Auroux, D	147	Fisher, TG	64	Kramer, RW	59
Baghani, A	69	Flores, CI	61	Krouskop, TA	96
Bamber, JC	47,71,86,107,126,142	Ford, MR	63	Kwon, SJ	28
Barbone, PE	32, 71, 86, 104, 107, 126, 141,143	Foroughi, P	137	Larrat, B	133-135
Barnes, SL	48, 118	Fournier, C	43	Lediju, M	146
Barr, RG	46, 59, 94	Frauscher, F	37, 38	Lee, WN	65, 80
Barrett, NK	128	Freiburger, P	68	Leiderman, R	86
Basset, O	144	Frinkley, KD	130	Lerouge, S	95
Bastard, C	87	Fromageau, J	95	Li, G	135
Baxter, L	73	Fujikura, K	109	Lin, F	31
Bercoff, J	84, 132	Gada, V	128	Lindop, JE	27, 29, 33, 66
Berry, GP	47, 86, 126	Gallippi, CM	146	Lindseth, F	67
Beuf, O	120	Garra, BS	96, 98, 125	Ling, HY	99
Bharat, S	64	Gee, AH	27, 29, 33, 66	Liu, J	76
Bilgen, M	60, 81, 108	Gennisson, JL	84, 101, 131-133	Lopata, RGP	30, 78, 122
Boctor, E	116, 137	Gerrits, IH	78	Lowery, C	68
Bohaty, B	102	Giroux, MF	77	Luo, J	80, 109, 111, 139
Booi, R	121	Goenzen, S	32, 107, 143	Lyschik, A	48, 118
Bradway, Dp	79, 123, 124	Gokhale, NH	143	Ma, Y	47
Braun, J	112	Goksel, O	115	Madsen, EL	64
Brekken, R	67	Gómez-Déniz, L	44, 53, 148	Maleke, C	139
Bruhns, OT	89	González-Fernández, J	44, 53, 148	Marangos, O	102
Brusseau, E	144	Gore, JC	48, 118	Martin, BJ	97
Burd, H	45	Grajo, J	46, 94	Masmoudi, M	113
Bush, NL	71, 126	Greenleaf, JF	119	Mastik, F	114
Cain, CA	70	Hadj Henni, A	106	Maurice, RL	77, 95
Carson, PL	121	Hager, G	116, 137	Mazza, E	91
Castañeda, B	31, 73, 136	Hall, AL	31, 121	Mazzucato, Al	57
Chan, QC	135	Hall, TJ	32, 64, 74, 143	McAleavey, SA	75
Chant, CM	96, 98, 125	Hall, TL	70	McGarry, MDJ	54
Chapelon, A	117	Hansen, HHG	30	McLaughlin, JR	62, 88
Chapelon, JY	117, 120	Harris, EJ	142	Melodelima, D	113, 117
Chase, JG	140	Harvey, SC	98	Menon, MG	75
Chen, DR	55	Haw, CJ	45	Metaxas, DN	65
Chen, H	52	Hayakawa, Y	42	Miette, V	43, 105
Chen, JG	99	Hazard, CR	31	Miga, MI	48, 118
Chen, S	119	He, X	76	Milkowski, A	68
Chesnais, S	117	Helvie, MM	121	Miller, NR	126, 142
Chopra, R	103	Higgins, P	93	Minami, A	40
Cloutier, G	77, 95, 106	Hiltawsky, K	31	Misra, A	102
Comitis, S	128	Hollenstein, M	91	Mobbs, LM	96, 98, 125
Couade, M	132	Hollister, SC	127	Montagnon, E	35
Crescenti, RA	71, 107	Hoyt, K	31, 73, 136	Montaldo, G	101
Curiel, L	103	Hsu, SJ	50,51,79,123,124,146	Morgan, EF	104
Dahl, JJ	50, 146	Huang, SW	56, 97	Mortimer, PS	126
Danilouchkine, MG	114	Huang, Y	103	Muller, M	101, 132
de Bruijn, M	102	Huang, YP	85, 99	Muller, S	67
de Korte, CL	30, 78, 122	Hynynen, K	103	Naik, N	54
Defieux, T	84, 101, 132, 133	Hyun, DG	28	Nazarian, A	104
Delabrousse, E	117	Inoue, K	40	Nelson, RC	123, 124
Déprez, JF	144	Ishida, K	42	Nightingale, KR	49, 129, 130
di Sant'Agnese, PA	73	Itoh, T	39, 41, 90, 100	Nightingale, RW	130
Dione, D	110	Jeong, CA	127	Nigwekar, P	73
Douglas, PS	51	Jeong, MK	28	Nillesen, MM	78
Duboeuf, F	144	Jen, CH	55	Noble, A	45
Dumont, DM	123, 124	Jia, C	56, 93, 110	O'Donnell, M	56, 97, 110, 121
Duncan, JS	110	Jiang, J	32, 64, 74, 143	O'Hagan, JJ	82
Dupps, WJ	63	Johnson, L	93	Oberai, AA	32, 71, 86, 88, 104, 107, 141, 143
Eder, A	145	Joseph, J	73	Olafsson, R	56, 107, 141, 143
Egorov, V	92	Joyce, JC	93	Oliveira de M Correia, M	117
		Kalayeh, MM	102		

AUTHOR INDEX

AUTHOR	PAGE	AUTHOR	PAGE	AUTHOR	PAGE
Ooba, T	40	Thijssen, JM	78, 122		
Ophir, J	36, 96, 98, 125, 138	ThitaiKumar,A	36, 125		
Osanai, O	41	Thomas, A	62		
Ou, JJ	118	Thomenius, KE	31		
Oudry, J	105	Tilson III, MD	109		
Pallwein, E	37, 38	Trahey, GE	49, 50, 79, 123, 124 130, 146		
Pallwein, L	37, 38	Tranquart, F	35		
Palmeri, ML	49, 129, 130	Treece, GM	27, 29, 33, 66		
Parker, KJ	31, 73, 136	Tsuji, K	42		
Pasternack, D	73	Tyrie, LS	109		
Patat, F	35	Uchida, T	40		
Perrey, C	31	Unsgaard, G	67		
Peters, A	140	van Beers, B	133		
Pihl, MJ	146	vanderSteen, AFW	114		
Pinton, GF	49, 50	van Hees, N	122		
Pollak, SB	92	Van Houten, EEW	54, 140		
Prager, RW	27, 29, 33, 66	Varghese, T	52, 64		
Qian, Z	65	Wakeham, NR	128		
Rachele, LV	57	Wang, MH	129		
Rahko, PS	52	Wang, S	80		
Ralleigh, G	128	Wang, SZ	85		
Reichling, S	89	Wang, Y	102		
Remeniéras, JP	35, 87	Webb, S	71		
Rénier, M	131	Weijers, G	122		
Renzi, D	62	Weitzel, WF	110		
Richards, MS	107, 121, 127, 141	Willinger, R	105		
Richter, JP	71, 107	Witte, R	56, 97		
Rigby, KW	31	Wu, ZC	31		
Righetti, R	96, 138	Xu, L	47		
Rivas, C	107	Yan, P	110		
Rivaz, H	116, 137	Yang, ES	135		
Rivens, I	47	Yang, XF	135		
Rohling, R	69, 83	Yen, PL	55		
Rollins, AM	63	Yoon, JR	88		
Rosenzweig, SJ	129	Zaman, N	128		
Roubidoux, MA	121	Zagzebski, JA	52, 64		
Rouvière, O	120	Zahiri-Azar, R	36, 115, 138		
Royer, D	131	Zellars, R	116, 137		
Rubens, DJ	73	Zervantonakis,IK	111		
Rubin, JM	56, 70, 93, 110, 121, 127, 141	Zhang, M	73		
Ruiz-Alzola, J	44, 53, 148	Zhang, Y	59		
Rump, J	112	Zheng, YP	58, 85, 99		
Sack, I	112	Zhou, YJ	58		
Salameh, N	133, 134	zurNedden, D	37, 38		
Salcudean, SE	36, 83, 115, 138				
Salomir, R	120				
Samani, A	82, 112				
Sandrin, L	43, 72, 87, 105				
Sarvazyan, A	92				
Satchithananda, K	128				
Sato, M	41				
Schmitt, C	106				
Selbekk, T	67				
Seyed-Bolorforosh, M	31				
Sinkus, R	101, 133-135				
Sinusas, AJ	110				
Sommer, AM	32, 143				
Sosa-Cabrera,D	44, 148				
Souchon, R	117, 120, 147				
Soulez, G	77, 95				
Spencer, P	102				
Strang, J	73				
Sumi, C	39-41, 90, 100				
Svensson, WE	25, 128				
Symonds-Tayler, RN	142				
Takahashi, D	39, 41, 90, 100				
Tanter, M	84, 101, 131-134				
Tanuna, A	39, 41, 90, 100				
ter Haar, GR	47				



An Evening of Latin American and Spanish Guitar Music

Roberto Capocchi Classical Guitar

Roberto Capocchi was born in Brazil, where he received music degrees from the Lins de Vasconcelos Conservatory and Carlos Gomes College. He holds a Master of Music Degree in Music Performance and a doctorate in Performance and Music Theory from the University of Arizona.

He has taught at MUSICI, Souza Lima Conservatory, Santa Fe Waldorf High School, Ortiz Middle School, Sweeney Elementary and University of Arizona, where his students have won competitions and scholarships. Currently, he has a private teaching studio in Santa Fe, New Mexico, where he resides.

Dr. Capocchi has performed to critical acclaim throughout the United States, Brazil, Mexico, Canada and Belgium. He often plays and offers workshops at festivals in North and South America. He has won top prizes in several competitions including semi-finals at the prestigious Guitar Foundation of America Solo Guitar Competition and the Portland Guitar Festival. He was the only solo guitarist selected for the 1997 Premio Eldorado de Musica. Roberto also performs regularly with local violinist Ellen Chavez de Leitner as Duo Guadalupe.

Tonight's concert features the rich sonority of the nineteenth and twentieth century classical guitar music of Central and South America and Spain. Dr. Capocchi is able to capture the unique and original musical flavor of these guitar classics.

A detailed program will be available at the Conference Dinner.

Saturday, November 3rd, 2007

Performance will start at 9:30 pm

ABSTRACTS

Sixth International Conference on the Ultrasonic Measurement and Imaging of Tissue Elasticity[©]

Santa Fe, New Mexico, USA
November 2–5, 2007

Session TUT: Tutorials

Friday, November 2 12:00P – 2:00P

122 **FROM PHYSICS TO PHYSIC – A HANDS ON APPROACH TO BREAST ELASTICITY IMAGING: IS IT JUST SHEAR STRESS AND STRAIN?**

William E Svensson^{1}*.

¹Breast Imaging and Radiology Department, Charing Cross Hospital, Imperial College Healthcare NHS Trust, Academic Health Science Centre, London, England, UK.

Real time freehand, minimal compression, comparative elasticity, breast ultrasound imaging is showing great promise as a new tool in the armamentarium of the breast ultrasonologist. This tutorial will show how the technique is used in current practice and how a good understanding of the underlying science is necessary to avoid potential pitfalls in interpretation. Real time image clips will be used to demonstrate the technique, different pathologies and the factors which effect interpretation and the clinical decision making process. The way a physician utilises his understanding of physics to explain imaging appearances will also become apparent.

The physics of the changes which occur when soft tissues are deformed are of much greater complexity than in a simple isotropic body such as a piece of steel. Soft tissues are a solid matrix with over 70% fluid content. There are many factors which affect the coefficient of elasticity within the tissues. Hooke's Law, Young's Modulus and Poisson's Ratio, boundary effects, poroelasticity and viscoelasticity are only a start to the understanding of the physics of elasticity imaging.

When tumours grow in or infiltrate through tissues, they change tissue stiffness or hardness. This change is well demonstrated on elasticity imaging in relatively homogeneous tissues. It becomes more complex in inhomogeneous tissues with different inherent stiffness or elasticity, as occurs in many breasts with mixed fat and glandular tissue. Provided uniform force fields (stress) are applied through a region of breast being imaged, good comparative distortion (strain) data can be obtained giving good comparative strain or elasticity images.

Interpretation of elasticity imaging requires a good understanding of: (1) the histology and pathophysiology of the tissues being imaged; (2) the basis of elasticity physics in an inhomogeneous matrix; (3) the factors which affect uniformity or non-uniformity of the stress and shear forces within the tissues when they are deformed; (4) the relative differences in coefficients of elasticity of the tissues within the image and in the tissues adjacent to the plane of the image.

Potential problems include: (1) over reliance on a new technique due to a lack of understanding of the way in which it works; (2) failure to correlate results with existing imaging modalities and other information such as clinical history, patient age and results of pathology; (3) failure to recognise poor technique, inhomogeneity of the tissues within, and adjacent to, the area being imaged; (4) lack of understanding of the complexities which can occur due to irregular stress or shear within the region of interest being imaged.

Early results using real time elasticity imaging in the clinic have been good at distinguishing benign from malignant tissue based on the higher coefficients of elasticity of malignant tumours compared with benign pathology and normal tissues. Though there is overlap, a significant number of benign lesions never reach the coefficients of elasticity of malignant tumours. Elasticity imaging has the potential to focus biopsies for more consistent diagnosis of cancer, determine tumour extent, measure response to therapy and to exclude malignancy with potential to reduce benign biopsy rates. Elasticity imaging, used in addition to conventional B-mode and colour Doppler, should improve diagnostic accuracy.

123 OPTICAL ELASTOGRAPHY – HIGH RESOLUTION AT A COST.

Sean J. Kirkpatrick^{1*}.

¹Oregon Health & Science University, Department of Biomedical Engineering, 20000 NW Walker Rd., Beaverton, OR, 97006, USA

Elastography in general has not caught on in the optics community as well as it has in the ultrasound community – this in spite of a long and prolific history of optical techniques in the non-destructive evaluation of materials in structures. This tutorial will attempt to address the question of “Why not?”

In general, optical techniques for evaluating mechanical behavior yield both better spatial and strain resolutions than do ultrasound and MR techniques, and the financial cost for optical elastography systems is relatively trivial. Yet, this increased resolution and affordability is gained at the expense of other considerations. Penetration depth into tissue is relatively shallow, perhaps restricting the applicability of optical elastography to the mucosal or sub-mucosal layers of internal organs and to the upper dermal layers in skin. Optical elastography is very sensitive to environmental vibrations and patient movements, making such issues as breathing artifacts and even ambient air currents a challenge to overcome. Even with these limitations, however, optical elastography is a potentially useful technique for both clinical and non-clinical applications such as in tissue engineering and developmental biology.

Similar to US elastography, most optical elastography techniques rely upon tracking the motion of speckle, both from highly coherent sources such as lasers and low-coherence sources such as super-luminescent diodes.

This tutorial will discuss:

- the origins and statistical nature of (optical) speckle;
- techniques for modeling speckle phenomena;
- high resolution methods for tracking the shifts in speckle patterns;
- elastography approaches based upon spatio-temporal contrast of translating speckle patterns;
- optical approaches to displacement and strain imaging along with estimation of viscoelastic parameters;

and practical issues regarding the implementation of optical elastography in both laboratory and clinical settings.

Where appropriate, comparisons to ultrasound-based techniques will be made.

The presentation will conclude with a discussion of where and how ultrasound and optics can interface with each other to provide improved elastographic measurements.

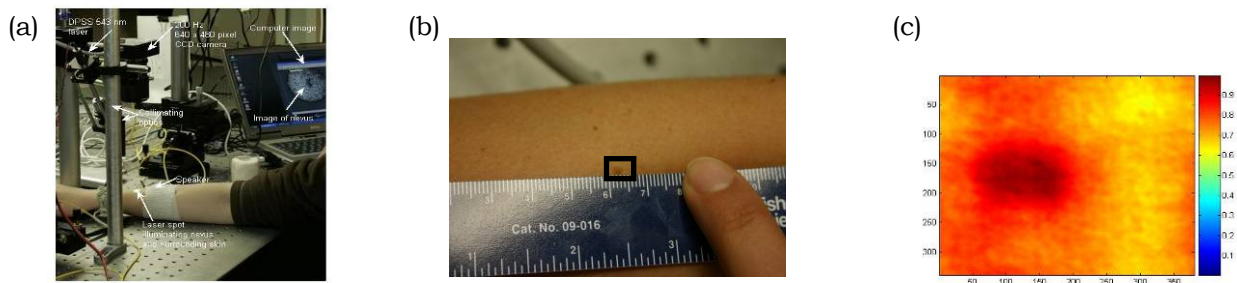


Figure 1: *In vivo* optical elastography measurements on a benign compound nevus. (c) shows the cumulative in-plane strain resulting from a driving low-frequency acoustic radiation force. The nevus displayed a higher strain than the surrounding tissue, indicating a decrease in local stiffness.

001 **NORMALISATION IN FREEHAND STRAIN IMAGING.**

GM Treece^{1*}, JE Lindop¹, AH Gee¹, RW Prager¹.

¹University of Cambridge, Department of Engineering, Cambridge, UK.

Background: In freehand quasi-static strain imaging, the stress is applied manually and varies greatly both in magnitude and distribution. Strain images hence require some form of normalisation in order to ensure that they are independent of the applied stress. This has generally been achieved by mapping the display brightness to a range between the minimum and maximum strain [1], or from zero to twice the average strain [2]. In effect, this mapping is an estimate of the stress field, and hence can be regarded as the simplest possible form of inversion: the stress field is assumed to be uniform but the magnitude is at least predicted. In practice stress is not uniform, resulting in confusing artifacts in such strain images [3].

Aims: To generate a pseudo-strain image (or pseudo-stiffness) image, closer to that which would be achieved by inversion techniques, but following the form (and simplicity) of strain normalisation schemes. This would have the two-fold advantage of a very small processing overhead and significantly improved reliability of quasi-static strain images derived from scans with non-uniform stress distributions. It would make images easier to interpret and extend the range of probe movements for meaningful data generation.

Methods: We normalise (divide) each strain estimate by a value derived from a relative stress function, s . A function $s = a$ models normalisation using average strain; however, we also use $s = a(1+by)$, which models a dissipation of stress with depth, and $s = a(1+by)(1+cx)$ which also models lateral variation in applied pressure. In each case, the constants a , b and c are found by a weighted least-squares fit to the strain data. The underlying assumption is that the Young's Modulus in the anatomy does not itself vary in the same manner as the stress model. At each pixel, we display the strain divided by some multiple (typically two) of the relative stress estimate, s , calculated at pixel (x, y) . The normalised data are clamped between zero and one, then mapped to display brightness or colour corresponding to pseudo-strain.

Results: We have tested numerous quasi-static freehand data sets acquired with a Dynamic Imaging Ltd Diasus and a Terason T3000, equipped with live streaming RF interfaces respectively via a Gage CompuScope 14200 analogue to digital conversion card, and an ActiveX control. Acquisition and live display of the RF data was performed by Stradwin software, at 5 to 10 frames per second. The images below are from a Terason T3000 scan with a 5–8 MHz linear probe at a 4 cm depth, of a Computerised Imaging Reference Systems phantom. Figure 1 shows a typical scan with gradually oscillating slight axial pressure. The stress dissipates with depth, but this apparent hardening is corrected in (b), also revealing the lower quality of the data at this depth. Lateral pressure variation is also corrected in (c), resulting in a uniform brightness over the uniform background. Figure 2 shows data acquired by rocking the probe to and fro laterally. This generates meaningless data with conventional schemes, but the new technique shows good definition, except below the axis of rotation where the movement is entirely lateral. With image persistence, it is possible to produce good pseudo-strain images even from such awkward probe motion.

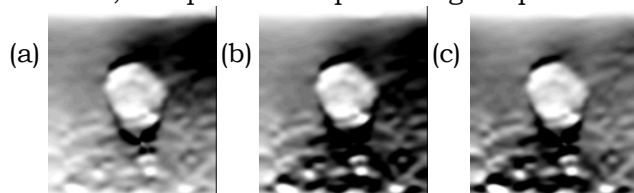


Figure 1: Strain images from a biopsy phantom:
(a) normalized to a ; (b) normalised to $a(1+by)$;
(c) normalised to $a(1+by)(1+cx)$

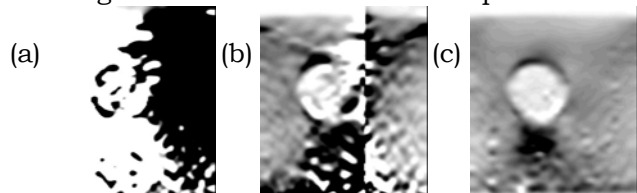


Figure 2: Strain from probe rotation: (a) normalized to a ;
(b) normalised to $a(1+by)(1+cx)$;
(c) with persistence

Conclusions: The technique enables easily interpretable strain images to be generated from a wider range of probe movements, with negligible processing overhead. The exact form of the relative stress function may require optimisation for specific targets – if, for instance, it is known that the stiffness really does gradually increase with depth – however, we have not yet found this to be necessary in practice.

Acknowledgments: Graham Treece is supported by a Fellowship from the Royal Academy of Engineering and the EPSRC.

References:

- [1] JE Lindop, GM Treece et al. 3D elastography using freehand ultrasound. UMB 32(4):529–545, 2006.
- [2] J Jiang, TJ Hall and AM Sommer. A novel image formation method for ultrasonic strain imaging. UMB 33(4):643–652, 2007.
- [3] J Ophir, et al. Elastography: a quantitative method for imaging the elasticity of biological tissues. Ultras Imag, 13:111–134, 1991.

Background: In strain imaging using quasi-static compression, displacements are first determined from successive image frames, and then are differentiated to produce strain images [1]. A major problem with this approach is that the strain image quality is dependent on the amount of manually applied compression.

Aims: In order to assess the quality of strain image, we measured the non-uniformity of compression using a quality metric computed from the estimated displacements. Based on the quality metric, we regularized the strain image and improved the strain image quality by applying adaptive and motion-compensated persistence.

Methods: We estimate displacements from data acquired before and after compression, and use them to estimate strain. Because displacements in soft tissue tend to be proportional to the amount of applied compression, a one-dimensional graph that connects the displacements of all scan lines at a fixed depth may be a good indicator of strain image quality. For a medium with a uniform elasticity distribution under a uniform compression, all scan lines should have the same displacement at some selected depth. However, the displacement curve at some depths exhibits a complicated pattern depending on both the manual compression applied and the elasticity distribution of a medium of interest. We perform second-order polynomial curve fitting to the displacement curve. Then the average amount of compression can be determined from the mean of the fitting second-order polynomial curve. The sum of squared errors between the displacement curve and its fitting curve represents the error of estimating displacements due to hand movements or medium characteristics. If compression is applied such that compressive force is applied on one side of a transducer and tensile force on the other side of it, the fitting curve has a zero-crossing and the scan line corresponding to the zero-crossing point has an erroneous displacement estimate, since it implies that there has been no compression applied to the scan line. When the compression force applied to one side of the transducer is greater than that applied to the other side, the compression profile inside the medium becomes non-uniform and the CNR of strain images differs from one scan line to another. In this case, we can use the fitted second-order polynomial curve to compensate the compression for its non-uniformity. Noise in strain image can be further reduced in successive strain image frames using adaptive persistence processing based on the mean of the fitting curve and the sum of squared errors between it and the estimated displacement curve. Our algorithm has been implemented on a clinical scanner (Accuvix XQ, Medison, Seoul, Korea) using Microsoft Visual C++[®]. We conducted experiments with a 7.5 MHz linear array, acquired both I and Q data in real time, and successfully verified the algorithm on a PC. We estimated displacements in consecutive image frames, fitted a second-order polynomial function to them, and assessed strain image quality from its mean and variance.

Results: We confirmed that either too large or small mean and variance degraded the CNR of strain image. We also found that when the fitting function has a zero-crossing, the strain image quality suffers. Using adaptive persistence based on these characteristics, we have been able to produce high-quality moving images of strain. Implemented in software on the scanner, our method can produce strain images at a rate of 25 frames/s.

Conclusions: We implemented a new regularization technique on a commercial clinical scanner to obtain quality strain images. By compensating for the non-uniformity of manual compression applied to elasticity phantoms and humans, we obtained real time strain images whose quality is uniform over all image regions.

Reference:

- [1] A. Pesavento, M. Krueger, and H. Ermert, "A Time-Efficient and Accurate Strain Estimation Concept for Ultrasonic Elastography Using Iterative Phase Zero Estimation", *IEEE Trans. On UFFC*, vol. 46, no. 5, Sept., 1999.
-

Background: Real time, freehand, quasistatic strain imaging holds promise for numerous clinical applications, so the development of a successful clinical interface has become important. After strain estimates have been calculated, there are still many options regarding the ultimate display. Sophisticated “inversion” or “normalisation” [1] schemes may partly adjust for aspects of the varying stress field in the tissue, and data from multiple frames may be compounded to boost the signal-to-noise ratio. Relatively superficial aspects of the display format may also significantly affect its usefulness for sonographers.

Aims: We describe a novel display method that not only reduces the level of noise in strain image sequences, but also (1) presents data in an intuitively meaningful format, (2) avoids presenting data that are dominated by errors and (3) provides intelligent feedback to support sonographers learning the required scanning technique.

Methods: The variance of each strain estimate from the analysis of radiofrequency (RF) ultrasound data is calculated following the method described in [2]. Subsequently the strain estimates are converted to “pseudo-strain” in a normalisation stage, applying a scaling that varies over image position; the variance estimates are also scaled accordingly [1]. The precision of each pseudo-strain estimate is the reciprocal of its variance. To reduce the level of pseudo-strain noise, we perform compounding, both over time (i.e., persistence) and spatially (in images with recorded 3D positions), weighting the strain value at every pixel by the corresponding precision estimate. We also infer the precision of each compounded pseudo-strain estimate. The final display employs a two-dimensional colour map to indicate precision as well as pseudo-strain, e.g., colour may be used to indicate pseudo-strain, with brightness indicating precision, or greyscale may be used to indicate pseudo-strain, fading to a masking colour where the precision is poor.

Results: In common with other systems, we provide a simultaneous B-mode display alongside pseudo-strain when undertaking real time scanning. Images from real time freehand scanning using the 5–8 MHz 7L3-V Terason probe are shown in Figures 1 and 2, illustrating the advantages of the new system in terms of usability and simplicity of image interpretation. The example colour maps are: (1) strain indicated by green-magenta scale with precision indicated by intensity; (2) greyscale strain with a red mask. The images are best viewed in full colour, but after black and white printing the “green-magenta” images indicate quality, and strain is indicated by greyscale in the “black-white” images.

Conclusions: The novel display has been welcomed by our clinical collaborators and is being incorporated in the strain imaging system for which clinical trials have recently begun at Addenbrooke’s Hospital, Cambridge, England, UK.

References:

- [1] JE Lindop, GM Treece, AH Gee, RW Prager. An intelligent interface for freehand strain imaging. Technical report CUED/F-INFENG/TR 578, 2007.
- [2] JE Lindop, GM Treece, AH Gee, RW Prager. Dynamic resolution selection in ultrasonic strain imaging. Technical report CUED/F-INFENG/TR 566, 2006.

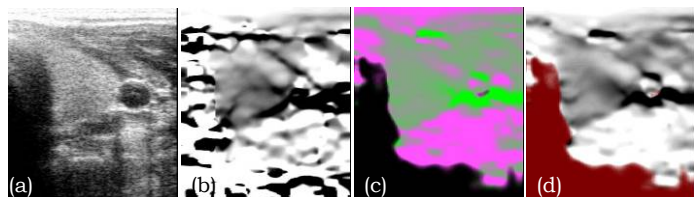


Figure 1: Images from a freehand scan of a thyroid.

- (a): B-scan.
- (b): typical pseudo-strain image.
- (c): first example pseudo-strain image using the new interface (green-magenta/black colour map).
- (d): second example of new interface (black-white/red colour map). Some tissue regions in this scan provide no ultrasound data, so the pseudo-strain estimates inevitably consist only of noise, but these are not displayed by the new interface, which also reduces the noise in the displayed regions by means of precision-weighted persistence.

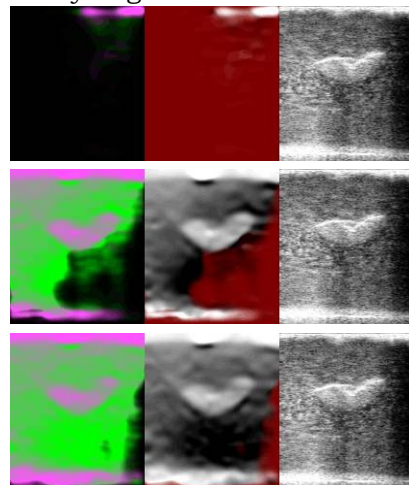


Figure 2: Three successive displays at the start of freehand scanning of a gelatin phantom with a relatively stiff inclusion, showing strain (both colour maps) next to B-mode images. When the probe initially comes into contact with the phantom, the first B-scan precedes the availability of strain data. In any single freehand strain image it is rare that the entire display contains good strain data, but the display rapidly fills with good data because of the persistence.

046 **COMPOUNDING NON-INVASIVELY OBTAINED STRAIN IMAGES AT LARGE INSONIFICATION ANGLES.**

Hendrik HG Hansen^{1}, Richard GP Lopata¹, Chris L de Korte¹.*

¹Clinical Physics Laboratory, Radboud University Nijmegen Medical Center, Nijmegen, The NETHERLANDS.

Background: Intravascular ultrasound elastography is a powerful technique for vulnerable plaque identification. However, its invasive character prevents the technique from being applied on a broad scale. Therefore, conversion to a non-invasive technique is needed. When measuring non-invasively, the radial strain and ultrasound beams are not aligned, which requires the use of axial and lateral strain. However, due to the lower lateral resolution the resulting strain images are of poorer quality.

Aims: Improvement of image quality, by compounding of non-invasively acquired strain images at beam-steered angles of -45, 0 and 45 degrees is investigated. Various compounding techniques are compared.

Methods: A homogeneous vessel phantom was created by filling a cylindrical mold with a 9% PVA solution with 1% SiC scatterers and subjecting it to three freeze thaw cycles. To create the lumen, a rod was placed concentrically before freezing and removed afterwards. The phantom was placed in a saltwater tank and attached to a saltwater column. A 5.3% salt solution was used to minimize speed of sound differences between solution and phantom material. Radiofrequency (RF) data at different intraluminal pressures and at the different angles were obtained using a Philips SONOS 7500 modified for large angle beam-steering and equipped with an L11-3 (3 to 11 MHz) linear array transducer. A 2D coarse-to-fine strain algorithm [1] that used a 2D least squares strain estimator was applied to calculate lateral and axial strain data. By principle component analysis and by radial projection of axial and lateral strain, radial strain estimates at all three angles were acquired. Compound images were constructed of weighted segments of these radial strain estimates. Different segment combinations and weighting methods were considered; compounded elastograms were based on principal strain images acquired at different angles or based on axial strain images acquired at different angles complemented with lateral or principal strain values for regions where axial and radial strain are perpendicular (3 and 9 o'clock). The elastographic SNR of the images was calculated, assuming a $1/r^2$ strain decay in the vessel wall.

Results: Radial strain images determined by principal component analysis of data acquired at one angle revealed strain values in accordance with theory. However, artifacts in the lower part of the vessel at 5 and 7 o'clock were present. These artifacts were also present in the lateral strain images and are caused by a remaining speed of sound mismatch between vessel wall and salt solution [2]. A compound image created by averaging of the principal strain images resulted in an image with similar SNR. However, the larger the angle between the principle strain and the ultrasound beam, the more the lateral strain contributes to the principle strain. Based on this knowledge, an increase in SNR of 3 dB could be achieved. The contribution of the individual principle strain images was gradually reduced towards -90 and +90 degrees with respect to the ultrasound beam. However, in some regions, artifacts were still visible and resolution was decreased. To further diminish the deterioration caused by the lateral strain contribution, another approach was investigated. Radial projections of the axial strains in regions between -30 and +30, and 150 and 210 degrees with respect to the ultrasound beam were determined and combined using a triangular window with 15 degrees overlap. The images were complemented with lateral or principal strain values at 3 and 9 o'clock, in which the latter resulted in slightly higher SNR values (+0.5 dB). Although the resulting compounded elastograms are based on axial strain estimates with higher elastographic SNR than the principal strain images, lower SNR values were measured than in the compounded principal strain images. However, more detail was observed in these images. Acquiring data at more than three insonification angles might be beneficial to this latter technique.

Conclusions: Combining data obtained at large insonification angles, enables constructing radial strain images of high quality.

Acknowledgements: The support of the Dutch Technology Foundation (STW) and Philips Medical Systems is acknowledged.

References:

- [1] R.G.P. Lopata, M.M. Nillesen, I.H. Gerrits, L. Kapusta, J.M. Thijssen, C.L. de Korte. BiPlane Cardiac Strain Imaging: a Feasibility Study, submitted.
- [2] R.S. Thompson, C. Macaskill, W.B. Fraser, L. Farnell. Acoustic Intensity for a Long Vessel with Noncircular Cross Section. IEEE Trans Ultrason Ferroelectr Freq Control. 2004 May; 51(5):566-75.

Background: Freehand elastography has been shown to be effective at imaging the stiffness changes caused by High Intensity Focused Ultrasound (HIFU). Fromageau et al. developed a direct strain estimation algorithm that avoids the noise introduced by the differentiation of displacements in standard elastography algorithms [1]. We have modified the direct strain algorithm to provide improved strain estimates.

Aims: The aim of this study is to show that the direct strain algorithm presented can be used to visualize HIFU induced lesions.

Methods: A research version of the GE Logiq 9 was modified to produce relative strain maps using the direct strain algorithm presented. HIFU lesions were generated in fresh veal liver samples. The tissue samples were embedded in a 6.9% gelatin mold. An M12L transducer was used to gently compress the liver sample and real-time elasticity images were made. The hand manipulation of the transducer was adjusted to give the best elasticity images. The liver sample was then sliced at approximately the plane used for imaging so that a visual inspection of the tissue could be made.

Direct Strain Estimation Algorithm: Fromageau [1] estimated the strain by iteratively finding the zero of the cross-correlation between the real part of the post-compression signal (S(t)) and imaginary part of the pre-compression signal (R(t)). Using only the real signals reduces the computational burden at the cost of increased noise in the estimate. Our approach finds the zero of the imaginary part of the complex cross-correlation without simplification. This means that our estimate uses all of the data, not just half, and, therefore, has improved noise characteristics. The denominator of Equation 1 is more robust for broadband signals than that used in the original Fromageau algorithm. The algorithm iterates Equation 1 to obtain the strain estimate.

$$\Delta\varepsilon = (\varepsilon - \varepsilon') = \frac{\text{Im}\left\{\int R(t)S^*(t)dt\right\}}{\omega_0 \int \|R(t)\|^2 t dt} \quad \text{Equation 1}$$

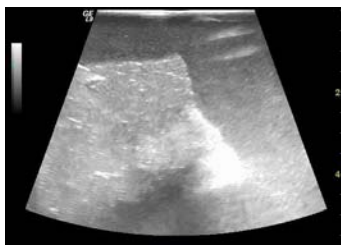
Where $\Delta\varepsilon$ is the correction to the strain from the initial guess or the previous iteration, ε' is the strain estimate, ε is the actual strain, ω_0 is the angular frequency, and all integration is done over the window of the estimation.

Results: Figure 1 shows the B-mode image, an elasticity image, and the corresponding tissue cross-section for a HIFU induced lesion. The lesion is visible on the B-mode image but is visualized with better contrast on the elasticity image. The size and location of the lesion on the strain image is well correlated with the visual appearance of the lesion.

Conclusions: The direct strain algorithm is able to visualize the stiffness changes in the tissue caused by HIFU lesion formation.

References:

- [1] J. Fromageau, P. Delachartre. Description of a new strain and displacement estimator for elastography. IEEE Ultrasonics Symposium, 2003, pp. 1911-1914.



B-mode



Elasticity Image



Photograph of Lesion

Figure 1: Comparison of B-mode, elasticity image, and photograph of *ex-vivo* HIFU treated veal liver.

Background and Aims: Current strain imaging methods display frame-to-frame strain which is related to the tangent or cord modulus of the material. The secant modulus images show the distribution of relative intrinsic properties that are obtained with constraint functions that trade off spatial resolution for contrast and a reduction in artifacts. Our goal was to compare frame-to-frame strain images, accumulated strain images and relative secant modulus images of *in vivo* breast tissue to determine their relative merits for distinguishing between benign and malignant lesions.

Methods: Radiofrequency (RF) echo data was acquired from a Siemens Elegra (Siemens Medical Solutions USA, Inc., Issaquah, WA, USA) with real-time freehand elasticity imaging of *in vivo* breast tissue. An offline 2-D block matching algorithm was used to estimate tissue displacements and strain for a sequence of data. A reference frame in the sequence was chosen, and the displacement field for each frame of RF data was used to warp that RF field, and similarly the strain image, back into the coordinate system of the reference frame (referred to as motion-compensated images) providing a temporally stationary region of interest. The motion-compensated strain and deformation fields were then accumulated from the least to the most deformation within the sequence, providing a sequence of accumulated strain images and accumulated displacement fields. Accumulated strain image sequences have been obtained for a total of 49 benign (27 fibroadenomas, FA) and 46 malignant (31 invasive ductal carcinoma, IDC) *in vivo* breast lesions. The accumulated displacement fields were then used to generate secant modulus reconstructions using a quasi-Newton method. Modulus reconstruction has been performed so far on five fibroadenomas (FA, benign) and five invasive ductal carcinomas (IDC, malignant).

Results: Accumulated strain images provide higher contrast-to-noise ratio and better lesion boundary definition than in conventional strain images. Typically, malignant lesions have either ill-defined or micro-lobulated boundaries while benign lesions tend to have more clearly defined boundaries, as seen in the figures below. The accumulated strain images also provide higher spatial resolution than the modulus reconstructions.

Conclusions: Initial comparisons of accumulated strain images and conventional strain images show that accumulated strain images provide better lesion boundary definition and that provides additional information for distinguishing between benign and malignant solid breast lesions. There are tradeoffs between accumulated strain images and secant modulus images. The advantages of accumulated strain images are the ability to retain changing lesion contrast and higher spatial resolution. The secant modulus images provide a quantitative difference in the elastic modulus but lower spatial resolution.

Acknowledgements: We are grateful for the support from the NIH (R01-CA100373) and NSF, and to colleagues at the Mayo Clinic in Rochester, MN, USA, and the Charing Cross Hospital in London, UK, for providing some of the data used in this study.

Figure 1: Invasive Ductal Carcinoma

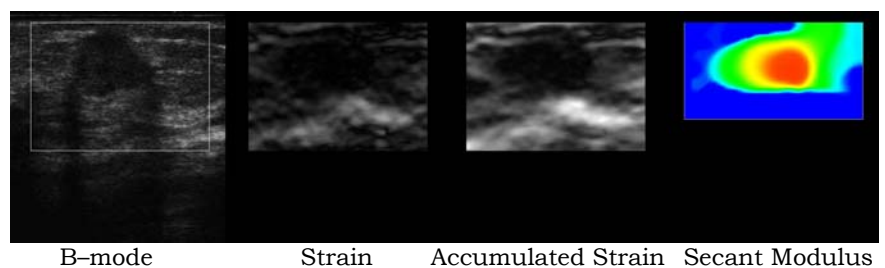
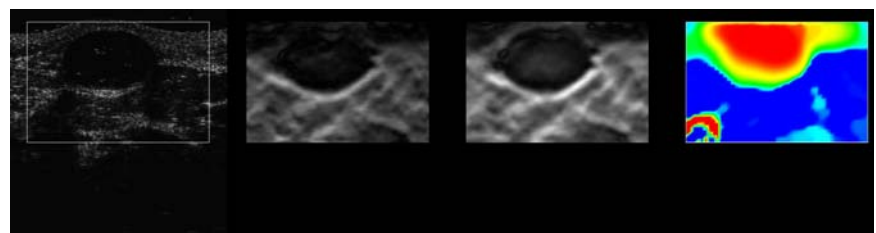


Figure 2: Fibroadenoma



004 **STRAIN ESTIMATION BY NON-PARAMETRIC SURFACE REGRESSION.**

JE Lindop^{1}, GM Treece¹, AH Gee¹, RW Prager¹.*

¹University of Cambridge, Cambridge, England, UK.

Background: For all forms of displacement estimation, the level of noise in strain images is also affected substantially by the method of strain (i.e., gradient) estimation. The most popular method is piecewise-linear least squares regression [1], but the statistics literature offers a wealth of alternatives [2], such as non-parametric surface regression, i.e., fitting a unique surface to a grid of displacement estimates, globally minimising the total cost of weighted residuals and roughness (i.e., second derivatives squared).

Aims: To improve the accuracy of strain estimation by applying non-parametric surface regression.

Methods: Each image derives from a $w \times h$ grid of displacement estimates, with associated precision data calculated per $c/(1-c)$, where c is the correlation coefficient between pre- and post-deformation displacement estimation windows. Non-parametric surface regression requires the numerical inversion of a symmetric positive-definite matrix of size $w \times h$, describing the cost derivative with respect to every grid position. For a direct solution, we exploit matrix sparsity in efficient Cholesky decomposition. We have also developed iterative methods that converge rapidly on the same solution. The regression surface is extended by B-spline approximation to fill the grid of image pixels; gradients are taken by differencing neighbouring pixels. We compare with the familiar method of piecewise-linear least squares regression, testing a wide range of kernel sizes, again extending to image pixels by B-spline approximation.

Figure 1: Field II simulation [3] – diagonal band pattern against a 1% background strain: fine bands (width 1.5mm) within coarse bands at 14mm intervals. Top left: B-scan. Top right: conventional least squares (kernel sizes: 3×3 , 9×9 , 15×15 and 21×21). Bottom left: difference of successive displacements. Bottom right: surface regression (relative smoothness: 0.01, 5, 30 and 100). High decorrelation away from the focus results from shear with lateral blurring. Surface regression preserves fine detail where possible, and also makes optimal use of poorer data.

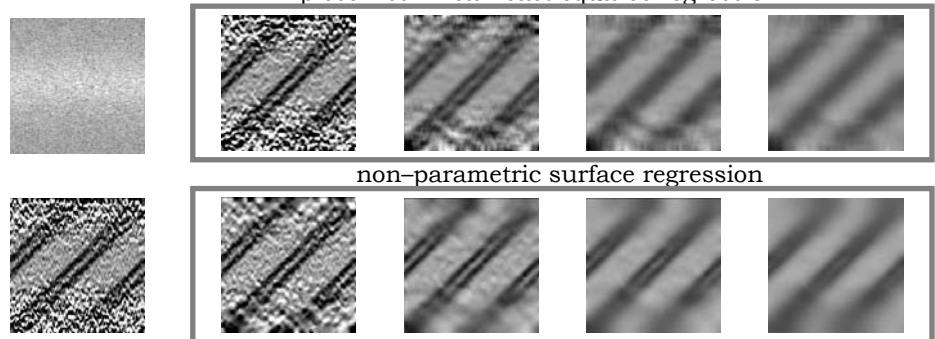


Figure 1: Field II simulation [3] – diagonal band pattern against a 1% background strain: fine bands (width 1.5mm) within coarse bands at 14mm intervals. Top left: B-scan. Top right: conventional least squares (kernel sizes: 3×3 , 9×9 , 15×15 and 21×21). Bottom left: difference of successive displacements. Bottom right: surface regression (relative smoothness: 0.01, 5, 30 and 100). High decorrelation away from the focus results from shear with lateral blurring. Surface regression preserves fine detail where possible, and also makes optimal use of poorer data.

Results: Figures 1 and 2 are examples for 128×115 grids of data output by a real time displacement estimator, spanning $40\text{mm} \times 40\text{mm}$ in physical space. Surface regression takes $\sim 5\text{s}$ by our Cholesky method. The fastest iterative method usually takes $\sim 20\text{ms}$, but some frames converge slowly.

Conclusions: Progress in surface regression may substantially improve real time strain images. Partly, this is by suitable modulation of the resolution [4].

References:

- [1] F Kallel, J Ophir. A least-squares strain estimator for elastography. *Ultrason Imag*, 19:195–208, 1997.
- [2] PJ Green, BW Silverman. *Nonparametric regression and generalized linear models: a roughness penalty approach*. Chapman & Hall, 1994.
- [3] JA Jensen. Field: a program for simulating ultrasound systems. *Proc 10th Nordic-Baltic Conf Biomed Imag*, 4(1):351:353, 1996.
- [4] JE Lindop, GM Treece, AH Gee, RW Prager. Dynamic resolution selection in ultrasonic strain imaging. Technical Report CUED/F-INFENG/TR 566, 2006.

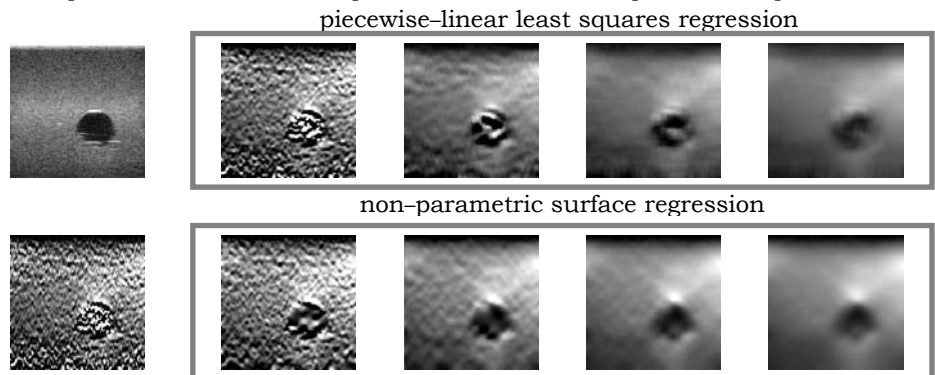


Figure 2: Freehand scan of a cyst in a breast biopsy phantom. Image ordering is as per Figure 1. Data from the hypoechoic region have very poor SNR, so the displacement estimates are also extremely noisy, resulting in misleading images from conventional least squares, even for very large kernels. On the other hand, global optimality of the lower regression surface means that it smoothes poor data correctly, without introducing excessive blurring elsewhere in the image.

Background: The problems of an isotropic homogeneous infinite plate weakened by a curvilinear hole have been investigated by many authors. Some authors used Laurent's theorem to express the solution, complex potential functions, Goursat functions $\phi(z)$ and $\psi(z)$ where $z=x+iy; i=\sqrt{-1}$ as a power series. Others, used complex variable method of Cauchy type integrals to express Goursat functions in a convenient form for applications by spending a rapid time.

Aims: The complex variable method, Cauchy method, is applied to derive exact expressions for Goursat functions for the boundary value problem of an infinite plate weakened by a curvilinear hole in the presence of uniform heat flowing in the direction perpendicular to the hole.

Methods: If heat, $\Theta=qy$, is flowing uniformly in the negative direction of y - axis, where the increasing temperature Θ is assumed to be constant across the thickness of the plate i.e. $\Theta=\Theta(x, y)$, and q is the constant temperature gradient. Thereon, the uniform flow of heat is distributed by the presence of an insulated curvilinear hole C , and the heat equation satisfies the relation:

i) $\nabla^2\Theta=0, \nabla^2 = \frac{\partial^2}{\partial x^2} + \frac{\partial^2}{\partial y^2} = \frac{\partial^2}{\partial r^2} + \frac{1}{r} \frac{\partial}{\partial r} + \frac{1}{r^2} \frac{\partial^2}{\partial \theta^2}$, ii) $\frac{\partial \Theta}{\partial r} = 0$ on the boundary $r = r_0$.

The first and second boundary value problems in the plane theory of thermoelasticity are equivalent to finding two analytic functions $\phi_1(z)$ and $\psi_1(z)$. These two functions must satisfy the boundary conditions $K\phi_1(t) - t\phi_1'(t) - \psi_1(t) = f(t)$, where for the first boundary value problem $K = -1$, $f(t)$ is a given function of stress, while for the second boundary value problem $K = \kappa > 1$, and $f(t)$ is a given function of strain, κ is called thermal conductivity of the material and t denotes the affix of a point on the boundary.

In the plane theory of thermoelasticity the two complex functions $\phi_1(z)$ and $\psi_1(z)$ are written in the forms $\phi_1(z) = -\frac{S_x + iS_y}{2\pi(1+\kappa)} \ln \zeta + c\Gamma \zeta + \phi(\zeta)$, $\psi_1(z) = \frac{\kappa(S_x - iS_y)}{2\pi(1+\kappa)} \ln \zeta + c\Gamma^* \zeta + \psi(\zeta)$, here S_x and S_y are the components of the resultant vectors of all external forces acting on the boundary, Γ and Γ^* , which also are complex constants that represents the stresses at infinity.

The stress components for the problem are given by $\sigma_{xx} + \sigma_{yy} = 4G[\phi'(z) + \overline{\phi'(z)} - \lambda\Theta]$ and $\sigma_{yy} - \sigma_{xx} + 2i\sigma_{xy} = 2G\left[\frac{\partial^2 \Phi}{\partial y^2} - \frac{\partial^2 \Phi}{\partial x^2} + 2i\frac{\partial^2 \Phi}{\partial x \partial y}\right] + 4G[\bar{z}\phi''(z) + \Psi''(z)]$ where $\lambda = (1 + \nu) \alpha/2$ is the coefficient of heat transfer and G is the shear modulus, α is a scalar which presents the coefficient of the thermal expansion and ν is Poisson's ratio. The thermoelastic potential $\Phi(x, y)$ satisfies the partial differential equation $\nabla^2 \Phi(x, y) = (1 + \nu)\alpha\Theta$.

Using the rational mapping function $z = \omega(\zeta) = l\zeta + \sum_{j=1}^M m_j \zeta^{-j}$, $l = l_1 + il_2$, $m = m_{j1} + im_{j2}$, in the boundary conditions adopted by using the complex variable method of Cauchy type integrals gives the stress components of the problem. Noteworthy, that $\omega'(\zeta)$ must not vanish or become infinite for $|\zeta| > 1$.

The process of the complex variable method of Cauchy type integrals can be amounted in multiplying both sides of the boundary conditions by $\frac{1}{2\pi i} \frac{1}{\sigma - \zeta}$ and integrating with respect to σ on γ . This gives the Goursat functions $\phi(\zeta)$ and $\psi(\zeta)$.

Results: The forms of Goursat functions are resulted as follows:

$$-K\phi(\zeta) = A(\zeta) - \frac{i\bar{\Gamma}^*}{\zeta} - \frac{1}{|\zeta|^2} \sum_{j=1}^M \sum_{k=0}^{j-1} \frac{1}{(j-1)! \binom{j-1}{k}} k m_j \overline{\phi^{j-k}(0)} \zeta^{k+1} - \frac{1}{|\zeta|^2} \sum_{j=1}^M \frac{m_j N(0)}{\zeta^j} \quad \text{and} \quad \psi(\zeta) = \frac{K\bar{\Gamma}}{\zeta} \frac{\alpha \zeta^{-1}}{\omega(\zeta)} [\phi(\zeta) + \overline{N(\zeta)}] + \frac{i}{|\zeta|^2} \sum_{j=1}^M \sum_{k=0}^{j-1} \frac{1}{(j-1)! \binom{j-1}{k}} k \bar{m}_j \phi^{j-k}(0) \zeta^{k+1} + \frac{i}{|\zeta|^2} \sum_{j=1}^M \bar{m}_j N(0) \zeta^j + B(\zeta) - B$$

where $A(\zeta) = \frac{1}{2\pi i} \int_{\gamma} \frac{F(\sigma) d\sigma}{\sigma - \zeta}$, $\overline{\phi^{j-k}(0)} = \frac{1}{K} \overline{A^{j-k}(0)}$, $k=0,1,2,\dots,j-1$, $B(\zeta) = \frac{1}{2\pi} \int_{\gamma} \frac{\overline{F(\sigma)} d\sigma}{\sigma - \zeta}$, $B = \frac{1}{2\pi} \int_{\gamma} \frac{\overline{F(\sigma)} d\sigma}{\sigma}$, $N(\zeta) = i\bar{\Gamma} - \frac{S_x - iS_y}{2\pi(1+\kappa)} \zeta$.

Conclusions: The importance of the work comes from its wide applications in mathematical engineering and mathematical physics. The works of the most previous authors can be considered as special cases of this work.

References:

[1] N.I Muskhelishvili, Some Basic Problems of Mathematical Theory of Elasticity, Holland, 1953.
 [2] H. Parkus, Thermoelasticity, Springer-Verlag, 1976.
 [3] M.A. Abdou, Fundamental problems for infinite plate with a curvilinear hole having finite poles, Appl. Math. Comput. 125(2002)177-193.

022 **MEASUREMENT OF THE NATURAL PULSATILE MOTION OF THE CEREBRAL TISSUE DUE TO CARDIAC CYCLES.**

Emmanuel Montagnon¹, Jean-Pierre Remeniéras¹, Melouka Elkateb^{1*}, F. Tranquart², F. Patat¹.

¹Tours University, LUSI-CNRS FRE 2448, 10 Bld Tonnelles, 37032 Tours, FRANCE;

²INSERM U619, CHU of Tours, FRANCE.

Background: Brain tissue pulsatility imaging (BTPI) is a new ultrasonic technique being developed to map brain movements due to perfusion [1]. The technique is based in principle on plethysmography, a technology used to measure expansion of a whole limb or body part due to perfusion. During a cardiac cycle, perfused tissue expands when arterial inflow exceeds venous outflow and relaxes later in the cardiac cycle when venous drainage dominates.

Aims: A feasibility study was conducted to determine if BTPI could be used to map tissue displacements during cardiac cycles. The efficient frame rate of 60Hz allows assessment of spatial and temporal evolution of these displacements in the ultrasound image plane. The circle of Willis, situated at the center of the brain, dispatches arterial inflow to the peripheral tissues. The goal of our study is to characterize displacement signature of the brain tissue to differentiate between global motion and mechanical wave propagation.

Methods: Data were acquired using a medical ultrasound scanner (Acuson Antares), with a 2 MHz curved array and frame rate varying from 10 to 60 Hz. The classical RF line is sampled at 40 MHz, has 5000 points, and each image is compounded of typically one hundred lines. The duration of acquisition was about seven cardiac cycles. Displacements were estimated by 1D correlation method with a noise level of 0.5 μ m. Repeating this process to consecutive lines results in a 2D displacement matrix obtain every 16 ms.

Results: Due to the difficulty of holding the probe precisely for a few seconds, some of the data sets were strongly decorrelated. However, it was possible to clearly observe systole peaks with displacement estimations. Figure 1 shows tissue motion versus depth during two cardiac cycles. The amplitude of these displacements was typically 30 μ m, and varied with depth. Figure 1 shows the decrease of these displacements from the center of the brain (35 μ m near the circle of Willis) situated at 10cm depth to 5 μ m near the skull wall. Figure 2 shows differences between displacements at three different fixed depths.

Conclusions: Natural pulsatile motion of brain tissue can be assessed with ultrasonic methods. The image resulting from displacement matrix permits us to say that tissue moves at any depth, and amplitude displacement decreases with distance from circle of Willis. Preliminary results in Figure 2 highlight the presence of a time delay between displacements at different depths. This particular result is currently in progress at our laboratory.

Acknowledgements: Siemens-Acuson for their assistance in providing access to RF data (URI).

References:

- [1] JC Kucewicz, "Functional Tissue Pulsatility Imaging During Brain Stimulation", *Ultrasound Med Biol.* 2007 May; 33(5):681-90.

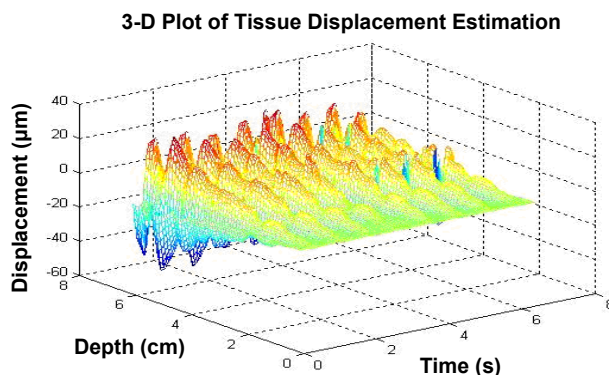


Figure 1: Tissue motion vs depth during seven cardiac cycles.

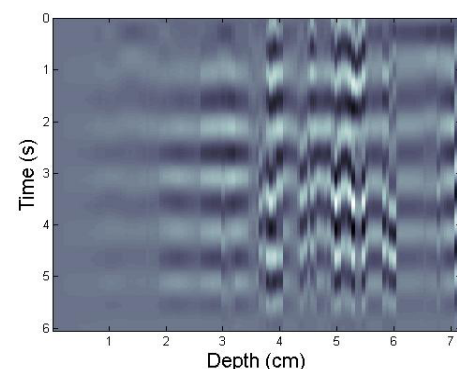


Figure 2: Variation of the displacements with depth.

030 REAL-TIME AXIAL SHEAR STRAIN ELASTOGRAPHY.

R. Zahiri-Azar^{1*}, A. Thitai Kumar², J. Ophir², S.E. Salcudean¹.

¹The University of British Columbia, Vancouver, BC, Canada; ²The University of Texas Health Science Center Houston, Houston, TX, USA.

Background: It is known that malignant tumors of the breast are generally more firmly bonded to their surroundings than benign tumors [1]. When an inhomogeneous tissue is subjected to an axial compression, it experiences not only normal strains (axial/lateral) but also shear strains at internal tissue boundaries. Recently, it has been demonstrated through simulation, experiments, and *in-vivo* imaging that axial-shear strain elastograms provide a way to visualize bonding information at the boundary [2].

Aim: To evaluate the feasibility of implementing a real-time axial-shear strain imaging system.

Methods: Real-time axial-shear strain imaging was implemented on a Sonix-RP Ultrasound (US) machine (Ultrasonix Medical Corp., Richmond, Canada) as a client-software. The software connects to the US machine and captures RF frames and B-mode images. The relative/absolute displacements are then estimated from sets of RF signals. Time Domain Cross Correlation with Prior Estimates (TDPE), a predictive-corrective motion tracking algorithm [3] was used to estimate the axial component of the displacement. The Least Squares Strain Estimator (LSE) with adjustable kernel size was then used as a strain estimation algorithm [4]. Finally, the estimated axial-shear strains were spatially filtered, scan converted, color coded, and displayed on the screen beside the corresponding B-mode images in real-time at 30 frames per second. For qualitative validation, several experiments were run using two types of phantoms with similar mechanical but different bonding properties. Both phantoms had stiffer (x2) cylindrical inclusions. One phantom had a firmly-bonded inclusion while the other phantom had a loosely-bonded inclusion. The phantoms were imaged to a depth of 70mm with a linear array of 128 elements transducer with 3.3-lines per millimeter in the lateral direction with a 6.6MHz center frequency digitized at 40MHz. A mechanical compressor was used to apply the axial compression. RF frames were captured and processed in real-time. Axial displacements were estimated using 1mm windows with 50% window overlap. Both axial strains and axial-shear strains were estimated using LSE with a kernel size of 6.

Results: Screenshots from the real-time elastography movie obtained from the phantom experiments are shown in Figure 1 below. The axial-shear strain elastograms obtained from the real-time implementation were comparable to those reported in Thitai Kumar et al. 2007 [2] using off-line processing.

Conclusions: The results demonstrate the feasibility of producing axial-shear strain elastograms in conjunction with axial strain elastograms in real-time. Furthermore, the real-time feedback can provide insight during data acquisition or even diagnosis to determine whether satisfactory manual compressions are being applied. In the future, attention must be paid to the development of methods to normalize the results for the applied compression [2].

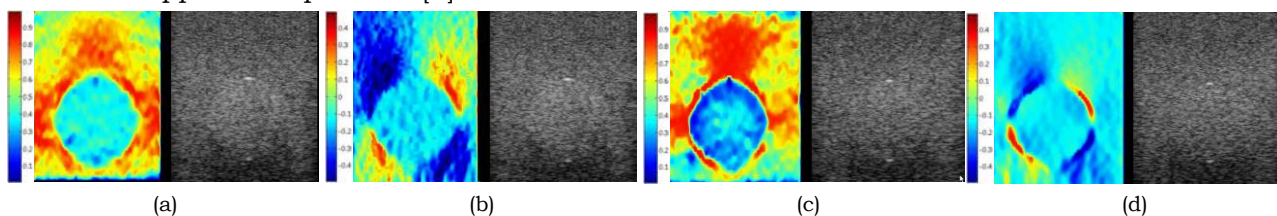


Figure 1: Screen shots (color) from real-time movie showing [a] axial strain; [b] axial-shear strain from a phantom with a firmly-bonded inclusion; axial strain [c] and axial-shear strain [d] from a phantom with a loosely-bonded inclusion. The B&W images are the corresponding sonograms.

Acknowledgements: This work is collaboration between the University of British Columbia and the University of Texas Health Science Center Houston. The work at Texas was supported by NIH program project grant P01-CA64597-13.

References:

- [1] Chen EJ, Adler RS, Carson PL, et al. Ultrasound tissue displacement imaging with application to breast cancer, *Ultrasound in Medicine and Biology*, 21(9), 1153-1162 (1995).
- [2] Thitai Kumar A, et al. Visualization of bonding at an inclusion boundary using axial-shear strain elastography: a feasibility study, *Physics in Medicine and Biology*, 52(9), 2615-2633 (2007).
- [3] R. Zahiri-Azar, S. Salcudean, Motion Estimation in Ultrasound Images using Time Domain Cross Correlation with Prior Estimates, *IEEE Transactions on Biomedical Imaging*, 53(10), 1990-2000, (2006).
- [4] R. Zahiri-Azar, S. Salcudean, Real-Time Least Squares Strain Estimator for Elastography, Fifth International Conf. on Ultrasonic Measurement and Imaging of Tissue Elasticity, Snowbird, USA, Page: 109 (2006).

033 **PROSTATE CANCER AND EXTRACAPSULAR EXTENSION (ECE): ASSESSMENT BY SONOELASTOGRAPHY IN COMPARISON WITH MRI – A PRELIMINARY STUDY.**

L. Pallwein¹, F.H. Aigner^{1*}, E. Pallwein¹, D. zurNedden¹, F. Frauscher¹.

¹Medical University Innsbruck, Department of Radiology 2, Innsbruck, AUSTRIA.

Background: SonoElastography (SE) has already shown its ability to detect prostate cancer areas based on increased tissue stiffness. Furthermore, this method is able to delineate the integrity of the prostate capsule as a soft rim artifact surrounding the outer border of the organ.

Aims: The goal of this study was the comparison of SE to structural MRI for assessment of the organ exceeding growth (ECE) of prostate cancer.

Methods: 15 patients with clearly elevated PSA (> 10, mean PSA 21± 9) and suspicious digital rectal examination findings were included in this study. Pretreatment staging was performed with SonoElastography (EUB-8500, Hitachi Ultrasound, Japan) for cancer detection and delineation of the prostate capsule, based on the fact that tumor tissue is displayed as a stiff area (colored in blue) and a regular bordered prostate is surrounded by a “soft rim artifact” (colored in red). At the site of ECE, this sign is interrupted (arrows in Figure 1 c and d). The results of SonoElastography were compared with T2 and contrast enhanced T1 weighted MRI images using an endorectal coil (Siemens Symphony, 1.5 T). Both imaging methods were compared to the histopathologic findings after radical prostatectomy.

Results: The histopathologic findings after radical prostatectomy showed an infiltration of the prostate capsule and a cancer extending into the periprostatic fat tissue (9 cases) or into the seminal vesicles (5 cases) in 11 of 15 patients. All of these tumors were staged T3b and T4. Cancers could be well detected with SonoElastography in all patients. SonoElastography showed an interruption of the soft rim sign in 8 patients and an increased stiffness of seminal vesicles in 4 cases. MRI was also able to delineate cancer areas in all cases and showed a bulging of the capsule and other signs of infiltration of the periprostatic fat tissue clearly in 7 cases (arrows in Figure 1 a and b). An infiltration of the seminal vesicles could be detected with MRI in 5 cases.

Conclusion: On the one hand, SonoElastography detected all cancer areas. On the other hand, this method was able to delineate the prostate capsule and showed remarkable strength in the prediction of ECE. These results correlated well with MRI and histopathologic findings.

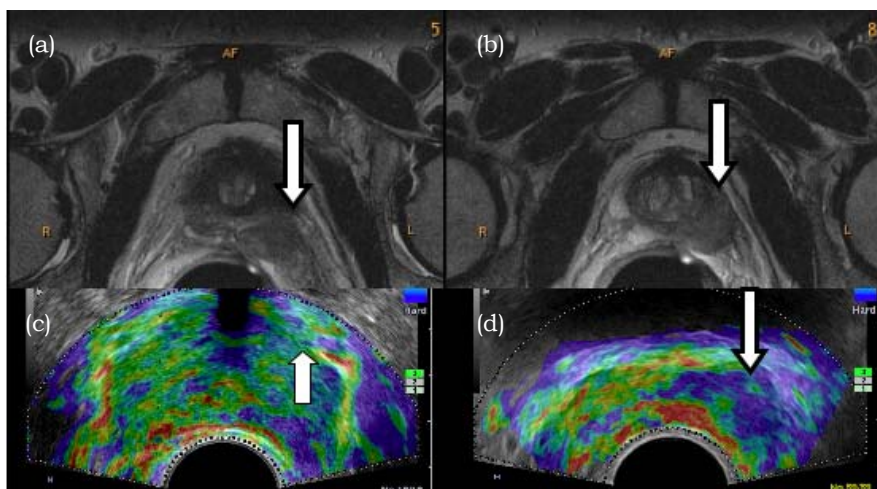


Figure 1: (a) and (b) MRI Images
(c) and (d) SonoElastography Images

034 EARLY PROSTATE CANCER DETECTION: FINDINGS OF SONOELASTOGRAPHY IN COMPARISON TO ENDORECTAL MRI.

L. Pallwein^{1*}, F.H. Aigner¹, E. Pallwein¹, D. zurNedden¹, F. Frauscher¹.

¹Medical University Innsbruck, Department of Radiology 2, Innsbruck, AUSTRIA.

Aims: To assess the value of SonoElastography for detection of early prostate cancer in comparison to endorectal MRI.

Material and Methods: Fifty patients with elevated PSA blood values (ranging from 1.5 to 6.0) were examined with endorectal SonoElastography (Examiner 1; Hitachi, Japan), during which the elasticity of prostate tissue was displayed from red (soft) to blue (hard). Hard lesions were considered as malignant. The findings of SonoElastography were compared with T2w and contrast enhanced T1w endorectal MRI images (Examiner 2; Siemens, 1.5T). Suspicious areas were divided in 3 groups.

Group A: tissue changes in both methods, (see figure)

Group B: changes in SonoElastography alone,

Group C: changes in MRI alone.

All these areas were selected for US guided targeted prostate biopsy with 2 cores from each lesion. Subsequently systematic biopsy was performed.

Results: Overall 87 areas (174 cores) were selected in Group A, 24 in Group B (48 cores), and 14 in Group C (28 cores) for targeted biopsy. Targeted biopsy detected cancer in 18/50 patients (Gleason 5–7), whereas the systematic biopsy detected cancer in 14 patients. In Group A 32 cores (18%) were positive for cancer, in Group B 6 cores (13%), in Group C 4 cores (12%) and in the systematic biopsy 31/500 cores (6%).

Conclusion: With the limitation of a small study population SonoElastography combined with MRI seems to be able to enhance visualization of early prostate cancer.

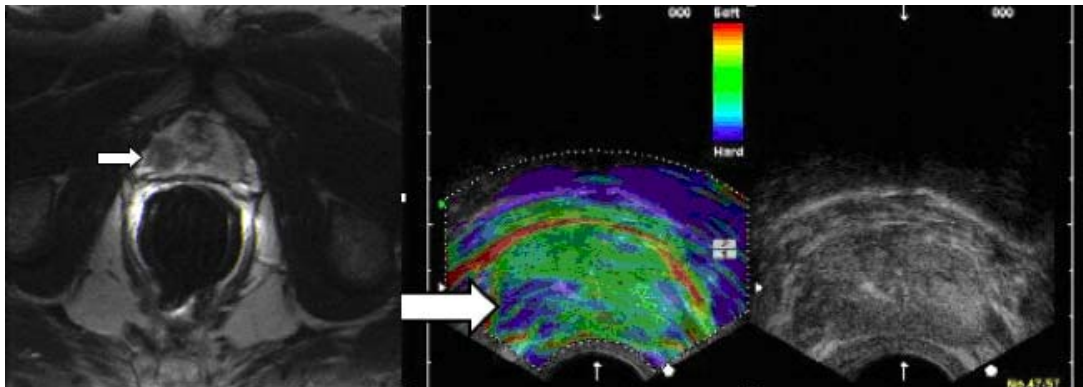


Figure 1:

Background: We have developed several strain-measurement-based shear modulus reconstruction methods [1–4], e.g., 1-dimensional [1] and multidimensional (2D and 3D) [2–4]. Regarding the multidimensional methods, both Methods B [3] and C [4] use a mean normal stress as an unknown. Briefly, Method B yields a mean normal stress reconstruction as well, whereas Method C leaves the mean normal stress unknown. Method F described in [2] uses a typical Poisson's ratio. While all 3D reconstructions listed above can deal with mechanical sources of arbitrary size, the 1D and 2D reconstructions are affected by the size of mechanical sources, i.e., artifacts occur with smaller sources.

Aims: In this study, we evaluate the quality of low dimensional reconstructions by changing the size of mechanical sources.

Methods: Simulations were performed using deformation data obtained by compressing a numerical phantom (50 mm sides) in the axial direction. The phantom had a central spherical inclusion (radius, 5 mm) that had a shear modulus twofold that of the surrounding region. The width of a mechanical source (i.e., the width of the contact surface) was changed from 50 to 20 mm. Methods B [3], C [4] and F [2] were used under a 3D condition, or a 2D stress or 2D strain assumption. The 1D reconstruction [1] was also performed.

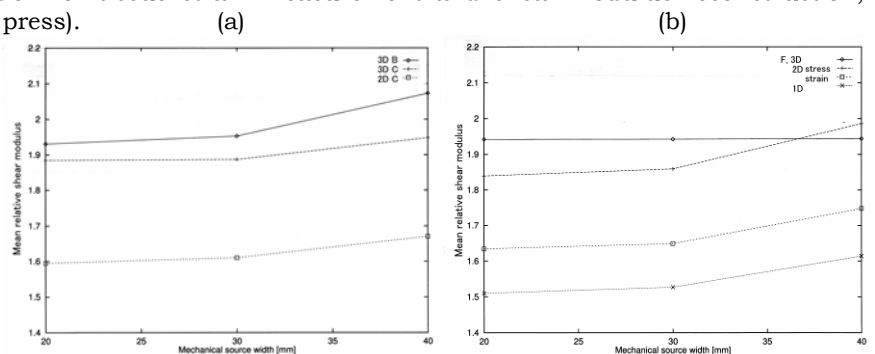
Results: Figure 1 shows the mechanical source width vs the mean relative shear modulus reconstruction in the central square region (5 mm sides) in the inclusion. For the 3D reconstructions using Methods B, C and F, the mean relative shear moduli were estimated with high accuracies regardless of the mechanical source width. However, except for a reconstruction using Method F under a 2D stress assumption (Figure 1b), the narrower the mechanical source width, the lower the mean shear moduli (than the original) of the low dimensional reconstructions using B, C, F and 1D methods, although the shape of the inclusion was estimated to be almost spherical as in the 3D reconstructions except for the 1D reconstruction [1] (omitted). For the low dimensional reconstructions, artifacts due to stress concentrations are also confirmed [2,3].

Conclusions: As confirmed, the 3D reconstructions by Methods B, C and F and the 2D reconstruction using a 2D stress assumption can deal with mechanical sources of arbitrary size. Then, regarding a ultrasonic reconstruction, we are conducting two approaches in that (1) a special 3D ultrasound system (that realizes our developed special beamforming [5] for a displacement vector measurement) is developed and (2) use of conventional 2D ultrasound system is performed, particularly combined with a regularization of lateral/elevational displacements (i.e., spatially variant, displacement-component-dependent regularization) [6,7].

References:

- [1] C. Sumi *et al.*, "Shear modulus reconstruction by ultrasonically measured strain ratio," *J Med Ultrason*, vol. 34, no. 4, 2007 (in press).
- [2] C. Sumi, *IEEE Trans UFFC*, vol. 52, pp. 1670–1689, 2005.
- [3] C. Sumi, *IEEE Trans UFFC*, vol. 53, p. 2416–2434, 2006.
- [4] C. Sumi, "Effective shear modulus reconstruction obtained with approximate mean normal stress remaining unknown," *IEEE Trans UFFC* (in press).
- [5] C. Sumi, "Displacement vector measurement using instantaneous ultrasound signal phase–Multidimensional autocorrelation and Doppler methods," *IEEE Trans UFFC* (in press).
- [6] C. Sumi, "Regularization for ultrasonic measurements of displacement vector and strain tensor" (under review).
- [7] C. Sumi, "Spatially variant regularization for tissue strain measurement and shear modulus reconstruction," *J Med Ultrason*, vol. 34, no. 3, 2007 (in press).

Figure 1: Compression width vs mean shear modulus reconstructions obtained using
(a) a mean normal stress as an unknown (Methods B and C) and
(b) a typical Poisson's ratio (Method F) and a 1D method.



Background: A robust non-invasive technique for reconstructing the thermal properties of living tissues-thermal conductivity, thermal capacity and thermal diffusivity - and thermal quantities such as thermal source/sink and perfusion for diagnosis, and monitoring and planning thermal treatments such as a high-intensity focused ultrasound (HIFU) and interstitial rf or microwave electromagnetic coagulation therapy are reported by us [1]. Perfusion is also a measure for differentiating tumor progress. Internal tissue temperature distributions can be measured using ultrasonic imaging [2] or magnetic resonance imaging.

Aims: In this study, we dealt with the case of performing reconstruction after stopping heating and perfusion. That is, only the thermal properties of living tissues were reconstructed. However, the perfusion cannot always be stopped. In such a case, by increasing the independent temperature data, the perfusion can also be reconstructed [1]. Typical property values may also be used.

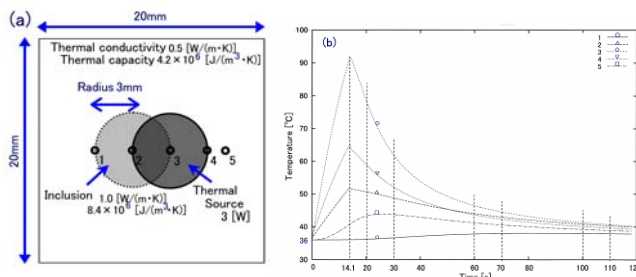
Methods and results: To verify the feasibility of the reconstruction, simulations were performed. A cubic tissue phantom (50.0mm sides; x, y and z = 0.0–50.0mm) was simulated. It contained a spherical inclusion (dia = 6.0mm), which had a conductivity and a specific heat twice those of the surrounding medium, i.e., 1.0 vs 0.5W/(mK), and 8,400 vs 4,200J/(Kkg) (typical values similar to those of water). The density was uniform at 1,000kg/m³. A cubic ROI (20.0mm sides) was set at the center of the phantom with the spherical inclusion, as shown in Figure 1a (z = 25mm). The phantom has a uniform temperature of 36.0. As shown in Figure 1a, a spherical heat source Q of 3W (dia = 6.0mm) was set at t = 0 sec such that it overlaps with the inclusion. The time series of temperature distribution was calculated by the successive over-relaxation (SOR) method using a time step of 0.1sec. Figure 1b shows the time courses of temperatures at the five positions shown in Figure 1a. When the highest temperature in the ROI exceeded 100°C, the heating was stopped (t = 14.1sec). After stopping the heating, two sets of sequential temperatures shown in Table 1 were used. The means of the reconstructions evaluated in the central square region of 1.0x1.0mm² in the inclusion are also shown in Table 1. As shown, the thermal properties are accurately reconstructed. Because the temperature change does not yet occur at t = 20 and 30sec in the peripheral region of the ROI, the reconstructions are unstable. However, the regularization was effective in stabilizing the reconstructions [omitted].

Conclusions: From the successful numerical estimations of thermal properties, the reconstruction proposed here enables the real-time planning of conditions for thermal treatment, i.e., the next spatial position to be heated, the thermal source shape and the ultrasound intensity etc. This is a practical protocol for such treatment for the following steps can be studied i.e., (0) to stop perfusion or not, and planning the conditions for thermal treatment, i.e., the next iteration of (1) heating, (2) stopping heating, (3) immediate reconstruction, and (4) the determination of the next heating. Due to the low tissue diffusivity, for the treatment of a local tumor, the size of the region of reconstruction cannot be made too large and the use of a small thermal source is required. That is, large and small thermal sources must be respectively used to heat the center of a tumor and a marginal region. Furthermore, from a deep region to a shallow region, heating must be performed. Thus, by using our proposed reconstruction technique during thermal treatment, a minimally invasive treatment will be realized. In the near future, the use of MR temperature measurement, and the experimental reconstruction of thermal sources/sinks and perfusion will be reported elsewhere.

References:

- [1] C. Sumi, H. Yanagimura, "Reconstruction of thermal property distributions of tissue phantoms from temperature measurements," *Phys Med Biol*, vol. 52, pp. 2845–2863, 2007.
- [2] C. Sumi, H. Yanagimura, "Spatial inhomogeneity of tissue thermal parameter of Ebbini's model and its dependency on temperature," *JJAP*, vol. 46, no. 7B pp. 4790–4792, 2007.

Figure 1:
(a) Central plane in ROI [z = 25 mm].
(b) Time courses of temperatures at five positions depicted in (a).



Times sec	Conductivity W/(m·K)	Capacity ($\times 10^6$) J/(m ³ ·K)	Diffusivity ($\times 10^{-7}$) m ² /s
Original	1.00	8.40	1.19
20 and 30	0.78	6.30	1.24
60 and 70	1.06	8.71	1.22
100 and 110	0.90	7.87	1.15
30 and 70	1.02	8.69	1.18

Table 1: Reconstructions in inclusion.

Background: We have been developing several strain measurement methods [1,2] and several shear modulus reconstruction methods [3-5] for the differential diagnosis of diseases. Recently, we also started other applications of the shear modulus reconstructions (e.g., on normal physical motions of arms, legs, etc [6] and cultured tissues). In this context, we started the evaluations of the skin shear moduli (i.e., those of the epidermis, dermis, subcutaneous tissue) of various body parts, e.g., face, arm, leg, abdomen, breast. This will lead to developments of various techniques (e.g., using medicines, cosmetics, equipment) for skin care and culture (e.g., dry skin, crack, callosity, oily skin, crease, chloasma, sun burn, dermatitis, acme, baldness, relations with clavus, damage hair, achromachia, dandruff). This is a collaboration study with the Kao corporation. Various clinical applications can also be considered. Thus far, regarding skin, various evaluations by ultrasonic and magnetic resonance imaging, and a strain measurement (a burn case [7]) have been reported.

Aims: To report the preliminary measurement results of skin elasticity.

Methods: The facial skin of two female volunteers, 20 and 63 years old, was studied. The multidimensional cross-spectrum phase gradient method (MCSPGM) [1] was used to measure displacement vector distributions during the iterations of compressing and releasing their cheeks with an ultrasound transducer (up to 20 MHz). After the evaluations of the axial strain distributions from the measured axial displacement distributions, we reconstructed 1D shear modulus distributions [8]. Because we did not use a reference material here, we were able to evaluate only the relative shear modulus distributions.

Results: Strains were measured in the dermal regions and subcutaneous tissue regions of the two volunteers. The ratio of the mean relative shear modulus of the dermis to that of the subcutaneous tissues was calculated as the reciprocal of the ratio of the mean strains in the two regions, and found to be 3.04 (age 20) and 3.98 (age 63). The normalized standard deviations (STDs) of strains (std/mean) were 1.06 and 1.76 (greater than 1) in the dermis, and 0.83 and 0.82 (less than 1) in subcutaneous tissues.

Conclusions: For the two volunteers, the dermis had higher shear modulus than the subcutaneous tissues. That is, the dermis was stiffer than the subcutaneous tissues. The variation of the mean dermal shear modulus was larger than that of the subcutaneous tissues. These reflect well the respective tissue structures and compositions.

The relative shear modulus and STD of dermal strains of the volunteer aged 63 were larger than those of the volunteer aged 20. By collecting absolute shear modulus data using a reference, the changes of absolute shear moduli of dermis and subcutaneous tissues due to aging may be investigated in more detail. For the two volunteers, the STDs of the subcutaneous tissue strains were almost the same.

In the future, the shear moduli of other parts of the face and body will be measured. Together with the elasticity, the viscosity and plasticity will also be evaluated. As is well known, such mechanical properties are determined by personal factors (e.g., physical constitution, etc.) and those of the environment (e.g., time, temperature, humidity, season, living area, human race, sex, foods, quantity of motion, i.e., physical exercise, etc.). These will also be used as measures, for comparison with skin mechanical properties. In addition, thickness, pH, microscopically observed geometric information, color, water content, blood content, lipid content, gas content (tPO₂, tPO₂), interactions with water (measured by techniques such as transepidermal water loss) and exposure to light will be measured. They will then be studied for correlation with the mechanical properties and with each other.

References:

- [1] C. Sumi, *IEEE Trans UFFC*, vol. 46, pp. 158-166, 1999.
- [2] C. Sumi, "Displacement vector measurement using instantaneous ultrasound signal phase - Multidimensional autocorrelation and Doppler methods," *IEEE Trans UFFC* (in press).
- [3] C. Sumi, *IEEE Trans UFFC*, vol. 52, pp. 1670-1689, 2005.
- [4] C. Sumi, *IEEE Trans UFFC*, vol. 53, pp. 2416-2434, 2006.
- [5] C. Sumi, "Effective shear modulus reconstruction obtained with approximate mean normal stress remaining unknown," *IEEE Trans UFFC* (in press).
- [6] C. Sumi, "Ultrasonic axial strain measurement for lateral tissue deformation," *Ultrason Med Biol* (in press).
- [7] M. Vogt et al, *IEEE Trans UFFC*, vol. 52, pp. 375-385, 2005.
- [8] C. Sumi et al, "Shear modulus reconstruction by ultrasonically measured strain ratio," *J Med Ultrason*, vol. 34, no. 4, 2007 (in press).

041 **METHOD OF ELASTICITY MEASUREMENT OF BREAST CANCER BY UNIFORM PRESSURE COMPRESSION.**

Y Hayakawa^{1}, K Ishida¹, K Ando¹, Y Amano¹, K Tsuji¹.*

¹Toin University of Yokohama, 1614 Kurogane-cho, Aoba-ku, Yokohama, Kanagawa-ken, 225-8502, JAPAN.

Background: Breast elastography using a planar ultrasound transducer for compressing tissue has been developed by T Shiina and Hitachi Medico Co., Ltd. [1]. Compressing by using a planar structure creates a non-uniform pressure in the breast. It gives higher pressure where breast is thicker. The pressure distribution makes the deformation of the lesion irregular and difficult to analyze theoretically. We propose applying uniform pressure by using a water bag compressor.

Aims: Our present intension is to obtain an estimate of the elastic modulus of the hypothetic lesion assumed in the computer simulation by using an iteration technique, without referring to the original elastic modulus assumed in the simulation.

Methods: We are currently making computer simulations using a Finite Element Method prior to actual experiments.

Results: One of the results is shown in Figure 1, where two regions of normal glandular tissue with a modulus of 28kPa are embedded in fat tissue with an elasticity modulus of 18kPa (Figure 1a) and compressed with a uniform pressure of 5000Pa (Figure 1b) [2]. Both normal glandular tissues are deformed approximately in the same manner unlike when they are compressed using a planar structure.

Conclusions: Compressing with uniform pressure seems to give more regular deformation of lesions than compressing with a planar structure. Analysis of the elasticity modulus from these simulation data is in progress, together with real phantom experiments.

Acknowledgements: Authors are indebted to Dr. Mitsuchika Nakamura for his valuable discussions.

References:

- [1] Yamada M, Shiina T, et al., (2001) Jpn. J. Appl. Phys. 40:3872–3876.
- [2] Krouskop TA, Wheeler TM, Kallel K, et al., (1998) Ultrasonic Imaging 26, 260–274.

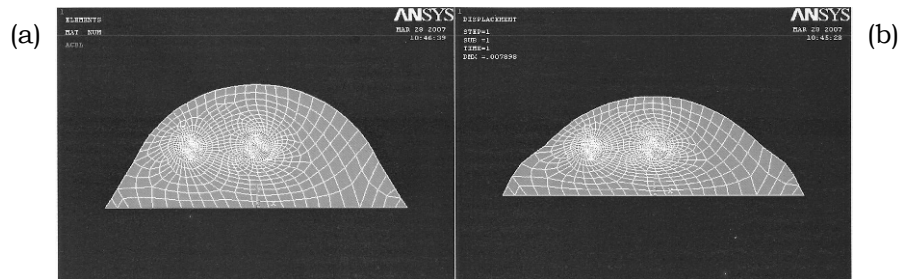


Figure 1: Result of computer simulation by Finite Element Method.

(a): breast without pressure;

(b): breast with uniform pressure of 5000Pa from upward. Circles are mammary glands.

044 **LIVER STIFFNESS MEASUREMENT (LSM) BY TRANSIENT ELASTOGRAPHY IN THE PREDICTION OF HEPATIC FIBROSIS IN NON-ALCOHOLIC STEATOHEPATITIS (NASH).**

Laurent Sandrin¹, Véronique Miette^{1}, Céline Fournier¹.*

¹Echosens, Research and Development Department, 153 avenue d'Italie, 75013 Paris, FRANCE.

Background: Around 20–30% of the population in western industrialized countries is affected by non-alcoholic fatty liver disease (NAFLD), and figures are rising. Around 10–20% of affected patients develop fatty liver inflammation which is referred to as fatty liver hepatitis (non-alcoholic steatohepatitis-NASH) and run the risk developing liver fibrosis and cirrhosis. Globally, 2–4% of the overall population may be affected by NASH making it one of the most common liver diseases in western industrialized countries. Transient elastography (Fibroscan[®], Echosens, Paris, France) is a non-invasive and rapid technique used to assess liver fibrosis by liver stiffness measurement (LSM).

Aims: Until now a definite diagnosis of NAFLD was only possible with a liver biopsy. The purpose of this clinical study was to evaluate the diagnostic accuracy of LSM in NASH patients [1,2]. The Fibroscan[®] does not detect the increased fatty deposits in the liver, but rather hepatic fibrosis changes which are a result of fatty degeneration and inflammation.

Methods: Liver fibrosis was assessed histologically using a semi-quantitative scoring system: F0 = no fibrosis, F1 = fibrosis without septa, F2 = few septa, F3 = significant fibrosis, F4 = cirrhosis.

The first study involved 110 patients. On the same day, liver biopsy, LSM and standard laboratory blood tests were performed to compute two scores (APRI and Forns) based on two simple models to predict fibrosis.

In the second study, the liver fibrosis degree of 124 patients (78 viral hepatitis and 46 NASH) was scored by liver biopsy and LSM.

LSM were carried out with Fibroscan[®] using a standard probe, a 3.5 MHz transducer. Then, the diagnostic accuracy was estimated by using the area under the receiver operating characteristic curves (AUROC).

Results: In the first study, the AUROCs for LSM and the best blood test were, respectively, 0.83 and 0.74 for $F \geq 2$ ($p=0.01$); 0.88 and 0.84 for $F \geq 3$ ($p=0.02$) and 0.97 and 0.83 for F4 ($p=0.003$). The second study reported AUROC of 0.84, 0.74 and 0.98 for $F \geq 2$, ≥ 3 and $= 4$ in NASH patients and cut-off values for cirrhosis of 14.5 kPa in viral hepatitis (diagnostic accuracy: 0.83) and 10.5 kPa in NASH (diagnostic accuracy: 0.98).

Conclusions: Non-alcoholic fatty liver disease (NAFLD) is the most common liver disease, and the development of novel procedures for definitively diagnosing the disease and assessing its prognosis is extremely important for tailoring effective treatments. This study suggests that LSM is useful for assessing the progression of hepatic fibrosis in patients with NASH. Thus, LSM represents an excellent initial screening test for NASH patients for whom a liver biopsy is not possible, periodically or frequently.

References:

- [1] Marin, JC et al. Prospective comparison between transient elastography (Fibroscan[®], APRI and Forns test for assessing liver fibrosis in patients with histological features of NAFLD, 42th Annual Meeting of the EASL, Barcelona, Spain, 2007.
- [2] Gaia, S et al. Is liver stiffness measurement different in patients with NASH or with viral hepatitis? 42th Annual Meeting of the EASL, Barcelona, Spain, 2007.

Background and Aims: In elastography the estimation of the gradient of the displacement field is a main concern. Displacements are obtained through the computation of the pre- and post-compression scans (either A-line echoes or B-mode images) with different algorithms. The derivative estimation methods are classified as direct and indirect, the former computing the strain from the input without the need of the displacement estimation. In this work, we compare the performance of two methods: one implementation of a Kalman filter and one of a least-square (LSQ) estimator, in order to obtain the strain. The study was carried out on a commercial tissue-mimicking breast phantom (Mod. 059, CIRS Inc., USA) and on Field II simulations.

Methods: The Kalman filter [1] is an efficient recursive filter that estimates the state of a dynamic system from a series of incomplete and noisy measurements. This filter is capable of estimating the position, velocity and acceleration of an object. Tracking targets in radar applications is one of its main uses. Elastography is classified as a direct strain estimator. The velocity of the model corresponds to the strain in this case. The process must be modeled in accordance with the framework specifying the matrices that define it. It assumes that the true state at time k is evolved from the state at $(k-1)$ according to:

$$x_k = A_k * x_{k-1} + B_k * U_k + w_k;$$

where A_k is the state transition model which is applied to the previous state x_{k-1} ;

B_k is the control-input model which is applied to the control vector U_k ; and

w_k is the process noise, assumed to be drawn from a zero mean multivariate normal distribution with covariance Q_k .

The least-squares analysis is a method for linear regression that determines the values in a statistical model by minimizing the sum of the residuals (the difference between the predicted and observed values) squared [2].

Results and Conclusions: In Figures 1 and 2 (a and b), it can be observed how the Kalman estimation suffers a delay, making the inclusion appear in a lower position than where it is actually located. However the size is similar to that found in the B-mode image (Figure 2a) of the breast phantom. The LSQ estimator does not shift the prediction of the inclusion, but it loses its true size and CNR. The performance of the Kalman filter fitting the displacement curve of one representative axial line along the center of the inclusion is presented in Figures 1c and 2d. It can be appreciated how smooth the estimation is and how the filter is “late” in predicting the decrease of the slope at the inclusion’s region. This might be overcome at expenses of CNR. Optimization and correction of the delay are under study.

Figure 1: (a) Field simulation phantom – Kalman estimator strain elastogram, (b) LSQ strain elastogram and (c) Kalman displacement fitting curve.

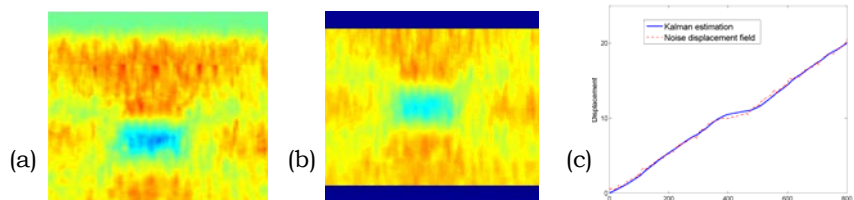
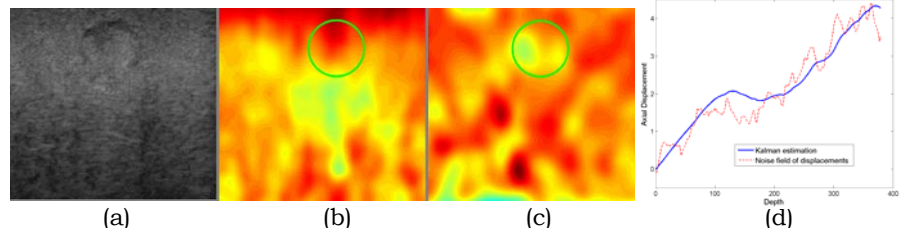


Figure 2: (a) B-mode image of commercial breast phantom, (b) Field simulation phantom-Kalman estimator strain elastogram, (c) LSQ strain elastogram and (d) Kalman displacement fitting curve.



Acknowledgements: Spanish Gov. USIMAG grant (TEC2004-06647-C03-02), and CEE SIMILAR NoE (FP6-507609).

References:

- [1] Peter S. Maybeck. Kalman Filtering in: Stochastic Models, Estimation, and Control, vol. 1.
- [2] F. Kallel and J. Ophir. A least-square strain estimator for elastography. Ultrasonic Imaging, v.19, pp. 195-208, 1997.

Background: In transient elastography [1], the propagation of a single wave front (as opposed to a continuous stream of waves) generated from some excitation source is used to calculate tissue material properties. Previous research has claimed accurate measurements of tissue stiffness by measuring wave velocity from the vertical (i.e., perpendicular to the skin surface) displacement of tissue caused by a wave propagating through the tissue in the same direction as the displacements, at a velocity similar to that of a shear wave. This contradicts the classical definition of a shear wave as being a wave with displacements in any plane perpendicular to the direction of propagation [2]. Some researchers [3] have proposed that the effect is caused by the coupling of a compression and a shear wave existing only in the near field, using the combination of three Green's functions to describe the behavior mathematically. So far, to our knowledge, no analysis of this wave behavior based on fundamental equations of motion has been carried out.

Aims: To compare previous results obtained from transient elastography to a finite element model implementation in order to better understand the nature of the wave being measured. This understanding will help improve the accuracy of stiffness calculations and may help in the development of elasticity measurement systems that do not require ultra-fast ultrasound frame rates.

Methods: We have constructed an axi-symmetric finite element model of an isotropic, elastic body with material properties similar to those used in previous literature [1]. Using this model, we present the expected displacements and velocities associated with a sinusoidal excitation of a section of the body's surface, thus simulating the experiment carried out in [1]. Empirical results obtained in a separate experiment on a phantom using an ultrasound probe are compared to these simulations.

Results: A wave front displacing tissue in the direction of propagation is recorded below the exciter with initial velocity given by the Young's velocity equation (similar to that found axially in a rod after a vertical displacement of the free end). After some distance, related to the diameter of the excitation source, we see this wave changing velocity to that given by the shear wave velocity equation (see Figure 1).

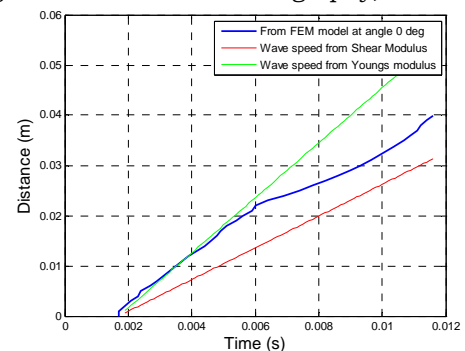
Conclusions: New information about the velocity of the wave close to the excitation source indicates that the wave initially behaves as if propagating axially within a rod. Its velocity here cannot be used in conjunction with the shear wave propagation equation to calculate the shear modulus; rather the results suggest the use of the Young's velocity equation for this region. Further investigation is required to determine the parameters upon which the size of this region depends. These parameters will allow us to control the nature of the propagated wave more carefully and, thus, increase the accuracy in the estimation of the tissue material properties based on this wave.

Acknowledgements: The authors wish to thank Laurent Sandrin and Mikael Tanter for their useful discussions.

References:

- [1] S. Catheline, J. Thomas, F. Wu, and M. Fink, Diffraction field of a low frequency vibrator in soft tissues using transient elastography, *IEEE Trans Ultrason. Fer. and Freq. Contr.* 46 (1999), no. 4, 1013–1019.
- [2] J. D. Achenbach, *Wave propagation in elastic solids*, North Holland Publishing company, 1973.
- [3] L. Sandrin, D. Cassereau, Mathias Fink, The role of the coupling term in transient elastography, *J. Acoust. Soc. Am.* 115 (1) 2004.

Figure 1: The velocity of the wave front as it moves through the tissue. The two ideal lines show the Young's wave speed (above in green) and the shear wave speed (below in red)



055 **SONOELASTICITY IMAGING OF THE BREAST.**

Joseph R Grajo^{1}, Richard G Barr¹.*

Radiology Consultants, 250 DeBartolo Place Bldg B, Youngstown, OH44512, USA.

Background: Sonoelasticity has recently been FDA approved for clinical use. The technique can provide additional information in the evaluation of breast pathology which is not available from present mammography or B-mode ultrasound [1].

Aims: This poster reviews clinically useful information obtained using Sonoelasticity in the evaluation of breast lesions during routine clinical examination.

Methods: Sonoelasticity was utilized in over 300 breast cases during routine clinical evaluation. 210 of these lesions were biopsied for histological confirmation of pathology. Elastograms were obtained on a commercially available ultrasound system (Antares, Siemens Ultrasound, USA) using a 13 MHz probe. This system uses a speckle tracking to generate the elastogram. The system displays the B-mode image and corresponding elastogram simultaneously in real-time. The algorithm is sensitive for a 0.1% strain and uses temporal persistency strategy to enhance the descriptive pattern in the elastogram. With this sensitivity, no additional equipment is required other than the standard ultrasound probe. Normal patient motion from respiration is adequate in most patients to generate the elastogram. When this was not sufficient, slight rhythmic compression was applied. Real-time imaging allowed for rapid determination of the compression needed. Cases were selected that demonstrate how the information obtained from Elasticity Imaging was helpful in diagnosis.

Results: A bull-eye appearance in the elastogram was identified in both simple cysts and complex cysts. Cystic lesions which appeared solid on B-mode sonograms demonstrated the bull-eye appearance on elasticity imaging and were confirmed to be cystic by needle aspiration of the fluid. These patients therefore were diagnosed with a small needle used in fine needle aspiration as opposed to a large needle used in core biopsies. Elasticity Imaging was helpful in determining if a questionable lesion on B-mode ultrasound was a fat lobule or a lesion (based on relative elasticity). Difference in the size of a lesion on B-mode ultrasound vs. Elasticity Imaging was helpful in predicting whether a lesion was benign or malignant. The longest length of a malignant lesion was equal to or larger on the elastogram as compared to the corresponding B-mode image.

Conclusions: Sonoelasticity Imaging provides additional diagnostic information over B-mode imaging in evaluation of breast lesions.

Acknowledgements: This work was supported in part by an equipment loan from Siemens Ultrasound.

References:

- [1] Barr RG. Initial Results of Breast Real-Time Elasticity Imaging to Characterize Lesions. RSNA 2006.
 - [2] Svensson WE et al. Elasticity Imaging of 67 Cancers and 167 Benign Breast Lesions Shows That It Could Halve Biopsy Rates of Benign Lesions. Proceedings of the 4th Int'l Conference on the Measurement and Imaging of Tissue Elasticity, Lake Travis, Texas, October 2005, p. 87.
 - [3] Garra, B.S., Cespedes, I., Ophir, J., et. al.: Elasticity of Breast lesions: Initial clinical results. Radiology, Vol. 202, pp79-86, 1997.
-

Background: High Intensity Focused Ultrasound (HIFU) has previously been used to destroy tumor tissue near the focus of the ultrasound beam. However, it can be difficult to guide the HIFU treatment, i.e. to predict in advance where the lesion associated with a given exposure will form, thus raising the possibility that nearby healthy tissue will be accidentally damaged. Furthermore, a means of monitoring the treatment to verify that the entire tumour mass has been ablated is required.

Aims: The aim of this study was to investigate whether transient acoustic radiation force displacement and strain imaging can be used in the guidance and monitoring of HIFU treatment.

Methods: In this study, the acoustic radiation force associated with a focused ultrasound beam was used to generate localised stresses inside samples of *ex-vivo* bovine liver tissue. Acoustic elastographic techniques were then applied to image the induced displacement and strain distributions using commercial diagnostic ultrasound scanners (Acuson XP128, Mountain View, CA, USA, and Z.one, Zonare, Mountain View, CA, USA). Two modes of operation were investigated. First, a short duration (10 ms) sub-ablative pulse from the HIFU transducer (Imasonic, Besancon, France) was initially used to help localise the focus of the ultrasound beam before any lesions were formed. Finite element modeling simulation software (Marc, MSC Software Corp, Santa Ana, CA, USA) was employed to assist with the interpretation of the displacement images obtained. Second, subsequent to lesion formation, multiple sub-ablative pulses were applied to the tissue, and the position of the focus was translated between exposures. At each focus position, the local induced strain was calculated and was ultimately used to construct a composite image of local strain inside the tissue using a method described previously [1]. For both modes of operation, the imaging array used to visualize displacement or strain was positioned in a 50 mm diameter aperture at the centre of the HIFU transducer (120 mm diameter focused bowl, 1.7MHz). For creating transient strain images both transducers, locked together, were mechanically scanned to translate the pushing focus.

Results: The simulations suggested that a short-duration HIFU burst would induce a complicated time-dependent displacement pattern inside the tissue and that, at early times, a localised region of high displacement would reveal the position of the focus. Using sub-ablative intensities, such a region of high displacement was also observed experimentally and, when higher (ablative) intensities were subsequently used, this region was ultimately found to coincide with the location of the lesion. Furthermore, in the composite post-ablation strain images obtained from multiple exposures, regions of low strain were found to reveal the location of tissue damage.

Conclusions: We conclude that elastographic strain imaging, in which acoustic radiation force is used to provide the necessary local tissue mechanical excitation, has considerable potential to be used in the guidance and monitoring of HIFU treatment.

Acknowledgements: We thank the EPSRC and the ICR for funding this research.

References:

- [1] Melodelima D, Bamber JC, Duck FA, Shipley JA. Transient elastography using impulsive ultrasound radiation force: a preliminary comparison with surface palpation elastography. *Ultrasound Med Biol* 2007;33:959–969.

060 **DEVELOPMENT OF A MECHANICAL TESTING ASSAY FOR MODULUS ANALYSIS OF FIBROTIC MURINE LIVER.**

SL Barnes^{1*}, *A Lyschik*^{1,2,3}, *JC Gore*^{1,2,3}, *MI Miga*^{1,2,3}.

¹Biomedical Engineering Department, Vanderbilt University, Nashville, TN, USA; ²Radiology and Radiological Sciences Department, ³Vanderbilt University for Imaging Science, Vanderbilt University Medical Center, Nashville, TN, USA.

Background: Hepatic fibrosis is a progressive disease caused by incessant irritation of the liver tissue, which results in the formation of scar tissue. Fibrotic progression and subsequent scar tissue formation is correlated to changing liver mechanical properties. This correlation may be used to assess the state of the disease, and hence methods to determine the elastic modulus of the liver are of considerable interest. In order to assess the diseased state of the liver accurately, controlled experiments to establish baseline modulus values for healthy livers as well as diseased livers must be conducted.

Aims: The focus of this work is the development of a protocol for mechanical testing combined with finite element modeling to allow for the evaluation of normal and fibrotic murine livers using multiple testing methods. This system can potentially be utilized for tissue characterization. In addition, current techniques are being developed to assess tissue stiffness, and this testing assay could be utilized for verification of the assessment technique.

Methods: The developed system employs a portion of liver tissue suspended in a cylindrical gel for CT imaging and mechanical testing. A finite element model is built from the CT images, and boundary conditions are imposed in order to simulate the testing conditions of the gels. The resulting model surface stress is compared to that obtained during mechanical testing, which subsequently allows for direct evaluation of the liver modulus. In addition, a separate mechanical indentation test was performed on each liver specimen, and histological analysis was performed for fibrosis staging. This system was used to study a total of fourteen livers: eight livers which were chemically-induced to develop fibrosis, three control livers, which were given placebo injections, and three normal livers, which were not subjected to any injections or treatment. The eight challenged mice were sacrificed at differing time points to study the fibrosis degree with modulus. The fibrotic livers are referred to as the diseased group, and the control and normal livers are collectively referred to as non-diseased.

Results: Though the sample sizes for this initial work were small, the preliminary results indicate that the livers can be identified within the gel, and the fibrotic livers can be identified as having a higher modulus than the control livers. The moduli evaluations for non-diseased livers were estimated as 0.62 ± 0.09 kPa, and 0.59 ± 0.09 kPa for indenter and model-analysis tests, respectively. Moduli estimates for diseased liver ranged from 0.85 to 1.64 kPa and 1.10 to 1.88 kPa for indenter and model-analysis tests, respectively. For diseased mice, scores ranged from 2–4 on the Ishak scale of 0–6 with 6 being the most severe (i.e. cirrhosis).

Conclusions: The model-calculated modulus was well correlated to the indenter modulus, excluding one presumed outlier. The results also showed a clear difference between non-diseased and diseased livers with qualitative agreement between disease scores and mechanical properties. Further testing is necessary to corroborate these initial results, but the preliminary implication is that the developed gel-tissue assay system could be utilized for controlled evaluation of soft-tissue moduli.

Acknowledgements: This material is based upon work supported under a National Science Foundation Graduate Research Fellowship.

064 **THE EFFECT OF NONLINEARITY ON FOCUSED IMPULSIVE ACOUSTIC RADIATION FORCE EXCITATIONS.**

Gianmarco F. Pinton¹, Mark L. Palmeri^{1*}, K. R. Nightingale¹, Gregg E. Trahey¹.

¹Duke University, Durham, NC, USA.

Background: Focused, impulsive acoustic radiation force can be used to induce localized displacement in tissue. Linear models, such as Field II [1], can be used to predict the intensity for an acoustic radiation force excitation. However, the intensity levels used to generate appreciable radiation force may be large enough to require a nonlinear description of wave propagation. Although calculation of the force can be approximated with the intensity field, the radiation force depends on the absorbed acoustical energy. An ideal numerical solution also calculates the loss term resulting from nonlinear wave propagation.

Aims: The purpose of this study is to calculate the spatially varying intensity and absorbed acoustical energy. These results will be used to calculate tissue heating and improve the mechanical simulations of tissue response to radiation force excitations.

Methods: The Westervelt equation is a full-wave description of ultrasound propagating in a nonlinear thermoviscous medium. This equation has previously been solved in axisymmetric coordinates. We have solved the Westervelt equation in full, three-dimensional Cartesian coordinates with finite differences in the time domain [2]. The pressure and absorption terms are calculated at 400 MHz with a spatial resolution of 20 microns in all three spatial dimensions for a 4.2 MHz diagnostic ultrasound transducer focused at 2.4 cm, with an F-number of 1.5. The simulation results have been validated in the linear regime with Field II. The lateral beam plot has been shown to be in agreement to within 0.3 dB and the axial intensity plot also shows excellent agreement. Simulation results have also been validated with a water tank experiment and by comparison with a solution to a nonlinear planar wave where the agreement is approximately 2 dB or better across a frequency range that spans four times the fundamental. The force calculated from the output of the nonlinear simulation is used as an input to an already established Finite Element Model of the tissue mechanical properties [3].

Results: Simulations show the differences in intensities and absorption for varying initial pressures. For example, for an initial pressure of 1.5 MPa and a pulse length of 2.4 μ s, the -10 dB beamwidth is 80% larger for the linear simulation when compared to the nonlinear simulation, which is consistent with experimental evidence of self-focusing in nonlinear propagation. The peak intensity along the axis is 23% larger for the nonlinear simulation and 30% narrower, indicating a more localized radiation force distribution than a linear simulation would predict.

Conclusions: A nonlinear simulation that calculates the intensity and absorption in the acoustic field with fine spatial and temporal resolution has been established for a diagnostic imaging transducer. For large intensities, a nonlinear description of ultrasonic propagation predicts a higher peak intensity and a narrower lateral and axial distribution than a linear description. The radiation force calculated from this more accurate simulation is closer to a point impulse than linear theory would predict.

Acknowledgements: This work is supported by NIH grants R01-HL075485 and R01-CA114093.

References:

- [1] Jensen et al. "Calculation of pressure fields for arbitrarily shaped, apodized, and excited ultrasound transducers," IEEE UFFC, 39(2):262-267, 1992.
 - [2] Pinton et al. "Full-wave modeling of finite-amplitude waves in diagnostic ultrasound", in review.
 - [3] Palmeri et al. "A finite-element method model of soft tissue response to impulsive acoustic radiation force," IEEE UFFC, 52(10):1699-1712, 2005.
-

065 A REAL-TIME ARFI IMAGING SYSTEM ON A DIAGNOSTIC ULTRASOUND SCANNER.

Jeremy J. Dahl^{1*}, Gianmarco F. Pinton¹, Stephen J. Hsu¹, Liexiang Fan², Gregg E. Trahey¹.

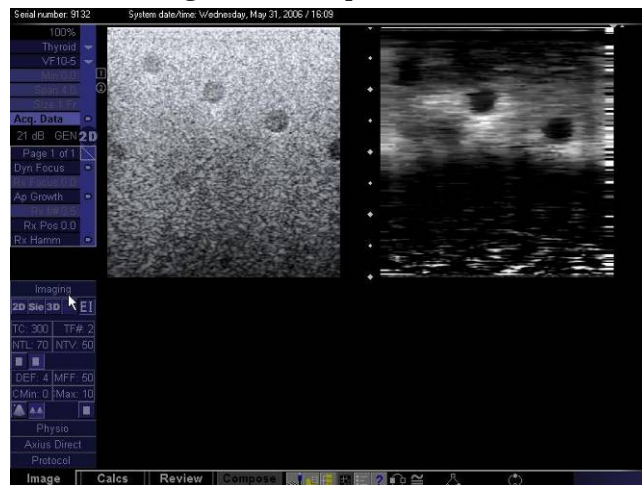
¹Duke University, Durham, NC, USA; ²Siemens Medical System USA, Inc., Issaquah, WA, USA.

Background: Radiation force based imaging methods have demonstrated the ability to measure the mechanical properties of tissue noninvasively. Acoustic Radiation Force Impulse (ARFI) imaging is one such method that uses high energy, focused ultrasound pulses to generate small displacements (1-10 μm) in tissue. The response of tissue to these localized forces is observed using a series of imaging pulses which track the displacement of tissue. Relevant issues in creating a real-time ARFI imaging system include patient acoustic exposure, observation time per image location, field-of-view and data porting and processing.

Aims: Several clinical applications may benefit from ARFI imaging in a real-time or fast imaging mode. Images generated from mechanical properties are most useful if the time from data acquisition to display can be reduced to less than 1 second. Clinical applications that may benefit most from ARFI imaging at this time are those involved in liver imaging, including monitoring of radiofrequency (RF) ablation lesions, biopsy guidance and at-risk patient screening.

Methods: We have developed a near real-time ARFI imaging system on a Siemens AntaresTM ultrasound scanner. The system runs real-time B-mode imaging in a panel on the left side of the screen, while the right side of the screen is reserved for ARFI images. At the request of the user, the system will run an ARFI pulse sequence, acquire the resulting data, process the data, and display the final result in the panel on the right. Parallel tracking is utilized in the ARFI pulse sequence to minimize tissue and transducer heating and increase the speed at which an image can be produced [1].

Results: The system is capable of producing ARFI images in approximately 1 second. The images produced by the real-time system have similar image quality to those produce by offline processing. The user is allowed control of the ARFI sequence including push duration, observation time, field-of-view and push F/#. The user also has control of some post-processing features including display range (in microns), motion filter function and ARFI display frame. An example image produced by the real-time system is shown below. The image shows hard spherical inclusions (31 kPa) surrounded by a soft medium (4 kPa) in a tissue-mimicking phantom. The focal point of the ARFI excitation pulse was 2 cm, although the B-mode image extends to a depth of 4 cm. The image shows displacements 0.22 ms after excitation.



Conclusions: We have developed an ARFI imaging system capable of generating images of tissue displacement in approximately 1 second. We anticipate that such a system will be useful liver procedures such as RF ablation monitoring, biopsy guidance and patient screening.

Acknowledgements: This work is supported by NIH grant R01-CA-114093. The authors would like to thank Siemens Medical Solutions USA, Inc. for their technical and in kind support.

References:

- [1] J. J. Dahl, G. F. Pinton, M. L. Palmeri, V. Agrawal, K. R. Nightingale, and G. E. Trahey. A parallel tracking method for acoustic radiation force impulse imaging. *IEEE Trans Ultrason., Ferr., Freq. Contr.*, 54(2):301-312, 2007.
-

Background: Diastolic dysfunction is a major cause of cardiovascular morbidity and mortality. Approximately 50% of patients who present with congestive heart failure symptoms have normal left ventricular ejection fractions and are symptomatic due to left ventricular diastolic dysfunction [1]. Unlike resting left ventricular systolic function, measures of diastolic function correlate closely with exercise performance. This suggests that exercise training may have salutary effects on diastolic performance [2]. The most widely used methods for measuring diastolic function include Doppler interrogation of trans-mitral blood flow and tissue Doppler interrogation of the translational movement of the mitral valve annulus during diastole. A direct measurement of myocardial relaxation during diastole is not available.

Aims: To evaluate the use of myocardial elastography to quantify left ventricular diastolic function. To compare the sensitivity of strain and strain rate imaging with more traditional Doppler-based measurements for the detection of improvements in diastolic function with exercise training.

Methods: Fourteen overweight, dyslipidemic, sedentary subjects with no overt evidence of cardiovascular disease (age 18–70 years) were enrolled in an eight month exercise program. Comprehensive echocardiograms were obtained before and after the exercise training. Speckle tracking methods were used to extract left ventricular longitudinal strain curves from images obtained from the apical four-chamber view. These curves were examined for indications of improvement in diastolic function and compared to traditional Doppler derived measures of diastolic function.

Results: Improved diastolic function can be observed through a variety of parameters within the strain and strain rate images. The exercise program resulted in an average 16.6% improvement in the peak longitudinal early (E) diastolic strain rate, an average 14.0% improvement in the peak longitudinal late (A) diastolic strain rate, and an average 13.1% improvement in the peak longitudinal diastolic strain first-third percent restoration. The most commonly used traditional measure of diastolic function, the ratio of early to late (E/A) diastolic trans-mitral blood flow peak velocities, improved by an average 6.7%.

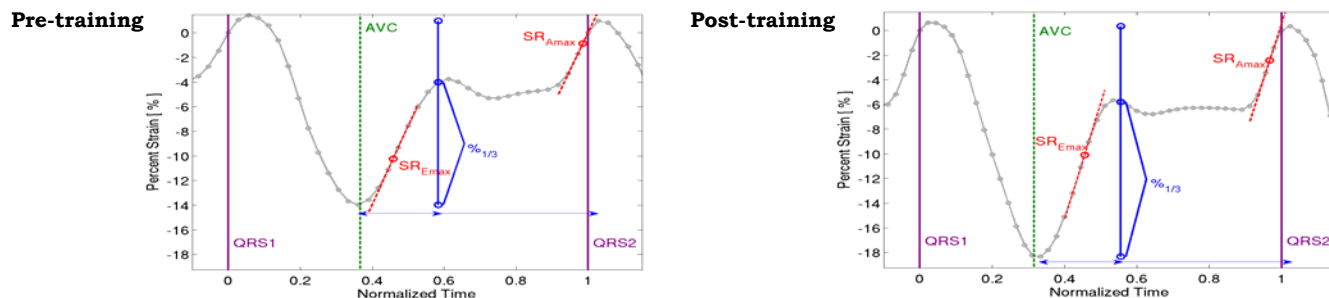


Figure 1: Pre- and post-training four chamber longitudinal strain curves, normalized by heart rate, are presented. Upon completion of the exercise program, the improved diastolic function of the subject is evident by increased early and late diastolic strain rates ($SR_{E_{max}}$ and $SR_{A_{max}}$) and increased first third diastolic percent strain restoration ($\%_{1/3}$).

Conclusions: Myocardial strain imaging can directly measure left ventricular diastolic function. Strain imaging proved more sensitive than currently used methods in detecting exercise induced improvements in diastolic function.

Acknowledgements: This research was funded by an American Society of Echocardiography Echo Investigator Award (Douglas PI); and by 2R01 HL57354: Peripheral Effects of Exercise on Cardiovascular Health study (STRIDE II; William E. Kraus, PI). We would also like to thank Dr. William Kraus.

References:

- [1] Ramachandran SV, Larson MG, Benjamin EJ et al. Congestive heart failure in subjects with normal ventricular ejection fraction. *J Am Coll Cardiol* 1999; 33: 1948–55.
- [2] Arbab-Zadeh A, Dijk E, Prasad A et al. Effect of aging and physical activity on left ventricular compliance. *Circulation* 2004; 110: 1799–805.

Hao Chen^{1,3*}, Tomy Varghese^{1*}, Peter S. Rahko², J.A. Zagzebski¹.

¹Medical Physics Department, ²Cardiovascular Medicine, University of Wisconsin Hospital and Clinics,

³Electrical and Computer Engineering Department, University of Wisconsin–Madison, Madison, WI, USA.

Background: Strain and strain rate imaging are relatively new techniques in non-invasive cardiac diagnosis. [1]. Myocardial strain imaging has potential clinical application for the detection of acute myocardial ischemia, assessment of regional left ventricular function, monitoring the outcome of cardiac resynchronization therapy, etc. Cardiac motion estimation methods such as Tissue Doppler imaging (TDI) have been used to assess myocardial muscle displacements using the strain-rate and strain. However, most techniques based on TDI are being replaced by direct 2D speckle tracking methods that utilize 2D B-mode images on commercial cardiac scanners [2,3]. Cardiac elastography using radiofrequency (RF) echo signals can provide more accurate 2D strain information when compared to B-mode signals, provided RF data frames at a sufficient frame rate are acquired.

Aims: Strain and strain rate imaging, as adjuncts to traditional echocardiography, are developing into techniques that provide new information for evaluation of regional myocardial function. Cardiac strain imaging using RF data can provide higher quality displacement and strain estimates than those obtained from B-Mode speckle tracking currently available on commercial clinical ultrasound systems. The purpose of this study is to compare the tracking performance between B-mode and RF data over a cardiac cycle. In addition, frame rate requirements with RF data are assessed.

Methods: Five healthy volunteers were scanned using a GE Vingmed Vivid 7 Ultrasound system (GEMS Inc., USA), using a 2.5 MHz phased array transducer with an approximate 60% bandwidth. RF data over an 80mm depth at a 20MHz sampling rate and at a frame rate of 43.7 frames per second (FPS) were acquired. Each data set contains 201 RF data frames, and each frame contains 95 A-lines over a 60° sector angle. Data was transferred to a personal computer for off-line analysis.

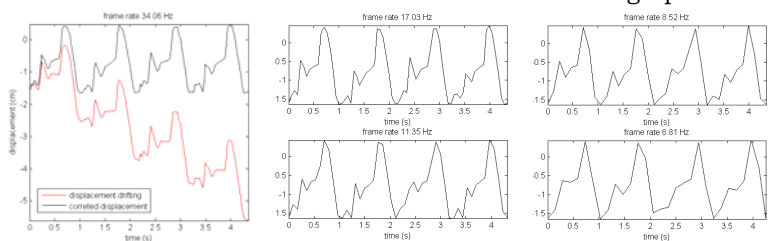
A two step 2D cross-correlation algorithm [3] was used to estimate local displacements within the heart wall between consecutive RF data frames. The first correlation step uses 50% overlapped gated windows with a 28 wavelength window length along the beam direction and 7 A-lines along the azimuthal direction, while the second correlation step uses 75% overlapped gated windows with a 12 wavelength window length and 5 A-lines. RF data in the frame sequence acquired were registered using B-Mode image data prior to tracking the displacements and strain. The displacement drift during the cardiac cycle is corrected before least square estimation method is applied to obtain strain estimates.

Results: The 2D two-step cross-correlation method [4] provides more efficient and accurate estimation of local displacements and strain than the 1-D cross-correlation method. Accumulated displacements (over a cardiac cycle) and strains obtained from different regions of interest (ROI) marked on the B-Mode image were tracked over the entire 201 frames of RF data collected. Accumulated displacements and strains over different ROI's within the cardiac muscle can be compared to evaluate differences and synchrony in the displacement and strain patterns over several cardiac cycles using both B-mode and RF data.

Conclusions: Displacement and strain information obtained using RF data can provide accurate information over the cardiac cycle for cardiac resynchronization therapy and regional LV function.

Reference:

- [1] D'hooge, J., A. Heimdal, et al. (2000). "Regional Strain and Strain Rate Measurements by Cardiac Ultrasound: Principles, Implementation and Limitations." *European Journal of Echocardiography* 1(3): 154–170.
- [2] Becker, M., et al., Analysis of myocardial deformation based on pixel tracking in two dimensional echocardiographic images enables quantitative assessment of regional left ventricular function. *Heart*, 2005. 92(8): p. 1102–1108.
- [3] Suffoletto, M.S., et al., Novel speckle-tracking radial strain from routine black-and-white echocardiographic images to quantify dyssynchrony and predict response to cardiac resynchronization therapy. *Circulation.*, 2006. 113(7): p. 960–8.
- [4] Chen H, Shi H, Varghese T., Improvement of elastographic displacement estimation using a two-step cross-correlation method, *Ultrasound Med Biol.* 2007;33(1):48–56.



J González-Fernández^{1}, L Gómez-Déniz¹, J Ruiz-Alzola^{1,2}.*

¹University of Las Palmas de Gran Canaria, CTM Center for Technology in Medicine, Signals and Communications Department, Pabellón B Edif. Telecomunicaciones Lab. 203, Campus de Tafira s/n, 35017 Las Palmas de Gran Canaria, Canary Islands, SPAIN; ²Canary Islands Institute of Technology, Playa de Pozo Izquierdo, s/n 35119 Santa Lucía (Las Palmas), Canary Islands, SPAIN.

Background: Several materials have been successfully utilized in the fabrication of tissue mimicking phantoms for elasticity imaging, including agar-gelatin and polyvinyl alcohol. Although they have shown similar acoustic and elastic properties to those of living tissues, it would be desirable to develop phantom materials that combined stability over time with ease of use and preparation. Gelled mineral oil is a low cost material that resembles soft tissue in appearance and viscosity. It is a colorless oil composed mainly of cyclic paraffins and suitable gellants. It exhibits the remarkable property of softening by heating above 70°C, becoming fluid enough to incorporate inclusions and be poured into desirable molds, and hardening again when cooled down. The process can be repeated several times thus permitting its reutilization. It is a very stable material that can be kept at room temperature and remains unaffected by most common chemical reagents.

Aims: The objective of this study is to test the feasibility of gelled mineral oil as a phantom material for elastography.

Methods: A mixture of 90% white mineral oil (CAS 8042-47-5), 9% gellants and 1% butylhydroxytoluene (CAS 128-37-0) was slowly heated and stirred until the temperature reached approximately 100°C and completely liquefied. At that time, 0.2% glass microspheres (3M Scotchlite) and 1% cellulose (CAS 9004-34--6) were added to obtain appropriate scattering and absorption properties. In order to achieve an adequate range of Young's moduli, increasing quantities (2.5%, 5.5% and 11%) of higher density mineral oil were added, hence obtaining four different homogeneous phantoms. Air bubbles formed during mixing were removed by placing the mixture into a vacuum chamber. It was then poured into a cylindrical container 6 cm in diameter for subsequent mechanical elasticity testing, and allowed to cool until the temperature decreased to 25°C. Young's modulus measurements were performed at room temperature (25°C) using a computer-controlled servo testing machine integrating a 10N load-cell. Ultrasound propagation speed was measured under similar testing conditions described in [1] using an ultrasound pulser/receiver (Model 5800PR, Panametrics-NDT).

Results: Four homogeneous phantoms were produced with added concentrations of high-density mineral oil ranging from 0 to 11%. Young's modulus ranges from approximately 4.5 to 6.5 kPa as shown in Figure 1. The addition of high-density mineral oil increases stiffness linearly. Elastic properties are not influenced apparently by the rate of refrigeration. Several mechanical and acoustic properties are summarized as follows:

Specific Gravity: 0.90 (25°C)
 Melting Point (pseudo): 70–90°C (160–200°F)
 Flash Point: 221°C (430°F)
 Ultrasound speed: 1440 m/s (7.5 MHz, 25°C)

Conclusions: The results indicate that gelled mineral oil can be successfully used as a stable, low-cost phantom material for rapid prototyping. In addition it is non-toxic and reusable. It exhibits an ultrasound propagation speed substantially comparable to that of adipose tissue. The process of heating and cooling can be repeated several times without degradation, hence making it possible to precisely readjust its elastic behavior.

Acknowledgements: This work is supported by Spanish Gov. USIMAG grant (TEC2004-06647-C03-02, and CEE SIMILAR NoE (FP6-507609). Mr. Ricardo Ibañez Serrano is specially thanked for valuable advice and essential contributions.

References:

[1] Kondo, T.; Kitatuji, M.; Kanda, H., New tissue mimicking materials for ultrasound phantoms. Ultrasonics Symposium, 2005 IEEE Volume 3, 18–21 Sept. 2005 Page(s): 1664–1667.

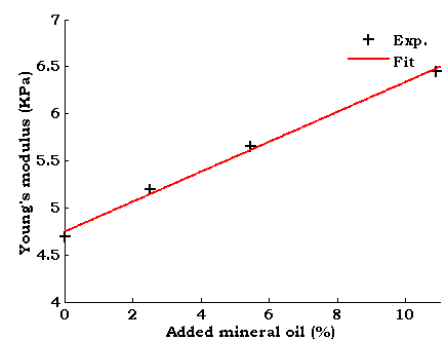


Figure 1: Young's modulus vs. concentration of high-density mineral oil.

Background: It is well known that soft tissue is best described as a viscoelastic material given the attenuation observed in mechanical waves through various imaging methods. Traditionally, viscoelasticity has been implemented in time-harmonic elastography through the use of complex moduli relating shear stresses to resulting shear strains [1–3]. It is also possible to model attenuation behavior from an inertial standpoint, which corresponds to the use of a complex density term in time-harmonic conditions. The combination of both of these effects is known as Rayleigh, or proportional, damping [4,5].

Aims: This work discusses the implementation of Rayleigh damping in full-field elastography (i.e. cases where the entire displacement field is measured). This method reconstructs a spatially varying Rayleigh damping parameter description through the use of the adjoint residual calculation [6,7].

Methods: Rayleigh damping is reconstructed through the use of spatially varying complex shear modulus and density, $\mu = \mu_R + i\mu_I$ and $\rho = \rho_R + i\rho_I$ respectively, in a nearly incompressible elastic material. Using this formulation, the real and imaginary shear modulus components can be interpreted through the use of any traditional rheological model for a viscoelastic solid while the form of the imaginary density component, $\rho_I = -\alpha/\omega$, can be obtained from the damped dynamic wave equation, $\mu \frac{\partial^2 u}{\partial x^2} = \rho \frac{\partial^2 u}{\partial t^2} + \alpha \frac{\partial u}{\partial t}$, for time-harmonic

motion at an angular frequency ω . The real density term, ρ_R , describes the mass per-unit-volume of the material just as in the normal elastic case and can either be reconstructed to determine a spatial distribution or left as a constant, usually at the density of water for soft tissue. Reconstruction of these complex parameters is performed with either conjugate gradient or quasi-Newton based methods.

Results: Reconstruction typically progresses initially towards a consistent damping ratio, followed by movement along the line of constant damping ratio towards the correct values of μ_I and ρ_I .

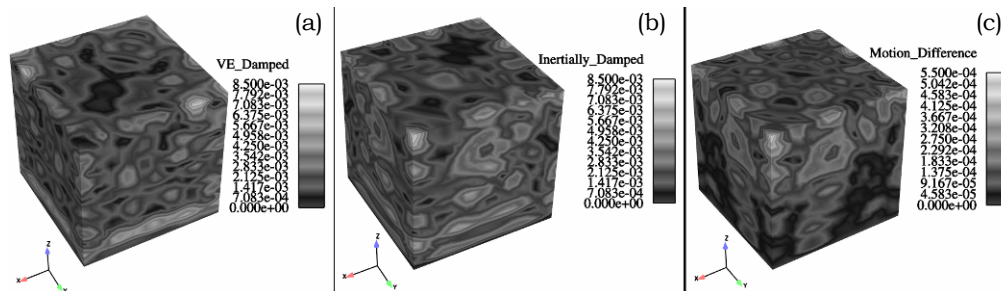


Figure 1: A motion comparison between a viscoelastic material (a) and an inertially damped material (b), where an inclusion of 10x higher real shear modulus is located in the +x, +y, +z corner. The difference between the two cases is shown in (c).

Conclusions: In reality, viscoelastic models are an approximation to the mechanical behavior of real tissue. The increased detail with which a Rayleigh model can describe attenuation behavior leads to a more complete parameterization of the observed behavior. This may include information pertinent to medical diagnosis. It can be shown that reconstructing the elastic properties of a material containing Rayleigh damping characteristics using a purely viscoelastic model (i.e. no inertial damping component) can lead to artifacts.

Acknowledgements: We gratefully acknowledge support from NIH/NIBIB R01-EB004632-02.

References:

- [1] TE Oliphant et al, “Complex valued stiffness reconstruction for magnetic resonance elastography by algebraic inversion of the differential equation.” *Mag. Res. Med.*, 45:299–310, 2001.
- [2] R Sinkus et al, “Viscoelastic shear properties of *in vivo* breast lesions measured by MR Elastography.” *Mag. Res. Imag.* 23:159-165, 2005.
- [3] R Sinkus et al, “Imaging anisotropic and viscous properties of breast tissue by magnetic resonance elastography” *Mag. Res. Imag.* 23:372–387, 2005.
- [4] RD Cook et al, “Concepts and applications of finite element analysis; 4th Ed.” Wiley Press, New York, 2002.
- [5] MDJ McGarry et al, “Damping models in elastography.” *Proceedings of SPIE Medical Imaging*, San Diego, USA, vol. 6511, 2007.
- [6] AA Oberai et al, “Solution of inverse problems in elasticity imaging using the adjoint method.” *Inverse Problems*, 19:297–313, 2003.
- [7] HL Liew et al, “Recovery of shear modulus in elastography using an adjoint method with B-spline representation.” *Fin. Elem. Anal. Desig.* 41:778–799.

P-L Yen^{1}, D-R Chen², C-H Jen³.*

¹National Taipei University of Technology, Taipei, Taiwan; ²ChangHua Christian Hospital, ChangHua, Taiwan; ³Vehicle Engineering Department, National Army Academy, Chung-Li, Taiwan.

Background: Soft tissue abnormalities are often correlated to local change in mechanical properties [1,2], and some tactile methods under the framework of inverse problem solutions were proposed to determine the elastic properties of tumors embedded in soft tissue [1–3]. In general, inverse problems are ill-posed. In this study, we assume the information of the tumor shape and location can be acquired from ultrasonic images and an artificial neural network (ANN) based inverse method is used to efficiently explore a nonlinear multivariate relationship between parameters and responses.

Aims: The goal of this study is to determine the elastic property of the tumor accurately to distinguish cancerous/non-cancerous abnormalities in surrounding soft tissue.

Methods: Real breast tissue and lung are often of relatively uniform thickness and large extent when compared to the probe size. The simplified 2-D model shown in Figure 1 is analyzed using finite element method (FEM). By changing different size, depth and stiffness ratio of tumors hundreds of force distribution data and extracted parameters were obtained along the surface of the tissue by FEM forward model. The ANN model was trained using Levenberg–Marquardt Back Propagation (LMBP) [4]. After training, testing and validation, the ANN model was used for determination of elastic properties of tumors embedded in soft tissue inversely.

Results: The stiffness ratios predicted by the proposed ANN inverse model are shown in Figure 2. It is found that the inverse model is capable of accurate predicting the stiffness ratio for all tested cases. The prediction errors of stiffness ratios are within 3% in mean and 5% in standard deviation for very hard and hard inclusions, 40% in mean and 65% in standard deviation for soft inclusion.

Conclusions: Based on the results obtained from this study, the ANN inverse model demonstrates promising stiffness ratio predictability, which is sufficiently accurate to distinguish cancerous/non-cancerous abnormalities in surrounding soft tissue. In comparison to the other methods, the LMBP ANN represents an efficient method to explore a nonlinear multivariate relationship between parameters and responses. Its success and effectiveness for stiffness ratio prediction have been demonstrated in this study. The proposed method can be complementary to other image modalities to provide a second opinion for cancer diagnosis.

References:

- [1] Itoh, A. et al, Radiology 239(2):341-350, 2006.
- [2] Wellman PS et al. Arch Surg 136:204-208, 2001.
- [3] Abbas Samani et al. Phys. Med. Biol. 52:565-1576, 2007.
- [4] Martin et al. IEEE Transactions on neural networks.vol.5, No.6, November, 1994.

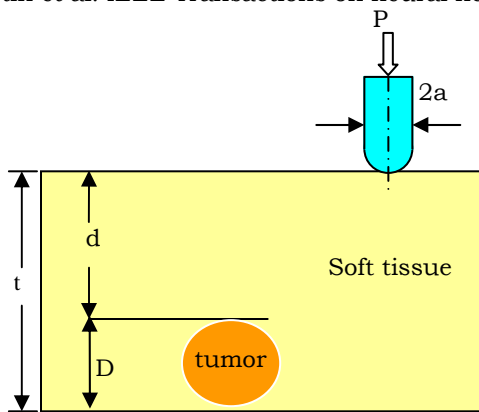


Figure 1: Geometry of the Finite Element Model.

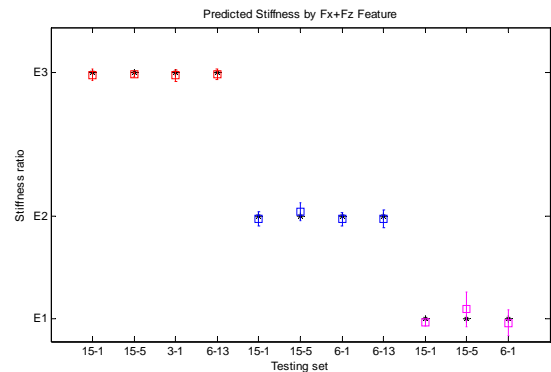


Figure 2: Testing Results of Stiffness Prediction.

Background: Correlation-based speckle tracking methods are commonly used in elasticity imaging to estimate displacements. In the presence of local strain, displacement error cannot be reduced using a larger window size (in cross-correlation calculations). One way to reduce tracking error is to temporally stretch the RF data after compression [1]. As an alternative, we proposed using a short window followed by a correlation coefficient filter [2]. Simulation and experimental results demonstrated the efficacy of the method.

Aims: Using a short window reduces displacement error by reducing signal decorrelation due to strain. The study aimed at further reducing the decorrelation and, therefore, improving the tracking performance without increasing the computational effort.

Methods: A new 2D speckle tracking algorithm has been developed. First, forward phase rotation based on the applied axial strain is applied to the RF data before compression. Second, complex cross-correlation coefficients between windowed blocks from RF data before and after compression are calculated and filtered. Third, inverse phase rotation is applied to the filtered cross-correlation coefficients to zero the mean phases of the cross-correlation coefficient peak. Finally, displacements are estimated via peak searching and phase zero-crossing of the cross-correlation coefficients. The basic difference between the proposed algorithm and that in [2] is the inclusion of phase rotations, which take little time compared to the remaining part of tracking.

Simulations were performed using Field II [3] assuming a 1D linear array with a center frequency of 7.5 MHz, a 0.2mm element spacing, a 6mm element height, a 30mm elevational focus. 128 channels were used for imaging. On transmit, the focus was set to 30mm and Hanning apodization was applied. On receive, dynamic focusing and dynamic aperture with an F-number of 1.1 were applied. Speckle images without and with an average strain of 3% were generated and used to test the proposed algorithm.

Results: Figure 1 shows the tracking results. Compared to the algorithm in [2], the new one reduced the lateral and axial displacement errors by 40% and 14%, respectively, on average.

Conclusions: With little increase of computational effort, the proposed algorithm with phase rotation can significantly improve speckle tracking in elasticity imaging compared to the one without phase rotation, especially in the lateral direction. Although a simple case is used to demonstrate the efficacy here, this algorithm can be applied to more complicated cases. To optimize the performance, iterative tracking with axial displacement feedback for phase rotation may be used.

Acknowledgements: Support from NIH grants HL-68658 and CA-109440 is gratefully acknowledged.

References:

- [1] T. Varghese and J. Ophir, "Enhancement of echo-signal correlation in elastography using temporal stretching," *IEEE Trans. Ultrason., Ferroelect., Freq. Contr.*, vol. 44, no. 1, pp. 173-180, 1997.
- [2] M. A. Lubinski, S. Y. Emelianov, and M. O'Donnell, "Speckle tracking methods for ultrasonic elasticity imaging using short-time correlation," *IEEE Trans. Ultrason., Ferroelect., Freq. Contr.*, vol. 46, no. 1, pp. 82-96, 1999.
- [3] J. A. Jensen and N. B. Svendsen, "Calculation of pressure fields from arbitrarily shaped, apodized, and excited ultrasound transducers," *IEEE Trans. Ultrason., Ferroelec., Freq. Contr.*, vol. 39, no. 2, pp. 262-267, 1992.

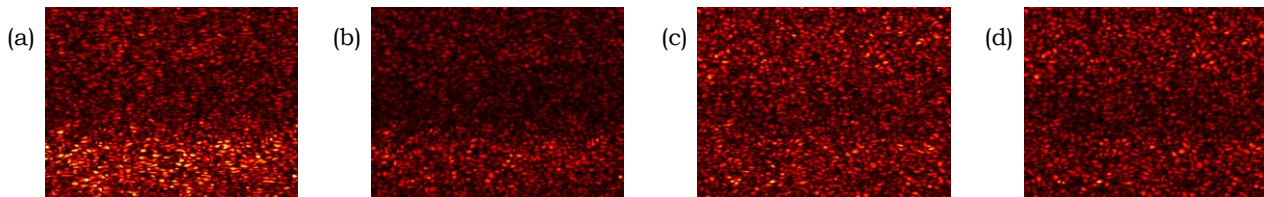


Figure 1: Tracking results. (a) and (b) show the absolute lateral displacement errors (with a dynamic range of [0, 0.1] mm) without and with phase rotation, respectively. (c) and (d) show the absolute axial displacement errors (with a dynamic range of [0, 0.006] mm) without and with phase rotation, respectively. All the images have a size of 21mm (axial/vertical, 16~37mm) by 27mm (lateral/horizontal).

110 **SURFACE DISPLACEMENT–TRACTION MEASUREMENTS DO NOT UNIQUELY DETERMINE THE STIFFNESS AND DENSITY IN ANISOTROPIC ELASTIC MEDIA.**

*Anna L Mazzucato*¹, *Lizabeth V Rachele*^{2*}.

¹Penn State University, University Park, PA 16802, USA; ²Rensselaer Polytechnic Institute, Troy, NY 12180, USA.

Background: In the case of isotropic elastic media [1,2] and isotropic elastic media with residual stress [3,4], it has been shown that the collection of all surface–displacement and the corresponding surface-traction data uniquely determines the stiffness and density in the interior. It was not known until recently, though, whether this type of surface data carries enough information to uniquely reconstruct the material properties of anisotropic elastic media.

Aims: The purpose of this work is to determine whether mathematical models predict any ambiguities in the sensing of the internal stiffness and density of an anisotropic elastic body from surface displacement-traction measurements and, if so, to characterize features of the elastic media that are “hidden” from the surface.

Methods: We model elastic media via the linear or non-linear differential equations for elastodynamics. The surface displacement–traction correspondence is modeled by the boundary operator (the Dirichlet-to-Neumann map) for the associated initial–boundary–value problem over a finite time interval. Our main tool, a new approach in inverse problems for elastic media, is the representation of the equations of motion in a covariant form (following Marsden and Hughes [5]) that preserves the underlying physics.

Results: We show [6] that for any given anisotropic elastic body with smoothly varying density and elastic properties, there is a family of anisotropic media that would each result in the same surface displacement–traction data.

Conclusions: For general anisotropic elastic media, it is not possible to unambiguously reconstruct the internal stiffness and density from surface displacement–traction measurements alone. It remains to be seen whether this is the only obstruction to uniqueness for anisotropic media, and whether the same problem arises within subclasses of anisotropic media (for example, within the class of transversely isotropic media).

Acknowledgements: Each of the authors was partially supported by MSRI Postdoctoral Fellowships. (Research at MSRI is supported in part by NSF grant DMS–9850361.) This work was conducted while the first author was a Gibbs Instructor at Yale University. The work of the second author was partially supported by NSF grants DMS–9801664 (9996350) and DMS–0340530.

References:

- [1] L. Rachele, Uniqueness of the density in an inverse problem for isotropic elastodynamics. *Trans. Am. Math. Soc.* 355(12) (2003) 4781–4806.
 - [2] L. Rachele, An inverse problem in elastodynamics: Determination of the wave speeds in the interior. *J. Differ. Equ.* 162(2) (2000) 300–325.
 - [3] S. Hansen and G. Uhlmann, Propagation of polarization in elastodynamics with residual stress and travel times. *Math. Ann.* 326(3) (2003) 563–587.
 - [4] L. Rachele, Uniqueness in inverse problems for elastic media with residual stress. *Commun. Partial Differ. Equ.* 28(11–12) (2003) 1787–1806.
 - [5] J.E. Marsden and T.J.R. Hughes, *Mathematical Foundations of Elasticity*. Dover, New York (1994).
 - [6] A.L. Mazzucato and L.V. Rachele, Partial Uniqueness and Obstruction to Uniqueness in Inverse Problems for Anisotropic Elastic Media. *Journal of Elasticity* 83 (2006) 205–245.
-
-

113 **DEVELOPMENT OF A STRAIN IMAGING METHOD USING LUCAS-KANADE OPTICAL FLOW METHOD IN CONJUNCTION WITH EXPECTATION-MAXIMIZATION ALGORITHM.**

Yong-Jin Zhou^{1*}, Yong-Ping Zheng¹.

¹Department of Health Technology and Informatics, The Hong Kong Polytechnic University, Hong Kong, CHINA.

Background: In traditional soft tissue ultrasound elastography [1], phantoms or tissues can be compressed slightly (<1% for *in vivo*) and the pre- and post-compression radio frequency (RF) data are collected. Other elastography reconstruction mainly includes two problems, the displacement estimation and the strain reconstruction. From the point of view of computer vision and video processing, the first problem is equivalent to quantitatively distinguishing the motion of the surrounding tissues and inclusions with different stiffness. For the second problem, strain in traditional elastography is estimated from the gradient of the displacement estimate. However, the gradient operation would introduce additional noise amplification into the strain estimation process.

Aims: We proposed a new method, using the Lucas-Kanade optical flow algorithm in conjunction with the Expectation-maximization (EM) algorithm, to simultaneously segment and estimate motion in the ultrasound RF data sequence. For strain reconstruction, we evaluated the application performance of a modified Sobel operator together with anisotropic diffusion.

Methods: The EM algorithm [2] is used in statistics for finding maximum likelihood estimates of parameters in probabilistic models, where the model depends on unobserved latent variables. This algorithm includes performing an expectation (E) step, which computes an expectation of the likelihood by including the latent variables as if they were observed, and a maximization (M) step, which computes the maximum likelihood estimates of the parameters by maximizing the expected likelihood found in the E step. The parameters found in the M step are then used to begin another E step, and the process is iterated. In our study, the motion patterns, to which the inclusions and surrounding tissues were subjected, were the latent variables. Therefore, in the E step we segmented the data based on the motion patterns. With the pixels assigned to a motion model, we recomputed the motion parameters based on the assignments to select the parameters that minimized the deviation error weighted by the motion segmentation. For the M step in this work, we used the Lucas-Kanade optical flow algorithm [3] to solve for the motion parameters. After obtaining the displacement field, a modified Sobel filter was used to get the raw displacement gradient, and then an anisotropic diffusion method was applied to improve the strain estimation. To test the feasibility of the algorithm, a breast phantom (Model 047, CIRS, Inc., Norfolk, VA, USA) was pressed from the top using a 10–5 MHz ultrasound probe (Model 75H38A, Mindary Electronic Co., China), and the RF data were acquired using a customized digital ultrasound scanner (Model DP 9900, Mindary Electronic Co., China).

Results: Figure 1 shows typical strain estimation results obtained from the breast phantom using the proposed method under a freehand protocol. The obtained CNRe for (d) is 7.2 dB which is comparable to previous results using traditional cross-correlation method. More detailed results will be reported during presentation.

Conclusions: The preliminary results demonstrated that the proposed method could provide strain imaging of the tissue phantom. Further studies are being conducted with more tests on phantoms and human subjects *in vivo*.

Acknowledgements: Supported by Hong Kong Innovation and Technology Commission (GHP/061/05).

References:

- [1] J. Ophir, I. Cespedes, H. Ponnekanti, Y. Yazdi and X. Li, Elastography: a quantitative method for imaging the elasticity of biological tissues. *Ultrason. Imag.* 13, 111–134 (1991).
- [2] A.P. Dempster, Laird N.M., and Rubin D.B., Maximum-likelihood from incomplete data via the EM algorithm." *J. Royal Statist. Soc. Ser. B.*, 39, (1997).
- [3] B.D Lucas., and Kanade T., An iterative Image Registration Technique with an Application to Stereo Vision, in *Proc. Imaging Understanding Workshop* (1981).

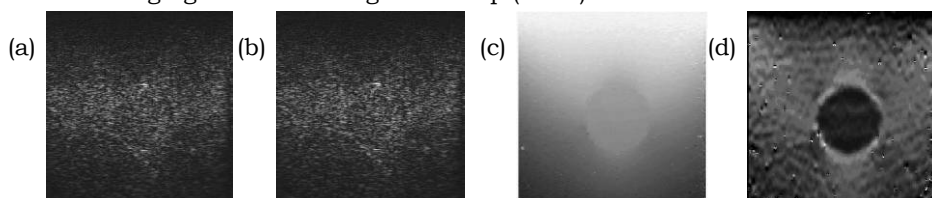


Figure 1: (a) (b) Two sonograms in sequence;
(c) displacement field;
(d) strain estimation

Yong Zhang¹, Robert W. Kramer¹, Richard G. Barr^{2*}.¹Youngstown State University, Meshell Hall, One University Plaza, Youngstown, OH, 44555, USA;²Southwoods Radiology Consult. Inc., 250 DeBartolo Place, Bldg. B, Youngstown, OH 44512, USA.

Background: Elastography research employs two basic imaging techniques: (i) property abnormalities of diseased tissues are indirectly inferred from strain images [1]; (ii) elastic properties (such as Young's modulus) are reconstructed from the observed tissue deformations by solving an inverse problem [2]. In the second approach, various regularization schemes have to be applied to alleviate the ill-posedness of the inverse solution, especially its numerical instability. However, as a global term, the regularization prior in the Tikhonov functional has a tendency of over-smoothing the solution, which makes it difficult to identify and examine the tissue abnormalities accurately.

Aims: Our aim is to develop an algorithm that utilizes a local constraint that is adaptive to the property discontinuities. This adaptive prior allows us to reconstruct an elasticity distribution with sharper boundaries between the normal and diseased tissues.

Methods: Handling solution discontinuities with an adaptive constraint has been intensely studied in the context of edge-preserving image reconstruction [3]. The basic strategy is to use a controller function, $w(e'(x))$, to adjust the degree of smoothing, where $e'(x)$ is the derivative of elasticity and x denotes the spatial coordinates. If the controller function is properly defined so that the penalty term has a continuous and bounded relationship with the magnitude of $e'(x)$, a smoother solution yet with sharp discontinuities can be obtained. In this study, we used a controller function of exponential form: $w(e'(x)) = \exp(-e'(x)^2/r)$, where r is a parameter chosen empirically, depending on the data and model configuration. In a 2D mesh, the controller is implemented via a forward difference scheme. A Gauss-Newton iterative solver with an embedded conjugate gradient method is used to minimize the regularization functional.

Results: The tissue deformation was simulated using a finite element model of heterogeneous material properties (Figure 1). The model configuration was specified as a mixed type problem with a fixed boundary condition at the bottom and a compression condition on the top. The size of the model is $5 \times 5 \text{ cm}^2$ that was discretized into a square mesh of 2500 quadrilateral elements. The modeling domain has a Young's modulus of 50 kPa, while a small area in the upper-left corner was assigned a value of 400 kPa to represent the property abnormality. 1% white noise was added to the displacement data. Two simulations were carried out, one using a regular smoothness prior and the other using an adaptive regularization function. The results are shown in Figures 2 and 3. A marked improvement has been observed in terms of the shape of abnormal tissues and the contrast across the property boundaries.

Conclusions: By allowing the smoothness prior to vary spatially based on the magnitude of solution derivative, we can improve elastograms with clear boundaries between the normal and diseased tissues. Numerical experiments have shown encouraging results. Future work will be extended to the use of both phantoms and real tissues.

Acknowledgements: This work was supported in part by Ohio Board of Regents Research Incentive Grant #34241 of NEOUCOM and Youngstown State University URC Grant 08-#8.

References:

- [1] J. Ophir, E. I. Cespedes, H. Ponnekanti, Y. Yazdi, and X. Li, "Elastography: a quantitative method for imaging the elasticity of biological tissues", *Ultrasonic Imaging*, vol. 13, pp. 111-134, 1991.
- [2] F. Kallel and M. Bertrand, "Tissue elasticity reconstruction using linear perturbation method", *IEEE Trans. on Medical Imaging*, vol. 15, pp. 299-313, 1996.
- [3] S. Z. Li, "On Discontinuity-Adaptive Smoothness Priors in Computer Vision", *IEEE Trans. on Pattern Analysis and Machine Intelligence*, vol.17, pp. 576-586, 1995.

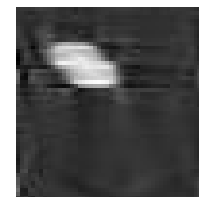
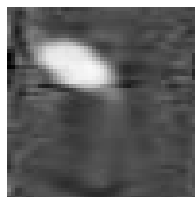
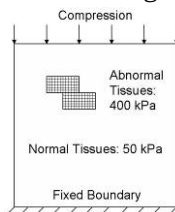


Figure 1: Model configuration with heterogeneous properties.

Figure 2: Recovered elasticity using a generic smoothing prior.

Figure 3: Recovered elasticity using an adaptive smoothing prior.

120 **TIME-REVERSAL OPERATION TO IMPROVE ESTIMATION PERFORMANCE OF LEFT VENTRICLE MOTION USING TAGGED MRI.**

T Alrefae^{1,2*} and M Bilgen^{2,3}.

¹Physics and Astronomy Department, University of Kansas, Lawrence, KS, USA; ²Hoglund Brain Imaging Center, ³Integrative and Molecular Physiology Department, University of Kansas Medical Center, Kansas City, KS, USA.

Background: Quantifying the regional myocardial tissue deformation and assessing its local function and viability require accurate estimates of displacements. During a cardiac cycle, the left ventricle (LV) wall experiences relatively large motion. Under such conditions, statistical errors made during the motion estimation process increase [1,2]. Consequently, the displacement measurements become challenging tasks to perform. This presentation provides a novel approach to address this issue.

Aims: The goal of this presentation is to introduce a radial time reversal operation based on a simple LV motion model to increase the performance of motion estimation in evaluating the cardiac function.

Methods: Forward LV motion model at the mid-ventricle and its characterization were described using a Gaussian-based spatial transformation T . In the current application, however, this function is utilized to stretch the cardiac image back in a radial fashion. The result is a time-reversed pseudo image where the LV wall shape and size are expected to be close to those seen in the image in frame I_1 , acquired at the beginning of the systole in the tagged MRI data set. Thus, in a cause and event terminology, the time-reversal operation attempts to reverse the displacement event, by inverting its cause, namely the systolic contraction. Mathematically, the time reversal of motion can be obtained by the operator T^{-1} , i.e., the matrix-inverse of the forward motion operator, T . The true displacement, d , of myocardial tissue at a spatial location in the LV wall can be decomposed into two components $d = \Delta + \delta$. Here Δ denotes the bulk motion predicted by the time-reversal model, and its elements along the x and y directions are given by a simple matrix multiplication with T^{-1} . The term, δ , is the residual displacement that is not accounted for by the time-reversal operation and remains to be estimated using a method of preference by the user applied between I_1 and the time-reversed (TR) image such as harmonic phase methods (HARP) [3].

Results: As shown in Figure 1, application of T^{-1} accounts for Δ component of the motion and consequently produces a time reversed (TR) image that is closer to the end-diastole image I_1 . The overall motion computation still requires estimating smaller residual displacements δ , which can be performed more effectively using standard estimators. In this regard, our multi-level processing approach improves the motion estimation performance. Furthermore, this treatment also improves HARP calculations since phase wraps experienced in this technique (Figure 2) are avoided due to the absence of the large motion (Figure 3).

Conclusions: Applying time-reversal utilizes empirically derived information that aids in providing more accurate estimation of myocardial motion. Moreover, time-reversal helps in improving HARP [3] by producing motion maps free of phase-wrapping.

References:

- [1] Bilgen, M. and Insana, M. F. J Acoust Soc Am, 1996. 99(5): p. 3212–24.
- [2] Bilgen, M. and Insana, M. F. J Acoust Soc Am, 1997. 101(2): p. 1139–46.
- [3] Osman, N. F., et al. IEEE Trans Med Imaging, 2000. 19(3): p. 186–202.

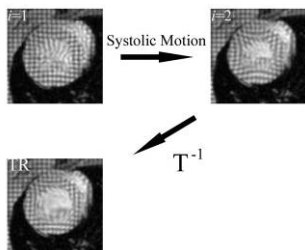


Figure 1: Application of T^{-1} reverses motion.

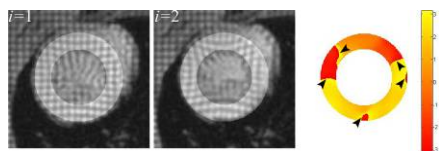


Figure 2: Phase wraps (arrowhead) are evident in the HARP map in areas experiencing large motion.

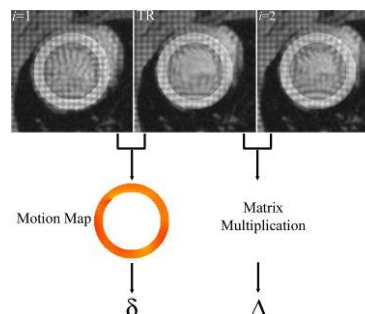


Figure 3: Bulk and residual motions are separated using time-reversal and HARP respectively. HARP map is free of phase wraps due to small motion between TR and I_1 ,

Carolina I. Flores¹, Jean Jacques Ammann¹.

¹Universidad de Santiago de Chile, Physics Department, Santiago, CHILE.

Background: The evaluation of the viscoelastic behavior of tissue may improve the differentiation between normal and pathological conditions. The temporal strain behavior of biomimetic materials has been shown to follow a continuous bimodal rheological model characterized by two different relaxation times through a set of elastic and viscoelastic parameters related to poroelastic mechanisms [1].

Aims: To develop a creep test method designed to extract viscoelastic parameters from a specimen through the viscoelastic characterization of synthetic foam materials suffused in viscous liquids.

Methods: The experiment consists of placing a foam specimen in an acrylic immersion chamber above a 5.0 MHz broadband transducer mounted on the bottom wall with its acoustic axis oriented vertically upward. A load is applied to the top of the specimen through a loading device composed of an acrylic disk with mobility in the vertical direction only. The device is loaded with a suitable weight and successive RF traces are acquired. The local displacements in the specimen are extracted from the RF data through a running cross-correlation between each pair of the successive traces and the strains are determined by applying the gradient operator (Figure 1).

The behavior of the temporal strain curves $\varepsilon(t)$ acquired at constant depths during the application of a constant load is fitted to a Continuous Bimodal Viscoelastic Model "CBV" formed by an elastic element (E_{elast}) in series with a continuous Kelvin/Voigt element holding bimodal Gaussian distributions of the

viscosity coefficient η [1]:
$$\varepsilon(t) = \frac{\sigma_L}{E_{Elast}} + \frac{\sigma_L}{E_{Vel}} \int_0^\infty \left(G_1 e^{-\frac{(\eta-\eta_1)^2}{2\sigma_1^2}} + G_2 e^{-\frac{(\eta-\eta_2)^2}{2\sigma_2^2}} \right) \left(1 - e^{-\frac{E_{Vel}}{\eta} t} \right) d\eta$$
 Equation 1

where σ_L , E_{Elast} and E_{Vel} denote the applied stress, the elastic constant of the material and the elastic constant of the Kelvin cells respectively, and G_i , η_i and σ_i the individual Gaussian amplitudes, central viscosities and standard deviations. The first and second Gaussian terms can be defined by a short and long mean relaxation time respectively, by $\tau_i = E_{Vel} / \eta_i$. After processing, the viscoelastic parameters $\{E_{Vel}, G_i, \eta_i$ and $\sigma_i (i = 1,2)\}$ are obtained through a trial and error fit of the $\varepsilon(t)$ curves, extracted at any specific location along the depth axis according to Equation 1.

Results: The method has been implemented on biphasic poroelastic materials made of open-cell foam matrices impregnated in liquids that develop different creep responses as a function of the interaction between the elastic and viscous phases. The contribution of the elastic matrix to the viscoelastic response has been evaluated by varying the nature of the foam matrix while maintaining the impregnating liquid (water). We observe in Table 1 the main differences in the short τ_1 and long-term τ_2 parameters in the CBV for different matrices.

Foam	d [mm]	σ_0 [kPa]	G_1	τ_1 [s]	G_2	τ_2 [s]	E_{Vel} [kPa]
WWOS	4.0	1.2	6.0E-07	0.48	9.0E-09	33	6.0
WS	5.0	2.3	3.0E-06	2.90	5.0E-08	350	350.0
GS	17.0	2.3	1.9E-07	1.45	3.0E-07	290	290.0

Uncertainty on parameters: 5%

The respective behavior of the temporal strains and their numerical fit can be compared through the normalized elastic modulus $E_{app}^*(t) = \sigma_0 / \varepsilon(t)$. In Figure 2, we observe temporal strain curves for three synthetic sponges in water. The short relaxation time associated with the WWS latex foam illustrates a significantly different behavior compared to the GS and WS polyurethane foams. Additional results for viscous liquids will be presented at the conference.

Conclusions: Synthetic biphasic specimens represent an effective tool in the ultrasonic characterization of viscoelastic behavior, which allows evaluation of specific viscoelastic behavior at low cost. Poroelastic mechanisms are expected to be related to the material properties of the matrix, pore size and capillarity effects of the liquid suffusing the elastic matrix.

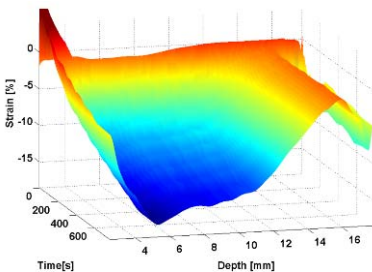
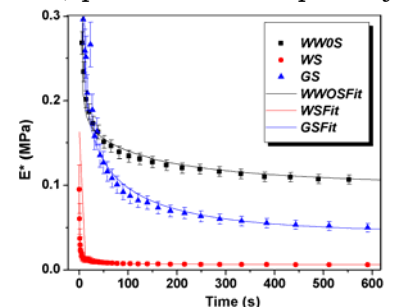


Figure 1: Temporal strain in function of depths for GS polyurethane foam in water.

Figure 2: Apparent modulus ($E_{app}^*(t)$) and the CBV numeric fit (Lines) for three type of synthetic foam.



Acknowledgements: Authors are very thankful to Prof. J. Ophir for his assistance in the conduct of this work. This work is supported by Fondecyt project No. 1040206, and Fondap project No. 11980002, Chile.

References: [1] J Ammann, et al., Proc. of the Fifth Int. Conf. Ultrasonic Meas. Imaging Tissue Elasticity©. October 8–11, 2006, p36.

Background: Sonoelastography is an ultrasound imaging technique where low frequency time harmonic shear waves are propagated through a medium while real time Doppler techniques are used to image the resulting vibrational amplitude. It has been shown that stiff regions correspond to areas of small amplitude. To better quantify tissue stiffness, a new experiment known as the crawling wave experiment has been developed at the University of Rochester Center for Biomedical Ultrasound [1]. In this experiment, two excitations at nearby, but not equal, frequencies create time harmonic shear waves originating from opposite sides of the medium. The resulting vibrational pattern imaged using Doppler techniques exhibits an interference pattern, or “crawling wave”, which travels through the medium at a very small fraction of the shear wave speed. The speed of the crawling wave correlates very well with tissue stiffness, and several techniques have been developed to image the crawling wave speed [1,2].

Aims: The relationship between the shear wave speed and the crawling wave speed was developed in [1,2] and is highly nonlinear. Therefore, using the crawling wave speed as an imaging functional for the shear wave speed can result in artifacts. The goal of this research is to remove these artifacts by calculating the shear wave speed of the tissue using the crawling wave experiment.

Methods: We have developed a first order partial differential equation that relates the phase of an underlying shear wave to the crawling wave speed. Once the crawling wave speed has been calculated using the methods given in [2], the phase of either of the underlying shear waves can be determined using this equation. Then the methods in [2] are again used to find the shear wave speed.

Results: We have tested our new method for determining the shear wave speed on synthetic data (see example medium in Figure 1a). The first step is to calculate the crawling wave speed (Figure 1b). The crawling wave speed image is well-correlated with the shear wave speed and gives a good qualitative recovery, but there are some artifacts due to the nonlinear relationship between the shear wave speed and the crawling wave speed. In this example, the size and shape of the inclusion have been distorted. We then use our new equation to calculate the phase of a related shear wave and, from this phase, determine the shear wave speed (Figure 1c). This image gives an excellent quantitative recovery and, in particular, the size, shape and contrast of the inclusion have all been successfully recovered.

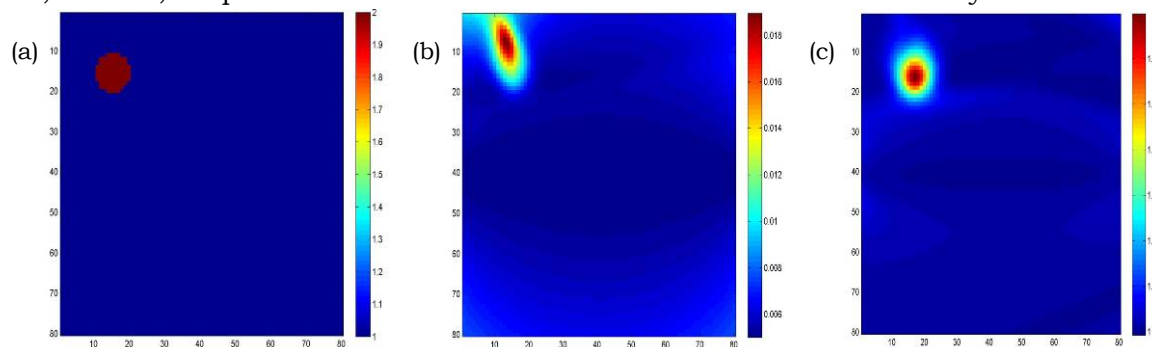


Figure 1: (a) Numerical medium with 1cm diameter circular high speed inclusion. The wave speed is two times higher in the inclusion (b) crawling wave speed. Note that the location and shape of the inclusion has been distorted. (c) Shear wave speed reconstruction from new method.

Conclusions: Shear stiffness images obtained from the crawling wave experiment are typically generated by imaging the speed of the crawling wave. We have developed a new algorithm that images the shear wave speed of the underlying shear waves. This new method removes artifacts due to the nonlinear relationship between the shear wave speed and crawling wave speed and yields an improved image.

References:

- [1] ZC Wu, DJ Rubens, KJ Parker, (2006) “Sonoelastographic imaging of interference patterns for estimation of shear velocity distribution in biomaterials” JASA 120 pp 535–545.
- [2] J McLaughlin, D Renzi, K Parker, Z Wu, (2007) “Shear wave speed recovery using moving interference patterns obtained in sonoelastography”, JASA 121, pp. 2438–2446.

049 CORNEAL DISPLACEMENT MAPPING BY OPTICAL COHERENCE ELASTOGRAPHY.

WJ Dupps^{1*}, MR Ford², AM Rollins².

¹Cleveland Clinic, 9500 Euclid Avenue/i-32, Cleveland, OH, 44195, USA; ²Case Western Reserve University, 10900 Euclid Avenue, Cleveland, OH, 44106, USA.

Background: The cornea relies upon its material properties in its role as a mechanical barrier to injury and the chief structural constituent of the ocular refracting system. These properties influence the safety and optical predictability of surgery and play an important role in the pathogenesis of diseases such as keratoconus [1]. Ultrastructural analyses have demonstrated that the posterior corneal stroma has less collagen interweaving [2], more hydrophilic glycosaminoglycans, and lower resistance to swelling than the anterior stroma. These differences, and the ability to measure their mechanical analogues nondestructively with high spatial resolution, may be important in early identification of keratoconus and in assessing the susceptibility of patients to post-refractive surgery optical instability. We previously described an approach to intracorneal displacement analysis using optical coherence tomography (OCT) [3].

Aims: The current work assesses the capability of OCT-based elastography to quantify spatial differences in intrastromal displacement induced by a physiological pressure perturbation.

Methods: Paired human donor globes were imaged with a laboratory-based high-speed Fourier-domain optical coherence tomography scanner (OCT) while intraocular pressure (IOP) was decreased from 20 to 13±1 mmHg in replicate experiments. Pressure was directly controlled and monitored by intravitreal infusion. Scan frames included full-thickness, 3.3 mm widths of central cornea imaged with lateral and axial sampling densities of 4 and 8 microns, respectively. Two-dimensional patterns of optical feature flow over the stress decrement were analyzed with custom cross-correlation routines to derive displacement fields indicative of biomechanical strain. Three anterior and 3 axially corresponding posterior corneal 10x10-pixel regions of interest (ROI) were defined. Paired t-tests were used to compare displacement across ROIs in replicate experiments.

Results: Axial displacements were much higher than lateral displacements during modest pressure decrements and differed significantly between eyes from the same donor (means for all ROI's combined = 30.6±6.3 µm and 52.5±10.2 µm, p<0.001). In 4 of 5 ipsilateral replicate analyses, smaller displacements occurred in anterior stromal regions than in posterior stromal regions (mean difference 3.4 µm), while differences between laterally separated regions in the central 3.3 mm of the cornea were small. Displacement magnitudes within each ROI varied by less than 3 µm (sd) on average during a single imaging sequence.

Conclusions: Optical coherence elastography can be used to detect differences in the local response to a physiologic stress within and between individual eyes. Our results in this very small sample are consistent with existing anatomic and biomechanical evidence for greater material strength in the anterior stroma and much greater resistance to deformation in the lateral directions that correspond to the plane of collagen lamellar orientation. The capability to detect low-contrast spatial differences in strain behavior in individual eyes may provide more sensitivity for detecting early keratoconus and discerning preoperative material heterogeneity that could impact the optical response to surgery.

Acknowledgements: Supported in part by Research to Prevent Blindness (WJD), NIH 8K12 RR023264 (WJD), 1L30 EY017803-01 (WJD), Visual Sciences Resource Center at CWRU P30 Core Grant EY11373 (AMR), VSTP Training Grant T32 EY07157 (MF), and CCF Innovations (WJD).

References:

- [1] Dupps WJ, Wilson SE. Biomechanics and wound healing in the cornea. *Exp Eye Res* 2006;83(4):709–720 (E-pub May 20, 2006).
- [2] Komai Y, Ushiki T. The three-dimensional organization of collagen fibrils in the human cornea and sclera. *Invest Ophthalmol Vis Sci* 1991;32(8):2244–58.
- [3] Ford M, Dupps WJ, Huprikar N, Lin R, Rollins AM. OCT elastography by pressure-induced optical feature flow. *Progress in biomedical optics and imaging – Proc SPIE* 2006. 6138OP (E-pub March 7, 2006).

025 **3D IMAGING OF RADIOFREQUENCY-ABLATED LESIONS USING THE SIEMENS C7F2 FOURSIGHT 4D ULTRASOUND TRANSDUCER FOR ELECTRODE DISPLACEMENT ELASTOGRAPHY.**

Shyam Bharat¹, Ted G. Fisher¹, Tomy Varghese^{1*}, Timothy J. Hall¹, Jingfeng Jiang¹, Ernest L. Madsen¹, James A. Zagzebski¹.

¹University of Wisconsin – Madison, 1530 MSC, 1300 University Avenue, Madison, WI, USA.

Background: Strain imaging to determine the location and boundaries of thermal lesions created using radiofrequency (RF) ablation is a topic of considerable interest. Electrode displacement elastography is a new method of strain imaging tailored specifically to electrode-based ablative therapies. Here, tissue deformation is achieved via small perturbations applied to the unconstrained end of the treatment electrode, which results in localized motion around the electrode tip embedded in tissue [1]. Two-dimensional images of the ablated region may not be indicative of maximum lesion size if the lesion formation is non-uniform, necessitating three-dimensional (3D) imaging to determine lesion volumes.

Aims: To present a method for 3D elastographic reconstruction from volumetric data acquired using the C7F2 *fourSight* 4D ultrasound transducer (Siemens Medical Solutions). Radiofrequency (RF) echo data from this transducer are processed to extract information on the lesion shape and size in the elevational direction, in addition to cross-sectional information.

Methods: 3D electrode displacement elastography is tested on a specially-constructed tissue mimicking (TM) phantom [2] and is subsequently evaluated on thermal lesions created in canine liver tissue *in vitro*. The TM phantom is a cubic block containing a spherical inclusion with an embedded RF electrode. Displacements in the ± 0.2 mm range are applied to the RF electrode under stepper motor control. For each position of the electrode, a 3D sector volume of raw RF data is recorded by virtue of the C7F2 transducer's curvilinear 192-element array that can be mechanically wobbled to scan different imaging planes of the inclusion. Cross correlation analysis to estimate displacements followed by linear least squares estimation are performed on corresponding RF frames from each pre- and post-displacement 3D RF data set to form a set of 2D strain images. These strain images are stacked together in the elevational direction and used to obtain a 3D surface rendering of the inclusion or lesion, as shown in Figure 1.

Results: Volume estimates of the spherical inclusion in the TM phantom indicate that electrode displacement elastography underestimates the actual volume of the inclusion. This result is consistent with earlier findings based on area and volume estimates of thermal lesions [3]. The high contrast in the depiction of the inclusion or lesion on strain images at different elevational planes enables 3D surface rendering. Results from *in vitro* tissue experiments further confirm the ability of this method to image RF-ablated lesions.

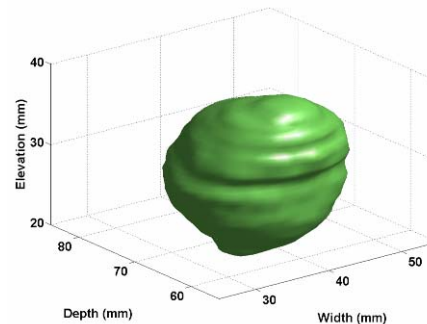
Conclusions: 3D electrode displacement elastography may be used as an effective follow-up imaging tool to provide the clinician with lesion volume estimates post-ablation. Currently, the longer data acquisition times preclude real-time usage of this method. Faster processors and improved image processing techniques may help realize the goal of real-time 3D elasticity imaging in the future.

Acknowledgements: This work is supported by NIH Grant R01CA112192.

References:

- [1] Varghese T, Zagzebski JA and Lee FT Jr. 2002. Elastographic Imaging of Thermal Lesions in the Liver *in vivo* following Radiofrequency Ablation: Preliminary results, *Ultrasound Med Biol*, 28, 1467-73.
- [2] Madsen EL, Hobson MA, Shi H, Varghese T and Frank GR 2006. Stability of Heterogeneous Elastography Phantoms made from Oil Dispersions in Aqueous Gels, *Ultrasound Med Biol*, 32, 261-270.
- [3] Varghese T, Techavipoo U, Liu W, Zagzebski JA, Chen Q, Frank G and Lee FT Jr. 2003. Elastographic Measurement of the Areas and Volumes of Thermal Lesions resulting from Radiofrequency Ablation: Pathologic Correlation, *AJR*, 181, 701-707.

Figure 1: 3D surface rendering of the inclusion obtained by stacking together segmented versions of 2D strain images of all the planes of the TM phantom scanned by the 4D transducer.



W-N Lee^{1*}, Z Qian², DN Metaxas² and EE Konofagou^{1,3}.¹Biomedical Engineering and ³Radiology Departments, Columbia University, New York, NY, USA;²Biomedical Engineering Department, Rutgers University, Piscataway, NJ, USA.

Background: Myocardial elastography (ME), depicting the full myocardial deformation field, was previously shown to have excellent performance using a 3D, left-ventricular finite-element model, in normal and ischemic cases [1, 2]. Moreover, angle-independent measures, principal strains, were proven to be a reliable indicator of differentiating pathologic from normal myocardium in the previously established theoretical framework [2, 3].

Aims: The principal strain estimation in ME was tested as well as validated against that in MRI tagging (tMRI) in normal and pathological human subjects, showing the robustness of principal strains when comparing estimates across different imaging modalities.

Methods: A GE Vivid FiVe[®] system with a 2.5MHz phased array probe was used to acquire in-phase and quadrature (I/Q) ultrasound data at the papillary muscle level in 2D standard short-axis views at a frame rate of 136 fps. The radio-frequency (RF) signals were further retrieved from the I/Q data. Two-dimensional tagged MR images were obtained on a Philips Intera[®] 1.5T scanner equipped with a five-channel SENSE cardiac coil from the same subjects. The RF-based myocardial elastography is comprised of: 1) 2D, orthogonal (lateral and axial), displacement estimation using 1D cross-correlation and recorrelation (7.7 mm window and 80% overlap); 2) 2D strain estimation using a least-squares strain estimator [4]; and 3) angle-independent estimates, i.e., 1st (radial) and 2nd (circumferential) classified principal strains, by solving the eigenvalue problem with a classification strategy [2, 3].

Results: Myocardial elastography using classified principal strains is capable of assessing myocardial deformation with estimates highly comparable to those obtained from tMRI. Unlike lateral and axial strains, principal strains show deformation independent of coordinate systems. Figure 1 shows the 1st and 2nd classified principal strains of a normal human ventricle with (ME-tMRI)/tMRI percentage ratios of 4.34% and 3.33%, respectively, in a posterior wall (PW) region of 7.5 mm by 7.5 mm. The normal left ventricle in Figure 1 shows radial thickening (a & b) and circumferential shortening (c & d). Figure 2 shows the principal strains in a reperfused left ventricle with a history of infarction caused by the occlusion of the left anterior descending (LAD) coronary artery with reduced radial thickening (a & b) in the septal wall and slight circumferential stretching (5% strain in (c & d)) in the anterior region, opposite the circumferential shortening in the normal case. The same percentage ratios in the anterior region for the pathological ventricle are 7.44% in the 1st and 4.51% in the 2nd classified principal strains. Possible discrepancy sources include the inexact image-plane acquisition, sparse tagging grids inherent to tMRI, and higher spatial resolution of the ME strains.

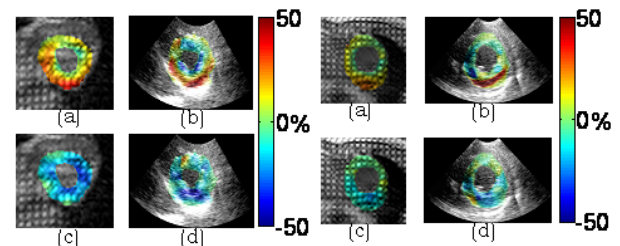


Figure 1: A normal human left ventricle

Figure 2: A reperfused human left ventricle.

(a) & (b) are 1st (radial) classified principal strains from tMRI and ME, respectively; (c) & (d) are 2nd (circumferential) classified principal strains from tMRI and ME, respectively. All the images show total systolic strains between end-diastole and end-systole and are displayed at end-systolic

Conclusions: These preliminary clinical results show that ME can obtain strain estimates of similar accuracy and quality to tMRI techniques, at higher spatial and temporal resolution and lower cost. In spite of the strain discrepancy, the classified principal strains are proven to be independent of the reference coordinate systems used in different imaging modalities. Ongoing work focuses on exact image registration and study of the tradeoff between spatial resolution and strain accuracy.

Acknowledgements: This study was supported in part by the NIH (R01EB006042-01) and AHA (SDG 0435444T). The authors wish to thank Hamed Mojahed and Christina L. Tosti for acquiring the tagged MR images and Kana Fujikura and Donna Macmillan-Marotti for acquiring ultrasound data.

References:

- [1] W.-N. Lee et al., *IEEE Trans. Ultrason. Ferroelectr. Freq. Control*, 2007 (in press).
- [2] S. D. Fung-Kee-Fung et al., *Proc. IEEE Ultrason. Symp.*, pp. 516-519, 2005.
- [3] I. K. Zervantonakis et al., *Phys. Med. Biol.*, 2007 (in press).
- [4] F. Kallel and J. Ophir, *Ultrason. Imaging*, vol. 19, pp.195-208, 1997.

Background: The stress and strain fields in ultrasound strain imaging are inherently 3D, and can only be fully measured with 3D imaging, which would also reveal the full anatomy and an accurate volume of any stiff inclusion. There have been few attempts at 3D strain imaging, consisting of either essentially 2D strain images stacked together to create a 3D data set [3], or carefully controlled scanning conditions, either using mechanical probe movement, or no probe movement at all [2]. Processing restrictions have generally precluded the use of full 3D windows and kernels, despite the increased resolution for a given data quality, since they can be matched to the fundamental resolution of the ultrasound probe.

Aims: To generate a 3D axial strain image from a mechanically swept 3D probe moved in a freehand manner, using 3D windows for displacement tracking, in all three directions, 3D kernels for gradient estimation and true 3D normalisation of strain values, in as near real-time as is practical.

Methods: We use an efficient phase-zero axial displacement search, with correlation maximisation in the lateral and elevational directions, using 3D windows. Correlation-based tracking schemes [1], allow small search ranges. 3D least-squares gradient estimation is efficiently implemented by taking differences of statistics summed across the whole volume. Strain normalisation is applied by fitting a stress estimating function to the entire data set. A GE RSP6-12 3D probe matched to a Dynamic Imaging ultrasound machine is moved in a quasi-static freehand manner: the first volume is acquired, the probe contact pressure is adjusted slightly, then a second volume is acquired, the whole process lasting less than two seconds. RF acquisition and control of the probe stepper motor were performed using Stradwin software.

Results: Figure 1 demonstrates the achievable resolution in all dimensions. The strain normalisation is good even for unconventional targets like the half olive. The technique can successfully be applied *in vivo*, as in Figure 2. On a 3 GHz desktop PC, the total processing time was roughly 20 seconds in each case.

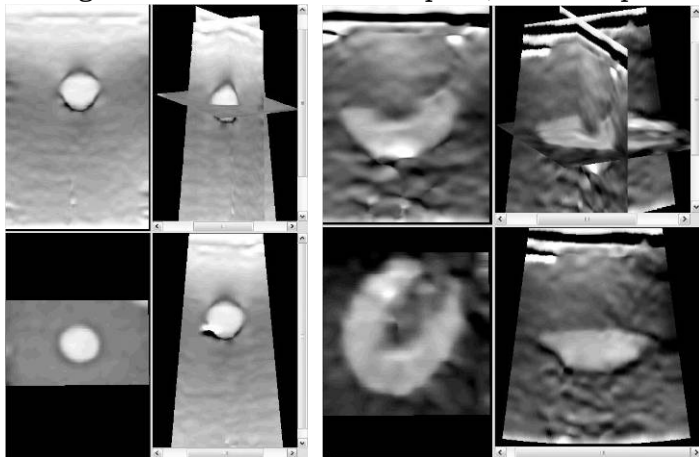


Figure 1: Three views and a corresponding 3D strain image of a biopsy phantom with 5mm inclusion and a half olive in gelatin.

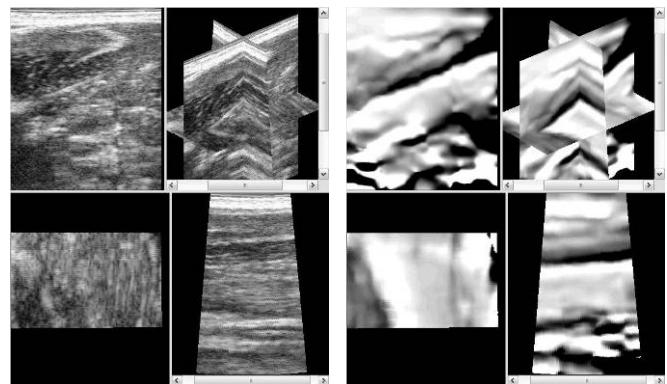


Figure 2: Human forearm, display as in Figure 1, showing a 3D B-scan and 3D strain images.

Conclusions: It is possible to generate high quality 3D images of axial strain with very good resolution in all dimensions and fairly short processing times. The technique is fairly straightforward in practice-currently roughly one out of two acquisitions generate good strain images – due to the balance between generating a useful stress field over the volume and maintaining reasonable correlation of the data.

Acknowledgments: Graham Treece is supported by a Fellowship from the Royal Academy of Engineering and the EPSRC. Dynamic Imaging provided modified hardware to allow the acquisition of 3D RF data.

References:

- [1] GM Treece, JE Lindop et al. Near real-time 3D ultrasonic strain imaging. In press *Acoustical Imaging*, 29, Springer 2008.
- [2] A Anand, D Savary and C Hall. Three-dimensional spatial and temporal temperature imaging in gel phantoms using backscattered ultrasound. *IEEE Trans Ultrasonics, Ferroelectrics and Frequency Control* 54(1):23-31, 2007.
- [3] A Lorenz, A Pesavento et al. Three-dimensional strain imaging and related strain artefacts using an ultrasonic 3D abdominal probe, *Proceedings of the IEEE Ultrasonics Symposium* 2:1657-1660, 1999.

051 **COMPARISON OF TISSUE VELOCITY AND STRAIN IN NORMAL BRAIN AND GLIAL TUMORS AS QUANTIFIED BY PROCESSING OF ULTRASOUND DATA.**

Tormod Selbekk^{1,2}, Reidar Brekken^{1,2}, Sebastien Muller^{1,2}, Frank Lindseth^{1,2}, Geirmund Unsgaard^{2,3,4}.*

¹SINTEF Health Research, Trondheim, NORWAY; ²National Centre for 3D Ultrasound in Surgery, Trondheim, NORWAY; ³St. Olav Hospital, Trondheim University Hospital, Trondheim, NORWAY;

⁴The Norwegian University of Science and Technology, Trondheim, NORWAY.

Background: Our research group has previously reported a method suitable for detection of very small deformations in tissue and our initial experience in using this method for ultrasound strain imaging of tumors in the human brain [1]. The tissue motion caused by arterial pulsation during a cardiac heart cycle was shown to be sufficient for generating strain images of brain tumors, but differences between normal and pathological tissue was not quantified. Since no external force should be applied during the acquisition of ultrasound RF data, the processing method is here used to quantify tissue velocity and strain occurring in the brain during a cardiac cycle.

Aims: The purpose of the study was to investigate whether or not a) tissue velocity and b) strain as calculated from ultrasound RF data using a previously described method is able to differentiate between glial tumors and normal brain tissue.

Methods: Ultrasound RF data was acquired intraoperatively in 16 patients with glial tumors. The ECG signal was simultaneously recorded with the RF data in 13 of the patients. After craniotomy, the surgeon held the linear ultrasound probe (10 MHz) motionless on intact dura, while a data sequence covering at least one cardiac cycle was acquired. The tissue displacements and strain were found by using correlation and phase sensitive processing techniques. In each of the ultrasound datasets, we selected four regions of interest (ROIs), 2 in expected normal tissue and 2 in expected tumor tissue (except in two datasets where only one ROI could fit in normal tissue). In the ROIs, the average velocity and strain magnitude was calculated as a function of time. The maximum magnitude of the tissue velocity observed during a cardiac cycle (or alternatively in a time period of at least 1 s if the ECG was not recorded) was found, as well as the average strain magnitude for the time sequence. The range and median for the measurements were calculated. The tissue velocity and strain magnitude in normal and pathological brain tissue were statistically compared using paired non-parametric tests.

Results: Tissue velocity and strain could be successfully calculated in all patients. The maximum magnitude of the observed tissue velocity ranged between 0.15 mm/s to 2.9 mm/s for all observations (N=62), with a median velocity of 0.82 mm/s for measurements in expected normal tissue (N=30) and a median velocity of 0.75 mm/s for measurements in expected tumor tissue (N=32). The difference between the velocities found in tumor and normal tissue was not statistically significant. The average strain magnitude for the data sequences ranged from 0.60‰ to 24.4‰ (note per mill) for all calculations (N=62). The median strain magnitude for ROIs in expected normal tissue was 9.5‰ and 1.30‰ for ROIs in expected tumor tissue. The statistical analyses indicate a significant difference ($p < 0.05$) between strain magnitude values in normal brain and tumor tissue.

Conclusions: We have quantified tissue velocity and strain in brain by processing ultrasound RF data acquired *in vivo* from 16 patients with glial tumors. Our results indicate that tissue velocity is not a suitable parameter to discriminate between glial tumors and normal brain tissue. However, strain is a tissue parameter that can be used to differentiate between pathological and normal brain tissue. In our observations the strain magnitude was significantly lower in tumor tissue than in normal brain. This implies that the method used for strain processing might be a suitable tool for diagnostic imaging during brain tumor surgery.

Acknowledgements: This work was financed by the Norwegian Ministry of Health and Social Affairs through the National Centre for 3D Ultrasound in Surgery and by SINTEF. We acknowledge the work by Dr. Jon Bang, a former colleague at SINTEF, who implemented in Matlab some of the algorithms used in this study.

References:

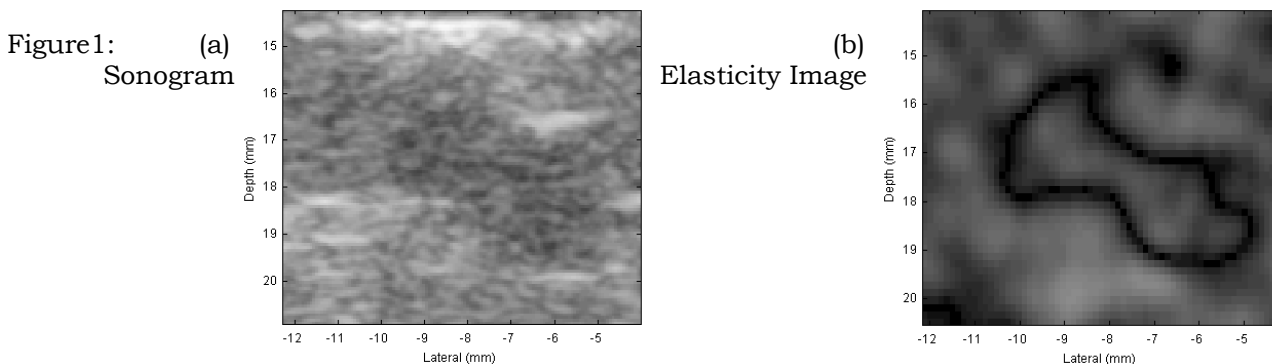
- [1] T Selbekk, J Bang, G. Unsgaard, Strain processing of intraoperative ultrasound images of brain tumours: Initial results, *Ultrasound Med Biol* 2005; 31: 45–51.
-

Background: Ultrasonic elasticity images generated under externally applied force depict the contrast of tissue moduli within the field of view (FOV). The contrast between a solid lesion and its surrounding tissue has been extensively studied in the past. Cystic lesions are not compressible when external force is applied. However, the deformation of the cystic shell or the motion of particles inside the cyst causes phase changes in the reference and target signals used in time delay estimation, resulting in a characteristic appearance of the cystic inclusion and its boundary. This characteristic appearance can either be suppressed or enhanced through different processing strategies. A good understanding of this characteristic appearance provides a means for better interpretation of elasticity images.

Aims: This study aims to understand the causes and effects of commonly observed characteristic appearances of fluid inclusions in elastic materials. This understanding enables methods to be developed to either suppress or make use of this characteristic in elasticity images.

Methods: The phase change of ultrasonic signals was analyzed for three influences: 1) The contribution of inclusion boundary motion to the phase change is analyzed using the general form of an Airy stress function. Reasonable assumptions for simplified pressure and boundary displacements are necessary to obtain a representation for a fluid inclusion in an elastic material. 2) The fluid of a cyst may contain electrolytes, trace elements, proteins, tumor associated antigen, steroid hormones and enzymes. The contribution of the motion of these particle components under external force and acoustic pressure to the phase change is analyzed. 3) Lastly, the contributions of the strong reflections from cyst boundaries to the phase change are analyzed.

Results: The Figure 1a is a traditional B-mode ultrasound image, and Figure 1b is a corresponding elasticity image. The hypoechoic area in the B-mode image is a cyst. The corresponding area in the elasticity image illustrates a characteristic appearance for cysts with brighter signals in the cyst fluid area and a dark ring on the boundary area.



Conclusions: Cyst inclusions in elastic materials show characteristic appearances in elasticity images. The size, applied stress, particle components inside the cysts, and the spatial and temporal filtering methods all affect the appearance of the elasticity image.

Background: Sonography is used in many medical procedures involving needle insertion into tissue. In some of these procedures, the aim is to guide the needle tip to a certain location in tissue for biopsy, injection or seed placement. In other procedures, the study of the injectate, such as its spread, is of interest. B-mode and Doppler imaging have been used for this purpose.

Aims: In this study, we examine the feasibility of monitoring injection using elastography. Of special interest is distinguishing the depot (the area where the injectate is deposited) from surrounding tissue.

Methods: Fresh lamb leg-muscle tissue is used for the experiments. A mechanical apparatus previously used for vibrating tissue in elastography studies is modified to move the plunger of an epidural glass syringe. This type of syringe has very low friction and is apt for controlling the position of the plunger. Degassed water is injected with an oscillatory motion of the plunger under computer control. Elastography images are taken using real-time elastography software developed at our lab [1] running on an Ultrasonix Sonix RP machine. A linear probe is used, and axial strain images are captured.

Results: Figure 1 shows successive axial strain images taken during a typical experiment with a ramp input. Figure 2 shows typical results with oscillatory inputs. The pure black areas of the images correspond to areas where the correlation between the RF data was less than 80%. As the entry of injectate alters the echogenicity of the tissue, the correlation between successive RF data is lost, and, thus, the depot appears as a black region. Moreover, because of the pressure caused by the depot, strains can be observed in surrounding tissue. The real-time capture allows both temporal and spatial analysis.

Conclusions: We have demonstrated the conceptual feasibility of injection studies using elastograms. The depot can be distinguished from the surrounding tissue using correlation data. Strains caused by the injection in surrounding tissue can be observed and measured using the elastogram. This study shows that elastogram can be used for a variety of purposes in the medical procedures mentioned in question. On-going experimentation is focused on further quantification. Needle tip tracking, avoiding pain and tissue damage during injections by limiting the strains, and characterizing mechanical properties of surrounding tissue, such as elasticity and porosity are some of the applications we are scrutinizing.

Acknowledgements: The authors wish to thank Reza Zahiri for the real-time elastography software. This research is supported by NSERC.

References:

- [1] R. Zahiri-Azar, S. Salcudean, "Motion Estimation in Ultrasound Images using Time Domain Cross Correlation with Prior Estimates", IEEE Transactions on Biomedical Imaging, Volume 53, Issue 10, Oct. 2006 Page(s):1990–2000.

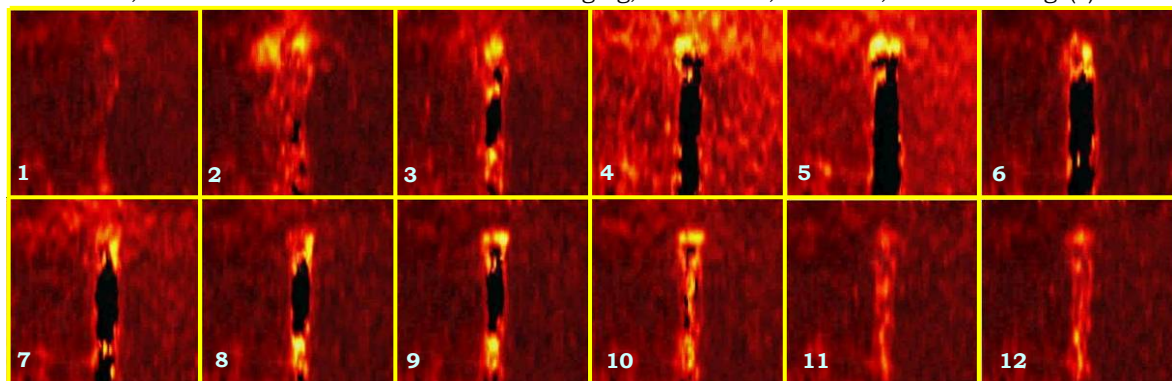
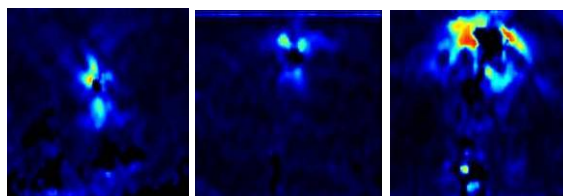


Figure 1: Successive snapshots of axial strain measurements during injection using a ramp input.

Figure 2: Snapshots of axial strain measurements during injection using oscillatory inputs.



083 **REAL-TIME FEEDBACK OF CAVITATION INDUCED PHANTOM ABLATION USING THE SPECKLE TRACKING CORRELATION COEFFICIENT.**

K. Kim^{1*}, T.L. Hall¹, C.A.Cain¹, J.M. Rubin².

¹Biomedical Engineering, ²Radiology Departments, University of Michigan, Ann Arbor, MI 48109, USA.

Background: Cavitation induced tissue disruption in ultrasound therapy turns bulk tissue into a volume of uniform liquid containing cellular fragments. This mechanical and structural change will alter the ultrasound characteristics, including backscatter reduction [1]. Ultrasound scattered from the tissues in fluid form also quickly decorrelates when being deformed compared to bulk tissue [2]. Correlation coefficient maps based on 2D speckle tracking will assess the degree of the tissue disruption.

Aims: To measure and monitor real-time phantom disruption by ultrasound cavitation, 2D speckle tracking was used and the tracking correlation coefficient was employed to estimate the solidity of the tissue structure during deformation.

Methods: A uniform cubic gel phantom made of 2% agarose embedded with ultrasound scatterers was positioned in a water tank in between the imaging and therapeutic transducers. A 512 element therapeutic ultrasound array was placed at the top of the water tank and a commercial ultrasound imaging linear array was positioned at the bottom of the tank. Therapy ultrasound pulses were delivered on a 7x7 grid of focal locations spaced by 1mm in the plane perpendicular to the therapy propagation direction (and imaging plane). 5 cycle long bursts were applied to each location sequentially in a random order at 500Hz PRF. The whole set was repeated 10K times for a total of 980 seconds for the complete disruption. Following the therapy pulses, pushing pulses were applied while RF data frames were captured at a frame rate of 95Hz using a commercial ultrasound scanner. The same grid locations and random ordering were used with 50 cycle (50 microseconds) bursts at each location with no delay between locations. Total pushing time was about 2.5ms. 6 pushes were applied spaced by 300ms. 2D speckle tracking was applied to two imaging frames before and after each pushing pulse. Contrast-to-noise ratios (CNR) were calculated from the correlation coefficient maps and compared with the associated B-scans.

Results: Overall, the correlation maps clearly differentiate the disrupted region from the background with enhanced CNR compared to the conventional B-scans (Figure 1). After the complete disruption of the phantom (Figure 1a and b), the CNR of the correlation coefficient map was estimated to be 5.2 while the CNR of the B-scan image was 2.3. When the phantom was half way through the disruption process, the CNR of the correlation coefficient map was estimated to be 2.7, while the CNR of the B-scan image was only 1.6 (Figure 1c and d). The percentage variations of the correlation maps were also observed to be an order of magnitude lower than those of the B-scans.

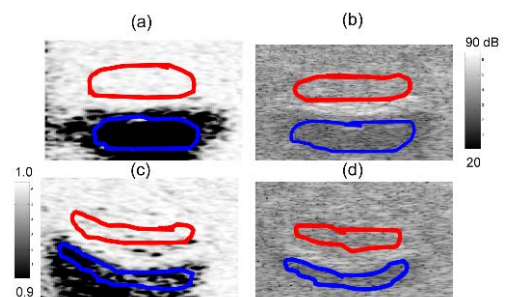
Conclusions: Preliminary results on the phantoms demonstrate the feasibility of speckle tracking correlation maps for real-time therapy feedback with enhanced CNR. Experiments on *ex-vivo* tissue samples are scheduled.

Acknowledgements: Work supported in part by NIH grants EB-003451, HL-67647, HL-68658, HL-082640, and CA-109440. Thanks to Philips Ultrasound, Bothell, WA, USA, for their system support.

References:

- [1] RC Booi, PL. Carson, M O'Donnell, MS Richards, and JM. Rubin, Diagnosing cysts with correlation coefficient images from 2D freehand elastography, JUM (in press).
- [2] TL. Hall, JB Fowlkes, and CA Cain, A real-time measure of cavitation induced tissue disruption by ultrasound imaging backscatter reduction. IEEE UFFC, 2007, 54(3) 569-75.

Figure1: Correlation coefficient maps (a, c) compared with B-scans (b, d). (a) and (b) are after the complete disruption and (c) and (d) are half way through the disruption process. Ablated regions are represented by blue circles and matching background for CNR estimates are represented by red circles. CNR in the correlation maps are twice as high as those of B-scans. Each panel measures about 13mm by 10mm.



026 **ULTRASONIC ELASTOGRAPHY AND PLANE STRAIN INVERSE ALGORITHMS FOR POLYMER GEL DOSIMETRY.**

Remo A Crescenti¹, Jeffrey C Bamber^{1*}, Assad A Oberai², Paul E Barbone³, Joseph P Richter², Nigel L Bush¹ and Steve Webb¹.

¹Institute of Cancer Research and Royal Marsden NHS Foundation Trust, Downs Road, Sutton, Surrey, England, UK; ²Rensselaer Polytechnic Institute, 110 8th Street, Troy, NY, USA; ³Boston University, 110 Cummington Street, Boston, MA, USA.

Background: Research on polymer gels for use in radiation dosimetry has been driven by the need for 3D-dosimeters. Under irradiation, monomers in such gels polymerize, and the molecular structure changes [1]. To date, for dose determination, predominantly irradiation induced changes of the magnetic properties have been investigated using magnetic resonance tomography (MRT) e.g. [2]. A quick, inexpensive and easy-to-use alternative for measuring dose, possibly using other dose dependent properties of these gels, would be appreciated. Elastography could provide those benefits, because the elastic properties of the gels change under irradiation.

Aims: This presentation describes a preliminary evaluation of the potential of quantitative elastography for dose imaging, using plane strain inverse algorithms.

Methods: A block of radiation sensitive polymer gel [3] (4x4x12 cm³ along x, y and z-axis, respectively) was irradiated to produce a relatively stiff rod-shaped region (1x1 cm²) along the z-axis. The gel, with oil-covered faces for slippery boundaries, was placed in a mechanical frame which allowed expansion in the x-direction, but prevented z-direction motion. The block was compressed in y-direction while radiofrequency (RF) ultrasonic echo data were acquired in one central plane. The local displacement was tracked in this plane, and the stiffness contrast between the stiff inclusion and the soft background was determined using an inverse algorithm. For inverse computation [4], a model with incompressible linear elements throughout the body and spring elements at the surface (to simulate the boundary conditions) was used. Independent calibration (direct stress versus strain measurement) was performed with smaller cylindrical and homogeneously irradiated samples to relate stiffness with dose. The dose distribution was determined in the central plane using MRT as a reference.

Results: Reasonable agreement between the reference and computed dose distributions was observed (see Figure 1). Some noise was present in the supposedly homogeneously soft background of the sample, although this might be resolved in the future by better regularization of the reconstruction. The stiffness contrast is estimated very well. A few stress artefacts remain at the edges. Better experimental control of the boundary conditions and averaging over several independent x-y-planes along the z-axis could potentially further improve the computed estimates.

Conclusions: We have successfully visualized irradiation-induced changes in elasticity in a polymer gel using a plane strain inverse algorithm. These preliminary results suggest that in future 3D-systems based on polymer gels combined with the readout of elastic properties using 3D echo data may be used for dose determination.

Acknowledgements: This project is funded by the Institute of Cancer Research and the URP program at RPI.

References:

- [1] Baldock C, Legape M, Rintoul L, Murry P and Whittaker A K 1999 Investigation of polymerisation of radiation dosimetry polymer gels DosGel'99, Schreiner L J. (ed) (Canadian Organization of Medical Physicists) 99-105.
- [2] De Deene Y, Vergote K, Claeys C and De Wagter C 2006 The fundamental radiation properties of normoxic polymer gel dosimeters: a comparison between a methacrylic acid based gel and acrylamide based gels Phys. Med. Biol. 51 653-673.
- [3] Fong P M, Keil D C, Does M D and Gore J C 2001 Polymer gels for magnetic resonance imaging of radiation dose distributions at normal room atmosphere Phys. Med. Biol. 46 3105-3113.
- [4] Oberai A A, Gokhale N H, Doyley M M, Bamber J C 2004 Evaluation of the Adjoint Equation Based Algorithm for Elasticity Imaging Physics in Medicine and Biology 49 2955-2974.

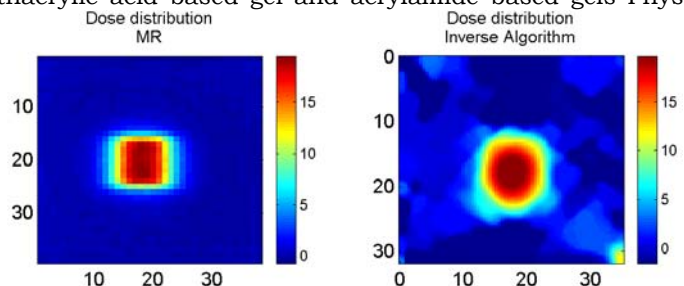


Figure 1

Laurent Sandrin^{1*}.

¹Echosens, Research and Development Department, 153 avenue d'Italie, 75013 Paris, FRANCE.

Background: Transient elastography (Fibroscan®, Echosens, Paris, France) is a noninvasive and rapid technique used to assess liver fibrosis by measuring liver stiffness [1]. It relies on the measurement of low-frequency shear elastic wave velocity. It has recently been studied in a multitude of chronic liver diseases, hepatitis B and/or C, HCV co-infection, HIV, alcoholism, non-alcoholic steato-hepatitis, haemochromatosis, etc. Studies report a strong correlation of shear wave velocity with the fibrosis stage obtained through liver biopsy. Though the clinical interest of transient elastography for liver fibrosis assessment has been clearly validated, the validation of transient elastography as a tool intended to quantitatively measure shear velocity is a difficult issue since there is no gold standard. Mechanical testing solutions for dynamic mechanical characterization such as rheometers, or other instruments (ElectroForce, Bose) are not adapted to *in vivo* measurements and require preparation of samples of predetermined shapes which might change the viscoelastic properties of biological tissues.

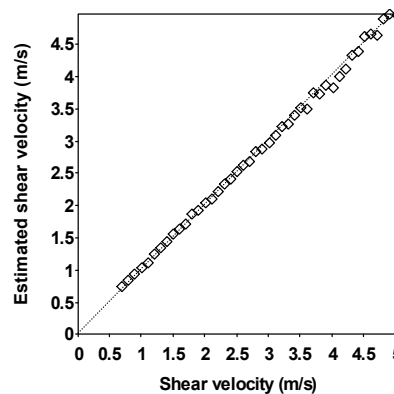
Aims: We aim to present a theoretical validation of the measurement of shear wave velocity using Fibroscan®.

Methods: The Green's function approach in a homogeneous, semi-infinite, isotropic and purely elastic medium [2] is used to compute the shear diffraction impulse response on the axis of a 9 mm diameter circular piston that vibrates longitudinally at the surface of a soft medium ($V_s \ll V_c$). The vibration shape is a period of a 50 Hz sinusoid of 2 mm peak-to-peak amplitude. The shear velocity in the model is varied between 0.7 and 5.0 m/s, which is representative of soft tissue stiffness range, 1.5 to 75.0 kPa. The strain rates are computed from the displacement evolution as a function of depth and time. Thereafter, the estimated shear velocity is compared to the shear velocity used in the model.

Results: Results show that the error on the estimated shear wave velocity remains less than 6% (Figure 1). It increases as the shear velocity increases. This is due to diffraction effects which become more important as the ratio between the wavelength and the diameter of the piston increases.

Conclusions: Validation of shear wave velocity measurements is feasible using a theoretical approach based on the computation of the shear diffraction impulse response using Green's functions.

Figure 1: Evolution of the estimated shear velocity as a function of the exact shear velocity of the model.



References:

- [1] Sandrin L, Tanter M, Gennisson JL, Catheline S, Fink M. Shear elasticity probe for soft tissues with 1-D transient elastography. IEEE UFFC 2002; 29 (4): 436–46.
- [2] Sandrin L, Cassereau D., Fink M. The role of the coupling term in transient elastography. J. Acoust. Soc. Am. 2004; 115 (1): 73–83.

Benjamin Castañeda^{1*}, Man Zhang², Kenneth Hoyt¹, David Pasternack³, Laurie Baxter³, Priya Nigwekar³, P. Anthony di Sant'Agnese³, Jean Joseph³, John Strang³, Deborah J. Rubens³, Kevin J. Parker¹.

¹Electrical & Computer Engineering and ²Biomedical Engineering Departments, ³University of Rochester Medical Center, University of Rochester, Rochester, NY, USA.

Background: Prostate cancer is the most prevalent type of cancer in men and the second most frequent cause of cancer death in adult males after lung cancer. Detection of prostate cancer can be very difficult with most clinicians relying on a combination of prostate-specific antigen levels (PSA), a digital rectal examination and transrectal ultrasound (TRUS) imaging. However, these methods have shown shortcomings in both accuracy and specificity. Previous work has shown that sonoelastography is a promising imaging technique for tumor detection in prostate [1].

Aims: This work evaluates the feasibility of sonoelastography to guide biopsy for prostate cancer detection.

Methods: Five prostate glands were examined *ex vivo*. For these cases, the specimen was received after radical prostatectomy and embedded in a 10.5% gelatin mold. An external piston was used to vibrate the embedded gland at low frequencies (chords composed of 105, 140, 175 and 210 Hz). A GE Logiq 9 ultrasound scanner was used in conjunction with a positioning device to acquire B-mode and sonoelastographic volumes. The surface of the gland was segmented from the US images and the tumors from sonoelastographic images using a 3D segmentation algorithm [2]. Additionally, both sonoelastographic and B-mode images were independently analyzed by an experienced radiologist in order to find suspicious nodules where biopsy would have been targeted. After imaging, the gland was step-sectioned following a whole-mount histological procedure [1]. From these histological images, a volume was reconstructed and registered to the US and sonoelastographic volume using the surface of the gland as a marker. To assess detection performance, both 3D US and sonoelastographic findings were compared in size and position to 3D pathology.

Results: There were nine tumors in the five *ex vivo* prostate glands as verified by pathology (from 6.3 mm to 16.3 mm in diameter). Seven of these tumors were successfully detected by sonoelastography, and only two were detected using B-mode alone. The average diameter of the detected tumors was 10.2 mm measured in sonoelastographic images versus 10.7 mm measured in the histological images.

Conclusions: These preliminary results suggest that potential applications for sonoelastography include improved tumor localization for US guided biopsy or therapy for prostate cancer.

Acknowledgements: This study was partly supported by NIH grant 5 RO1 AG016317-06.

References:

- [1] L. Taylor et al., "Prostate cancer: three-dimensional sonoelastography for *in vitro* detection", *Radiology*, 2005 Dec; 237(3):981-5.
 - [2] B. Castañeda et al., "Semiautomatic measurement of thermally ablated lesions in sonoelastographic images", *Journal of Ultrasound in Medicine*, 2007, 26:S87-S88.
-

050 **SURFACE PRESSURE MEASUREMENTS IN ULTRASOUND STRAIN IMAGING.**

Lee M. Kiessel¹, Timothy J Hall^{1*}, Jingfeng Jiang¹.

¹University of Wisconsin – Madison, Madison, WI, USA.

Background: Mechanical *in vitro* tests and *in vivo* elasticity imaging have shown differences between fibroadenomas and invasive ductal carcinomas (IDCs) in their nonlinear stress/strain behavior [1], which could be utilized to differentiate between benign and malignant lesions thus potentially reducing the benign biopsy rate. Stress and strain measurements are required for absolute measures of this nonlinear behavior *in vivo*.

Aims: The aim of this work is to design a pressure sensor array for use in ultrasound strain imaging. The feasibility of the approach as well as adequacy of the current pressure sensing technology will be examined.

Methods: A prototype pressure sensing array (Figure 1) was designed and obtained from Pressure Profile Systems, Inc. A variety of tests were performed with the array to gauge its stability, sensitivity and calibration in reference to its application in ultrasound elastography. Measurements on elastographic phantoms were also performed and compared to finite element analysis (FEA) simulations. In addition, data were collected from patients undergoing ultrasound elasticity imaging at the University of Wisconsin Breast Center.

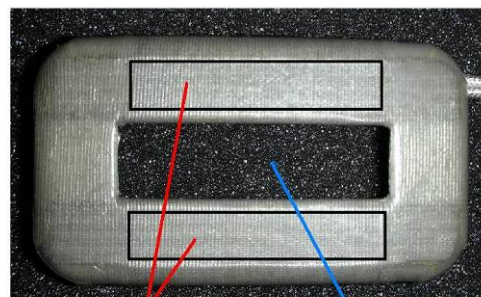
Results: Initial tests show that the pressure sensor array is stable in an ultrasound imaging environment. A reliable calibration technique was also developed, with reproducibility to within 5% for most elements. Tests also show a wide disparity among the elements in terms of their sensitivity. The best performing elements are capable of detecting pressure as low as about 100 Pa. The average minimum detectable pressure was about 800 Pa. Surface pressure distribution measurements on phantoms showed only modest agreement with the FEA simulations.

Conclusions: The results suggest that the array is capable of detecting initial contact and subsequently measuring the contact force during a compression of the breast, a critical task for quantifying stress/strain nonlinearities. Clinical trial confirmed this prediction. Geometric uncertainties on the surface of the sensor as well as the variability of the absolute calibration were the main contributors to the disparity between the phantom measurements and the FEA simulations. Thus, the array is likely ill suited to measure accurate maps of the surface pressure distribution which might limit its utility for elastic modulus reconstructions.

Acknowledgements: Pressure Profile Systems, Inc. provided technical support for the pressure sensing array.

References:

[1] Wellman, P.S., *Tactile Imaging*, in *Engineering and Applied Sciences*. 1999, Harvard University: Cambridge, MA. p. 137.



Active Sensing Area Gap for Ultrasound Transducer

Figure 1: Pressure sensing array mounted on a plate that attaches to an ultrasound transducer.

Background: Acoustic Radiation Force Impulse (ARFI) imaging measures the mechanical properties of tissue by generating a local acoustic radiation force using a standard diagnostic ultrasound scanner. Short duration, high intensity ultrasound pulses are used to induce impulsive acoustic radiation forces that result in micron-scale tissue displacements. Displacements are tracked using ultrasound tracking pulses and are quantified using conventional correlation-based methods. ARFI imaging may be used to find objects of various shapes and sizes; therefore, it is important to quantify its resolution capabilities. Many groups have measured resolution in elasticity imaging [1–3]. The imaging of adjacent white and black regions gives the step response of an imaging system. The derivative of the step response results in a point response of the system. The full width at half maximum (FWHM) of the point response may be reported as the lower resolution limit.

Aims: The goal of this study was to measure the lateral and axial resolution of an ARFI imaging system and compare those measurements to data from a simulation developed using FIELD II [4]. The dependences of axial resolution on correlation window length were also investigated.

Methods: The ARFI imaging system used was a Siemens Antares ultrasound scanner (Siemens Medical Systems) and a VF10–5 linear array transducer. Each beam sequence included a 30 μ s pushing pulse followed by 29 – 0.15 μ s tracking pulses (at a pulse repetition period (PRP) of 79 μ s), both with a 6.67 MHz center frequency. For this study, we captured and analyzed images 0.40 ms after the push, where optimal contrast was achieved. A phantom was created with adjacent hard and soft regions (greater than 30 kPa, and less than 4 kPa, respectively) which provided the contrast necessary for a step response. The resolution measurement was limited by the low line density of a typical ARFI image in the lateral direction (13.4 lines/cm). In order to increase the line density, the transducer was positioned above the sample and mechanically translated in 100 – 7.49 μ m steps. By combining the images, we created an image with a higher lateral line density (1340 lines/cm). The axial and lateral step responses were found by choosing lines in the image that included the interface between the hard and soft regions of the phantom. Instead of filtering the data, a representative sigmoid function was found to represent the step responses using a least squares curve fitting routine. The derivative of the sigmoid function was calculated, and the FWHM of the resulting point response was measured. To study the dependence of axial resolution on correlation window length, one set of image data was used with various correlation window lengths (1–10 mm), and the axial FWHM resolution was measured.

Results: Axial resolution with a 1 mm correlation window was measured to be 1.00 ± 0.40 mm experimentally and 1.40 ± 0.19 mm using the model. Lateral resolution was measured experimentally to be 0.39 ± 0.05 mm. Axial resolution was linearly dependent on correlation window length.

Conclusions: A protocol was designed and used to reliably and accurately measure the resolution capabilities of an ARFI imaging system. Using the protocol, the axial resolution was found to decrease with an increase in correlation window length.

Acknowledgements: Grants include US ARMY/CDMRP W81XWH-04-1-0034 and the Wallace H. Coulter Foundation Early Career Award. In-kind and technical support was provided by Siemens Medical Solutions USA, Ultrasound Group.

References:

- [1] N. A. Cohn, S. Y. Emelianov, M. O'Donnell, An Elasticity Microscope. Part II: Experimental Results, IEEE Trans. Ultrason., Ferroelect., Freq. Contr., Vol. 44, No. 6, pp. 1320–1331, 1997.
- [2] R. Righetti, S. Srinivasan, J. Ophir, Lateral Resolution in Elastography, Ultrasound in Med. & Biol., Vol. 29, No. 5, pp. 695–704, 2003.
- [3] S. K. Alam, J. Ophir, T. Varghese, Elastographic Axial Resolution Criteria: An Experimental Study, IEEE Trans. Ultrason., Ferroelect., Freq. Contr., Vol. 47, No. 1, pp. 304–309, 2000.
- [4] J.A. Jensen, Field: A program for simulating ultrasound systems, Med. Biol. Eng. Comp., 10th Nordic Baltic Conference on Biomedical Imaging, Vol. 4, Supplement 1, Part 1, pp. 351–353, 1996.

082 **ULTRASONIC DETECTION OF CHANGES IN CORNEAL BIOMECHANICAL PROPERTIES ASSOCIATED WITH HYDRATION EFFECTS.**

Xiaoyin He¹, Jun Liu^{1*}.

¹The Ohio State University, Columbus, Ohio, USA.

Background: *Ex vivo* corneal tissue hydrates and thickens swiftly and irreversibly in a moist environment [1]. Under certain clinical conditions, this swelling may take place *in vivo* and cause impaired vision. Studies have shown that corneal swelling happens in the direction of the optic axis, when the collagen fibers of the cornea become thicker and pushed apart as water is imbibed. The mobility of water in biological tissue is an extremely complex problem in studying tissue biomechanics. Few quantitative studies have been performed to investigate the hydration effects on corneal biomechanics.

Aims: In this study, we developed a non-invasive ultrasonic method to monitor the changes in corneal biomechanical properties associated with swelling.

Methods: Five enucleated porcine eyes were obtained. The corneas were first dehydrated in a 20% Dextran solution for 30 minutes to allow them to resume their normal thickness and hydration status. The intraocular pressures (IOP) of the eyes were maintained at 10 mmHg with a pressure control system. The normalized central corneal thickness changes, that is, stain increment along the normal direction of the apex, was monitored using a non-destructive ultrasonic method. The ultrasonic system is composed of a broadband transducer (10 MHz, XMS, Panametrics-NDT), a pulser-receiver (Panametrics-NDT, 5900PR), a digitizer (Acqiris, DP105, 500 MHz/8-bit), and a PC (Figure 1). The transducer generates an ultrasound beam, which was centered at the corneal apex by using precision linear stages. The biomechanical properties of the cornea including corneal stiffness and density were simultaneously reconstructed using an inverse algorithm in combination with a wave propagation model.

Results: The central corneal thickness increased significantly (up to 20%) over a one hour period suggesting postmortem swelling of the corneas in intact, enucleated eyes. The corneal stiffness (i.e., aggregated modulus) decreased during the experimental period, indicating that the corneas were softened due to the imbibed water.

Conclusions: This study demonstrated the feasibility of using a non-invasive ultrasonic system to detect and characterize the changes in corneal biomechanical properties associated with hydration in intact eyes.

References:

[1] Hodson, S. A., 1997, "Corneal stromal swelling," *Progress in Retinal and Eye Research*, 16(1), pp. 99–116.

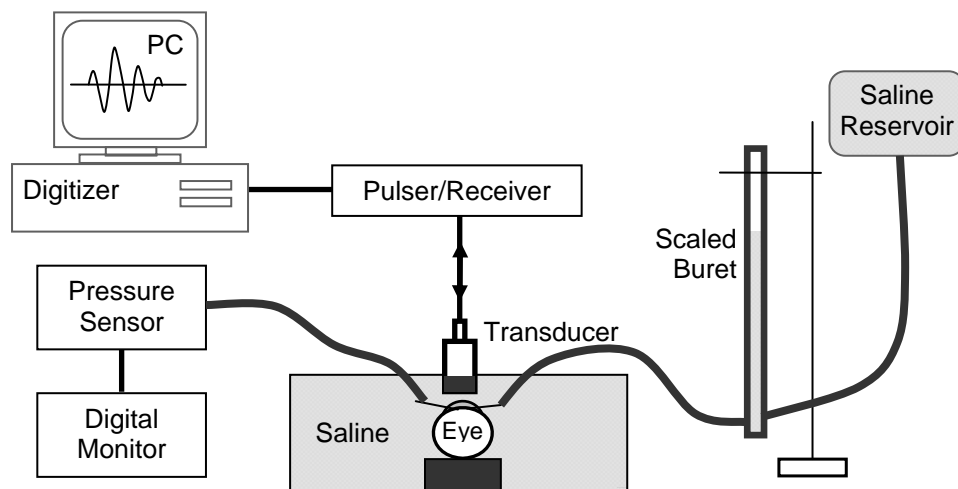


Figure 1: Schematics of the ultrasound measurement system with intraocular pressure control.

012 **NON-INVASIVE VASCULAR ELASTOGRAPHY FOR CAROTID ARTERY CHARACTERIZATION: IN VIVO VALIDATION ON SUBJECTS WITHOUT PREVIOUS HISTORY OF CAROTID ATHEROSCLEROSIS.**

Roch L. Maurice^{1,2,3*}, Gilles Soulez³, Marie-France Giroux³ and Guy Cloutier^{1,2,3}.

¹Laboratory of Biorheology and Medical Ultrasonics, Research Center, University of Montreal Hospital, Montreal, Quebec, CANADA; ²Institute of Biomedical Engineering, ³Radiology, Radio-Oncology and Nuclear Medicine Department, University of Montreal, Montreal, Quebec, CANADA.

Background: Non-invasive vascular ultrasound elastography (NIVE) was recently introduced to assess mechanical properties within peripheral vessel walls. In this context, radio-frequency (RF) ultrasound data are transcutaneously recorded, while the vessel wall is pressurized by the physiological blood flow pulsation.

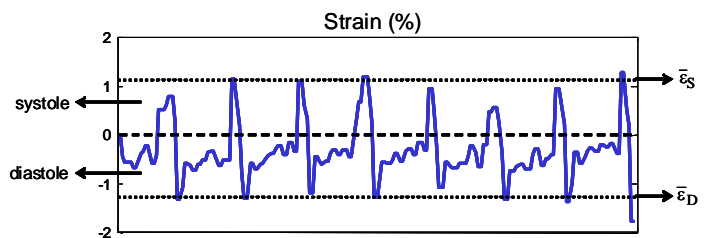
Aims: Whereas the potential of NIVE was previously demonstrated to characterize the carotid artery, this presentation addresses its reproducibility over several cardiac cycles (CC), between left and right carotids, and between radiologists.

Methods: Sixteen subjects (8 males and 7 females), without previous history of carotid atherosclerosis, were investigated. Four groups of ages, which are (40–49), (50–59), (60–69) and (70–79) years old, were included in this study. The left and right common and internal carotids (LCC, LIC, RCC and RIC, respectively) were independently scanned by two radiologists (RAD-A and RAD-B) with the Sonix-RP system (Ultrasonix, Vancouver, Canada), which was equipped with a 7 MHz linear array probe. The elastograms, axial strain images in this case, were computed using the Lagrangian Speckle Model Estimator (LSME) applied on RF data provided by the Sonix scanner.

Results: To illustrate the reproducibility of NIVE between CC, Figure 1 shows the instantaneous strain-curve that was computed along 8 complete CC for one male subject's LCC. Good reproducibility is observed between CC; furthermore, it can be noted that the temporal mean strains at peak diastole ($\bar{\epsilon}_D$) and at peak systole ($\bar{\epsilon}_S$) are about the same in absolute terms. Provided that artifactual motions are observed less during vascular relaxation, comparisons were performed according to $\bar{\epsilon}_D$. Strain values between LCC and RCC were found highly similar with Pearson correlation coefficient (r) = 0.83 ($p < 0.00001$), whereas comparisons between LIC and RIC exhibited $r = 0.54$ ($p < 0.01$). Equivalently, very good reproducibility was found between RAD-A and RAD-B for the common carotids with $r = 0.76$ ($p < 0.00005$), whereas the internal carotids showed $r = 0.581$ ($p < 0.005$). The decrease of r for the internal carotid strain measurements can be explained for the most part by the difficulty to image this vessel, specifically because its visualization can be obstructed by the external carotid. Additionally, male subjects' carotid elastic modulus was observed to increase with age, ranging from 30 to 115 kPa.

Conclusions: It is concluded that NIVE is reproducible. This new imaging method might provide a unique approach for stroke prevention.

Figure 1: Strain-curve for one male subject's LCC, over 8 consecutive cardiac cycles. The diastolic and systolic phases are characterized by negative and positive strain values, respectively. $\bar{\epsilon}_D$ and $\bar{\epsilon}_S$ define the temporal mean of the peak diastolic and peak systolic values, respectively.



Acknowledgements: This work was jointly supported by the Canadian Institutes of Health Research (Grant #PPP-78763) and the Natural Sciences and Engineering Research Council of Canada (Grant #312136-06). The works of Dr. Soulez and Dr. Maurice are partially supported by the Fonds de la Recherche en Santé du Québec (FRSQ) through clinical and research scholarship awards, respectively. Dr. Cloutier is recipient of the National Scientist award of the FRSQ (2004–2009). The authors acknowledge Mrs. Vicky Thiffault for helping in subjects' recruitment and data management.

047 4D CARDIAC STRAIN IMAGING IN THE HUMAN HEART: INITIAL *IN VIVO* RESULTS.

Richard GP Lopata^{1*}, Maartje M Nillesen¹, Inge H Gerrits¹, Johan M Thijssen¹, Livia Kapusta², Chris L de Korte¹.

¹Clinical Physics Laboratory, ² Children's Heart Center, Radboud University Nijmegen Medical Center, Nijmegen, The NETHERLANDS.

Background: Cardiac strain imaging shows great potential for the diagnosis and monitoring of heart disease or even heart failure. New 3D ultrasound techniques have enabled 3D strain imaging. The advantage is that strain in three orthogonal directions in 3D space can be determined and out-of-plane motion can be corrected. However, a possible and important limitation is the relatively low frame rate.

Aims: Developing and validating 3D strain estimation for cardiac strain imaging.

Methods: Raw (rf) ultrasound data were acquired with a Philips SONOS 7500 live 3D ultrasound system, equipped with an X4 matrix array transducer and an RF-interface. In this study, two different approaches are introduced and compared. Method 1 used an iterative 3D coarse-to-fine strain algorithm, with additional aligning and stretching of rf-data to estimate displacements. This method is based on a previously developed 2D strain algorithm [1] that was modified to enable 3D strain imaging in both the axial/lateral and the axial/elevational plane. Hence, the lateral and elevational displacements were estimated independently and both were used as an offset for subsequent iterations. Method 2 is based on 3D cross-correlation of 3D kernels, in which all displacement components were estimated simultaneously. This method also used a coarse-to-fine approach for improving the axial resolution despite large translations and strain levels. A newly developed 3D least-squares strain estimator was used to determine the three strain components in full 3D space after applying a 3D median filter to the displacements.

The method was validated using a tissue-mimicking phantom (10x10x10 cm³, 8% gelatin, 1% agar-agar) with a hard cylindrical inclusion (3% agar-agar). The phantom was compressed by a plate compressor in steps of 0.5 mm with a total range of 5.0 mm. Preliminary *in vivo* validation was performed by acquiring 3D Full Volume data (frame rate = 19 Hz) and BiPlane data (frame rate = 72 Hz) of the left ventricle of a trained athlete with a relatively low heart rate (40 - 45 bpm). Strain imaging was performed, and cumulative strain curves for a manually segmented ROI in the lateral wall were calculated. The frame rate of the BiPlane data was artificially lowered to 36 and 18 Hz, respectively, by omitting frames to study the effects of the lower frame rate on the shape of the strain curves.

Results: Comparison of both methods revealed high quality elastograms in the phantom up to an applied compression of 3% strain (resulting in 0.5-5% axial strain). No difference in SNR between the two methods was found. Method 1 is favored for its considerably lower computation time. The signal- and contrast-to-noise ratios of the axial elastograms increased by 6 and 13 dB respectively with respect to BiPlane data. Lateral and elevational elastograms were also in accordance with finite element solutions of the phantom model with an increase in SNR and CNR (3 dB and 12 dB respectively). However, the SNR and CNR were considerably lower than the axial elastograms, which is presumably caused by the lower in-plane spatial resolution of the 3D full volume data. Initial *in vivo* results revealed mean strain profiles in three orthogonal directions, similar to previous studies. Since no tracking of the tissue was performed, the linear trend of the strain curves had to be removed. Reducing the sample frequency revealed lower strain values in the systolic phase with fast contraction of the heart resulting in lower maximum cumulative strain values. The strain values of the 3D data were in correspondence with the BiPlane data at a reduced frame rate (18 Hz). This implies that higher frame rates are necessary for obtaining valid cardiac strain measurements, especially considering the lower heart rate of the studied subject. Recent developments in 3D ultrasound equipment will solve this issue.

Conclusions: Firstly, for 3D strain imaging a semi-3D strain estimation approach is favored considering the lower computational cost and similar accuracy. Secondly, the relatively low frame rate restricts the accuracy of 3D cardiac strain imaging techniques.

Acknowledgements: Funded by the Dutch Technology Foundation and Philips Medical Systems.

References:

- [1] Lopata R.G.P. et al; *In Vivo* 3D Cardiac Elastography in an Animal Model and Human Heart, 5th Internatl. Conf. on the Ultrasonic Measurement and Imaging of Tissue Elasticity. Snowbird, Utah, USA, Oct. 2006.
-

Background: Myocardial stiffness is an important physiological parameter that can be used to assess myocardial function [1]. Acoustic radiation force impulse (ARFI) imaging has been shown to be capable of visualizing variations in radiation force induced tissue displacements that reflect the apparent changes in stiffness through the cardiac cycle [2]. However, these images were formed with the transducer placed directly on an exposed heart. In order to be of clinical use, a non-invasive method of ARFI image acquisition is necessary.

Aims: To explore potential of transthoracic ARFI imaging to non-invasively measure myocardial stiffness.

Methods: We imaged the hearts of two live porcine subjects, weighing approximately 20 kg, and heart rates up to 150 bpm. An abdominal (2.2 MHz) probe was used with a radiation force pulse length of 360 μ s to produce tissue displacements within the heart. The ARFI images were motion filtered to remove any physiological cardiac motion artifacts. These motion filters estimated physiological motion artifacts within the ARFI imaging tracking intervals (\sim 5 ms) via a least-squares parabolic approximation. Single line M-mode and two-dimensional ARFI images of the heart were formed from an intercostal viewing angle. Passive ARFI images, where the radiation force pulse amplitude was set to zero, were also acquired to assess effectiveness of these motion filters.

Results: The passive ARFI images indicated that the motion filter effectively removed physiological cardiac motion within the ventricular septum to below 2 μ m throughout the entire heartbeat. The active ARFI images measured radiation force induced tissue displacements above 10 μ m during diastole, and observed differences in systolic and diastolic tissue displacements greater than the physiological motion noise floor. Therefore, we believe these variations reflected changes in myocardial stiffness through the cardiac cycle.

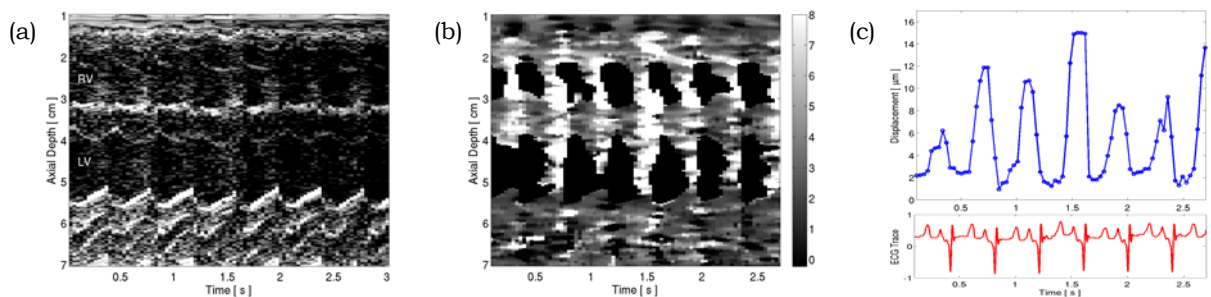


Figure 1: Single-line M-mode (a) and ARFI (b) images of a porcine heart through six complete heartbeats. The images were formed from an intercostal, short-axis view with the right ventricle (RV) above, the left ventricle (LV) below, and the ventricular septum separating the two. The average displacements (μ m away from the transducer) within the ventricular septum are plotted through time and matched with its corresponding electrocardiogram (c). From this plot, maximum displacements can be observed to coincide with cardiac diastole while minimum displacements occur at ventricular systole.

Conclusions: Although fair degree of variability is present within the measured maximum and minimum displacement values, transthoracic ARFI images of the heart showed cyclic displacements that reflected the expected myocardial stiffness changes through the cardiac cycle.

Acknowledgements: This research was funded by NIH Grants #1R01-HL-075485-01 and 1R01-CA-114093-02. We would like to thank Siemens Medical Solutions USA, Inc., for their hardware and system support. We would also like to thank: Kathy Nightingale, Jeremy Dahl, Joshua Baker-LePain, Melissa Caughey, Caterina Gallippi, Timothy Nichols, Russ Behler, Robin Raymer, and Kent Passingham.

References:

- [1] L. Zhong, D.N. Ghista, E.Y.K. Ng and S.T. Lim. Passive and active ventricular elastances of the left ventricle. *Biomedical Engineering Online*. vol 4:10, 2005.
- [2] S.J. Hsu, R.R. Bouchard, D.M. Dumont, P.D. Wolf and G.E. Trahey. *In vivo* assessment of myocardial stiffness with acoustic radiation force impulse imaging. *Ultrasound Med Bio*. in press.

Background: Myocardial elastography has been developed into a non-invasive method for regional myocardial function estimation [1]. However, the requirement and optimization of the frame rate for accurate estimation of displacements and strains in myocardial elastography has not been thoroughly studied.

Aims: To study the minimum requirement of the frame rate and optimization of the frame rate for optimal image quality for myocardial elastography.

Methods: *In-vivo* transthoracic radiofrequency (RF) data of the entire left ventricle of a normal mouse and a healthy human subject were acquired in a long-axis view at extremely high frame rates (up to 8 kHz) using a retrospective ECG-gating technique. In the mouse case, a Vevo 770 system (VisualSonics Inc., Toronto, Canada) was used with a mechanical sector probe (30 MHz) working on a line-by-line basis [2,3]. In the human case, an Ultrasonix RP system (Ultrasonix Corp., Burnaby, Canada) was used with a phased array (3.3 MHz) working on a sector by sector basis. The sampling frequency of the RF signals was 160 MHz and 20 MHz, respectively. 2D full long-axis view RF frames were reconstructed from multiple RF signals or narrow RF sector images acquired from different cardiac cycles, at high frame rates of 8 kHz and 480 Hz, or equivalently 880 and 360 frames per cardiac cycle (fpc), for the mouse and human subjects, respectively. The effects of the frame rate were studied quantitatively by using different frame number decimation applied to the original RF data. Incremental axial displacements of the myocardia at rapid ejection (RE) and fast filling (FF) phases, which incur the highest strain rate, were estimated using RF speckle tracking using a 1D cross-correlation function. The elastographic signal-to-noise ratios (SNRe) were calculated as the average strain divided by the standard deviation of the strain in small regions of the septum (i.e., 0.3mm x 0.3mm and 4mm x 4mm for mice and humans, respectively).

Results: In the case of the mice, the correlation coefficient between two RF frames decreases from 0.96 to 0.94 and from 0.95 to 0.93 in the RE and FF phases, respectively, when the frame rate decreases from 880 to 220 fpc. When the frame rate dropped below 147 fpc, the correlation decreased significantly to below 0.85. The peak SNRe's were 8.2 and 8.4 at the frame rates of 220 and 293 fpc, in the RE and FF phases, respectively. At the maximum frame rate (880 fpc), the SNRe was limited by noise ambiguity and was 4.5 and 5.3, respectively. The SNRe was deteriorated by the increased decorrelation when the frame rate decreased to below 147 fpc, with a value smaller than 5.2 and 3.7, in the RE and FF phases, respectively. The results in the human case were in good agreement with those in the mouse when heart rate differences were adjusted. The correlation coefficient was lower than 0.90 and 0.88, when the frame rate dropped below 180 and 360 fpc, in the RE and FF phases, respectively. The SNRe reached its maximum value of 7.5 and 3.6 at the frame rates of 180 and 360 fpc, in the RE and FF phases, respectively.

Conclusions: A frame rate between 200–360 fpc is suggested for myocardial elastography in order to obtain the highest SNRe during the entire cardiac cycle. The diastolic phase requires a higher frame rate than the systolic phase because of larger strain rate incurred. Comparison with B-mode speckle tracking will also be shown.

Acknowledgements: This study was supported in part by the American Heart Association (SDG0435444T) and the National Institutes of Health (R01EB006042-01).

References:

- [1] E. E. Konofagou, J. D'hooge and J. Ophir, "Myocardial elastography – A feasibility study *in vivo*," *Ultrasound Med. Biol.*, vol. 28, pp. 475–482, 2002.
- [2] J. Luo, K. Fujikura, S. Homma and E. E. Konofagou, "Imaging of murine infarcts using myocardial elastography at both high temporal and spatial resolution," *IEEE Ultrasonics Symp Proc*, pp. 752–755, 2006.
- [3] J. Luo, K. Fujikura, S. Homma and E. E. Konofagou, "Myocardial elastography at both high temporal and spatial resolution for the detection of infarcts," *Ultrasound in Med. Biol.*, 2007 (in press).

M Bilgen^{1,2*}.¹Hoglund Brain Imaging Center, ²Integrative and Molecular Physiology Department, University of Kansas Medical Center, Kansas City, KS, USA.

Background: Tagged magnetic resonance imaging (tMRI) is an established radiological technique for regional assessment of myocardial contractility in the left ventricle (LV) wall under different pathological conditions. The dark tag lines in this technique follow the motion of the underlying tissue, as the heart beats, thereby revealing the localized deformation in the myocardium. Currently, harmonic phase (HARP) and homogenous strain analysis (HSA) are the two approaches commonly employed for post processing of the acquired tMRI data to quantify the spatial distribution of strain in the LV wall [1,2]. In HSA, the intersections of the tagged lines in the LV wall are first identified and tracked to determine the myocardial motion. The intersection points in this technique also serve as coordinates for the vertices of triangle-shaped tiles organized to cover the whole heart wall in a non-overlapping fashion. The deformation during the cardiac cycle is quantified by assuming that the strain is uniform within each triangle element. In numerically analyzing the data, these elements are generated automatically by using Delaunay triangulation. However, in sequential images within the cardiac cycle, this approach may miss making the correct connections between the corner points and consequently results in triangles with different orientations. This limits the analysis of the deformation experienced by the same myocardial tissue. In this presentation, we address this issue and provide a robust triangularization technique using the HARP information.

Aims: The first goal of this work is to show how the coordinates of the tag line intersections in tMRI can be obtained using HARP. The second goal is to use these points for an automatic triangulation of the LV wall with consistent orientations. The third goal is to demonstrate adaptive triangulation method with advanced features for motion analysis.

Methods: Cardiac MRI data were gathered from male Sprague–Dawley rats using a 9.4 T scanner and 60 mm radiofrequency (rf) volume coil. ECG gated gradient echo based tagged images were captured from the short-axis view of the heart, where the cardiac cycle was temporally resolved into ten equally incremented phases. Simulations and theoretical formulations were implemented and tMRI data analyses were performed using Matlab.

Results: Figure 1 shows simulation of tMRI and triangulation of tag cells in black and white using HARP processing for HSA analysis. Green lines in the figure denote the tag lines. Similarly, Figure 2 shows the triangulation of the tag cells using real data set.

Discussion: The presented simulated and real data show that our analytical approach correctly identifies the coordinates of the tag line intersections and produces triangulation in the LV wall with elements remaining oriented in the same direction as the wall moves. From these aspects alone, this new development can be used to explain the empirical data by Liu et al. [3] showing that strong correlation exists between HARP and HSA analysis of myocardial motion. In addition, although not shown here, our approach also provides a new capability to spatially shift the triangular elements an arbitrary amount. This ability offers new opportunities and freedom for characterizing the motion of myocardial tissue.

References:

- [1] Osman, N. F., et al. IEEE Trans Med Imaging, 2000. 19(3): p. 186–202.
- [2] Zhou, R., et. al. Magn Reson Med, 2003. 49: p. 760–4.
- [3] Liu, W., et al. Magn Reson Med, 2004. 52(6): p. 1282–90.

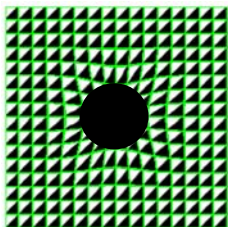
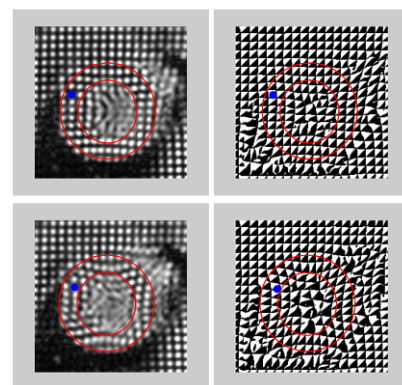


Figure 1: Simulation of tMRI and its analysis with the proposed approach developed for the triangulation of the tagged cells.

Figure 2: The triangulation of the tag cells using a real tMRI data set. Top row is the end-diastole and bottom row is the systolic data. Right column is the triangulated tag cells. Red circles identify the LV wall. The blue circles denote a tag cell, its triangulation and how it changes with systolic myocardial motion.



020 MEASUREMENT OF THE HYPERELASTIC PROPERTIES OF TISSUE MIMICKING PHANTOMS.

Joseph J. O'Hagan^{1*}, Abbas Samani^{1,2}.

¹Electrical and Computer Engineering, ²Medical Biophysics Departments, The University of Western Ontario, London, ON, CANADA.

Background: The elastic properties of soft tissues are of great interest to medical applications, especially in disease diagnosis, and more specifically in cancer diagnosis. Because of the well known fact that cancer is associated with an alteration of stiffness in the affected tissue(s), elastography, an imaging technique that images the mechanical stiffness of tissues, has been developed over the past two decades. To interpret images obtained from elastography, the elastic properties of various pathological tissues are needed as reference values; however, such data are relatively scarce. In addition to being crucial in cancer diagnosis, the elastic properties and more specifically the hyperelastic properties of tissues are critical for various medical applications, e.g. surgery simulation that involve tissue modeling. Our group has developed techniques to measure the hyperelastic properties of small excised breast tissue samples *ex vivo*, [1,2]. While normal tissue excision is acceptable, excising tumor tissues from tissue slices obtained post-surgery is normally not permissible to avoid compromising valuable information such as tumor margin. The goal of this work is to develop and validate a technique for measuring the hyperelastic properties of tumor tissue in an intact slice.

Aims: The objective of this work is to develop an indentation technique to measure the hyperelastic properties of tumor tissues in intact *ex vivo* tissue slices. This research involves developing an experimental setup to acquire the tissue mechanical response and a numerical model to determine the hyperelastic parameters from the measured response. The experimental setup is similar to the one previously proposed by our group [1,2]. In this current work, we will present a numerical technique of this measurement system followed by a phantom study to validate its performance.

Methods: A phantom study will be conducted using materials that will simulate the hyperelastic properties that soft tissues are known to exhibit. The phantoms will be constructed to contain two distinct regions, a background region and an inclusion region. The background region will be composed of gelatin, and the inclusion region will be composed of a polyvinyl alcohol-bacterial (PVA) and cellulose nanocomposite, a material developed by [3]. This composite has been shown to exhibit non-linear properties. The phantom will be tested by performing mechanical indentation from which force-deformation data will be acquired using an experimental setup similar to the one presented in [1,2]. This data will be used in a data inversion algorithm to obtain the sought after hyperelastic properties. This inversion algorithm involves inputting the applied indentation profile and an initial guess of the hyperelastic parameters, based upon a polynomial strain energy form, into a finite element model that will simulate the mechanical testing. The resulting force-deformation profile will be computed and compared to the experimental profile. The unknown hyperelastic parameters are systematically adjusted via an optimization algorithm until the simulated and experimental force-deformation data profiles match each other.

Results: Thus far we have formulated numerical experiments to validate the proposed methods. These numerical experiments involved the construction of a finite element model consisting of two regions, a background and inclusion. The background was modeled as having linear elasticity whereas the inclusion was formulated to be hyperelastic. An indentation profile was applied to the finite element mesh, and the resulting reaction forces were computed. These reaction forces and the indentation profile were input in the inversion algorithm as experimental data, and the hyperelastic parameters of the inclusion were reconstructed successfully.

Conclusions: We have designed a technique that may be used for measuring the hyperelastic properties of an inclusion within a larger piece of soft tissue, which we have also numerically validated. Work is under way to further validate the technique by performing a phantom study using tissue mimicking materials. In the future, these techniques will be used with real tissues to create a set of reference values that would be used to aid in the interpretation of elastography images.

References:

- [1] A. Samani, D. Plewes. An inverse problem solution for measuring the elastic modulus of intact *ex vivo* breast tissue tumors. *Physics in Medicine and Biology*, 52: 1247-1260, 2006.
- [2] A. Samani, D. Plewes. A method to measure the hyperelastic parameters of *ex vivo* breast tissue samples. *Physics in Medicine and Biology*, 49: 4395-4405, 2004.
- [3] L.E. Millon, W.K. Wan. The polyvinyl alcohol-bacterial cellulose system as a new nanocomposite for biomedical applications. *Journal of Biomedical Materials Research Part B: Applied Biomaterials*, 79B: 245-253, 2006.

Background: Many methods have been developed to estimate the static elasticity of soft tissue, while linear and nonlinear viscoelastic parameter estimation have also been explored recently [1-2]. Imaging the dynamic properties of tissue might have clinical applications in diagnosis and treatment.

Aims: In this work, the response of tissue to a wide-band excitation is studied. While the low-frequency spectral components of the displacements are mostly affected by the Young's modulus, the phase at higher frequencies varies as the viscosity in the medium changes. We propose a technique to reconstruct tissue relaxation-time from the phase of the transfer functions between the estimated displacements.

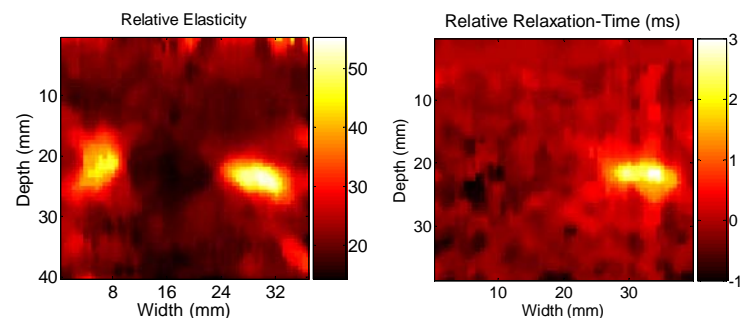
Methods: A tissue-mimicking phantom was fabricated using a homogeneous substrate of gelatin (12% by weight) and water. The phantom encloses two hard inclusions: a cylindrical inclusion made with more concentrated gelatin material making it twice as stiff as the substrate, and a small piece of PVA sponge soaked in water. A wide-band small-amplitude vibration was applied to one side of the phantom. Twenty seconds of radio frequency (RF) signals were recorded at 98 frames per second from a 40×40mm² window using a Sonix RP ultrasound machine (Ultrasonix Medical Corp., Richmond, BC, Canada). The displacements were estimated using a one-dimensional (1D) cross-correlation technique with block length of 1.6 mm and 60% overlap. For each RF line, transfer functions were computed for the displacements of each node with respect to an arbitrary node in the middle of the imaging window. Welch's method to calculate the periodograms with 0.5 second windows and 75% overlap was employed. It has been shown that the magnitudes of the transfer functions at low frequencies correlate with the static elastic properties of the tissue [3]. Furthermore, dynamic properties also introduce phase lag between consecutive displacements. It can be shown that this lag is proportional to the local relaxation-time, which can be defined as the ratio between the viscosity and elasticity.

Results: The elasticity was estimated from the spatial gradient of the magnitude of the transfer functions at low frequencies (6Hz in this case), and the relaxation-time was reconstructed from the phase of the spatial gradient of the transfer functions at a slightly higher frequency (21Hz in this case). The left image below shows the elasticity map, in which the gelatin inclusion appears on the left side of the image and the PVA sponge appears in the right as two bright spots. The relaxation-time is shown in the right image. The calculated relaxation-time values for the gel inclusion is similar to that of the gelatin background, but the PVA sponge has significantly different damping values. The mean of the correlation coefficients in this experiment was 97.6% with 3% standard deviation. The coherence functions were generally above 0.97 with an average of 0.986 over the frequency range of vibration. This indicates that the displacements could be fit well by a linear model, presumably a 1D network of Voigt's elements.

Conclusions: The results show that the relaxation-time images can provide contrast between materials that do not appear in elasticity images. The hard gelatin inclusion produces viscosity and elasticity that are higher than the background. This results in a small relaxation-time contrast for the hard gel, while the sponge, being a completely different material, exhibits a significant change in the relaxation-time. This demonstrates that tissue transfer function images [3] can produce contrast that is not normally seen in elasticity imaging. In further studies, we will study whether such contrast appears in *in-vivo* images.

References:

- [1] M.F. Insana, C. Pello-Barakat, M. Sridhar and K.K. Lindfors, "Viscoelastic Imaging of Breast Tumor Microenvironment with Ultrasound", *Mammary Gland Biology and Neoplasia*, Vol. 9, No. 4, pp. 393-404, Oct. 2004.
- [2] R. Sinkus, M. Tanter, T. Xydeas, S. Catheline, J. Bercoff and M. Fink, "Viscoelastic Shear Properties of *in vivo* Breast Lesions Measured by MR Elastography", *Mag. Res. Imag.*, Vol 23, No. 2, pp. 159-165, Feb. 2005.
- [3] E. Turgay, S.E. Salcudean and R. Rohling, "Identifying the Mechanical Properties of Tissue by Ultrasound Strain Imaging", *Ultras. Med. Bio.*, Vol 32, No. 2, pp. 221-235, Feb. 2006.



076 **MECHANICAL MUSCLE PROPERTIES: TRANSIENT ELASTOGRAPHY AND 3D ULTRASOUND ULTRAFAST IMAGING.**

T. Deffieux^{1*}, J.-L. Gennisson¹, M. Tanter¹, J. Bercoff², M. Fink¹.

¹Laboratoire Ondes et Acoustique, ESPCI – CNRS UMR7587 – INSERM – Université Paris VII, 10 rue Vauquelin 75231 Paris Cedex 5, FRANCE; ²Supersonic Imagine, Les Jardins de la Duranne, 510, rue René Descartes 13857 Aix-en-Provence Cedex, FRANCE.

Background: The non invasive and *in vivo* assessment of the active and passive properties of the musculoskeletal system remains a great challenge for the understanding of muscular diseases. In a previous paper, we showed that the transient contraction of a muscle fiber bundle triggered by electro-stimulation can be followed in space and time by an ultrafast ultrasound system. On the one hand, this experiment is generalized to measure the three dimensional velocity fields allowing much easier localization of the contracting fiber bundles. On the other hand, the supersonic shear imaging technique is applied to assess viscoelastic properties of the *biceps brachii* in different conditions.

Aims: By combining *in vivo* imaging of both passive and active muscle activity, this study aims to provide new potential ultrasonic tools for muscle diseases diagnosis and monitoring.

Methods: In order to image the contraction, which is a very rapid phenomenon, a modified ultrasound scanner able to take up to 5000 frames/s was used (ATL HDI 1000). Tissue velocities were obtained from conventional speckle tracking techniques. The probe, positioned perpendicularly to the arm in a water tank, was moved with a linear motor. For each position, the imaging system was set to trigger an electro-stimulation firing the contraction. A second experiment for the assessment of passive muscle elastic properties in different positions of the arm and contraction levels is then performed using the same probe in the supersonic shear imaging mode. Generated by the radiation force induced by a focused ultrasound beam, shear waves propagate in the medium and are imaged by an ultrafast ultrasound scanner allowing the reconstruction of viscoelastic maps (Figure 1a).

Results: The localization of the contracting fiber bundles and the resolution of its main temporal and spatial behavior are demonstrated (Figure 1b). Paving the way to a clinical protocol on muscle diseases, viscoelastic parameters are measured in different conditions and reproducibility is discussed.

Conclusions: These two complementary ultrasound ultrafast techniques offer new perspectives for muscle diagnosis both as an active contractile tissue and as a passive tissue. Moreover, coupled with electro-stimulation devices already used in clinical exams, these techniques could offer physicians both electrical and mechanical responses of muscles in order to better target muscle disorders and possible genetic alterations.

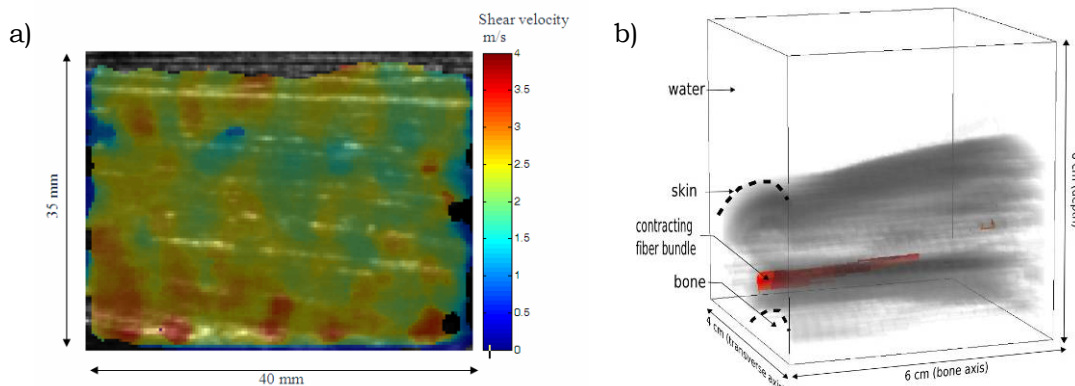


Figure 1: a) Shear wave velocity map of the *biceps brachii* at rest obtained with the supersonic shear imaging technique; b) 3D normalized and thresholded tissue velocity field (red) after electro-stimulation, tissue echogenicity is also visible (gray). (see CD for colors)

Yan-Ping Huang^{1*}, Yongping Zheng¹, Shu-Zhe Wang¹.

¹Health Technology and Informatics Department, Hong Kong Polytechnic University, Hong Kong, CHINA.

Background: Indentation is one of the most frequently used approaches for the quantitative assessment of mechanical properties of soft tissues. Traditional indentation involves a rigid indenter with a relatively large dimension and direct contact with the tissue to induce deformations. This may limit its use in small tissues and preclude fast-scanning capability. In the last decade, Optical Coherence Tomography (OCT) has become a more matured technique in measuring small tissues with very high resolution and sensitivity.

Aims: To develop a new OCT-based indentation system tailored for applications in small tissues and with a fast-scanning capability for measuring mechanical properties of soft tissues.

Methods: A nozzle with a 2mm bubbler diameter was attached to an OCT system (Figure 1). With this structure, an air jet was used for indentation, similar to a water jet ultrasound system reported previously [1]. The OCT system was used to detect the displacement of the sample surface during indentation based on a cross-correlation algorithm. A pressure sensor was adapted to measure the force induced on the specimen.

Preliminary experiments were performed to demonstrate the feasibility of the system. 27 silicon phantoms with a width and length of 10mm × 10mm and different heights (5, 10 and 15mm) having different stiffness were tested, and the results were compared with those obtained from the standard compression test. A stiffness coefficient (N/mm) defined by the regression of the force-displacement curve was used to indicate the stiffness of the tested phantoms. Tests were also performed *in vivo* on the soft tissue layer near the basal joint of the hand in 10 healthy subjects to differentiate the change of stiffness with muscles altered between relaxation and contraction states.

Results: For the phantom test, the stiffness coefficient measured by the developed system was well correlated with the Young's modulus obtained from the compression test ($r=0.89$, $p<0.001$, Figure 2). For the *in vivo* test, the tissue was significantly stiffer (0.150 ± 0.059 vs. 0.059 ± 0.031 N/mm, $p < 0.001$) when the muscles were contracted than relaxed.

Conclusions: Preliminary experiments on phantoms and *in vivo* tissues showed that it was feasible to measure the mechanical properties of soft tissues using the developed OCT-based air jet indentation system. Further studies are planned to investigate its potential applications in clinical diagnoses.

Acknowledgements: Supported by Hong Kong Research Grant Council (PolyU5318/05E, PolyU5245/03E).

References:

- [1] Lu M, Zheng YP, Huang QH. A novel noncontact ultrasound indentation system for measurement of tissue material properties using water jet compression. *Ultrasound Med Biol* 31: 817-826, 2005.

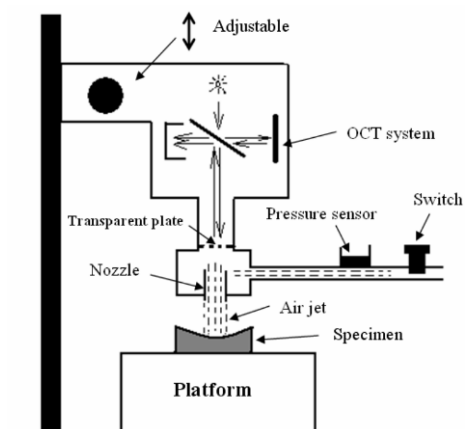


Figure 1: Schematic of the OCT-based air jet indentation system

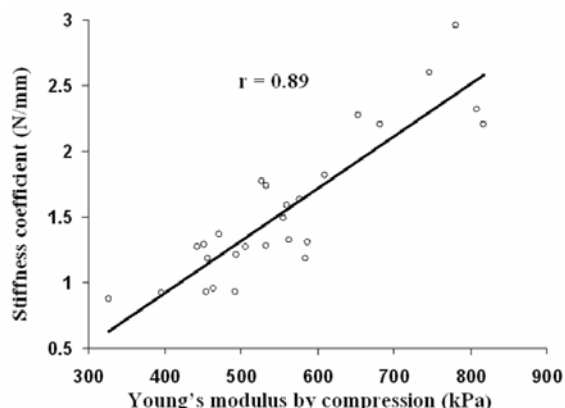


Figure 2: Correlation of stiffness measured by air jet indentation system (N/mm) and compression test (kPa).

105 **FLUID-FLOW RELATED STRAIN RELAXATION IN SOFT TISSUES: AN INVERSE PROBLEM AND SOLUTION FOR THE MICROVASCULAR FILTRATION COEFFICIENT.**

Ricardo Leiderman¹, Gearóid P Berry², Jeffrey C Bamber², Assad A Oberai³, Paul E Barbone^{4*}.

¹Federal University of Rio de Janeiro, Rio de Janeiro, BRAZIL; ²Institute of Cancer Research, Sutton, Surrey, England, UK; ³Rensselaer Polytechnic Institute, Troy, NY, USA; ⁴Boston University, Boston, MA, USA.

Background: The fluid and solid phases of soft tissues can move independently of each other. Furthermore, the fluid exists within several “compartments” of the soft tissue, notably, the vasculature (including both the hemal and lymphatic vessels) and the extravascular space [1]. Of course, due to permeability of the microvessels in both vascular networks, fluid is often exchanged between these compartments. It is recognized that fluid flow leads to a stress relaxation at fixed strain (or conversely, a strain relaxation at fixed stress) [2,3]. On the other hand, the solid phase of soft tissue is a gel like polymer network comprised primarily of crosslinked collagen and proteoglycans [4]. When subjected to stress, these molecules can undergo molecular rearrangement, which itself gives rise to macroscopic relaxation phenomena. These distinct microscopic relaxation mechanisms can be captured in mathematical models describing the macroscopic stress strain response of the tissue. Our earlier experimental work demonstrated the ability to measure and image the time–evolution of the strain in fluid–rich poroelastic phantom materials under sustained compression [5,6]. Our earlier theoretical work was based on a mathematical model describing multiphase mechanics of soft tissue deformation.

Aims: We focus on the inverse problem associated with determining the microvascular filtration coefficient (MFC) from hypothetically measured strain relaxation histories. The close link between MFC and microvessel density makes MFC an attractive imaging target.

Methods: We work with a mathematical model of tissue deformation given in [3]. This model depends upon four material properties: shear modulus, Poisson's ratio, interstitial permeability and the MFC. We use the finite element method to solve the mathematical equations and, thus, conduct computational experiments. This provides us with simulated “data” based on published physical properties representative of breast tissue. We invert this simulated data to recover the input microvascular filtration coefficient.

Results: We find that we can successfully reconstruct MFC under relatively idealized conditions. These include *a priori* knowledge of the elastic properties, measurement of the time dependent dilatation and neglect of the interstitial permeability. The impact of small errors in the assumed values for these parameters is found to lead to small errors in the reconstructions, as might be expected.

Conclusions: Under the conditions considered here, the reconstructions are remarkably accurate, stable, and fast. The data requirements for the current reconstruction method, however, make it impractical at present. Nevertheless, the accuracy and stability of the results are encouraging. This success, together with the knowledge that different microscopic relaxation mechanisms result in different spatio–temporal patterns of strain relaxation, suggest that a more advanced reconstruction method may succeed under more practical conditions. Furthermore, the current method motivates the development of a volumetric strain imaging capability.

Acknowledgements: EPSRC, ICR and NSF for funding this research.

References:

- [1] Levick JR. An introduction to cardiovascular physiology, 4th ed. London: Arnold Publishers, 2003.
- [2] Mow VC, Kuei SC, Lai WM, Armstrong CG. Biphasic creep and stress relaxation of articular cartilage in compression: theory and experiments. *J Biomech Eng* 1980;102:73–84.
- [3] Netti PA, Baxter LT, Boucher Y, Salak R and Jain RK 1997 Macro- and microscopic fluid transport in living tissues: Application to solid tumors *AIChE Journal* 43(3) 818–834.
- [4] M Sridhar, J Liu and M F Insana, 2007, Viscoelasticity imaging using ultrasound: parameters and error analysis, *Phys. Med. Biol.* 52 2425–2443.
- [5] Berry GP, Bamber JC, Armstrong CG, Miller NR, Barbone PE. Towards an acoustic model–based poroelastic imaging method: I. Theoretical Foundation. *Ultrasound Med Biol* 2006a;32:547–567.
- [6] Berry GP, Bamber JC, Miller NR, Barbone PE, Bush NL, Armstrong CG. Towards an acoustic model–based poroelastic imaging method: II. Experimental Investigation. *Ultrasound Med Biol* 2006b;32:1869–1885.

014 **SIMULATION OF SHEAR WAVES PROPAGATION IN HETEROGENEOUS MEDIA USING A PSEUDO-SPECTRAL TIME DOMAIN METHOD.**

Cécile Bastard^{1,2*}, Jean-Pierre Remeniéras¹, Laurent Sandrin².

¹Tours University, LUSI – CNRS FRE 2448, 10 boulevard Tonnellé, 37000 Tours, FRANCE;

²Echosens, Research and Development Department, 153 avenue d'Italie, 75013 Paris, FRANCE.

Background: Transient elastography consists of following the propagation of a low frequency shear wave generated in a tissue by an external vibrator. This technique allows the measurement of the shear wave velocity and, thus, the determination of the Young's modulus of the tissue. This method has been successfully applied to homogeneous tissues such as liver in patients with hepatitis C virus (HCV) [1], and its current developments are headed toward heterogeneous organs.

Aims: In order to optimize the source condition used in transient elastography, a precise understanding of tissue displacements in terms of amplitude and directivity is needed. To serve this purpose, a numerical model has been developed to simulate shear wave propagation in an axisymmetric heterogeneous soft medium.

Methods: The numerical model proposed is based on a pseudo-spectral time domain (PSTD) method which consists of calculating spatial derivatives in the Fourier domain. Perfectly Matched Layers (PML) are implemented to avoid reflections on the numerical grid boundaries and to counter the wrap around effect of the FFT. The temporal evolution of the model is computed with a staggered fourth order Adams-Bashforth method [2]. Axial and lateral displacements are obtained from the components of the stresses in three dimensions using the axisymmetric configuration.

As in finite difference methods, the solver temporal increment is linked to the celerity of the fastest wave. In soft tissue, the ratio between the compression and the shear wave velocity is about a thousand which makes the computation time prohibitive. To overcome this difficulty, the irrotational and solenoidal parts of the source, generating the compression and shear waves, respectively, have been separated and two independent simulations have been performed in heterogeneous media.

Results: These simulations have been validated for homogeneous media by comparison with an analytical model based on the elastodynamic Green function [3] and the contributions of the near field and far field terms have been studied. Simulations of the shear wave propagation in a medium having an inclusion stiffer than the surrounding tissue have been performed and compared with experimental data acquired in a tissue mimicking phantom in which the Young's modulus was 8 kPa and 19 kPa in the 30 mm diameter inclusion.

Conclusions: An independent simulation of the shear wave propagation has been developed leading to a better understanding of the displacements measured in transient elastography. This simulation should also be useful for the validation of inverse problem algorithms.

References:

- [1] L. Sandrin *et al.*, Transient elastography: a new non-invasive method for the assessment of hepatic fibrosis, *Ultrasound in Medicine and Biology*, Vol. 29, No.12, 2003.
- [2] S. Callé, J.P. Remeniéras, M. Elkateb Hachemi and F. Patat, A new numerical approach to simulate shear waves generated by a localized radiation force in heterogeneous media, *IEEE Ultrasonics Symposium proceedings*, p1676–1679, 2006.
- [3] K. Aki and P.G. Richards, *Quantitative seismology*, 2nd Ed, University Science Books, 2002.

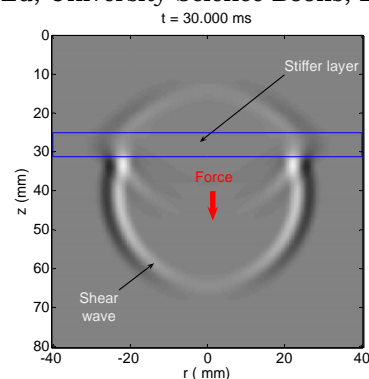
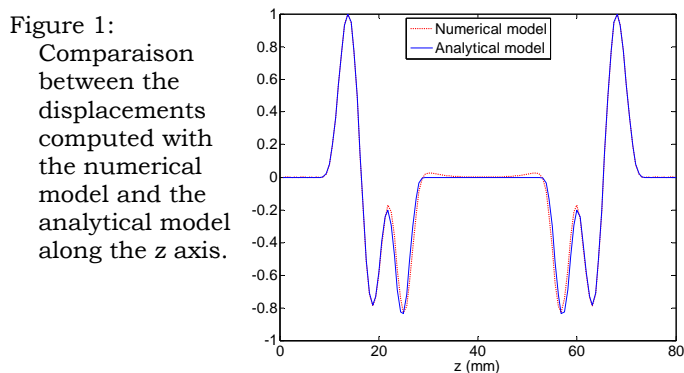


Figure 2:
Axial displacement induced in a medium including a stiffer layer by a force along the z axis.

Jeong-Rock Yoon^{1*}, Joyce McLaughlin², Assad Oberai².

¹Clemson University, O-225 Martin Hall, Box 340975, Clemson, SC 29634-0975, USA;

²Rensselaer Polytechnic Institute, 110 8th Street, Troy, NY 12180, USA.

Background: One of the advertising merits of elastography technique is the possibility of detecting early stage small cancerous tissue. It is believed that 3–5 mm diameter stiffer inclusion is a good model of the early stage cancer. In time harmonic elastography, the detection of this small inclusion is challenging, because the inclusion is quite small relative to the typical wavelength (10–30 mm) of time harmonic wave in a healthy background medium (3 m/sec shear wave speed) for 100–300 Hz excitation. Additionally, in a noisy environment the amplitude drop, which reflects the existence of the stiffer inclusion, should be above noise level in order to be detected. This presentation provides a theoretical bound of the smallest possible size of the detectable inclusion as a function of noise level, contrast ratio of the stiffness and the excitation frequency.

Aims: In a stiffer inclusion, the wave speed becomes bigger, and the amplitude becomes smaller. In the time harmonic elastography, the immediately distinguishable feature in the data is this amplitude drop. This amplitude drop is a function of the size of inclusion, its relative stiffness to the background and the excitation frequency. In this presentation, we derive this relation mathematically assuming a simple model (one single circular inclusion in the scalar Helmholtz equation model) and provide a theoretical bound of the smallest detectable inclusion in a noisy environment.

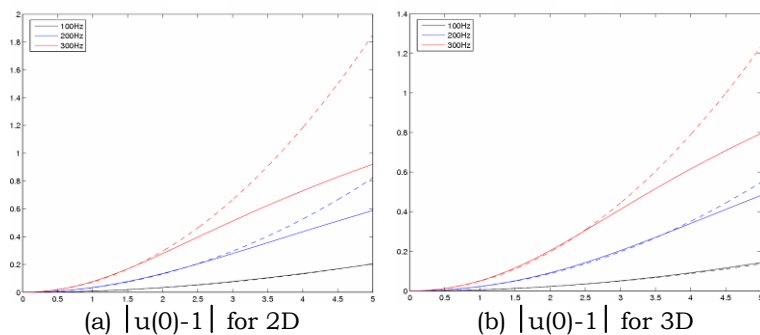
Methods: For simplicity, we assume one circular stiffer inclusion embedded in a homogeneous linear isotropic background medium, both in 2D and 3D. For the single frequency time harmonic excitation, the displacement is the solution of a scattering problem modeled by the Helmholtz equation. Taking advantage of the circular inclusion assumption, this solution can be explicitly represented by a Bessel-Hankel series solution. Then the amplitude drop in the inclusion, which is defined as our “detectability”, shows a nice relation with the size of inclusion, its stiffness and the excitation frequency.

Results: The amplitude drop at the center point of the circular inclusion (our detectability) is represented by a manageable Bessel-Hankel series (the solid lines in Figure 1), and, for small inclusions, it is asymptotically (dotted lines in Figure 1).

$$\frac{\rho\omega^2 R^2}{4} \left(\frac{1}{G_0} - \frac{1}{G} \right) \text{ in 2D, and } \frac{\rho\omega^2 R^2}{6} \left(\frac{1}{G_0} - \frac{1}{G} \right) \text{ in 3D,}$$

where ρ is the overall density, ω is the angular frequency of the excitation, R is the radius of the stiffer inclusion, G_0 is the background shear stiffness and G is the shear stiffness of the inclusion. Interestingly enough, the asymptotic formula is the same for 2D and 3D up to a constant.

Figure 1: Amplitude drop plot versus radius (mm) for a 4-times stiffer inclusion. Solid lines are exact Bessel-Hankel series, and dotted lines are the asymptotic formula for small inclusions. Top line pairs = 300 Hz, middle = 200 Hz and bottom = 100 Hz.



Conclusions: For time harmonic elastography, we derive a formula of the amplitude drop as a function of material parameters of a circular inclusion. With this formula, we can guess the smallest possible inclusion that can be detected with noisy displacement data. For example, allowing 10% noise in the measurement, the smallest detectable rigid inclusions are 6.04/7.40 mm in diameter for 2D/3D with 100Hz excitation, 3.02/3.70 mm with 200Hz excitation and 2.01/2.47 mm with 300Hz excitation. This rigid inclusion estimation provides a lower bound of non-rigid stiff inclusions.

035 RECONSTRUCTIVE ELASTOGRAPHY FOR FINITE-AMPLITUDE DEFORMATIONS.

Walaa Khaled^{1*}, Alexander Arnold², Stefan Reichling², Otto Timme Bruhns², Helmut Ermert¹.

¹Institute of High Frequency, Engineering Building IC, Number: IC6/43; ² Institute of Mechanics, Building IA, Number: IA3/36, Ruhr University Bochum, Universitaetsstr. 150, D-44807 Bochum, GERMANY.

Background and Aims: Conventional diagnostic imaging modalities such as X-ray, computer tomography (CT), ultrasound (US) or magnetic resonance imaging (MRI) are not able to visualize mechanical tissue properties directly. To non-invasively obtain quantitative mechanical properties of tissue, we developed an inverse ultrasound elastography approach based on real-time strain imaging by which the spatial distribution of the relative elastic modulus of tissue can be calculated from measured deformation. If the deformation of the object under investigation is too large, the theory of linear elasticity can no longer be applied. Therefore, in this presentation, a new approach is presented to solve the inverse problem of elastography taking into account fully elastic deformations. The shear modulus distribution in the region of interest is calculated using an iterative method minimizing the difference between the measured and the estimated displacement field. The applicability as well as the performance of the approach is demonstrated by numerical examples and phantom results.

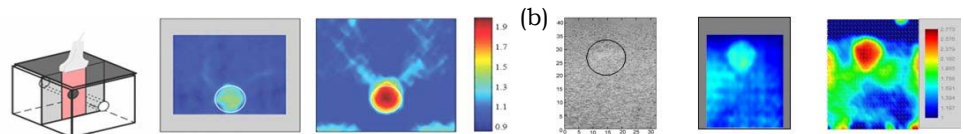
Methods: To simulate a measurement situation from mechanical and acoustical simulations, the noisy displacement field is obtained by adding white Gaussian noise with a noise level of 1% to the calculated displacement field. In the experimental setup, the ultrasonic radiofrequency (RF) data were acquired using a commercially available ultrasound system modified to get RF signals, equipped with a 9 MHz linear array probe and sampled by a conventional digitizer with a desktop PC. Measuring and predicting displacement and strain fields from the known target modulus is also defined as the forward elasticity problem. Once the displacement field is determined, the inverse elasticity problem can be solved using a direct or an iterative approach [1,2]. However, experimental results show that material behavior of soft tissue is strongly nonlinear. Therefore, we developed an iterative approach to solve the inverse problem taking fully elastic deformations into account. There are different possibilities to describe a nearly incompressible, nonlinear elastic material. In our approach, we used a standard mixed finite element method based on the Hu-Washizu principle [3]. The basic idea of this three field variation principle is to introduce a multiplicative split of the deformation gradient into volumetric and isochoric parts. Based on this multiplicative decomposition, decoupled constitutive representations of the free energy function are assumed. In our approach, we used a Neo-Hooke material law for the isochoric part and an iterative method using the weak form of the equilibrium equations. In these methods, the inverse problem is regarded as a minimization problem. The main advantages of these methods are the robustness with respect to the noisy measured data and that only a one-dimensional component of the displacement is needed. One disadvantage is that these algorithms are comparatively time-consuming.

Results: The above mentioned methods were implemented and applied to a number of numerical simulations and experimental data. As only the axial displacement can be measured with an adequate accuracy in real-time, only the one-dimensional simplification of the direct approach was used [1]. For this experimental set-up, both methods yielded only the relative shear modulus distribution. The ratio of the shear modulus between the inclusion and the matrix in the simulation was set to $\mu_{inc}/\mu_{mat} = 2/1$ and both materials were chosen to be nearly-incompressible. Experimental results were similar in the real-time experiment, in which we used tissue mimicking phantoms made of polyvinyl alcohol with different freeze and thaw cycles so that the relative shear modulus ratio was nearly the same as in the simulation above.

Conclusions: These examples demonstrate that both methods are able to localize inclusions, where only the iterative approach can be used for an acceptable quantitative shear modulus distribution value.

Acknowledgements: A project of the Ruhr Center of Excellence for Medical Engineering (KMR), supported by the DFG through grants BR 580/32-1 and ER 94/30-1.

Figure 1: (a) Numerical simulation and (b) experimental results of a hard cylindrical inclusion in a soft phantom.



References:

- [1] Sumi C. et al.: Estimation of shear modulus distribution in soft tissue from strain distribution. IEEE Trans. BME, 42(2):193-202, 1995.
- [2] Oberai A. et al.: Solution of inverse problems in elasticity imaging using the adjoint method. Inverse Problems, 19(2):297-313, 2003.
- [3] Simo, J. & Taylor, R.: Quasi-incompressible finite elasticity in principal stretches, continuum basis and numerical algorithms. CMAME, V 85, 273-310, 1991.

Background: We have been developing several strain-measurement-based shear modulus reconstruction methods [1]. For the multidimensional reconstructions, we have developed the multidimensional cross-spectrum phase gradient method (MCSPGM) [4], multidimensional autocorrelation method (MAM) [2] and multidimensional Doppler method (MDM) [2]. However, to enable us to use the multidimensional reconstruction methods practically, the high accuracy of the lateral/elevational displacements must be obtained. Thus far, we have been developing the displacement-component-dependent regularization method (DCDRM) [3,4], multidirectional synthetic aperture method (MDSAM) [2] and lateral modulation method (LMM) [1,2]. Spatially variant regularization can also be implemented together as in a shear modulus reconstruction [3,5]. Regarding the LLM, we previously confirmed that the uses of the parabolic functions and Hanning windows in the apodization function instead of the Gaussian functions were effective in that the high SNR echo signals can be obtained, particularly around instantaneous frequencies [2,6].

Aims: In this report, the effectiveness of the DCDRM, MDSAM and LMM on the multidimensional shear modulus reconstruction is reported. Regarding the shear modulus reconstruction, the uses of the finite difference method (FDM) and finite element method (FEM) [1] are also compared to each other.

Methods: (i) The effectiveness of the regularization was verified using simulated echo data in a finite region of interest having various echo signal-to-noise ratios. In addition, the accuracies realized by the MDSAM and LMM were compared each other through simulations when changing the beam angles [2]. The transmitting modulation was also performed [2]. (ii) The 3D and 2D shear modulus reconstructions were performed on agar phantoms. Collaborating simulations of reconstructions were also performed.

Results: (i) Using the DCDRM, both the stability and accuracy of the lateral/elevational displacements significantly increased [4]. Our LLM is effective in obtaining the axial displacement with high measurement accuracy as well as the lateral displacement. Our LMM also enables us to use a small aperture size and, therefore, increases the applicable targets. (ii) As shown in the use of DCDRM for 2D reconstruction [4], the shear modulus was reconstructed with high stability. Moreover, LMM increased the reconstruction accuracy. Figure 1 shows the reconstructions obtained on agar phantoms in a lateral compression case, i.e., 2D reconstructions using (a) MCSPGM, (b) MAM and (c) MDM, 1D reconstructions using ratios of (d) lateral strain and (e) axial strain, and (f) 2D reconstruction in a nonmodulated case. See also Table I, i.e., means and SDs evaluated in a stiff inclusion (original relative value, 3.7). When using FEM, which is different from the case of FDM, the regularization using an identity matrix was also available.

Conclusions: The effectiveness of the DCDRM, MDSAM and LLM was verified through simulations and agar phantom experiments. The comparison of the accuracies of the reconstructions using FDM and FEM will also be reported in detail.

References:

- [1] C. Sumi, "Effective shear modulus reconstruction obtained with approximate mean normal stress remaining unknown, *IEEE Trans UFFC*, vol. 54, November issue (in press).
- [2] C. Sumi, "Displacement vector measurement using instantaneous ultrasound signal phase-Multidimensional autocorrelation and Doppler methods," *IEEE Trans UFFC* (in press).
- [3] C. Sumi, *J Med Ultrason*, vol. 34, no. 3, pp. 125-131, 2007.
- [4] C. Sumi, "Regularization for ultrasonic measurements of displacement vector and strain tensor" (under review).
- [5] C. Sumi, "Regularization of shear modulus reconstruction using strain variance" (under review).
- [6] C. Sumi *et al*, "Lateral Gaussian envelope cosine modulation method (4th report) - A breakaway from Fraunhofer approximation," *Proc. of the 2006 Fall Meeting of the Acoustical Society of Japan*, pp. 1035-1036, September 2006 (Japanese).

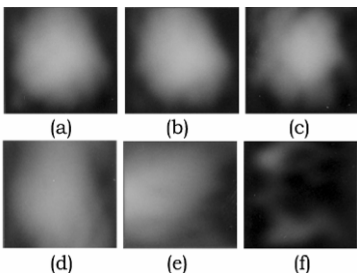


Figure 1: Regularized relative shear modulus reconstructions obtained on an agar phantom. DR=0.70-4.21. ROI=11.3x11.8mm.Original relative value=3.7. Laterally modulated 2D (a) MCSPGM (b) MAM and (c) MDM. 1D reconstructions using ratios of (d) lateral strain and (e) axial strain and (f) Nonmodulated 2D reconstruction.

	Disp./Recon.	2D	Lateral 1D	Axial 1D
MCSPGM		3.75 (0.28)	1.91 (0.11)	1.32 (0.10)
MAM		3.77 (0.28)	2.37 (0.10)	1.26 (0.05)
MDM		3.34 (0.30)	2.20 (0.12)	1.10 (0.03)
Nonmodulated		1.55 (0.18)	1.33 (0.16)	1.60 (0.11)

Table 1: Means and SDs of reconstructed shear moduli.

005 **CHARACTERIZATION OF THE MECHANICAL BEHAVIOR OF HUMAN LIVER.**

Edoardo Mazza^{1*}, Marc Hollenstein¹.

¹Mechanical Engineering Department, Swiss Federal Institute of Technology, 8092 Zurich, SWITZERLAND.

Aims: The characterization of the mechanical response of soft human organs provides essential information for surgery simulation and might complement existing methods for diagnosis. This presentation summarizes the results of our clinical studies on the mechanical behavior of human liver. Intra-operative mechanical measurements were performed on 16 livers. The scatter of the observed tissue response is analyzed considering the uncertainties related to the aspiration experiment as well as the inhomogeneity of the tissue's microstructure.

Methods: Human livers were tested *in vivo*, during open surgery under sterile conditions, using the aspiration device. Measurement results from 6 healthy organs were used to fit the parameters of a non-linear visco-elastic constitutive model. 10 diseased organs were tested before resection, tissue samples were removed after the operation and histological exams were carried out. The aspiration device used for the intra-operative mechanical measurements is shown in Figure 1. Mechanical parameters for the constitutive model of human liver were determined through an inverse finite element analysis, matching the time history of the average tissue deformation of the 6 healthy organs. The influence of the experimental errors has been investigated by numerical calculations, and the corresponding uncertainty of the mechanical parameters quantified. For the resected organs, liver tissue (including the adjacent organ capsule) was excised from the site of measurement using a surgical scalpel. Tissues were immersion-fixed in 4% neutral-buffered formalin, embedded in paraffin, sectioned and stained with haematoxylin and eosin using standard histological techniques. The proportion of connective tissue in the liver tissue samples was quantified in serial sections stained with Sirius red.

Results: The parameter of the hyperelastic-viscoelastic constitutive equations was determined and the predicted mechanical response compared with data obtained from *in vivo* indentation tests on human liver (Carter et al., 2001, Medical Image Analysis 5, 231-236). The relationship between the mechanical parameters and various pathologic conditions affecting the tissue samples has been quantified, with fibrosis leading to a response up to 3 times stiffer when compared with normal tissue. Increased stiffness can be detected by digital palpation (increased "consistency") and may suggest the presence of a tumor. Our observations indicate that stiffness increase cannot be attributed to the tumor tissue itself, but rather to the fibrotic stroma that often arise within or adjacent to the tumor. Furthermore, our results confirm a direct proportionality between stiffness and connective tissue percentage (Figure 2).

Conclusions: The present experience confirms the feasibility of clinical studies with intra-operative aspiration experiments. The data allowed fitting a constitutive model for the mechanical behavior of human liver *in vivo*. Quantitative observations were obtained on the relation between mechanical behavior and tissue histology.

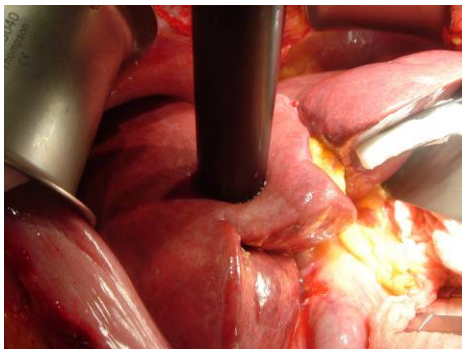


Figure 1: Aspiration experiment

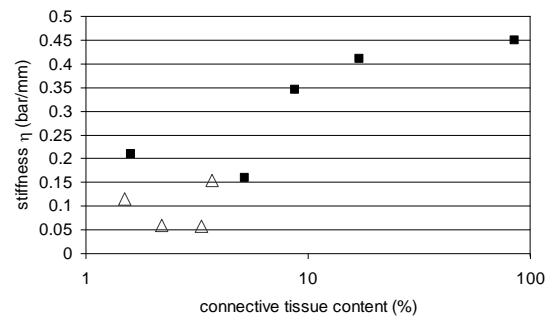


Figure 2: Stiffness (η) vs. connective tissue content. Triangles = normal liver tissue; Squares = carcinoma/fibrosis.

008 **BREAST LESION CHARACTERIZATION AND DIFFERENTIATION BY A MECHANICAL IMAGER: PRELIMINARY CLINICAL RESULTS.**

Vladimir Egorov^{1}, Suren Airapetian¹, Stanley B. Pollak² and Armen Sarvazyan¹.*

¹Artann Laboratories, 1459 Lower Ferry Rd., Trenton, NJ 08618, USA; ²Mercy Medical Center, Rockville Centre, NY 11510, USA.

Background: Mechanical Imaging (MI) yields 3-D map of tissue elasticity and provides quantitative characterization of a detected pathology [1]. MI is based on reconstructing the internal structure of soft tissues using the data obtained by a force sensor array pressed against the examined site. The changes in the surface stress patterns as a function of displacement, applied load and time provide information about elastic composition and geometry of the underlying tissue structures. In the previous International Tissue Elasticity Conference, we presented results of laboratory testing the MI device on the tissue models and breast phantoms which demonstrated accuracy of Young's moduli measurements to within 5 – 35% of their calibrated values, inclusion sizes to within 5 – 10%, and repeatability of elasticity measurements in the range of 5 – 15% [2].

Aim: The objective of this study is the clinical validation of the Breast Mechanical Imager (BMI) for breast lesion characterization and differentiation.

Methods: The BMI includes a probe with pressure sensor array, an electronic unit, and a touch-screen laptop computer (Medical Tactile, Inc., CA, USA). We developed algorithms which provide real time assessment of breast lesion features such as size, shape, cross-section area, consistency/hardness, strain hardening, mobility, margin and heterogeneity [2].

Results: Preliminary clinical results for 176 cases in an on-going clinical study demonstrated that current sensor sensitivity of 0.03 kPa and data acquisition rate 20 frames per second provide reliable 3-D image formation of underlying breast tissue abnormalities with increased hardness and calculation of lesion features. Characteristic elasticity patterns and lesion feature combinations for specific breast pathologies were identified. The range of lesion linear sizes evaluated by BMI is in reasonable agreement with lesion sizes evaluated by conventional ultrasound. Malignant breast lesions (histologically confirmed) had: (1) increased Young's modulus, compared to benign lesions; (2) increased heterogeneity of the surrounding tissue, compared to the tissue of the patients with benign lesions; and (3) decreased mobility compared to benign lesions.

Conclusions: Preliminary clinical results have demonstrated possibility of real time lesion characterization and differentiation as benign or malignant with the use of BMI with a quantitative evaluation of diagnostically relevant features of the lesion, such as size, shape, hardness, heterogeneity, and mobility. The BMI is superior to the Clinical Breast Examination, one of the current means for breast cancer screening according to the guidelines of American Cancer Society. The BMI has a potential to be positioned as an adjunct to mammography and a prescreening device for breast cancer detection.

Acknowledgements: This work is supported by NIH grant R44 CA091392.

References:

- [1] A. Sarvazyan, "Mechanical Imaging: A new technology for medical diagnostics." *Int. J. Med. Inf.*, 1998, vol. 49, pp. 195–216.
 - [2] V. Egorov, A. Sarvazyan. Breast tissue characterization by means of surface stress patterns analysis. Abstracts of 32nd International Symposium on Ultrasonic Imaging and Tissue Characterization, Arlington, Virginia, USA, May 16–18, 2007, p. 45.
-

019 **ULTRASOUND ELASTICITY IMAGING OF INTESTINAL FIBROSIS IN RATS.**

Jonathan M. Rubin^{1}, Peter Higgins², Laura Johnson², Joel C. Joyce², Congxian Jia³, Kang Kim³.*

¹Radiology, ²Internal Medicine, ³Biomedical Engineering Departments, University of Michigan, Ann Arbor, MI USA.

Background: Intestinal fibrosis is a common result of cycles of inflammation and healing in Crohn's disease. Intestinal fibrosis can lead to strictures and intestinal obstruction, for which there is no medical therapy. Patients with severe stricturing require repeated surgical resection, and rare patients need intestinal transplantation. Current diagnostic tests such as CT or MRI scans do not adequately differentiate between inflammation and fibrosis.

Aims: To evaluate the ability of ultrasound elasticity imaging (UEI) to determine the degree of intestinal fibrosis as a means of assessing inflammatory bowel disease (IBD) for therapy and progression. Given the prior history of elasticity imaging to measure the development of fibrosis in other pathological conditions such as DVT (1–4), we wanted to see if UEI could perform the same function in a rat model of Crohn's disease.

Methods: A Philips IU22 ultrasound scanner (Philips Ultrasound, Bothell, WA, USA) with a 12.0 MHz linear array scanhead was used to directly image and deform the distal sigmoid colons in female Lewis rats (150–180g) treated for up to 6 weeks per rectum with either 2,4,6-trinitrobenzenesulfonic acid (TNBS) or phosphate buffered saline (PBS) as controls. TNBS produced bowel inflammation is a well known model for IBD. The bowel was deformed in a controlled manner using a mechanical device attached to the scanhead. The abdomen was initially preloaded to remove any overlying bowel gas. The UEIs were then generated from the digitally acquired ultrasound radiofrequency (rf) signals, which were processed frame-to-frame using a 2-D correlation-based phase-sensitive speckle tracking algorithm. To account for deforming force differences, all strain measurements were normalized to the average strain between the skin surface and the spine. After sacrifice, the colon was removed and the Young's moduli of the distal sigmoid colons were directly measured using a specially designed elastometer (Artann Laboratories, Lambertville, NJ, USA). Values are quoted as means and standard deviations.

Results: We studied 5 control PBS rats and 5 diseased TNBS rats. The normalized strain in the control rats was -2.69 ± 0.55 and -0.48 ± 0.12 for the treated rats ($p < 0.001$, one-tailed t-test). The Young's moduli were 7.4 ± 2.0 (kPa) for the controls and 34.6 ± 26.6 (kPa) for the treated rats ($p < 0.05$, one-tailed t-test).

Conclusions: Intestinal fibrosis is a common complication of IBD. The ability to differentiate fibrosis from inflammation in IBD would have important consequences for treatment. Based on other disease models, such as deep venous thrombosis, UEI should be able to make this differentiation, and these preliminary experiments are consistent with this hypothesis.

Acknowledgements: Supported in part by NIH R21 CA109440.

References:

- [1] Emelianov SY, Chen X, O'Donnell M, Knipp B, Myers D, Wakefield TW, Rubin JM. Triplex ultrasound: elasticity imaging to age deep venous thrombosis. *UMB* 2002;28:757-767.
 - [2] Xie H, Kim K, Aglyamov SR, Emelianov SY, Chen X, O'Donnell M, Weitzel WF, Wroblewski SK, Myers DD, Wakefield TW, Rubin JM. Staging deep venous thrombosis using ultrasound elasticity imaging: animal model. *Ultra Med Biol* 2004;30:1385-1396.
 - [3] Xie H, Kim K, Aglyamov SR, Emelianov SY, O'Donnell M, Wroblewski SK, Myers DD, Wakefield TW, Rubin JM. Correspondence of ultrasound elasticity imaging to direct mechanical measurement in aging DVT in rats. *Ultrasound Med Biol* 2005;31:1351-1359.
 - [4] Rubin JM, Xie H, Kim K, Weitzel WF, Emelianov SY, Aglyamov SR, Wakefield TW, Urquhart AG, O'Donnell M. Ultrasound elasticity imaging of acute and chronic DVT in humans. *JUM* 2006;25:1179-1186.
-

Background: Elastography can provide diagnostic information of breast masses which is otherwise not available in routine clinical practice. This information can improve both sensitivity and specificity of ultrasound in characterizing breast masses [1–3].

Aims: To determine the clinical utility of a real-time robust elastographic technique in detection and characterization of breast masses, and to present additional results from a clinical trial.

Methods: 193 breast lesions were evaluated with a real time free hand elastography technique which displays both the B-mode image and its corresponding elastogram. Elastograms were obtained on a commercially available ultrasound system (Antares, Siemens Ultrasound, USA). This system uses a speckle tracking to generate the elastogram. The system displays the B-mode image and corresponding Elastogram simultaneously in real-time. The algorithm is sensitive for a 0.1% strain and uses temporal persistency strategy to enhance the descriptive pattern in elastograms. With this sensitivity, no additional equipment is required other than a standard ultrasound probe. Normal patient motion from respiration is adequate in most patients to generate the elastogram. If this was not sufficient, slight rhythmic compression was applied. Real-time imaging allowed for rapid determination of the compression needed. The lesions were pathologically proven by FNA, core biopsy or surgical biopsy. The lesions included both benign (cysts, complex cysts, fibroadenomas, lipoma, epidermoid cyst, hematoma) and malignant lesions. The largest dimension of a lesion obtained on an image pair (B-mode image and its corresponding elastogram) was used to characterize the lesion as benign or malignant. In the image pair, if the largest dimension of the lesion in the elastogram was equal to or larger than the corresponding dimension in the B-mode image, the lesion was characterized as malignant. If the largest dimension of the lesion in the B-mode image was larger than the corresponding dimension in the elastogram, the lesion was characterized as benign.

Results: 150 benign and 43 malignant lesions were evaluated. Of the 150 benign lesions, 146 demonstrated an elastographic image that was smaller in length than the B-mode image. Of the 43 malignant lesions, all demonstrated an elastogram image larger in length than the B-mode image. (Sensitivity: 100%, Specificity: 96%). Cystic lesions demonstrated a bulls-eye appearance. 10 lesions which appeared solid on B-mode ultrasound and had a bulls-eye elastogram were confirmed to be complicated cysts by FNA.

Conclusions: Initial results of adding a real-time breast elastography in the characterization of breast lesions demonstrate that the additional information provided by Elasticity Imaging can improve characterization of breast lesions over B-mode alone. If these results can be confirmed in a large multi-center trial a significant number of biopsies presently performed on benign lesions can be eliminated.

Acknowledgements: This work was supported in part by an equipment loan by Siemens Ultrasound.

References:

- [1] Barr RG. Initial Results of Breast Real-Time Elasticity Imaging to Characterize Lesions. RSNA 2006.
- [2] Svensson WE et al. Elasticity Imaging of 67 Cancers and 167 Benign Breast Lesions Shows That It Could Halve Biopsy Rates of Benign Lesions. Proceedings of the 4th Int'l Conference on the Measurement and Imaging of Tissue Elasticity, Lake Travis, Texas, October, 2005, p. 87.
- [3] Garra, B. S. et. al.: Elasticity of Breast lesions: Initial clinical results. Radiology, Vol. 202, pp 79–86, 1997.

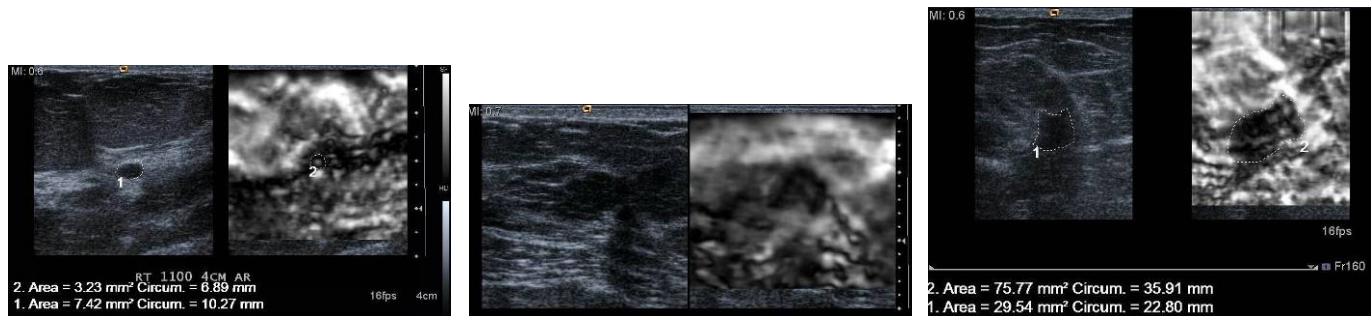


Figure 1: (a) Simple Cyst (b) Fibroadenoma (c) Invasive Ductal Carcinoma

059 **ULTRASOUND ELASTOGRAPHY FOR THE NON-INVASIVE CHARACTERIZATION AND FOLLOW-UP OF ABDOMINAL AORTIC ANEURYSMS AFTER ENDOVASCULAR REPAIR.**

J. Fromageau^{1}, S. Lerouge², R.L. Maurice¹, G. Soulez³, and G. Cloutier¹.*

¹Laboratory of Biorheology and Medical Ultrasonics, ²Laboratory of Endovascular Biomaterials, University of Montréal Hospital Research Center, Montréal, Québec, H2L 2W5, CANADA;

³Radiology Department, University of Montréal Hospital, Montréal, Québec, H2L 4M1, CANADA.

Background: Aortic Abdominal Aneurysm (AAA) is an asymptomatic disease affecting about 7% of people over 60 years old in western countries. Aneurysm enlargement can lead to aneurysm rupture and death. The decision to treat AAA is based on anatomical parameters such as the size of the aneurismal sac, its shape and its growth. Presently, mechanical properties of the aneurysm are not available by non-invasive methods. Endovascular aneurysm repair (EVAR) using stent-graft (SG) is one of the therapeutic options, offering the advantage of being minimally invasive but requires long-term follow-up to detect complications such as persistent blood flow in the aneurysm (endoleak).

Aims: In this work, we evaluated the potential of ultrasound elastography to characterize the mechanical properties of AAA before and after EVAR.

Methods: As a first step, elastography was tested to investigate the difference in elasticity of the arterial wall in a healthy section of the vessel and in the aneurismal sac (AS). For this purpose, aneurysms were created in 6 dogs by suturing a venous patch on both common iliac arteries (12 aneurysms). RF images of the arterial wall in the AS and in the neck of the aneurysm (healthy iliac artery) were acquired over several cardiac cycles. Deformations were cumulated during the whole diastolic phase, and compared for these two regions. As a second step, elastography was used to follow the healing process of the AS after EVAR in 17 dogs. Three months following the implantation of the SG, RF images were acquired over several cardiac cycles from within the AS deformation. The images were intended to detect endoleaks and to evaluate the ratio proportion of solid thrombus. Thereafter, deformation on the arterial wall of the aneurysm was calculated and correlated with the occurrence and magnitude of endoleak. Results obtained with elastography were compared with other imaging modalities (X-ray angiography, Doppler ultrasound).

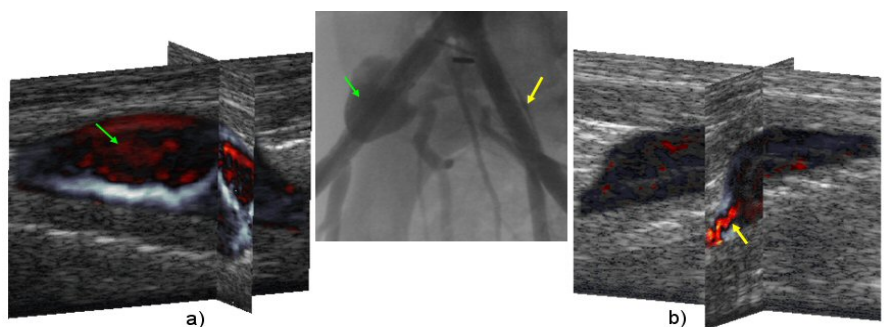
Results: The first study showed that there was a significant difference in deformation between the healthy artery and the venous patch. Cumulated strain was higher in the artery ($p < 0.001$), confirming that, at systemic pressure, veins are from 1.3 to 3 times less compliant than arteries [1]. The second part of the study revealed the ability to detect solid thrombus in the AS from qualitative elastograms (Figure 1). Deformation estimated within the aneurismal arterial wall permitted detection of the absence of leak ($p < 0.001$), but not differentiation of large endoleaks from smaller ones ($p = 0.08$). Kappa test showed that elastography was in good agreement with other imaging modalities, with a $\kappa = 0.76$ for X-ray angiography and $\kappa = 0.8$ for Doppler ultrasound.

Conclusions: This work shows that elastography can provide valuable information for AAA diagnosis. Difference of deformation in the healthy artery and the aneurysm wall could afford mechanical information to evaluate the risk of rupture. Regarding follow-up after EVAR, elastography can provide useful information complementary to other imaging modalities; it especially gives unique findings to characterize solid thrombus organization in the AS.

References:

[1] Salacinski et al. "The mechanical behavior of vascular grafts: a review", *J Biomater.Appl.*, vol. 15, (3), 2001.

Figure 1: X-ray angiogram and elastogram for one dog. An important leak (green arrows) is observed on the right artery (a), and the solid thrombus (light and dark grey area) is clearly visible on the elastogram. Left artery (b) is almost filled with a solid thrombus but a small leak (yellow arrows) is observed both on angiogram and elastogram. (see CD for color)



011 **THE FEASIBILITY OF USING POROELASTOGRAPHIC TECHNIQUES FOR THE STUDY OF LYMPHEDEMA *IN VIVO*.**

Raffaella Righetti^{1*}, Brian S. Garra², Christina M. Chant², Louise M. Mobbs², Jonathan Ophir¹, Thomas A. Krouskop³.

¹The University of Texas Health Science Center at Houston, Houston, TX, USA; ²The University of Vermont College of Medicine, Burlington, VT, USA; ³Baylor College of Medicine, Houston, TX, USA.

Background: Lymphedema is a significant relatively common condition involving an abnormal accumulation of lymphatic fluid in the interstitial space that causes swelling, most often in the arm(s) and leg(s). Lymphedema can be congenital or develop following cancer treatment or cancer metastasis. Common methods of evaluation of lymphedema are mostly qualitative, making it difficult to reliably assess its severity, a key factor in choosing the appropriate treatment. In this presentation, we investigate the feasibility of using novel poroelastographic techniques to differentiate between lymphedematous and normal tissues.

Methods: In this preliminary study, poroelastograms and effective Poisson’s ratio time–constant elastograms were generated from the leg and/or arm subcutis of five normal volunteers and seven volunteers having lymphedema. Data were acquired at the University of Vermont using the Philips HDI-1000 system with a 7.5 MHz transducer array, 50% bandwidth, 1 mm beamwidth and a 20 MHz sampling frequency. The RF data were then sent to The University of Texas, where they were used to generate poroelastographic images [1] and for statistical analyses.

Results: Figure 1 shows the results of a poroelastography experiment performed on the leg of a normal volunteer (a) and the results of a poroelastography experiment performed on the leg of a volunteer having lymphedema (b). In general, in all normal cases, we did not observe any statistically significant time-dependent changes occurring during the time that data were acquired. In all lymphedema cases, significant spatial and temporal changes were observed. The time constant values obtained from the lymphedematous tissues were found to be statistically significantly different from those obtained from normal tissues (using standard t-tests and a chi-square tests for histogram comparison) (Figure 2).

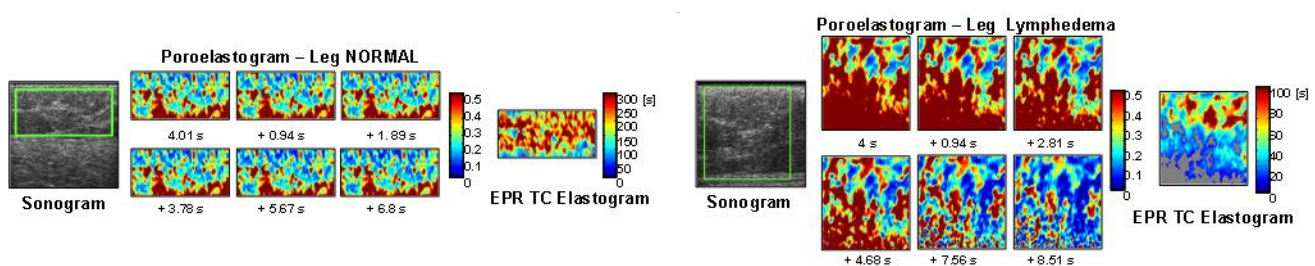
Conclusions: These preliminary results suggest that it may be feasible to generate poroelastograms from different lymphedematous tissues *in vivo*. They also suggest that lymphedematous tissues exhibit a temporal poroelastographic behavior that is significantly different from the behavior that characterizes normal tissues. Thus, poroelastographic techniques may be useful in the diagnosis and evaluation of lymphedema.

Acknowledgements: This work was supported by NCI Program Project PO1-CA64597-13 and by funding from John S. Dunn foundation to The University of Texas Health Science Center at Houston.

References:

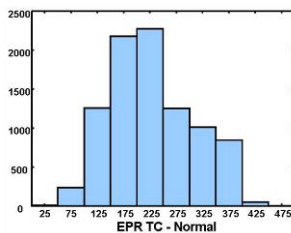
- [1] Righetti R, Ophir J, Krouskop TA. A method for generating permeability elastograms and Poisson’s ratio time-constant elastograms. *Ultras. Med. Biol.*, 31(6): 803–816 (2005).

Figure 1: (a)

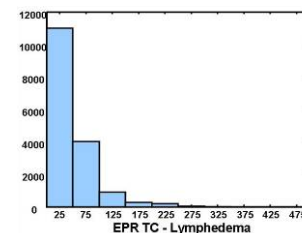


(b)

Figure 2: (a)



(b)



Background: Ultrasound muscle strain imaging (MSI) is potentially a powerful tool to diagnose cardiac and skeletal muscle disorders in humans. We have used MSI to assess mechanical properties of contracting skeletal muscle at several different scales from isolated single fibers and excised whole muscle to *in vivo* human forearm and leg [1,2]. Even at high frame rates, however, large muscle contractions can lead to poor estimates of displacement and strain. Speckle tracking error can be largely attributed to strain decorrelation and out-of-plane motion particularly at peak strain rates. Such error, which usually occurs early in the contraction, propagates through the accumulation process often corrupting total displacement and strain estimates. We introduce a weighted time domain least-squares spline to improve tracking results and dramatically reduce accumulation error.

Aims: Improve tracking results and reduce accumulation error during MSI. We implemented a constrained, least-squares spline to fit tracking estimates based on known accumulation displacements.

Methods: A 2D phase sensitive speckle tracking algorithm [3] was used to calculate frame-to-frame displacements in both a simulated muscle contraction, as well as an electrically-induced contraction in the human *flexor digitorum superficialis* (FDS). The weight was assigned to each track based on both the magnitude of the correlation coefficient and its spatial gradient [4]. Displacements were referenced to the original coordinates and integrated to produce accumulated values. The shift between the initial frame and a frame at the end of the contraction was also calculated to determine the “true” total displacement. Next, the referenced frame-to-frame displacements were fit with a weighted least-squares spline and an integral constraint determined from the “true” displacement estimate. Tracking errors were compared based on known displacements used in the simulations. Simulations were performed using Field II [5] with a linear array centered at 5.5 MHz, focused at 20mm, element spacing of 0.27mm, and height of 5mm. Fifty channels were used for imaging a simulated muscle contraction (peak lateral strain of 10%) sampled at 250Hz.

Results: The spline algorithm reduced accumulation error (spatial average) in both the transverse (56.1%) and lateral (80.8%) directions. It also corrected for accumulation error apparent in an electrically induced contraction of the human FDS muscle captured with a clinical scanner (Philips iU22) at 363Hz.

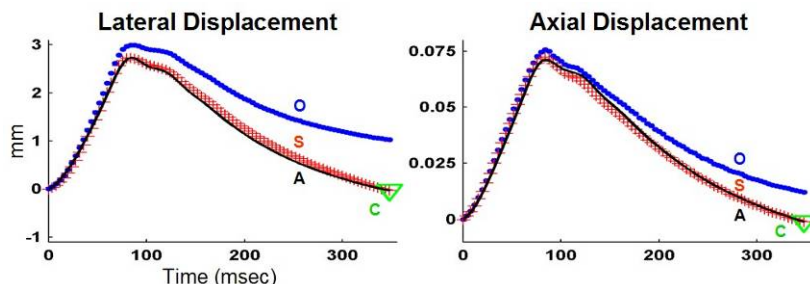
Conclusions: The spline algorithm proved effective in reducing tracking error in simulations and human forearm contractions. This relatively simple approach may be important for the accurate diagnosis of muscle disorders using ultrasound MSI.

Acknowledgements: Support from NIH grants HL-68658, DE-07057; John D'Errico for providing spline source code.

References:

- [1] R.S. Witte, D. E. Dow, R. Olafsson, Y. Shi, M. O'Donnell. "High resolution ultrasound imaging of skeletal muscle dynamics and effects of fatigue," Proc. 2004 IEEE Ultrasonics Symposium 764-767, 2004.
- [2] R.S. Witte, K. Kim, B. J. Martin, M. O'Donnell. "Effect of fatigue on muscle elasticity in the human forearm using ultrasound strain imaging," Proc. 28th IEEE EMBS in New York, SaA15.5 4490-4493, 2006.
- [3] M. A. Lubinski, S. Y. Emelianov, and M. O'Donnell, "Speckle tracking methods for ultrasonic elasticity imaging using short-time correlation," IEEE Trans. Ultrason., Ferroelect., Freq. Contr., vol. 46, no. 1, pp. 82-96, 1999.
- [4] M. O'Donnell, X. Chen, K. Kaluzynski, S.Y. Emelianov, and A.R. Skovoroda, "Strain Magnitude Estimation Based on Adaptive Incompressibility Processing," Proc. 2001 IEEE Ultrasonics Symposium 1643-1646, 2001.
- [5] J. A. Jensen and N. B. Svendsen, "Calculation of pressure fields from arbitrarily shaped, apodized, and excited ultrasound transducers," IEEE Trans. Ultrason., Ferroelec., Freq. Contr., vol. 39, no. 2, pp. 262-267, 1992.

Figure 1: Simulation results for lateral and transverse (axial) displacements at one muscle position: original track (O), actual displacements (A), spline-adjusted (S) and integral constraint (C) based on calculated displacement between first and last frame.



108 ELASTOGRAPHIC EVALUATION OF BREAST LESIONS: ADDITIONAL PERFORMANCE RESULTS FROM BLINDED READERS.

Brian S. Garra^{1*}, Louise M. Mobbs², Christina M. Chant¹, Susan C. Harvey¹, Jonathan Ophir³.

¹University of Vermont College of Medicine, Radiology Department, Burlington, VT, USA; ²Fletcher Allen Health Care, Burlington, VT, USA; ³The University of Texas Health Science Center Houston, Houston, TX, USA.

Background: Elastography appears to be gaining momentum as a tool for diagnosis of breast masses. We have previously reported results of blinded readings of clinical elastograms by a single observer. We now report on results from a larger number of patients.

Aims: The goal of this study is to demonstrate the performance of elastography as a stand-alone tool for diagnosis of solid breast lesions. These results, plus the results of a study where elastography is combined with mammography and state-of-the-art ultrasound, will be used to better establish the role of breast elastography in the diagnostic workup of patients with masses.

Methods: 220 patients with solid breast masses scheduled for biopsy were evaluated with elastography. A variety of elastographic systems have been used, including computer-controlled compression with the transducer clamped in a compression device, a hand-held transducer with manually applied compression, and a real-time elastographic system with a hand-held transducer and manual compression. Ultrasound systems used in the study included a Diasonics Spectra, Philips HDI 1000 and Ultrasonix Sonix RP500. Image processing using wavelet filtration was performed on some elastograms to improve their quality. Three to ten images of each lesion were viewed by an observer blinded to the clinical and pathology data. The observer scored his observations on a 100-point scale with respect to the following criteria: overall suspicion for cancer, lesion hardness relative to surrounding parenchyma, border irregularity and lesion size difference between the elastogram and a matched sonographic image. A second observer is also examining the images using the same methodology and those results, when complete, will be compared with the first observer. The results were analyzed using scatter plots and ROC analysis. To combine more than one feature, linear discriminant analysis was used to develop a classifier so that an ROC curve could be generated.

Results: For overall level of suspicion for cancer, the $A_z = 0.854 \pm 0.033$ and, when only patients with lesions visible on the elastogram were used, $A_z = 0.90 \pm 0.028$. Using only patients with visible lesions excluded approx. 12% of the lesions. Examining the missed cancers showed that 18% of ductal carcinomas were missed, but 50% of lobular cancers were not correctly classified. The lesion hardness estimates, size difference estimates and measured size differences were less effective, giving A_z values between 0.79 and 0.84. Using lesion hardness and size difference together gave an $A_z = 0.86$, similar to that of our earlier work [1]. No visible cancer had a hardness score < 50 (softer), but 15% of benign lesions had scores < 50 . The average maximum diameter of visible cancers was 15.8 mm (range 4-40 mm), whereas the non-visible cancers had a diameter of 14 mm (range 5-19 mm). Cancers thought to be benign had an average diameter of 21.8 mm compared to correctly classified cancers that had a mean diameter of 16.2 mm.

Conclusions:

1. It may be possible to use elastography to reduce the number of benign lesions biopsied by approximately 15% using a hardness score of 50 as the cutoff.
2. Small cancers can be detected using elastography. It appears that large cancers are harder to identify.
3. Human observers using a subjective assessment of suspicion for cancer perform well compared to quantitative measures.
4. Elastography is more accurate when only applied to lesions visible on both sonography and elastography. Hopefully, the percentage of lesions not seen on elastography will decline as better instrumentation becomes available.

Acknowledgements: This work was supported by NIH Program Project P01-CA64597-13.

Reference:

- [1] Garra BS, Cespedes EI, Ophir J, et al. Elastography of breast lesions: initial clinical results. *Radiology* 1997;202(1):79-86.
-

112 DEVELOPMENT OF ULTRASOUND PLATFORM FOR THE EVALUATION OF THE PLANTAR SOFT TISSUE PROPERTIES.

Jian-Gang Chen¹, Yongping Zheng^{1*}, Hang-Yin Ling¹, Yan-Ping Huang¹.

¹Health Technology and Informatics Department, Hong Kong Polytechnic University, Hong Kong, CHINA.

Background: Currently, foot problems are becoming one of the most prevalent diseases influencing our daily lives, especially in the elderly [1]. People with foot problems may experience foot lesions either consciously or unconsciously, such as with diabetic feet. It has been widely known that foot lesions cause changes in plantar tissue properties. Therefore, any abnormalities of plantar tissue properties would be useful for diagnosis of foot lesions [1]. Previously, we have developed an ultrasound indentation technique [2] for the measurement of the stiffness of plantar foot tissues [3]. However, the measurement using this device requires the subjects to pose their feet at a specific posture and cannot be conducted with the subjects in a standing position. This limitation hinders the device from being more widely used.

Aims: To develop an easy-to-use ultrasound platform for the evaluation of the mechanical properties of plantar tissues.

Methods: An ultrasound (US) platform, consisting of an embedded ultrasound transducer connected in series with a small circular silicone layer, was developed to measure the mechanical properties of human plantar tissues (Figure 1). The force exerted by the subjects was determined based on the deformation of the silicone layer which was measured by ultrasound. The deformation of the soft tissue was also obtained from the ultrasound signals. Tissue stiffness was then extracted from the force-deformation curves. To demonstrate the feasibility of the ultrasound platform, the stiffness of eight phantom feet with different ratios of silicon gel to oil was tested by this new system. The moduli of the phantom feet were also measured by an ultrasound indentation system [2].

Results: The stiffness of the phantom feet was successfully distinguished by the ultrasound platform. Results showed that the phantom stiffness measured by the platform had a linear correlation ($R^2=0.89$) with the corresponding modulus obtained using the ultrasound indentation method (Figure 2). Therefore, using the correlation factor between the tissue stiffness and modulus, the tissue stiffness was able to be measured by the current US platform, and the tissue modulus could be obtained. The repeatability of the measurement using the platform was very high with ICC of 0.984.

Conclusions: The results demonstrated that the tissue stiffness could be measured reliably by the presented method. The ultrasound platform offers a more convenient and cost-effective way to measure the plantar tissue properties.

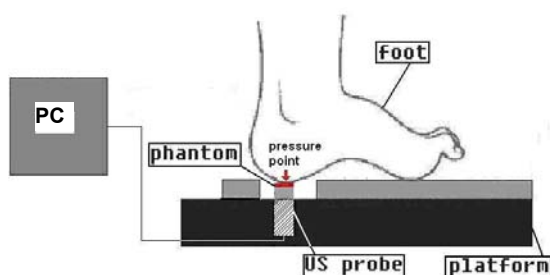


Figure 1: A schematic diagram of the US platform for plantar soft tissue assessment.

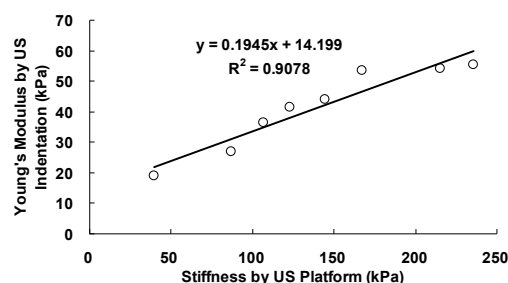


Figure 2: Correlation between stiffness measured by the platform and modulus measured by indentation.

Acknowledgements: Supported by Hong Kong Innovation and Technology Commission (GHP/061/05).

References:

- [1] Whitney K. Foot deformities, biomechanical and pathomechanical changes associated with aging including orthotic consideration, Part II. *Clin Podiatr Med Surg* 20:511-526, 2003.
- [2] Zheng YP, Mak AFT. An ultrasound indentation system for biomechanical properties assessment of soft tissues *in-vivo*. *IEEE Trans Biomed Eng* 43:912-918, 1996.
- [3] Zheng YP, Choi YKC, Wong K, Chan S, and Mak AFT. Biomechanical assessment of plantar foot tissue in diabetic patients using an ultrasound indentation system. *Ultrasound Med Biol* 26: 451-456, 2000.

Background: We have been developing several strain-measurement based shear modulus reconstruction methods, e.g., 1-dimensional (1D) [1,2] and multidimensional (2D and 3D) [2,4]. A statistical CNR defined by Bilgen [5] is often used to evaluate the contrast-to-noise ratio in an image of a measured axial strain. That is, the CNR is used to evaluate the detectability of the inhomogeneity of tissue elasticity. Hereafter, the CNR is referred to as CNR1. We also proposed a deterministic CNR (CNR2) for evaluating the images of the shear modulus reconstructions [1]. The CNR2 considers the respective generations of the stress concentration and stress weak regions in front of and behind the stiff and soft regions, whereas the CNR1 does not. In the CNR1, the evaluation of mean strain is performed in the surrounding region. We reported [1] an increase in the CNR2 for a 1D reconstruction by strain ratio [1,2] by setting the reference point properly, i.e., in the stress concentration or stress weak region.

Aims: Occasionally, the axial strain image can also be dealt with as an image of the relative shear modulus like the axial strain ratio image [1]. In this report, to enable the comparison of CNR of the axial strain with that of the 1D shear modulus reconstruction, the CNR1 is used, although such means are evaluated. Thus, here, the CNRs are also used to evaluate their measurement/reconstruction accuracies. From the results of CNR2 [1], the imaging of the axial strain ratio will yield a larger CNR than that of the axial strain. That of the inverse of the shear modulus (strain ratio) is also compared with them.

Methods: Numerical simulations are performed for two cases, i.e., Case A in which neither the occurrence of the stress concentration nor stress weak region is assumed, and Case B in which one of them occurs practically. In both cases, the CNR1s of both Cases are compared each other, i.e., between those of the axial strain, axial strain ratio, inverse of the axial strain ratio. The displacement data in both Cases are generated numerically. No noise-filled and noise-filled (various SNRs) cases are also determined for both Cases. For the noise-filled cases, to stabilize the statistical evaluations, 100 independent white noises are used. For comparison, the CNR1 of the strain and those [6] of the strain ratio and the inverse of the strain ratio that are theoretically expressed for Case A using the means and variances of strains in the inclusion and the surrounding region are also shown.

Results: Only for the noise-filled case (SNR of axial displacement, 40 dB) of a twofold stiff inclusion case, CNR1s vs the reference position are shown in Figure 1 (other SNRs omitted). All CNR1s obtained numerically of the axial strain, strain ratio and inverse of strain ratio in Cases A and B, and those obtained theoretically in Case A are shown. As shown, in the ideal Case A, the theoretically evaluated CNR1s of the axial strain, strain ratio and inverse of strain ratio coincide well with those obtained numerically. In Case A, the CNR1s of the axial strain ratio and inverse of strain ratio are smaller than those of the axial strain, as confirmed in Reference [6]. However, in the practical Case B, the CNR1s of the axial strain ratio and inverse of strain ratio are larger than that of the axial strain, particularly by setting the reference point properly. Moreover, because mean strains, -3.57 vs -5.08×10^{-3} and variances, 1.84 vs 0.95×10^{-7} , the CNR1 of the inverse of strain ratio is larger than that of the strain ratio as in Case A [6]. Also note that the increases in CNR1s are smaller than those in CNR2 [1]. Such results were also obtained in other SNR cases.

Conclusions: The evaluations of their CNR1s clarified that, for local tumors, the evaluations of means and variances of strains in the tumor and the surrounding region is very effective for determining which strain ratio or the inversion is imaged. The imaging of strain ratio is also more effective than the axial strain. Thus, robust 1D methods on the basis of the strain ratio [1] with respect to strain measurement noise are also effective. As confirmed by CNR2 [1], we should find suitable reference regions that are homogeneous and exist in the neighborhood of the target by viewing B-mode and strain images.

References:

- [1] C. Sumi *et al.*, "Shear modulus reconstruction by ultrasonically measured strain ratio," *J. Med. Ultrason*, vol. 34, no. 4, 2007 (in press).
- [2] C. Sumi, *IEEE Trans UFFC*, vol. 52, pp. 1670-1689, 2005.
- [3] C. Sumi, *IEEE Trans UFFC*, vol. 53, pp. 2416-2434, 2006.
- [4] C. Sumi, "Effective shear modulus reconstruction obtained with approximate mean normal stress remaining unknown," *IEEE Trans UFFC* (in press).
- [5] M. Bilgen *et al.*, *IEEE Trans UFFC*, vol. 46, pp. 1128-1133, 1999.
- [6] C. Sumi, "Ultrasonic axial strain measurement for lateral tissue deformation," *Ultrason Med Biol* (in press).

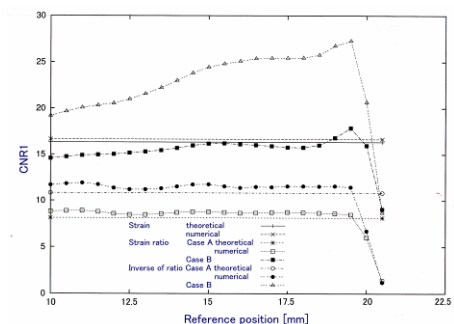


Figure 1: CNR1 vs reference position (40 dB SNR).

078 3D ULTRASOUND ELASTOGRAPHY FOR BREAST CANCER DIAGNOSIS.

M. Muller^{1*}, J.-L. Gennisson¹, T. Deffieux¹, R. Sinkus¹, P. Annic¹, G. Montaldo¹, M. Tanter¹, M. Fink¹.
Laboratoire Ondes et Acoustique, ESPCI – CNRS UMR7587 – INSERM – Université Paris VII,
10 rue Vauquelin 75231 Paris Cedex 5, FRANCE.

Background: An experimental three dimensional (3D) Ultrasound Elastography setup has been designed for improving breast cancer diagnosis. 3D Elastography assessment is generally based on the combination of adjacent 2D elasticity maps, obtained through simple 2D inverse problem resolution [1]. Meanwhile, 3D sonoelastography is based on simple inversion approaches to the viscoelasticity problem. The system presented here is based on the resolution of a full 3D inverse problem, from the complete ultrasound-based measurement of the three components of the 3D displacement field.

Aims: 3D information considerably improves the accuracy and reliability of quantitative measurements and circumvents the operator-dependent aspects of 2D echography diagnosis. The combination of 3D echography and elastography could be a very promising tool for *in vivo* breast cancer diagnosis.

Methods: The X-ray system of a commercial mammographic bed (Lorad Biopsy Bed) was replaced by an ultrasound device. Shear waves were generated using a low frequency vibrator. Resulting displacements in tissues were imaged using an echographic probe moving stepwise around the breast. Advanced techniques such as compounding echographic probe sub-apertures and 2D vector Doppler algorithms were used to assess the three components of the displacement. Shear elasticity, viscosity and anisotropy were quantified using a 3D elastic properties reconstruction algorithm.

A 3D finite difference simulation algorithm based on the viscoelastic propagation equation was used to model the 3D forward problem and validate the inverse reconstruction algorithm. Simulated displacements in a numerical phantom were used as inputs for the inverse problem resolution, allowing the reconstruction of elastic properties similar to that of the numerical phantom.

Similarly to MR-Elastography, the inverse problem was solved in the Fourier domain. However, overcoming the data acquisition limitations of MR-Elastography, the ultrasound-based approach enables the implementation of frequency compound methods based on averaging the data at different shear frequencies, increasing the measurement accuracy.

Results: In the present study, the experimental setup was optimized using numerical simulations and validated *in vitro* and *in vivo*. *In vitro* experiments were conducted on a calibrated phantom exhibiting harder inclusions. Its 3D elastic properties were reconstructed and found consistent with that given by the manufacturer [2].

Conclusions: This study allowed the numerical and experimental validation of the complete 3D Elastography protocol. A careless use of the curl operator for shear wave's extraction could adversely affect the measurement reliability, as shown numerically and experimentally.

References:

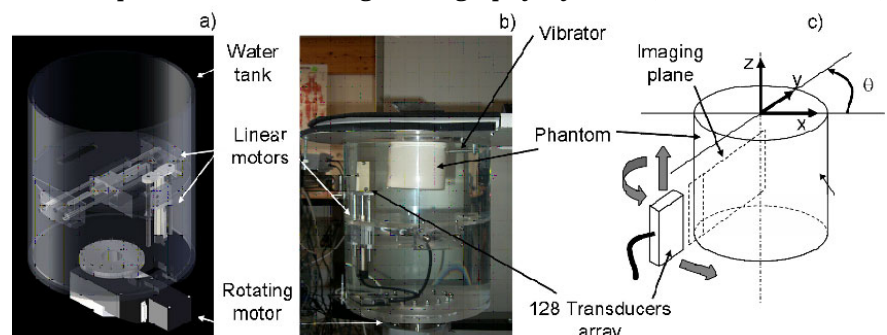
- [1] R. Sinkus, M. Tanter, T. Xydeas, S. Catheline, J. Bercoff, and M. Fink, "Viscoelastic shear properties of *in vivo* breast lesions measured by MR elastography," *Magn. Reson. Imaging.*, vol. 23, pp. 159–165, 2005.
- [2] E.L. Madsen *et al.*, "Anthropomorphic breast phantoms for testing elastography systems", *Ultra. Med. Biol.*, vol. 32 (6), pp. 857–874, 2006.

Figure 1:

a) 3D elastography setup.

b) The experimental setup is fixed under a clinical bed originally designed for X-ray mammography. A mini-shaker is placed on one side of the phantom in order to create shear waves.

c) Axis of the system.



117 **SCANNING ACOUSTIC MICROSCOPY IMAGING OF CARIES AFFECTED DENTIN MICROMECHANICAL PROPERTIES.**

Orestes Marangos¹, Anil Misra¹, Paulette Spencer¹, Brenda Bohaty¹, Yong Wang¹, Marlieke de Bruijn¹, Mona M. Kalayeh¹, J. Lawrence Katz^{1}.*

¹University of Missouri–Kansas City, 650 East 25th Street, Kansas City, MO, 64108–2784, USA.

Background: The micro–scale elastic properties of dentin are greatly reduced by dental caries. Scanning acoustic microscopy (SAM) has been used to characterize micro–scale elastic properties of caries affected dentin. For this material, reflected signal amplitude is weak and high amplification settings must be used to obtain measurable signals. Saturation effects of system electronics at high amplifications may influence this received signal. Thus, if the saturation effects are not properly accounted for, then the accuracy of the calculated micromechanical properties may be greatly compromised.

Aims: (1) Develop a methodology for characterizing the nonlinearity introduced by system electronics at high amplifications (2) Quantify the elastic properties of caries affected dentin.

Methods: A variety of independently characterized reference materials has been used to develop the relationships between the Fourier amplitude and reflection coefficient at various amplification (gain) settings for a transducer with 30 MHz central frequency. Validation of these relationships has been done by comparing the predicted reflection coefficients of very low acoustic impedance materials LDPE (reflection coefficient= 0.12) and TPX[®] (reflection coefficient= 0.09) with those obtained through independent measurements. These relationships have applied to obtain the reflection coefficients from 3 related regions of a caries affected dentin.

Results: The discrepancy between the values predicted using the developed relationships and the theoretical values for TPX[®] are less than 11% over a 6dB transducer bandwidth. For the 25.0 to 33.5 MHz frequency range, the discrepancy is <3%. Clearly, the developed relationships provide a closer prediction of unknown material whose reflection coefficient lies outside the range of reference materials.

Conclusion: The reflection coefficients, at the central frequency, from the 3 related regions of a caries affected dentin are found to be: 0.62–0.66 in the healthy dentin, 0.11–0.26 in the caries affected dentin.

Acknowledgement: Supported in part: NIH/NIDCR DE014392, NIH/NIDCR S10 RR16710, K23 DE/HD00468.

Background: Acoustic radiation force imaging allows mapping of tissue displacements induced by focused ultrasound pulses. These displacement values can be related to mechanical tissue properties which could be used for diagnostic and thermal therapy monitoring. Ultrasound (US) and Magnetic Resonance (MR) have been used to measure local harmonic motion (LHM) induced in tissues by acoustic radiation force [1,2]. Thus far, these studies have been performed in *ex vivo* tissues and phantoms, and no simultaneous measurements with these techniques have been reported.

Aims: This study presents simultaneous US and MR measurements of *in vivo* local harmonic motion (LHM). The main purpose was to prove that the measurements could be done simultaneously to obtain correlated and complementary information from the tissues.

Methods: A LHM was generated *in vivo* on rabbit thigh muscle by periodic inductions of the radiation force induced by a single-element Focused Ultrasound (FUS) transducer (80mm focal length, 100mm diameter, 1.536 MHz central frequency). The FUS transducer was excited at its central frequency by sinusoidal bursts (50% on/off duty cycle, burst repetition frequency of 100 Hz, 20W acoustic power). A separate MR-compatible US diagnostic transducer (5 MHz central frequency, 3 kHz PRF) was placed at the center of the FUS transducer and excited by a pulser/receiver to track the tissue motion using cross-correlation techniques. US displacement estimates were made relative to the initial position (i.e., instants before the application of the radiation force), and the displacement values were obtained during the first two cycles of the burst insonification. The tissue motion was simultaneously measured by MR using a modified phase-contrast spin-echo sequence (TE 50ms, bipolar gradient amplitude 2G/cm, FOV 12cm, 128x128 matrix, 3mm slice thickness, 8 phase offsets). A timing schema of the US/MR sequence is shown in Figure 1. Two-second intervals between the FUS excitations were applied to avoid heat accumulation. Once the MR measurement was completed, a lesion was formed by continuous application of the FUS, and the LHM measurements were repeated.

Results: The maximum of the averaged displacement measured by US was $18.3 \pm 8.8 \mu\text{m}$ before lesion formation and $9.3 \pm 5 \mu\text{m}$ after. In order to obtain the displacements as a function of time for the MR, the measurements were fitted using an exponential model. The maximum displacement obtained for the MR measurement was $11.62 \mu\text{m}$ before lesion formation (Figure 2). The smaller value in the MR measurement might be due to both spatial and temporal averaging.

Conclusions: The feasibility of *in vivo* LHM measurements simultaneously with US and MR was proved. US measures LHM at the focus with high temporal resolution, while MR is capable of measuring shear wave propagation in 1D or 2D. The combination of the two approaches provides complementary temporal and spatial information.

Acknowledgements: Work supported by NIH Grant R21/R33 CA102884-01.

References:

- [1] E. E. Konofagou and K. Hynynen, "Localized harmonic motion imaging: theory, simulations and experiments," *Ultrasound Med. Biol.*, vol. 29, pp. 1405-1413, Oct. 2003.
- [2] T. Wu, J. P. Felmlee, J. F. Greenleaf, S. J. Riederer and R. L. Ehman, "MR imaging of shear waves generated by focused ultrasound," *Magn. Reson. Med.*, vol. 43, pp. 111-115, Jan. 2000.

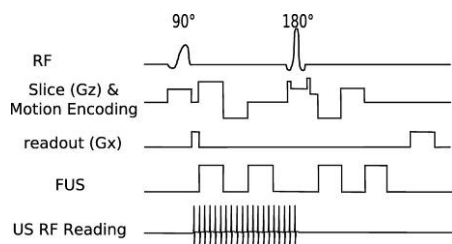
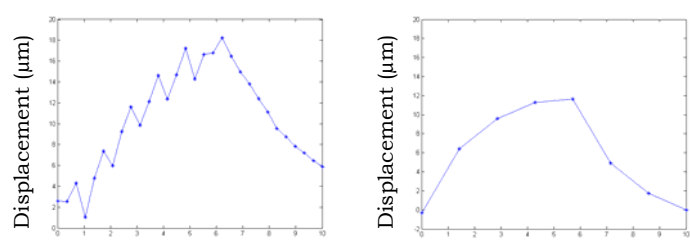


Figure 1: Timing schema for simultaneous MR/US.



(a) US Time (ms) Displacement (μm)
 (b) MR Time (ms) Displacement (μm)
 Figure 2: Tissue displacement as a function of time measured by US and MR.

103 **ANISOTROPIC ELASTICITY IMAGING WITH APPLICATION TO ELASTICITY IMAGING OF BONE.**

*EF Morgan*¹, *AA Oberai*^{2*}, *PE Barbone*¹, *A Nazarian*³.

¹Boston University, Boston, MA, USA; ²Rensselaer Polytechnic Institute, Troy, USA; ³Beth Israel Deaconess Medical Center, Boston, MA, USA.

Background: Many biological materials, such as cancellous (often called trabecular) bone, tendon and arterial walls are anisotropic materials that can display substantial variations in material properties even within a single anatomical site. Inhomogeneous material property distributions can also signal pathology, as in the case of breast carcinomas, fibrosis and arteriosclerosis. While spatial variations in elastic properties can be measured directly by excising multiple samples of tissue, there are many instances in which non-invasive measurement is desired. These instances include disease diagnosis and monitoring of disease progression. They also include “patient-specific” finite element modeling, in which computed tomography (CT) or magnetic resonance (MR) images of a bone or portion of the cardiovascular system are used to generate the model geometry. Non-invasive measurement of anisotropic elastic properties thus has many clinical and biomechanical applications.

Aims: Our focus in this presentation is to develop and test algorithms for non-invasively measuring the spatial distribution of anisotropic elastic parameters of tissue from the knowledge of the interior displacement fields. We assume that the measured deformation fields can be obtained by any of the now standard elasticity imaging techniques.

Methods: We develop an efficient and robust algorithm for solving the following inverse problem: “Given multiple measured deformation fields inside an elastic body find the spatial distribution of the anisotropic parameters.” When compared with the incompressible isotropic case [1], this problem has the additional complexity of determining several elastic parameters as opposed to just one. To accomplish this, multiple independent deformation fields within the elastic body are required. With this in mind, we propose an efficient strategy for evaluating the distribution of the parameters while accounting for all the measured displacement fields.

Our approach is based on posing the inverse problem as a minimization problem, wherein property distributions that provide the best fit simultaneously to all measured displacement fields are sought. This problem is solved using a quasi-Newton algorithm. At every iteration of this algorithm, the gradient is computed efficiently by solving the adjoint anisotropic elasticity equations.

Results: We describe the algorithm and analyze its performance, including its computational costs. We test its accuracy on synthetic (computer generated) tissue phantoms. The phantom material is a transversely isotropic solid with known material vector direction. The displacement fields are computed by subjecting the specimen to uniaxial loading along three orthogonal directions. Noise is then added to the computed displacements. The noisy displacement fields are used in the inverse algorithm to evaluate the distribution of five independent elastic parameters. It is observed that most anisotropic parameters are accurately reconstructed. Inaccuracies in some parameters suggest the use of independent shear loading in addition to the uniaxial compression tests. Some initial results using displacement fields evaluated from micro-computed tomography (micro-CT) images of trabecular bone are also presented.

Conclusions: An iterative algorithm for determining the distribution of anisotropic elastic parameters of tissue from the knowledge of its interior displacements is presented. It is demonstrated that this algorithm is efficient, accurate and holds the potential for practical use.

Acknowledgements: PEB acknowledges the support of NSF.

References:

- [1] Oberai AA, Gokhale NH, Feijoo GR. Solution of inverse problems in elasticity imaging using the adjoint method *Inverse Problems* 19:297–313 2003.
-

Jennifer Oudry^{1,2*}, Véronique Miette¹, Rémy Willinger², Laurent Sandrin¹.

¹Echosens, Research and Development Department, 153 avenue d'Italie, 75013 Paris, FRANCE;

²Institut de Mécanique des Fluides et des Solides, UMR7507, 2 rue Boussingault, 67000 Strasbourg, FRANCE.

Background: Low-frequency shear waves have led to the development of promising tools in tissue characterization. The interest in the propagation of shear waves in soft tissues relies on the relation between the shear wave velocity and the Young's modulus more generally referred to as elasticity ($E=3\rho V_s^2$). It is now well known that the pathological state of soft tissues is strongly correlated with changes in stiffness. The need for quantitative information yielded to the development of inversion algorithms which are based on the elastic wave propagation equation in isotropic solids. These algorithms consist of reconstructing the shear modulus distribution map from the estimates of the displacement spatio-temporal evolution.

Aims: We aim to study the bias induced by neglecting some second-order spatial derivative terms in the scalar shear wave propagation equation, which is a hypothesis generally assumed in the direct and local inversion algorithm.

Methods: Propagation of low-frequency transient elastic waves, induced by a circular piston, through isotropic and homogeneous soft media is investigated using two approaches: (1) a simulated method based on the Green's function [1], and (2) the transient elastography technique [2,3], an experimental approach. With the first approach, theoretical displacement fields are computed using the diffraction impulse response. Then, a direct inversion algorithm is performed from the axial component u_z of the simulated and experimental displacement fields to deduce the shear modulus or velocity distribution map. The shear velocity is computed as the square root of the ratio between the temporal and spatial second-order derivatives:

$$V_s = \sqrt{\frac{\partial^2 u_z}{\Delta t^2}} \quad \text{Equation (1)}$$

Also, the Laplacian is calculated for each of the following three:

$$\text{i) } \Delta u_z \approx \frac{\partial^2 u_z}{\partial z^2} \quad \text{Equation (2)}$$

$$\text{ii) } \Delta u_z \approx \frac{\partial^2 u_z}{\partial y^2} + \frac{\partial^2 u_z}{\partial z^2} \quad \text{Equation (3)}$$

$$\text{iii) } \Delta u_z = \frac{\partial^2 u_z}{\partial x^2} + \frac{\partial^2 u_z}{\partial y^2} + \frac{\partial^2 u_z}{\partial z^2} \quad \text{Equation (4)}$$

Thus, we will speak about respectively a one, two or three-dimensional direct problem.

Results: In a homogeneous medium, we show that the 1D and 2D assumptions are not valid in the near field (near the vibration source). The 2D Laplacian approximation is correct in the far field, if initial conditions are favorable (axisymmetric problem). The 3D direct problem gives good results in both cases.

Conclusions: In a homogeneous medium, the experimental conditions can be chosen so that the 2D direct inversion can be applied. However, in heterogeneous media, it might be rapidly limited. In such a case, a 3D direct inversion algorithm is required to accurately estimate the shear wave velocity map.

References:

- [1] Sandrin L, Cassereau D., Fink M. The role of the coupling term in transient elastography. *J. Acoust. Soc. Am.* 2004; 115 (1): 73–83.
- [2] Sandrin L, Tanter M, Gennisson JL, Catheline S, Fink M. Shear elasticity probe for soft tissues with 1-D transient elastography. *IEEE UFFC* 2002; 29 (4): 436–46.
- [3] Sandrin L, Tanter M, Catheline S, Fink M. Shear modulus imaging with 2-D transient elastography. *IEEE UFFC* 2002; 29 (4): 426–35.

048 3D ANALYTICAL MODELING OF TRANSIENT AND HARMONIC PLANE SHEAR WAVE DIFFRACTION BY A SOFT CYLINDER FOR DYNAMIC VASCULAR ELASTOGRAPHY.

A. Hadj Henni^{1*}, C. Schmitt¹, G. Cloutier¹.

¹Laboratory of Biorheology and Medical Ultrasonics, University of Montréal Hospital Research Center, Montréal, H2L 2W5, Québec, CANADA.

Background: By studying venous pathologies, such as deep vein thrombosis, it appears that the mechanical properties of clot are different from those of the surrounding media. In addition, these properties are time-varying regarding the blood coagulation process [1]. One can then use dynamic elastography to characterize such pathologies.

Aims: In this work, 3D analytical modeling of transient and harmonic shear wave diffraction by soft cylinders for dynamic vascular elastography is considered [2]. The general 3D simulation can be applied to the particular case of a normally incident plane shear wave (the acoustical problem is then 2D).

Methods: The blood vessel was assumed to be a cylinder, and the incident plane wave was considered to be transient or harmonic, polarized in the y direction and forming an arbitrary incidence angle with the x propagation axis (Figure 1). Vessel constitutive material and the surrounding medium were supposed to be homogeneous, isotropic and viscoelastic (governed by the Hooke-Voigt behavior law). The displacement field, solution of 3D Navier differential equation was expressed analytically as a combination of infinite cylindrical series satisfying the mechanical boundary conditions.

Results: As shown in Figure 1, the model permits calculation of the total 3D displacement field in the vessel and within the surrounding medium. It appears that the wave propagation properties, wavelength and phase velocity, depend strongly on the mechanical properties of both media. For a normal incidence, i.e. zero angle of incidence, the analytical simulation has been compared to experimental measurement of harmonic wave diffraction by a cylindrical coagulated blood inclusion contained in a phantom, Figure 1 (b). The measurement has been performed using our ultrafast ultrasonic imaging system, which permits tracking shear wave motion at a frame rate of 3200 Hz. The calculated phase velocity and attenuation were in good agreement with the same measured displacement field properties.

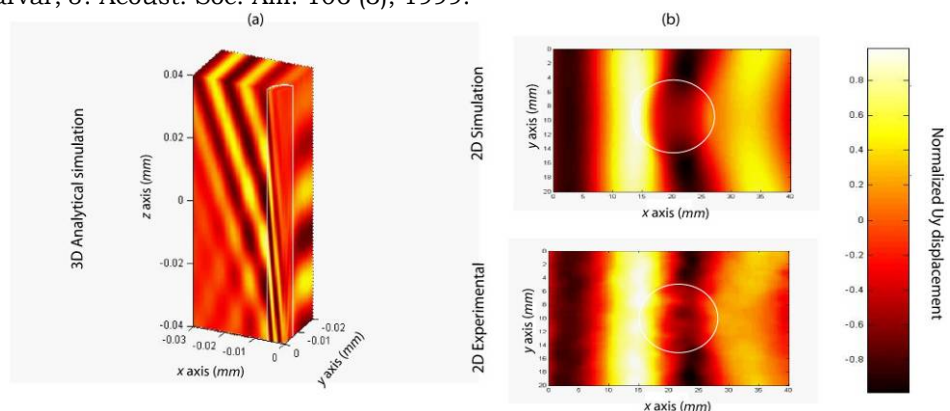
Conclusions: A fast and stable analytical model has been developed to simulate 3D diffraction of transient and harmonic plane shear wave by a soft cylindrical inclusion. The comparison of calculations with experimental measurements permits validation of the model. Simulations could then be integrated into an optimization process to characterize mechanically soft cylindrical inclusions and perform viscoelasticity imaging of vein and artery pathologies.

Acknowledgement: This work was supported by grant #MOP-36467 from the Canadian Institutes of Health Research. Dr. G. Cloutier is recipient of the National Scientist Award from the 'Fonds de la Recherche en Santé du Québec'.

References:

- [1] J.L. Gennisson, S. Lerouge and G. Cloutier, *Ultrasound Med. Biol.*, 32, 2006.
- [2] Y. Fan, A.N. Sinclair and F. Honarvar, *J. Acoust. Soc. Am.* 106 (3), 1999.

Figure 1: (a) Example of simulated 3D transient (5 modulated pulses at 350 Hz central frequency) plane shear wave diffraction by a soft cylinder with an incidence angle of 20°. (b) Comparison of simulation with experimental measurement of a harmonic plane shear wave diffraction by a cylindrical coagulated blood inclusion in a phantom (angle of incidence 0°, R = 6mm, $\mu=122$ Pa, $\eta=0.06$ Pa.s).



Michael S Richards¹, Carlos Rivas², Joseph P Richter³, Sevan Goenzen³, Remo A Crescenti⁴, Jeffrey C Bamber⁴, Assad A Oberai³, Paul E Barbone^{2*}.

¹University of Michigan, Ann Arbor, MI, USA; ²Boston University, Boston, MA, USA; ³Rensselaer Polytechnic Institute, Troy, NY, USA; ⁴Institute of Cancer Research, Sutton, Surrey, England, UK.

Background: It is widely recognized that soft tissue pathologies often change a tissue's mechanical properties. The inference of mechanical properties from a measured deformation field requires a mathematical model that accurately describes tissue deformation. In rare cases, given a measured deformation, the mathematical model can be used to solve directly for the sought material property. More typically, however, an iterative method is used. In an iterative method, predictions of the mathematical model are compared to observed tissue deformations. The material parameters that provide a match to the observed deformations are taken to be correct values for the tissue.

Over the past several years, our team has accumulated considerable experience in solving various biomechanical inverse problems, including plane stress incompressible elastic, plane strain compressible elastic, plane strain incompressible elastic, 3D incompressible isotropic elastic, 3D anisotropic elastic, plane strain biphasic and both plane stress and plane strain incompressible nonlinear elastic. Each problem class introduces new challenges, but some challenges span several problem classes.

Aims: This presentation focuses on challenges that have arisen again and again in different contexts. The purpose of this presentation is to discuss these remaining challenges in quantitative biomechanical imaging, their physical and/or mathematical origins and to propose some approaches that may overcome them. These include the roll of uncertainty in boundary conditions, insensitivity of the predicted displacement field to modulus changes near certain boundaries, insufficient data to ensure uniqueness of the solution and discretization induced instability.

Methods: We discuss almost exclusively iterative methods. We illustrate the problems through computational example and explain their origin through physics, where appropriate. We also compare the properties of certain unstable iterative inverse methods with certain (stable) direct methods. The direct methods help to identify the source of the instability in the iterative methods and a way to correct it.

Results: The problem of predicting a deformation field from a current guess of material properties requires knowledge of the boundary conditions in the problem. In most elasticity imaging situations, these are inaccurately and/or incompletely known. We find that in some sensitive cases, slight miscalibration of these properties can lead to gross reconstruction error. We have also encountered many situations where more than one modulus distribution provides a good fit to the measured data. While some of these are physical in origin, others are due entirely to discretization in the forward problem. (This is true even when the forward problem can be proved to converge optimally to the right solution.)

Conclusions: Suitable mathematical models of tissue deformation, coupled with precise and accurate observations of tissue behavior can be used to determine different biomechanical properties of soft tissue, including, but not limited to, shear elastic modulus. For some special cases of elasticity imaging, there is no open issue. For the rest, however, there remain challenges to overcome. We show that these challenges can typically be addressed by collecting additional data.

Acknowledgements: Partial funding through URP program at RPI, EPSRC, ICR , and NSF.

119 **A SIMPLE TIME-DEPENDENT MODEL OF THE LEFT VENTRICLE MOTION – IMPLEMENTATION USING TAGGED MRI.**

T Alrefae^{1,2*} and M Bilgen^{2,3}.

¹Physics and Astronomy Department, University of Kansas, Lawrence, KS, USA; ²Hoglund Brain Imaging Center, ³Integrative and Molecular Physiology Department, University of Kansas Medical Center, Kansas City, KS, USA.

Background: It has been shown that the local motion of the left ventricle (LV) wall in a diseased heart differs from that of healthy hearts due to variations in contractile behavior resulting from complications such as infarct or diabetic cardiomyopathy [1–3]. Magnetic resonance imaging (MRI) is an established radiological technique for the assessment of cardiac function under these pathological conditions. Particularly, tagged MRI method allows for regional evaluation of myocardium in the left ventricle (LV) [4]. The tag lines in this technique follow the motion of the underlying myocardial tissue, as the heart beats, thereby revealing localized deformation in the LV wall. Accurately representing myocardial deformation is a critical component of numerically modeling the LV wall motion. Keeping this in mind, in this presentation, we describe a new simplified LV motion model, which is built by taking advantage of the highly desirable motion tracking feature of the tagged MRI.

Aims: The goal of this work is to provide a simple, yet reliable computational model that describes the motion of the LV wall during systole.

Methods: Cardiac MRI data from the mid-ventricle level were gathered from five male Sprague-Dawley rats. Four of the rats were normal and the remaining one was made diabetic with the procedures described in [2]. The scans were performed using a 9.4 T scanner and 60 mm radiofrequency (rf) volume coil. ECG gated gradient echo based tagged images were captured from the short-axis view of the heart, where the cardiac cycle was temporally resolved into ten equally incremented phases. We constructed a mathematical model to describe the LV systolic motion at the mid-ventricle level. The model is based on a Gaussian function encapsulated in an affine-like transformation operator, T, with diagonal elements $1+\exp(-(x^2+y^2)/a^2)$ and off-diagonal elements identical to zero. The parameters x and y in this expression represent spatial coordinates, and a is a time-dependent parameter accounting for the temporal changes in the LV size. An algorithm was developed and implemented to find optimized values for a that best represent the systolic LV motion.

Results: Figure 1 shows how T acts on an image with numerical simulation. Figure 2 shows a regular grid deformed by T with different a values and overlaid on real systolic images. The grid lines are seen as overlapping the tag lines. The values of a are plotted against the time points equally spaced in the systolic phase in Figure 3 for both normal and diabetic groups. The values of a from the normal hearts established the normative database. The diseased diabetic heart is seen as having considerably different values and temporal profile for a than those of normal hearts. This difference is directly related to the variations in the myocardial contraction, which is attributed to the diabetic cardiomyopathy [2].

Conclusions: The Gaussian LV model presented here requires estimating a single deformation parameter a for quantifying the temporal myocardial motion in the systolic phase of the cardiac cycle with sufficient accuracy. Requiring only one parameter to reasonably describe the motion is an important advantage of this model. Moreover, the measurements of the deformation parameter a in our model can potentially be used to sensitively detect structural and functional changes in the myocardial tissue early on or to follow the progression of a disease longitudinally. In this regard, this parameter may offer a new biomarker not only in experimental studies but also in clinical applications.

References:

- [1] Liu, W., et al. Magn Reson Med, 2004. 52(6): p. 1282–90.
- [2] Loganathan, R., et al. Cardiovasc Diabetol, 2006. 5: p. 7.
- [3] Loganathan, R., et al. J Appl Physiol, 2007. 102(2): p. 665–72.
- [4] Osman, N. F., et al. IEEE Trans Med Imaging, 2000. 19(3): p. 186–202.

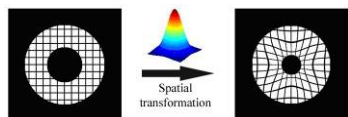


Figure 1: Effect of Gaussian spatial transformation on a tagged donut.

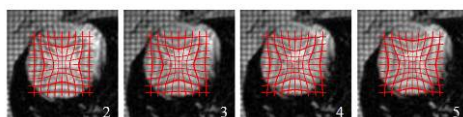


Figure 2: Deformed grid (red) superimposed on real tagged MRI data.

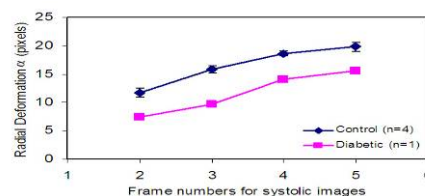


Figure 3: Values of a for normal and diabetic rats plotted against systolic time.

Background: Pulse waves are flow velocity, pressure and diameter waves generated by ventricular ejection. Their propagation speeds and patterns are related to vascular mechanical properties (e.g., arterial stiffness). Because of the limitation of temporal and spatial resolution, the widely used foot-to-foot method measures the average value of the pulse-wave velocity (PWV) between two points with a long distance apart (>10cm), instead of the regional value. However, mechanical properties are non-uniform along arteries and diseases are typically regional. Pulse-wave imaging (PWI) has been developed to visually map the pulse-wave propagation along the aortic wall (<12mm) in mice [1].

Aims: To compare the PWI results between control and Angiotensin II (Ang II) treated mice in order to demonstrate the feasibility of this state-of-the-art technique in the detection of abdominal aortic aneurysms (AAAs).

Methods: Thirty-five wild-type C57BL6 mice were divided into Ang II (+) (treated) and Ang II (–) (control) groups. A subcutaneous osmotic mini-pump (Alzet model 2004, Durect Corp, Cupertino, CA, USA) was implanted into the mice to deliver a slow release of Ang II (1.44mg/kg/day) or 1M phosphate buffered saline. On day 28, mice were first anesthetized with isoflurane. A high-resolution (30 MHz) Vevo 770 system (VisualSonics Inc., Toronto, Canada) was used to scan the abdominal aortas in the long-axis view. RF and ECG signals of the mice were simultaneously acquired. With the retrospective ECG-gating technique, the full field-of-view (12mm x 12mm) RF frames were reconstructed at an extremely high frame rate of 8 kHz [2,3]. The incremental displacements of the aortic walls during the entire cardiac cycle were estimated using a RF speckle tracking method. The regional PWV was equal to the slope determined through linear regression analysis of the displacement variation with time. The correlation coefficient of the linear regression represented the uniformity of the pulse-wave propagation along the aortic wall.

Results: Localized AAAs are observed in 17 mice of the Ang II (+) group, which are confirmed by histopathology (standard H&E and EVG stains), whereas the control mice did not develop aneurysms. Different propagation patterns are observed between control (n=5) and AAA mice (n=17). In the control mice, the pulse-wave propagates from the proximal to the distal side at constant speeds (2.1310 ± 0.8209 m/s). The correlation coefficient of the linear regression is 0.8587 ± 0.090 ($p < 0.001$) and the maximum incremental displacement is 0.00236 ± 0.00098 mm. In the AAA mice, the propagation of the pulse-wave is non-uniform, with a lower correlation coefficient (0.5149 ± 0.1795) and smaller displacement amplitude near the AAA. The maximum displacements at the proximal, middle (near AAA) and distal sites are 0.00159 ± 0.00072 , 0.00093 ± 0.00037 and 0.00108 ± 0.00048 mm, respectively.

Conclusions: The PWI estimates are shown capable of differentiating the controls from the AAAs ($p < 0.001$). Because of the high temporal (0.125ms) and spatial resolution (55 μ m), this state-of-the-art technique may allow early detection and non-invasive mapping of vascular diseases *in vivo*.

Acknowledgements: This study was supported in part by the American Heart Association (SDG0435444T) and by a grant from the associate trustees of St. Luke's–Roosevelt Hospital.

References:

- [1] K. Fujikura, J. Luo, M. Pernot, R. Fukumoto, D. Tilson III and E. E. Konofagou, "Pulse wave imaging in murine abdominal aortas," IEEE Ultrasonics Symp Proc, pp. 868–871, 2006.
- [2] M. Pernot and E. E. Konofagou, "Electromechanical imaging of the myocardium at normal and pathological states," IEEE Ultrasonics Symp Proc, pp. 1091–1094, 2005.
- [3] M. Pernot, K. Fujikura, S. D. Fung-Kee-Fung and E. E. Konofagou, "ECG-gated, mechanical and electromechanical wave imaging of cardiovascular tissues *in vivo*," Ultrasound in Med. Biol., 2007 (in press).

099 3D ELASTICITY IMAGING OF LV THROUGH SIMULATIONS AND PHANTOM EXPERIMENTS.

Congxian Jia^{1*}, Ping Yan², Kang Kim¹, Theodore J Kolias¹, Jonathan M Rubin¹, William F Weitzel¹, Don Dione², Albert J. Sinusas², James S. Duncan² and Matthew O'Donnell³.

¹University of Michigan Ann Arbor, MI, 48109-2099, USA; ²Yale University, New Haven, CT, 06520-8260, USA; ³University of Washington, Seattle, WA 98195-2180, USA.

Background: Myocardial ischemia or infarction results in alterations in myocardial contractility. Strain and strain rate imaging have the potential to detect changes in myocardial contractility and evaluate viability. A challenging issue with cardiac elasticity imaging is that heart motion is 3D and complex. Currently available 1D or 2D elasticity imaging techniques are often limited by significant out-of-imaging plane motion. 3D elasticity imaging will provide full assessment of cardiac elastic properties.

Aims: To evaluate phase-sensitive 3D speckle tracking [1] on complex cardiac motion, simulations were performed mimicking 3D motions of the left ventricle (LV) using a 3D ultrasound simulator. A phantom experiment was also performed using a commercial 2D phased array to image a Polyvinyl alcohol (PVA) cryogel LV phantom connected to a controlled pulsatile circulation system. 3D tracking results were compared with 2D tracking results.

Methods: A kinematic ellipsoidal 3D LV model was simulated using a 2D phased-array simulator at 3 MHz. Each volume in one heart cycle was generated assuming tissue incompressibility [2]. The performance of 3D tracking was evaluated for contraction, translation and torsion. 3D tracking was also directly applied to an LV phantom constructed using 8% PVA cryogel embedded with ultrasound scatterers (enamel paint) using three freeze-thaw cycles. The LV phantom was connected to a pulsatile pump. Internal pressure was recorded. Stroke volume, heart rate, and systole/diastole ratio were varied to mimic cardiac pulsation. 3D RF volume data were acquired in real time using a commercial 2D phased array (sono7500, Philips). The kernel size for speckle tracking was set to be about 2 speckles (3-4mm in each direction). Frame-to-frame tracking results were accumulated, referenced to the original geometry.

Results: 3D speckle tracking results in both simulations and phantom experiments outperformed 2D tracking, especially when out of plane motion is significant. The motion in the third dimension was well estimated in 3D tracking (Figure 1). The error of axial and azimuthal displacement estimates in 3D tracking was significantly smaller than those in 2D tracking.

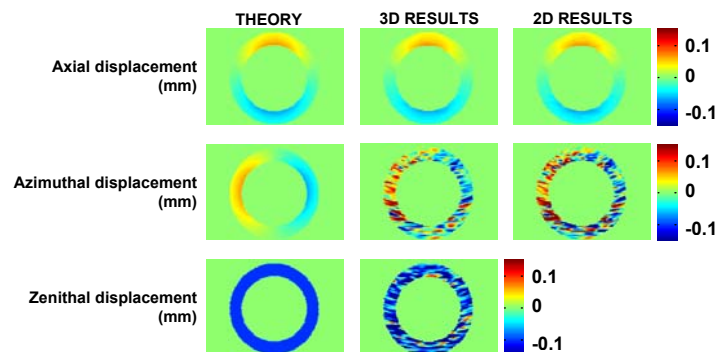
Conclusions: Displacement estimation errors in speckle tracking due to out-of-plane motion were significantly reduced using 3D speckle tracking. Preliminary results from both simulations and experiments demonstrate the feasibility of 3D elasticity imaging of complex cardiac motion.

Acknowledgements: This work was supported in part by HL-082640, HL-67647, HL-68658 and CA-109440.

References:

- [1] X. Chen, H. Xie, R. Erkamp, K. Kim, C. Jia, J.M. Rubin, and M. O'Donnell, "3-D Correlation-Based Speckle Tracking," *Ultrasonic Imaging*, Vol. 27, pp. 21-36 (2005).
- [2] S. I. Rabben, A. L. Haukanes, and F. Irgens, "A kinematic model for simulating physiological left ventricular deformation patterns - A tool for evaluation of myocardial strain imaging," *Proc. IEEE Ultrason. Symp.*, 2003, pp.134-137.

Figure 1: 3D (middle column) and 2D (right column) tracking results of simulated 3D LV on the central plane during systole. The left column shows the theoretical displacements.



Background: Computational cardiovascular biomechanics employ numerical methods to study blood flow and vessel wall mechanics in the circulatory system [1]. Biomechanical indices, such as arterial wall dynamics, hemodynamics and pulse wave propagation are being progressively used for diagnosis of cardiovascular disease and can be studied in great detail using computational methods [2]. As the heart pumps blood through the circulatory system, the compliant vessels adapt to the varying flow and pressure by extending or shrinking. The non-linear interplay between arterial wall and hemodynamics affects a blood vessel's biological function or dysfunction [3]. This interaction can be studied in high detail using numerical models employing fluid-structure interaction (FSI) techniques and the complex *in vivo* biomechanical environment can be quantified by combining computational and imaging techniques.

Aims: Our primary aim is to understand the regional pulsatile interaction between arterial wall and blood flow, and validate the numerical results with *in vivo* ultrasound measurements using pulse wave imaging. Furthermore, we perform a parameter analysis to quantify the factors influencing local arterial wall behavior and to get insight into the pulse wave propagation in healthy and diseased arteries.

Methods: The coupled FSI problem was solved on a 2D axisymmetric model based on *in vivo* mouse measurements, extending 12mm in the longitudinal and 0.7mm in the radial direction with a wall thickness of 0.2mm [4]. Newtonian blood flow with a constant fluid density of 1060kg/m³ and a dynamic viscosity of 0.004Pa·s was considered, while the maximum Reynold's number over one cardiac cycle (133ms) was 50 (i.e., laminar-flow). The arterial wall was modeled using a density of 1050kg/m³, a Poisson's ratio of 0.49 and a Young's modulus of 60kPa [4]. Pathologic conditions (aneurysm) were also modeled by altering the wall geometry and elastic properties. Realistic physiological boundary conditions were imposed based on pulsed Doppler data, and the coupled FSI models were solved using COMSOL (Burlington, MA, USA). For the experimental validation, the aortic wall motion and velocity were estimated using 1D cross-correlation on ECG-gated RF signals (frame-rate 8kHz) with a window of 0.24mm and an overlap of 90% [4].

Results: The arterial wall displacement and velocity time-profiles are shown over one cardiac cycle in a region located in the middle of the aortic wall for the simulations (Figure 1a) and the *in vivo* data (Figure 1b). Wall displacements and velocities, as estimated in the model and in the *in vivo* experiments, are in good agreement exhibiting the main features of pulsatile arterial wall behavior with increasing displacement (dilation – positive wall velocity) during the systolic phase (first half) and decreasing displacement (contraction – negative wall velocity) during the diastolic phase (second half).

Conclusions: A computational tool is presented for studying the coupled hemodynamics – arterial wall mechanics problem. Results were validated against *in vivo* data, showing a good qualitative agreement and the effects of different problem parameters on the global arterial wall behavior were investigated.

Acknowledgements: This study was supported in part by the American Heart Association (SDG0435444T) and NIH (R01EB006042-01).

References:

- [1] Yamaguchi, T., et al., Journal of Biomechanical Science and Engineering, 2006. 1(1): p. 29–50.
- [2] Tang, D., et al., Ann Biomed Eng, 2004. 32(7): p. 947–60.
- [3] Grotberg, J.B. and O.E. Jensen, Annual Review of Fluid Mechanics, 2004. 36: p. 121–147.
- [4] Fujikura, K., et al., IEEE Ultrasonics Symp Proc, pp. 868–871, 2006.

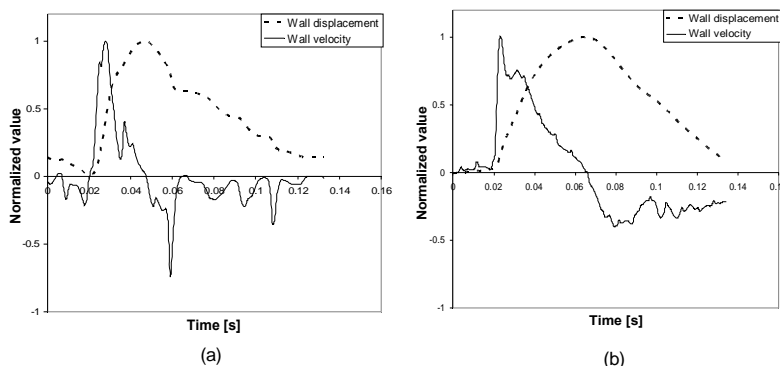


Figure 1

016 **IN VIVO ASSESSMENT OF ELASTICITY ALTERATIONS IN THE HUMAN HEART DURING THE CARDIAC CYCLE: SHEAR WAVE AMPLITUDE VARIATION MR ELASTOGRAPHY**

Ingolf Sack^{1*}, *Jens Rump*¹, *Thomas Elgeti*¹, *Abbas Samani*³, *Jürgen Braun*².

¹Radiology Department, ²Institute of Medical Informatics, Charité Berlin, Berlin, GERMANY;

³Medical Biophysics Department, University of Western Ontario, ON, CANADA.

Background: Many cardiovascular diseases and disorders are related to hemodynamic dysfunction. The functionality of the heart to pump blood through the vascular system is strongly associated with changes in the elasticity of the myocardium [1,2].

Aims: An MR elastography (MRE) experiment based on fractional motion encoding [3] is developed that allows non-invasively measuring time resolved myocardial elasticity changes.

Methods: Low frequency shear vibrations of 24.3 Hz are induced into the human heart via the anterior thorax wall. An ECG-triggered, fractional steady-state MRE sequence is used to capture shear oscillations with a frame-rate of eight images per vibration cycle. The time evolution of 2D-shear wave fields is observed in an image plane through the short axis of the heart of six healthy volunteers.

Results: Evaluation of the wave amplitudes clearly showed that wave deflection decreases during systole and increases again with myocardial relaxation. According to a linear elastic constitutive model, myocardial stiffness increases by about a factor of 37.7 ± 9.6 during heart contraction (inter-individual mean \pm SD). It was observed that the dynamics of the stiffness variation precedes changes in the left ventricular diameter on the order of 75 ± 9 ms at the beginning of the systole.

Conclusions: The time course of shear wave amplitude variations can help to assess myocardial function. Although wave amplitude variation MRE is not able to provide absolute values of myocardial elasticity, and the given ratios of elasticities at different times of the heart cycle represent only preliminary values, the dynamics of the measured shear wave amplitude variation allows insight into elasto-dynamic processes of the heart which are otherwise accessible only by invasive methods.

References:

- [1] Konofagou EE, D'Hooge J, Ophir J. Myocardial elastography—a feasibility study *in vivo*. *Ultrasound Med Biol* 2002;28(4):475–482.
 - [2] Kanai H. Propagation of spontaneously actuated pulsive vibration in human heart wall and *in vivo* viscoelasticity estimation. *IEEE Trans Ultrason Ferroelectr Freq Control* 2005;52(11):1931–1942.
 - [3] Rump J, Klatt D, Braun J, Warmuth C, Sack I. Fractional encoding of harmonic motions in MR elastography. *Magn Reson Med* 2007;57(2):388–395.
-

023 **FAST AND ACCURATE LIVER MOTION ESTIMATION.**

J Fehrenbach^{1*}, *D Melodelima*², *M Masmoudi*¹.

¹Institut de Mathematiques de Toulouse, Toulouse, FRANCE; ²Inserm U556, Lyon, FRANCE.

Background: High Intensity Focused Ultrasound (HIFU) has proved to be highly efficient in inducing homogeneous and reproducible tumour destruction by thermal coagulation necrosis. However, breathing motion induces difficulty when treating the liver because it makes the treatment imprecise. It is reported that the liver can move over 20 mm during one breathing cycle [1].

Aims: Here, we describe and evaluate an algorithm that tracks a region of interest (ROI) in a video sequence of sonograms of the liver. It should provide real time displacements in both directions.

Methods: The motion of the points of a ROI between successive frames is estimated under the assumption that the grey-level of the points is preserved. The squared-difference of the grey-level of the pixels in the ROI between the first and second frame is minimized (SSD), using a new technique. Unlike optical flow methods [2], the cost function is not linearized. Admissible displacements are piecewise linear with respect to each space variable; this reduces the number of unknowns. The Jacobian matrix of the cost function is computed rapidly, since only one reading of the data is required. *In-vivo* sonograms of a porcine liver were acquired using a 12 MHz ultrasound imaging probe (BK, Herlev, Denmark) positioned in contact with the liver via laparotomy.

Results: The algorithm was implemented using Matlab(R). It was applied to synthetic data, where the true motion is known. The displacement estimates agree with the true displacements, at least when the motion is not too fast. The algorithm was also applied to *in-vivo* data. The results are qualitatively encouraging, since the drift seems negligible over a few breathing cycles. An implementation on a small laptop computer allows processing 5 to 6 frames/sec.

Conclusions: We propose an algorithm that estimates the motion of the liver in both directions, from a video sequence of sonograms. The results on *in-vivo* data are qualitatively encouraging, and it is likely that this algorithm can provide real-time results. Motion in the third direction was not considered here and should be the object of further studies.

Acknowledgements: The authors thank the staff from the Laboratoire de Chirurgie Experimentale (Centre Leon Berard, Lyon, France). This work was granted by ACI-IMEG project from CNRS (France).

References:

- [1] Davies et al, Ultrasound quantitation of respiratory organ motion in the upper abdomen, Brit J Radiol 67(803):1096–1102 (1994).
- [2] Horn and Schunck, Determining optical flow, Artif Intel 17:185:204 (1981).

Figure 1: The liver and the ROI outlined at several time steps.

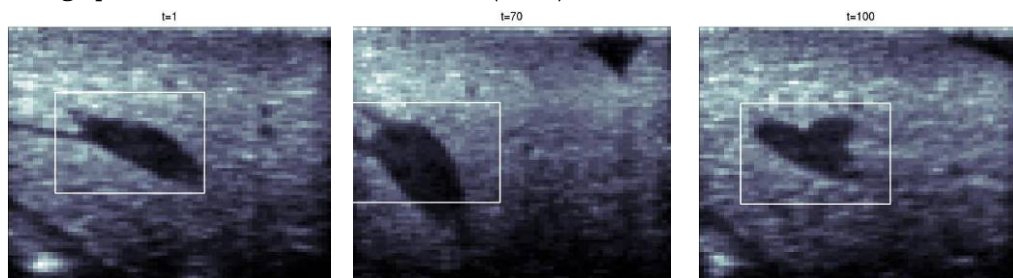
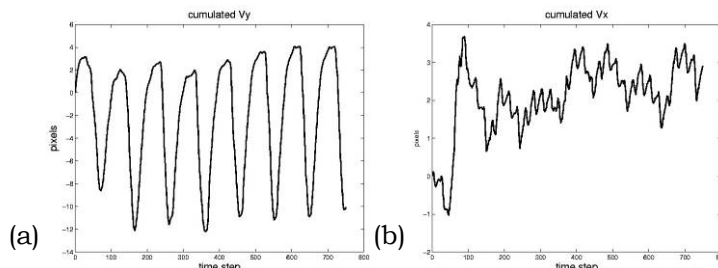


Figure 2: Cumulated horizontal (a) and vertical (b) displacements over a sequence of 750 frames. Breathing and heartbeat-induced motion are clearly visible.



028 **INCREASING THE NUMBER OF VALID STRAIN ESTIMATES IN IVUS PALPOGRAPHY WITH MOTION COMPENSATION TECHNIQUES.**

Mikhail G. Danilouchkine^{1*}, Frits Mastik¹, Anton F.W. van der Steen^{1,2}.

¹Erasmus Medical Center, Rotterdam, The NETHERLANDS; ² Interuniversity Cardiology Institute of the Netherlands, Utrecht, The NETHERLANDS.

Background: IVUS palpography was proven to be an indispensable tool for the semi-invasive characterization of atherosclerotic plaques in coronary arteries [1]. The occurrence of the neighboring high and low strain regions frequently indicates the rupture-prone location. A palpographic image, or palpogram, quantifies the strain profile along the luminal border by cross-correlating the radio frequency (RF) signals at different systemic pressures. However, inter-frame misalignment due to in-plane catheter motion gives rise to invalid strain estimates. The strain error occurs when the decorrelation of the RF signals exceeds the expected theoretical threshold.

Aim: The purpose of this study is clinical evaluation of two motion compensation methods and their impact on the quality of computed palpograms.

Methods: The compensation methods were devised based on local block matching (LBM) and optical flow (OF). LBM estimates the displacement of local tissue regions under the assumption of rigid body translation. OF, however, incorporates an affine motion model to achieve the same goal. The estimated displacements were used to align the RF signals of consecutive diastolic frames prior to strain calculation.

The methods were validated on 14 pullbacks in patients (1412 cardiac cycles in total), acquired on a clinical IVUS machine with a 20 MHz 64-element phased array transducer (both Volcano Corp.) at 30 frames per second. The efficacy of motion compensation methods was assessed via a relative increase in the number of valid strain estimates. It was expressed as a percentage of the increase in the number of valid strain estimates with motion compensation relative to the number of valid estimates without motion compensation.

Results: Figure 1 illustrates the relative increase in the number of valid strain estimates due to motion compensation during diastole.

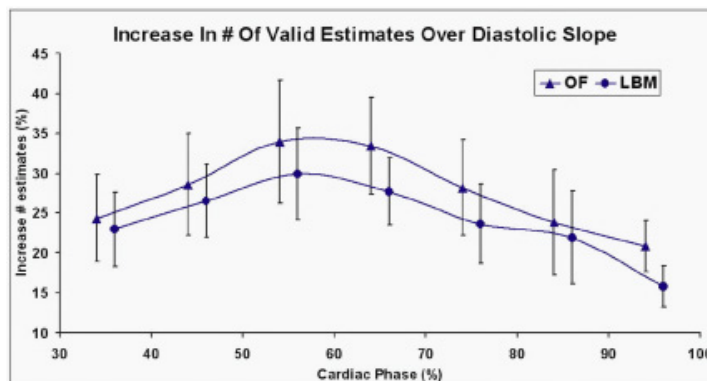
Conclusions: Both methods increase the number of valid strain estimates in computed palpograms. The average relative increase amounted to 27.5% and 23.1% for OF and LBM, respectively, with OF being significantly better (P=0.005). The most gain was observed at mid-diastole.

Acknowledgement: Volcano Corp. (Rancho Cordova, CA, USA) for financial support.

References:

- [1] J.A.Schaar et al. Incidence of high-strain patterns in human coronary arteries: assessment with three-dimensional intravascular palpography and correlation with clinical presentation. *Circ.*, 109(22): 2716-2719: 2004.

Figure 1



Background: Elastography aims to produce images that depict the mechanical properties of soft tissue for clinical applications. The goal is to investigate tissue deformation due to an applied external/internal force in order to produce images contrasting tissue mechanical properties. Color-coded strain, tissue displacement, and strain rate images are the most commonly displayed images. However, depending on the application, different visualization techniques might improve the understanding of tissue deformation.

Aim: To study real-time visualization techniques that best describe tissue deformation.

Methods: Simulations and *in-vivo* experimental data are presented. In simulations, a virtual phantom with a stiffer (2X) square inclusion was constructed (Figure 1a). The displacements of specified windows are computed for axial compression using the finite element method FEM. Real-time client software was implemented on a Sonix-RP Ultrasound (US) machine (Ultrasonix Medical Corp., Richmond, Canada) that connects to the US machine and captures radiofrequency (RF) frames and B-mode images. The relative/absolute displacements are then estimated from sets of RF signals. The Time Domain Cross Correlation with Prior Estimates (TDPE) [1] was used to estimate both in-plane components of the displacement. The estimated motions were then scan-converted and displayed, using several visualization techniques, alongside the corresponding B-mode images in real-time.

Results: The displacements vectors corresponding to the axial compression of the simulated phantom are shown in Figure 1a. The color-coded axial and lateral components of displacement are shown in Figures 1b & c. Equal cost contours of displacement norms are also shown in Figure 1d. For a qualitative evaluation of the real-time software and visualization methods, the carotid artery was also imaged in real-time without external excitation, just motion due to internal pressure changes, Figure 1e. Both axial and lateral displacements between the sequences of RF signals were estimated using 1 mm windows with 50% window overlap. Screen shots of color-coded contoured displacement magnitude and displacement vector images corresponding to the same set of echo signals are shown in Figures 1f-h.

Conclusions: In addition to color-coded axial/lateral displacement/strain, equal cost contours of the axial/lateral/norm displacement provide useful information about directional tissue deformation.

References:

- [1] R. Zahiri-Azar and S. Salcudean, Real-Time Estimation of Lateral Motion using Time Domain Cross Correlation with Prior Estimates, *IEEE Ultrasonics Symposium*, Vancouver, Pages: 1209-1212 (2006).

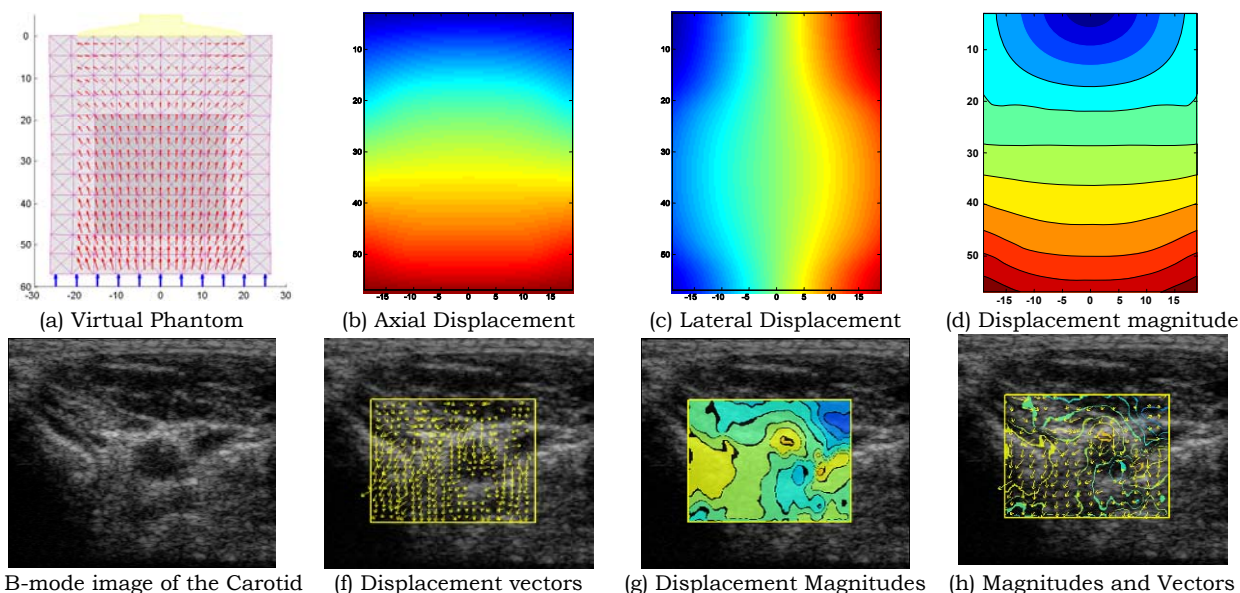


Figure 1: (a) The displacement vectors of a virtual phantom with a hard (2X) square inclusion; (b) with corresponding axial displacement; (c) lateral displacements; and (d) displacement magnitude resulting from the axial compression; (e) B-mode image of the carotid; (f) with corresponding displacement vectors; (g) displacement magnitude; and (h) displacement vectors superimposed on equal cost contours of displacement magnitudes resulting from blood pulsation.

091 **SPECKLE CHARACTERIZATION AND OUT-OF-PLANE MOTION ESTIMATION IN TISSUE.**

Hassan Rivaz^{1*}, Gregory Hager¹, Richard Zellars², Gabor Fichtinger^{1,3,4}, Emad Boctor⁴.

¹Computer Science (224 NEB), ³Mechanical Engineering (223 Latrobe Hall) Departments, Johns Hopkins University, 3400 N. Charles St, Baltimore, MD 21218, USA; ²Radiation Oncology & Molecular Radiation Sciences Department, Johns Hopkins Medical Institute, 401 North Broadway, Suite 1440, Baltimore, MD 21231, USA; ⁴Radiology Department, Johns Hopkins Medical Institute, 600 North Wolfe Street, Baltimore, MD 21287, USA.

Background: Signal to noise ratio (R) and skewness (S) of a patch (usually regular) are widely used to discriminate fully developed speckle (FDS) from coherent speckle. Having FDS patches in two images, the correlation between them is used to estimate the distance between the two images [1]. The R-S metrics requires about 4000 pixels per patch, but such large patches of FDS are unlikely to be found in real tissue because of its inhomogeneity [1]. Therefore, a compromise needs to be made, and the patches that are closest to FDS are selected for out-of-plane motion estimation [1]. We have previously shown that non-regular FDS patches can be found using a fast two-step meshing algorithm [2], leading to higher accuracy of out-of-plane motion estimation. Here, we use beam steering as another technique to further increase the accuracy.

Aims: We propose beam steering to obtain more data from a certain region from different angles, which enables us to reduce the size of the analysis patch. Smaller patch size is expected to increase the likelihood of finding FDS patches and, therefore, increase the accuracy of out-of-plane motion estimation.

Methods: Three radiofrequency (RF) data frames were acquired from an FDS phantom at steering angles of -6, 0 and 6 degrees. We applied the R-S test on 500 to 4000 pixel patches with and without using data from the steered images. The results showed that exploiting the data acquired at the three angles allows for nearly three-fold reduction in patch size.

Beam steering also improved the accuracy of distance estimation. To calibrate the rate of image decorrelation with out-of-plane motion, RF data of 3x51 parallel frames were acquired from an FDS phantom at an elevational distance of 0.05mm between consecutive images, three frames at each location with steering angles of -6, 0 and 6 degrees. Calibration results showed that the decorrelation rate is not affected by beam steering.

Results: Out-of-plane motion estimation was performed on *ex-vivo* liver data. 2x31 RF frames at an elevational distance of 0.2mm between consecutive frames were acquired, two images at each location with -6 and 6 degrees steering angles. In the first step, FDS patches were obtained using the data acquired at both steering angles. The correlation of the FDS patches was then calculated by combining the data of both steered images. For comparison, we used the same images to estimate their distance by analyzing the two sets of steered images separately and not combining them in the speckle characterization and correlation calculation steps. Without combining images, the error was 23% (as reported earlier [1]) compared to the 11% error achieved using small patches by combining steered images.

Conclusion: The significant improvement found in out-of-plane motion estimation using beam steering can be attributed to three factors:

- (1) Smaller patch size results in higher likelihood of finding uniform patches;
- (2) Boundaries appear fuzzy under an oblique ultrasound beam, which may lead to misclassification of the patch. Beam steering increases the chance of imaging boundaries from a more perpendicular angle, which reduces the likelihood of misclassification;
- (3) Averaging over more data simply increases the accuracy of estimation. These results seem highly applicable in sensorless freehand 3D ultrasound.

References:

- [1] Hassenpflug P., Prager, R., Treece, G., Gee, A, "Speckle classification for sensorless freehand 3-D ultrasound", *Ultrasound Med. Biol.*, v 31, pp 1499-1508, 2005.
 - [2] Rivaz, H., Boctor, E., Fichtinger, G., "A Robust Meshing and Calibration Approach for Sensorless Freehand 3D Ultrasound", *SPIE Medical Imaging*, v 6513, pp 6513181-6513188, 2007.
-

061 **HEATING SIMULATION FOR VIBRO-ACOUSTOGRAPHY.**

Shigao Chen^{1*}, James F Greenleaf¹, Mostafa Fatemi¹.

¹Mayo Clinic College of Medicine, Rochester, MN, USA.

Background: Vibro-acoustography (VA) is an elasticity imaging method which intersects two focused ultrasound beams with slightly different frequency to vibrate the studied object and detects the resulting acoustic emission at the difference frequency. A 2D image is formed by moving the confocal ultrasound beams over the object in a C-scan format. VA has shown promising results in imaging artery calcifications, breast lesions, liver lesions, and metal implants [1]. Safety of VA has been previously justified by estimating the averaged ultrasound intensity at the focal region. However, tissue heating has not been calculated.

Aims: Heating during VA imaging is estimated within a 3D volume from transducer surface to the C-scan plane and beyond to test imaging safety.

Methods: The 3D ultrasound intensity field simulated by Field II is normalized by the intensity measured at the transducer focus and derated for equivalent *in situ* value. The upper limit of heating due to each ultrasound beam is estimated from the bio-heat equation by neglecting heat taken away by convection and blood perfusion [2]. Accumulated heating is calculated by summing contributions from all ultrasound beams focused at each image pixel.

Results: Heating from a fixed focus transducer (focal depth 7cm, diameter 4.5cm, frequency 3MHz) scanning (mechanically driven by step motors) over a 4X4cm² region with 0.25mm resolution was calculated for different tissue attenuation values (0.5~1 dB/cm/MHz). Figure 1 shows the estimated 2D temperature field centered at 3D heating volume (X and Y (out of image plane); 2D VA scan axes; Z: axis along ultrasound beam). As shown in Figure 1, maximum heating occurs close to the transducer, not at the focal plane. This is because areas close to transducer are covered by many more ultrasound beams during the scan than areas within the focal plane. Heating for different attenuation is shown in Figures 2 and 3. Heating from scans (electronic scan over the transverse direction and mechanical scan over the elevation direction) of GE array transducers 7L and M4S is also calculated. Results are comparable to Figures 1–3, but images are not included here due to limited space.

Conclusions: Heating due to VA scan using confocal GE 7L and M4S transducers is under the FDA safety guideline of 6°C for tissue attenuation ranging from 0.5 to 1 dB/cm/MHz. Maximum heating occurs at the region below the transducer surface, not at transducer focal plane.

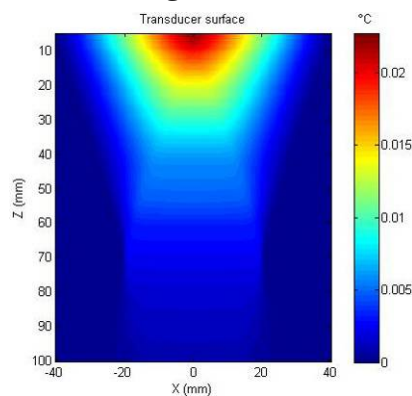


Figure 1:
Heating for attenuation
of 0.5 dB/cm/MHz.

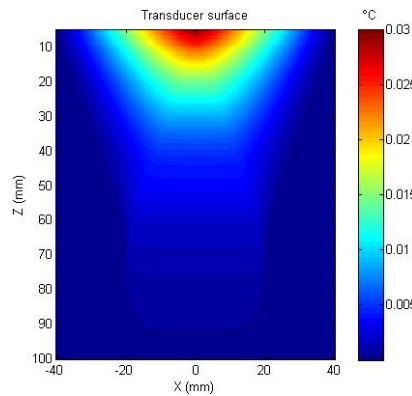


Figure 2:
Heating for attenuation
of 0.7 dB/cm/MHz.

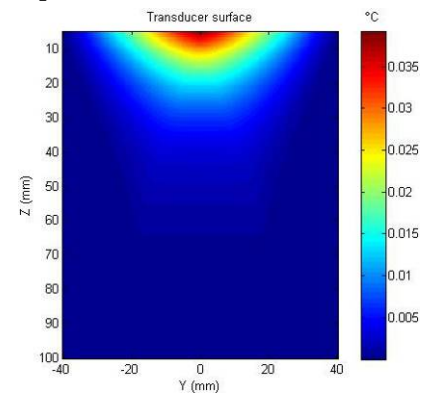


Figure 3:
Heating for attenuation
of 1 dB/cm/MHz.

Acknowledgements: This work is supported by grants CA 91956-06 P2 and EB00535.

References:

- [1] Fatemi, M. and Manduca A. et al., Imaging elastic properties of biological tissues by low-frequency harmonic vibration. Proceedings of the IEEE, 91(10): 1503-1518, 2003.
- [2] Palmeri, M.L. and Nightingale, K.R., On the thermal effects associated with radiation force imaging of soft tissue. IEEE Transactions on Ultrasonics Ferroelectrics and Frequency Control, 51(5): 551-565, 2004.

095 **MODALITY INDEPENDENT ELASTOGRAPHY: INITIAL RESULTS WITH A MURINE LIVER FIBROSIS MODEL.**

Michael I. Miga^{123*}, Jao J. Ou¹, Stephanie L. Barnes¹, Andrej Lyschik²³, John C. Gore¹²³.

¹Biomedical Engineering Department, Vanderbilt University, VU Station B, #351631, Nashville, TN, 37232, USA.; ²Radiology Department, Vanderbilt University Medical Center, Nashville, TN, 37235, USA; ³Vanderbilt University Institute for Imaging Science, Nashville, TN, 37235, USA.

Background: The predominant techniques in elastography utilize ultrasound or magnetic resonance imaging to spatially encode the measurement of displacements within tissue. Our laboratory has been investigating an approach that recasts the elastic inverse problem as a physically-constrained, non-rigid image registration problem utilizing numerical models and image similarity metrics to reconstruct the spatial distribution of elasticity parameters. While aspects to our approach are similar to conventional ultrasound elastography, the most notable difference with our method is that we construct elasticity information (Young's modulus) directly from similarity metrics rather than displacement fields. Over the past six years, we have successfully applied this technique to magnetic resonance, optical and X-ray computed tomographic imaging data. Given its relative independence on imaging data type, we have named the method 'modality-independent elastography' (MIE) [1-3].

Aims: In recent work, we have been investigating a chemically-induced murine liver fibrosis model for validation work and towards the development of a small-animal elastography platform. In this work, we present results that correlate mechanical properties as measured by a novel mechanical testing gel-liver assay and our elastography method on the same animal.

Methods: A mouse is subjected to weekly intraperitoneal injections of carbon tetrachloride (Sigma Chemical, St. Louis, MO, USA) mixed with olive oil in a 1:4 ratio to induce a fibrotic reaction within the liver. Upon sacrifice, a portion of liver tissue is suspended in a cylindrical gel for CT imaging, and subsequent mechanical testing; in addition, a second homogeneous gel is made concurrently. Within the CT environment, two image volumes of the gel-liver suspension are taken pre- and post-deformation using a custom compression device. A finite element model is built from the CT images, and boundary conditions are constructed in order to simulate the testing conditions on the gel-liver suspension. To assist in liver segmentation, the CT gel is doped with CT contrast agent. Using both the pre- and post-compression image volumes, MIE with spatial prior information is used to establish the elastic contrast ratio. In a second protocol to determine mechanical properties of the fibrotic liver independently, a separate mechanical testing unit (ELF 3100, Bose Corp., Enduratec Systems Group) is deployed. The protocol begins by acquiring force-displacement data from the homogeneous gel to determine its mechanical properties. Once established, force-displacement data is then collected on the gel-liver suspension. The elastic properties of the suspended liver are determined by matching the predicted applied stress from the finite element model to that determined from the mechanical tester while varying the liver modulus.

Results: The results indicate that our fibrotic murine liver had a Young's modulus of 1.31 kPa for the gel-tissue assay. Control mice indicated a normal Young's liver modulus of 0.62 +/- 0.09 kPa for the gel-tissue assay. Histological confirmation of the existence of fibrosis was also conducted. The elastic contrast ratio between gel and fibrotic liver tissue was established to be 4.23 for the gel-tissue assay. The elastic contrast ratio produced by MIE was 4.09 representing a remarkable 3% difference.

Conclusions: We are working towards a more complete understanding of elastographic measurements in controllable murine systems. Our goal is to correlate measurement, cellular mechanism and disease progression within the context of a novel murine elastography framework. The possibility of establishing metrics that correlate the cell and molecular biology of disease with the changes in organ integrity represent a new direction for elastographic research.

Acknowledgements: Work concerned with MIE reconstruction was funded in part by a Breast Cancer Research Program Predoctoral Traineeship Award (BC043661) of the Congressionally Directed Medical Research Program. Work conducted regarding mechanical testing was supported in part by a National Science Foundation Graduate Research Fellowship.

References:

- [1] M. I. Miga, "A new approach to elastographic imaging: Modality independent elastography," *Medical Imaging 2002: Image Processing*: Proc. of the SPIE, vol. 4684, pp. 604-611, 2002.
- [2] M. I. Miga, "A new approach to elastography using mutual information and finite elements," *Physics in Medicine and Biology*, vol. 48, pp. 467-480, 2003.
- [3] C. W. Washington and M. I. Miga, "Modality independent elastography (MIE): A new approach to elasticity imaging," *IEEE Transactions on Medical Imaging*, vol. 23, pp. 1117-1128, Sep 2004.

Rémi Souchon^{1*}, David Melodelima¹, Sabrina Chesnais^{1,2}, Marcela Oliveira de M Correia¹, Anthony Chapelon¹, Eric Delabrousse¹, Jean-Yves Chapelon¹.

¹INSERM Unité 556, Lyon, FRANCE; ²Institut de Chirurgie Expérimentale (ICE), Centre Régional Léon Bérard, Lyon, FRANCE.

Background: Good elastograms [1] can be obtained under laboratory conditions, but in order to become clinically useful, fast acquisition frame rate and real-time feedback are necessary [2,3,4].

Aims: Our aim is to develop a new real-time strain imaging platform for research purposes.

Methods: Our system, based on a standard PC, includes a fast digitizer and a digital I/O board for synchronization with the ultrasound scanner. It requires two digital signals from the scanner, start-of-frame and start-of-line. It can be connected to any ultrasound scanner equipped with an analogue radiofrequency (RF) output and these two digital signals. The system acquires RF frames at full bus speed and calculates elastograms in real-time using cross-correlation between consecutive RF frames. The strain, displacement and correlation images are displayed. A RF cineloop is stored in PC memory. It can be used to review the last images, to reprocess the RF data with different processing parameters and to save the RF data to files for off-line processing. In real-time mode, to gain speed, the system can use low lateral resolution and a small region of interest. In review mode, the acquisition is stopped and the system reprocesses the cineloop using high resolution and the full extent of the RF frames. The operator can quickly switch between the two modes. Using a BK-Medical scanner, we tested the system in phantoms, in rabbit liver and in various organs in a healthy volunteer.

Results: Figures 1–4 respectively show a gelatin phantom with an inclusion, a VX2 tumor in rabbit liver, the thyroid gland and the spleen in a healthy volunteer. The minimum speed required to obtain good quality elastograms was 5 frames per second (fps) in phantoms and 7 fps *in vivo*.

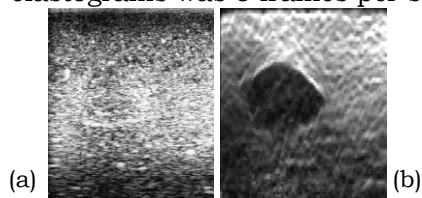


Figure 1: Gelatin phantom with a stiff inclusion. (a) B-mode, (b) Elastogram (3x4 cm, white=1.5% strain)

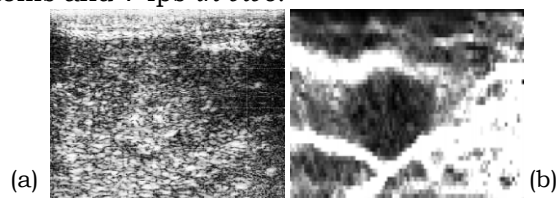


Figure 2: VX2 tumor in rabbit liver *in vivo*. (a) B-mode, (b) Elastogram (3x2.5 cm, white=2% strain)

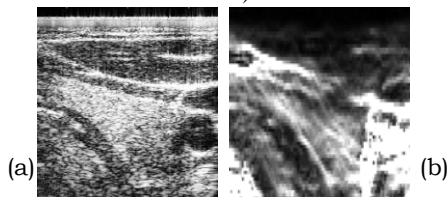


Figure 3: Thyroid gland in a healthy volunteer. (a) B-mode, (b) Elastogram (3x3.2 cm, white=4% strain)

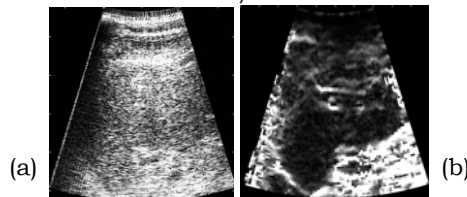


Figure 4: Spleen in a healthy volunteer. (a) B-mode, (b) Elastogram (10x10.5 cm, white=4% strain)

Conclusions: The prototype offers a scanner-independent platform for real-time strain imaging. It was able to acquire hand-held elastograms with a reasonable image quality in phantoms and *in vivo*. Real-time feedback was crucial to guide the compression direction and speed.

Acknowledgements: This project was supported in part by the National Cancer Institute (NCI) Program Project Grant P01-CA64957 to the University of Texas Health Science Center Houston.

References:

- [1] Ophir J et al. Elastography: a quantitative method for imaging the elasticity of biological tissues. *Ultrasonic Imaging* 13, 111–134, 1991.
- [2] Lorenz A et al. A new system for the acquisition of ultrasonic multicompression strain images of the human prostate *in vivo*. *IEEE Trans Ultrason Ferroelectr Freq Control* 46(5), 1147–1153, 1999.
- [3] Hall T et al. *In vivo* real-time freehand palpation imaging. *Ultrasound Med. Biol.* 29(3), 427–435, 2003.
- [4] Lindop JE et al. 3D elastography using freehand ultrasound. *Ultrasound Med. Biol.* 32(4), 529–545, 2006.

Background: Magnetic Resonance Elastography (MRE) is a technique for quantitatively imaging the elasticity of tissue [1]. MRE utilizes motion encoding gradients (MEG) to image shear waves. The waves are typically induced by a vibrating driver in contact with the skin. The waves are heavily attenuated and may not reach the structure of interest. An alternative approach is to use the radiation force of a focused ultrasonic transducer to induce transient shear waves directly inside the body [2,3].

Aims: Our aim is to develop a MRE system based on transient shear waves induced by radiation force.

Methods: To acquire wave images, we used a modified gradient echo sequence with an additional bipolar MEG. The sequence was implemented in a Siemens Symphony MR scanner equipped with a body coil. Typical acquisition parameters were TR=67 ms, 256x256 matrix, 20x20 cm field of view, slice thickness 10 mm, and TE varying between 14 and 25 ms depending on the duration of the MEG. The MEG direction was aligned with the acoustic axis of the transducer. The radiation force was generated using a spherical shell air-backed transducer operated at 2.4 MHz (diameter 70 mm, focus 90 mm). A programmable delay generator was used to allow for wave propagation between the firing of the transducer and the MEG. We tested our MRE sequence in *ex vivo* bovine liver.

We assessed the thermal effect of the sequence using an EPI MR thermometry sequence implemented in a Philips MR scanner [4]. The MR thermometry sequence was based on the shift of the proton resonance frequency with temperature.

Results: Figures 1 and 2 show typical coronal and transverse wave images. In these examples, the wave was detectable in a 6x4 cm region in longitudinal view and 4x4 cm in coronal view. In bovine liver, the shear wave propagated with a speed of 1.15 m/s (Figure 3), corresponding to a shear modulus of 1.3 kPa. The temperature rose by 10°C during the acquisition of one phase image, (Figure 4).

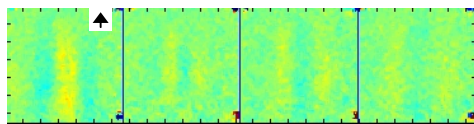


Figure 1: Phase (displacement) images acquired at 4 ms interval (longitudinal view). The arrow indicates the MEG direction (phase range $\pm \pi/4$, each tick = 1 cm).

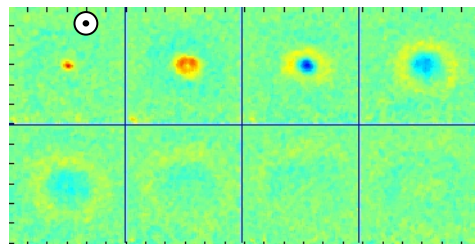


Figure 2: Phase (displacement) images acquired at 4 ms interval (coronal view, phase range $\pm \pi/4$, each tick = 1 cm).

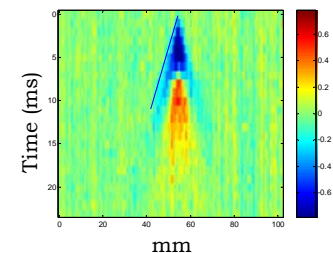


Figure 3: Phase vs. distance and time, showing wave speed of 1.15 m/s in bovine liver (shear modulus 1.3 kPa).

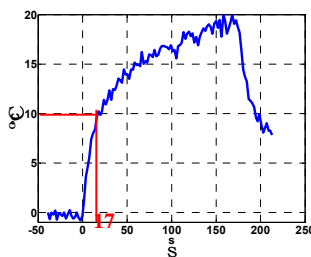


Figure 4: Temperature rise vs. time at the focus. The temperature rose by 10°C in 17 s (duration of the acquisition of one phase image).

Conclusions: The system was able to detect the shear waves induced by radiation force. Future work will include the development of an EPI sequence that will reduce the temperature rise by reducing the number of ultrasonic bursts.

References:

- [1] Sarvazyan AP et al. Shear wave elasticity imaging: a new ultrasonic technology of medical diagnostics. *Ultrasound Med Biol* 24(9), 1419–1435, 1998.
- [2] Muthupillai R et al. Magnetic resonance elastography by direct visualization of propagating acoustic strain waves. *Science* 269, 1854–1857, 1995.
- [3] Wu T et al. MR imaging of shear waves generated by focused ultrasound. *Magn Reson Med* 43(1), 111–115, 2000.
- [4] Salomir R et al. Local hyperthermia with MR-guided focused ultrasound: spiral trajectory of the focal point optimized for temperature uniformity in the target region. *J Magn Reson Imaging* 12(4), 571–583, 2000.

101 **MAMMOGRAPHIC THROUGH-PADDLE ELASTOGRAPHY FOR IMPROVED BREAST LESION CHARACTERIZATION.**

Rebecca C. Booi¹, Marilyn A. Roubidoux¹, Michael S. Richards¹, Jonathan M. Rubin^{1*}, Matthew O'Donnell², Mark M. Helvie¹, Anne L. Hall³, Paul L. Carson¹.

¹Radiology Department, University of Michigan Health System, Ann Arbor, MI, USA; ²Bioengineering Department, University of Washington, Seattle, WA, USA; ³General Electric Health Care, Milwaukee, WI, USA.

Background: Breast elastography has been performed most extensively in 2D using freehand techniques [1]. In freehand elastography, deformations are created when a skilled operator manually compresses the breast while holding the ultrasound transducer. These studies have shown that freehand elasticity imaging produces comparable sensitivity and contrast-to-noise ratio (CNR) to mechanically induced transducer motion [2]. However, freehand elastography often suffers from large out-of-plane motion, is highly operator dependent and it is difficult to obtain consistent or repeatable compression steps. Applying external strain with a mammographic paddle as part of a combined ultrasound/digital tomosynthesis x-ray system could provide more uniform deformation and breast stability than freehand elastography, offering opportunities to improve technique fidelity and 3D coverage. Because the compression process is automated, operator skill would no longer be a major determinant in image quality. Compression steps can be controlled with great precision and over a wide range of compression steps to obtain maximum strain signal-to-noise ratio (SNR). Finally, the efficacy of the proposed technique may be maximized when images are acquired in the same view as x-ray tomosynthesis images.

Aims: The goal of the current study was to assess the feasibility and quality of through-paddle elastography in a mammography mimicking unit. Additionally, to evaluate the characteristics of common breast masses (fibroadenomas, cancers and cysts) in elastograms and compare these characteristics with previous studies.

Methods: All elastography imaging experiments were conducted on a mammography-mimicking device which allowed for fine compression control. Images were acquired with a GE LOGIQ 9 system, providing IQ data capture, with a 7.5 MHz linear array imaging through a 2.5 mm thick TPX (polymethylpentene) paddle. Strain and differential correlation coefficient images were created from the acquired IQ images using phase-sensitive correlation-based speckle tracking algorithms [3]. Most patients in this study were additionally imaged in an x-ray tomosynthesis unit. *In vivo* studies were conducted on 28 consecutive human subjects, either imaged immediately before core biopsy (N=18) or following diagnosis from previous biopsies (solid lesions) or previous clinical mammograms/ultrasounds (cysts) (N=10). 20 cases were presented in a radiologist reader study to evaluate the appearances of different breast masses in elastograms and differential correlation coefficient images and compare results with the literature to determine whether elasticity imaging of this quality has promise of clinical utility when presented with high quality tomosynthesis and through-paddle ultrasound images.

Results: Through-paddle 2D elastography produced results comparable to the 2D freehand elastography at low strains ($\leq 0.5\%$). In the reader study 9 of 12 cysts were given a BI-RADS score of 3 or 4. The score was reduced to 2 in 4 of the 9, eliminating the need for intervention. The mean score for cysts fell from 3.2 to 2.8 based primarily on the differential correlation coefficient image. No fibroadenoma or cancer was given a score less than 3 for any modality or reader, so the elastography would not affect patient management. Only 2 of 8 of malignant lesions were judged more malignant after reviewing elasticity images, as they did not appear markedly stiffer than surrounding tissue. Comparing the lesion size in the elastogram versus the sonogram produced mixed results for malignant lesions, and produced a false positive result in 5 of 12 fibroadenomas.

Conclusions: The results of the reader study in this paper suggest that elastography might play a greater role in improving confidence that a benign lesion is benign, particularly in cases of benign cysts, rather than distinguishing malignant from benign masses.

Acknowledgements: This work was supported in part by NIH Grants RO1-CA91713 and R21-CA109440.

References:

- [1] Hall TJ, Zhu Y, Spalding CS. *In vivo* real-time freehand palpation imaging. *Ultras Med Biol* 2003; 29:427-435.
- [2] Doyley MM, Bamber JC, Fuechsel F, Bush N. A freehand elastographic imaging approach for clinical breast imaging: system development and performance evaluation. *Ultras Med Biol*, 2001; 27: 1347-1357.
- [3] Chen X, Xie H, Erkamp R, Kim K, Jia C, Rubin JM, O'Donnell M. 3-D correlation-based speckle tracking. *Ultrasonic Imaging* 2005; 27(1):21-36.

054 **QUANTIFICATION OF ORBICULAR MUSCLE CONTRACTION AND IDENTIFICATION OF SCAR TISSUE IN PATIENTS WITH A RECONSTRUCTED CLEFT LIP.**

Chris L de Korte^{1*}, Nancy van Hees², Richard GP Lopata¹, Gert Weijers¹, Christos Katsaros², Johan M Thijssen¹.

¹Clinical Physics Laboratory, ²Orthodontics and Oral Biology Department, Cleft Palate Craniofacial Unit, Radboud University Nijmegen Medical Center, Nijmegen, The NETHERLANDS.

Background: In patients with a schisis, the lip needs to be repaired. Restoring the continuity of the *orbicularis oris* muscle that is surrounding the mouth leads inevitably to scar formation. The amount of scar tissue and its position are directly related to the functional behavior and the cosmetic result of the procedure. With ultrasound, evaluation of the reconstruction of a cleft lip can be done based on geometrical features. However, functional information is lacking. With elastography, the deformation of the muscle might be assessed, and deformation might be an indicator of scar tissue position.

Aims: Quantification of orbicular muscle contraction as a marker for muscle function and identifier for scar tissue.

Methods: In this study, elastography is used to identify the presence and the amount of scar tissue in reconstructed cleft lips, as well as to investigate the functionality of the muscle. Elastograms of patients (3) and normal individuals (2) were acquired. Radiofrequency data (RF) were acquired at 50 frames per second for 3 seconds using an 11 MHz linear array (bandwidth of 7–11 MHz). During the acquisition, the subject was asked to contract the lips to a pout condition.

The raw ultrasound data was sampled at 39 MHz in the ultrasound machine and transmitted using a USB 2.0 interface to a workstation using a custom made module (AFLINK, Philips Medical Systems). The ultrasound signals were segmented into overlapping windows. Next, the displacement of the windows due to the deformation of the lip was determined using a coarse-to-fine strain estimation method [1]. This method is based on initially calculating the displacement using a large window (2.5 mm). Although the resolution is poor using such a large window, the accuracy is high. Then this estimate is used as the input for a strain estimate using a smaller window. The resolution of the displacement estimate is increased by using a 2D coarse to fine approach [1] resulting in a final resolution of 0.6 mm. Although the lateral strain estimate is not imaged, it is used to improve the axial strain estimate. Strain was calculated from the final displacement estimate using a least squares strain estimation (LSQSE) algorithm. Finally, the deformation of tissue over the full cycle was constructed from the strain data by cumulatively summing it.

Results: The cumulative strain images acquired in a representative normal volunteer over the full cycle show positive strain values in the orbicular muscle from initial resting state to pout condition and strain values returning to zero after release of the pout condition and going back to initial state. This corresponds to thickening of the muscle. The axial strain images were quantified by selecting regions in the *orbicularis oris* muscle. In normal lips, similar deformation patterns in the left, middle and right part of the muscle were observed with a maximum axial strain of 20%. In patients, strain patterns different from the normal strain patterns could be observed. Depending on the rate of success of the surgical procedure, small to large deviations were observed. In all regions with scar tissues decreased strain values were found. In a patient with severe disability, a maximum strain value of 5% was found in the scar tissue region. In a patient with a successful reconstruction, decreased strain values (up to 12% strain) were found in the scar tissue region, however, the regions were rather small. The observed strain curves might be enhanced further by tracking the region-of-interest in time during the contraction cycle.

Conclusions: Elastography of cleft lips is feasible and yields information that is additional to the information from conventional ultrasound images. Different contraction patterns in normal and cleft lips are found. The scar tissue can be differentiated from the muscle since lower deformation values were found in these regions. In this pilot study, the decrease of deformation in the scar tissue region was related with severity of disability.

References:

[1] R.G.P. Lopata, M.M. Nillesen, I.H. Gerrits, L. Kapusta, J.M. Thijssen, C.L. de Korte. Bi-Plane Cardiac Strain Imaging: a Feasibility Study, submitted.

009 **IN VIVO VISUALIZATION OF ABDOMINAL MALIGNANCIES WITH ACOUSTIC RADIATION FORCE IMPULSE IMAGING.**

Brian J. Fahey^{1*}, Rendon C. Nelson², Stephen J. Hsu¹, David P. Bradway¹, Douglas M. Dumont¹, Gregg E. Trahey^{1,2}.

¹Duke University, Durham, NC, USA; ²Duke University Medical Center, Durham, NC, USA.

Background: The feasibility of elasticity imaging as a useful mechanism for *in vivo* tumor visualization has been demonstrated in organs such as the breast, prostate, brain and thyroid. Although mechanical contrast also exists for abdominal masses [1], *in vivo* application of elasticity imaging for tumor visualization in organs such as the liver and kidneys has been extremely limited [2]. While investigations of diffuse diseases (such as liver fibrosis/cirrhosis) have garnered attention in elastography forums, difficulties associated with factors such as physiological motion and poor SNR at depth have hampered the success of two-dimensional displacement/strain imaging in these regions.

Aims: The goal of this study was to investigate the feasibility of visualizing tumors in the liver and kidneys with Acoustic Radiation Force Impulse (ARFI) imaging. In this presentation, we present the initial results from these investigations.

Methods: To date, 9 patients have been enrolled in one branch of an ongoing IRB-approved and NIH-funded clinical study. In this branch of the study, patients were imaged with both B-mode ultrasound and ARFI imaging immediately prior to either biopsy (n = 3) or treatment (n = 6) of suspicious/malignant masses in the liver (n = 7) or kidney (n = 2). The liver patient subset included 2 patients with hepatocellular carcinomas (HCCs) within cirrhotic livers and 5 patients with metastases in non-cirrhotic livers. Patient data were acquired using a Siemens Antares ultrasound scanner and a Siemens CH41 transducer operating at 2.2 or 1.8 MHz. All data were acquired during patient breath-hold, using ECG-triggering when possible. B-mode and ARFI images were compared both qualitatively and quantitatively.

Results: Quality ARFI images were successfully acquired of *in vivo* liver and kidney tumors at depths exceeding 10 cm. HCCs were visualized as more compliant than regional cirrhotic liver. Metastases were shown to be less compliant than regional non-cirrhotic liver. Renal tumors appeared as regions of low displacement. To date, displacement contrast in ARFI images has exceeded echo contrast for each mass encountered. Mean contrast for HCCs was 2.9 dB (range 1.5 - 4.2) in B-mode images vs. 7.5 dB (range 3.1 - 11.9) in ARFI images. Mean contrast for liver metastases was 3.0 dB (range 1.2 - 5.2) in B-mode images vs. 9.3 dB (range 5.7 - 13.9) in ARFI images.

Conclusions: The initial results of our study demonstrate the feasibility of visualizing liver and kidney malignancies with ARFI imaging. Given the low sensitivity of conventional B-mode ultrasound for detection of masses in these organs, contrast improvements available with the ARFI technique may hold several benefits for tumor characterization and for interventional device guidance. ARFI imaging is implemented entirely on a modified diagnostic scanner, and thus combined sonography/ARFI imaging allows for the benefits of both imaging techniques to be utilized in a highly complementary manner. Combined sonography/ARFI imaging may allow for contrast improvements *in vivo* without sacrificing the low cost, portability, or real-time visualization benefits of conventional ultrasound.

Acknowledgements: The authors would like to thank the nurses and staff at DUMC for their assistance with coordinating our clinical efforts. We thank Siemens Medical Solutions, USA, Ultrasound Division for their system support. This work was supported by NIH grants 1R01-HL-075485-02, 1R01-EB-002132-04, and 1R01-CA-114093-01.

References:

- [1] Yeh WC, Li PC, Jeng YM, et al. Elastic modulus measurements of human liver and correlation with pathology. *Ultrasound Med Biol.* 2002;28:467-474.
 - [2] Emelianov S, Rubin J, Lubinski M, et al. in *Proceedings of the 1998 IEEE Ultrasonics Symposium* 1749-1752 (IEEE, 1998).
-

010 **A FEASIBILITY STUDY OF CLINICAL RADIOFREQUENCY ABLATION ASSESSMENT WITH ACOUSTIC RADIATION FORCE IMPULSE IMAGING.**

Brian J. Fahey^{1*}, Rendon C. Nelson², Stephen J. Hsu¹, David P. Bradway¹, Douglas M. Dumont¹, Gregg E. Trahey^{1,2}.

¹Duke University, Durham, NC, USA; ²Duke University Medical Center, Durham, NC, USA.

Background: Radiofrequency ablation (RFA) is an increasingly popular, minimally invasive treatment option for malignancies located in structures such as the liver, kidneys, bones and prostate. Given its low cost, convenience and real-time capabilities, ultrasound (US) is the preferred mechanism for guiding the insertion of ablation electrodes at many institutions. However, US is notoriously unreliable for intra-procedure monitoring of developing thermal lesions [1]. Additionally, many patients present with isoechoic tumors that require the use of CT (with or without fluoroscopy) or MR imaging for electrode placement. Use of CT or MR methods for insertion guidance markedly increases the time requirements, cost and complexity of the procedure. CT and/or MR imaging are also relied upon for follow-up assessment of procedure success, in part due to the low sensitivity of US for detecting residual tumor.

Aims: Previous efforts by our group utilized an ovine model to demonstrate the potential of Acoustic Radiation Force Impulse (ARFI) imaging for real-time guidance of RFA and post-procedural assessment of induced thermal lesions [2]. The focus of the present study is to extend the investigation into a clinical forum and evaluate the feasibility of using ARFI imaging for guiding/assessing RFA in human subjects.

Methods: To date, 5 patients receiving RFA for liver malignancies have been recruited into an ongoing IRB-approved and NIH-funded clinical study. These patients were scanned with both B-mode ultrasound and ARFI imaging immediately before, during and in the first 45 min following their RFA procedure. In 3 patients, additional data were acquired when they returned for follow-up imaging 1-6 months post-procedure. Depths of target tumors in the patients ranged from 5-11 cm. Patient data were acquired using a Siemens Antares ultrasound scanner and a Siemens CH41 transducer operating at 2.2 or 1.8 MHz. All data were acquired during patient breath-hold. ECG-gated data acquisition was utilized during follow-up imaging but not during the patients' initial treatments. B-mode and ARFI images were compared both qualitatively and quantitatively.

Results: ARFI images were successfully acquired of target regions before, during and following RFA procedures. All tumors (both primary and secondary masses) and thermal lesions imaged to date were visualized with greater displacement contrast in ARFI images relative to echo contrast in B-mode images. Mean contrast of pre-ablation liver malignancies was 2.6 dB (range 1.2-4.2) in B-mode images vs. 7.9 dB (range 5.7-11.9) in ARFI images. Mean contrast of induced thermal lesions was 2.4 dB (range 2.0-2.9) in B-mode images vs. 6.2 dB (range 5.1-7.5) in ARFI images. Intra-procedure images provided real-time feedback related to the effectiveness of the procedure but, in some cases, were compromised in quality due to excessive gas bubble formation in the treatment region. Comparison of pre-ablation and follow-up ARFI images provided insight into the success of the procedures.

Conclusions: The preliminary results presented in this study show that ARFI imaging is a promising modality for use with clinical liver RFA procedures. ARFI imaging is implemented entirely on a modified diagnostic US scanner, making combined sonography/ARFI imaging a straightforward and convenient imaging protocol. Combined sonography/ARFI imaging may hold benefits for many stages of RFA treatment, including pre-procedure planning, electrode insertion guidance, visualization of thermal lesion growth, real-time detection of complications and post-procedure assessment of success. Although further investigations are required, it is possible that combined sonography/ARFI imaging may reduce the dependence on CT and/or MR methods for tumors difficult to visualize with US alone.

Acknowledgements: The authors would like to thank the nurses and staff at DUMC for their assistance with coordinating our clinical efforts. We thank Siemens Medical Solutions, USA, Ultrasound Division for their system support. This work was supported by NIH grants 1R01-HL-075485-02, 1R01-EB-002132-04, and 1R01-CA-114093-01.

References:

- [1] Gertner M, Worthington A, Wilson B, and Sherar M. Ultrasound imaging of thermal therapy in *in vitro* liver. *Ultrasound Med Biol.* 1998; 24(7): 1023-1032.
- [2] Fahey BJ, Hsu SJ, Wolf PD, et al. Liver ablation guidance with acoustic radiation force impulse imaging: challenges and opportunities. *Phys Med Biol.* 2006; 51: 3785-3808.

A Thitai Kumar^{1,2}, J Ophir^{1,2}, CM Chant³, LM Mobbs³ and BS Garra^{3*}.

¹The University of Texas Health Science Center Houston, Houston, TX, USA; ²University of Houston, Houston, TX, USA; ³University of Vermont, Burlington, VT, USA.

Background: It is known that among breast lesions, malignant tumors are generally more firmly bonded to their surroundings than are benign tumors [1]. Elastography is an imaging technique that applies a quasi-static compression to detect stiffness variations within ultrasonically scanned tissue to create strain elastograms. When the strain imaged is the axial-shear strain, the technique is referred to as axial-shear strain elastography [2]. It is known that the distribution of the axial-shear strain in an inclusion bearing material is determined by the degree of bonding at the inclusion-background interface. Thus, we hypothesize that imaging the axial-shear strain distribution may provide a method to visualize the degree of bonding of a tumor to its surrounding tissue, which may become useful in distinguishing between benign and malignant tumors.

Methods: The data reported in this study were acquired at University of Vermont by Dr. Garra. The data were acquired using a modified HDI-1000 (Philips) scanner. The acquisition protocol was multi-compression, with a step size of 0.25%. The total compression was 5% and thus each elastogram shown in this presentation is a multi-compression average of 20 realizations. The displacements from the pre- and post-compression radiofrequency data (rf) were estimated using an adaptive stretching algorithm while the axial-shear strain was estimated using the staggered strain estimator. A detailed list of references to these algorithms can be found in [2]. Axial-shear strain elastograms from a total of seven malignant tumors and seven benign tumors were investigated in this study. Pathological confirmation was obtained for all tumors.

Results: A typical set of axial-shear strain elastograms superimposed on the corresponding sonogram is shown in Figure 1. Only those pixels that had axial-shear strain values greater than 50% of the applied axial strain and the corresponding correlation coefficient was greater than 0.75 were overlaid on the corresponding sonogram to obtain the composite image. Observe that the extent of axial-shear strain region is different between both the types of tumor. Moreover, we also observe that the proximity of the axial-shear strain distribution to the tumor/background interface visible in sonogram is different for benign tumors compared to malignant tumors. This is consistent with earlier literature reports regarding a size discrepancy between sonograms and elastograms of malignant tumors [3]. These observations were consistent over the entire data set. A plot is shown in Figure 2 to visualize the clustering of benign and malignant cases using the normalized area of axial-shear strain region.

Conclusions: The results from preliminary data set suggest that the axial-shear strain elastograms can be used to visualize the degree of bonding at the lesion/background interface. A detailed study evaluating the potential utility of axial-shear strain elastograms in distinguishing between benign and malignant tumors is currently underway.

Acknowledgements: This work was supported in part by NIH program project grant P01-EB02105-13 awarded to the University of Texas Medical School Houston and by a grant from the University of Texas Medical School Houston.

References:

- [1] Chen EJ, Adler RS, Carson PL, et al. Ultrasound tissue displacement imaging with application to breast cancer, *Ultrasound in Medicine and Biology* 21(9), 1153-1162 (1995).
- [2] ThitaiKumar A, Krouskop TA, Garra BS and Ophir J. Visualization of bonding at an inclusion boundary using axial-shear strain elastography: A feasibility study, *Physics in Medicine and Biology* 52(5), 2615-2633 (2007).

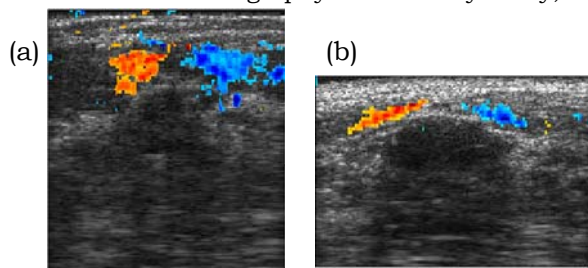
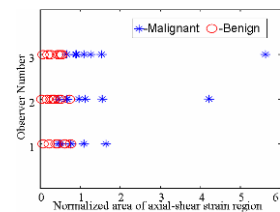


Figure 1: Composite images obtained by superimposing the axial-shear strain elastogram (color patches, see CD version) on top of corresponding sonogram of a cancer (a) and benign lesion (b).

Figure 2: Plot of the normalized values of the area of the axial-shear strain region feature from ASSE as obtained by three different observers. Notice that the malignant cases tend to cluster towards larger feature values compared to the benign cases, as determined by all observers.



057 **THE SPATIO-TEMPORAL STRAIN RESPONSE OF OEDEMATOUS AND NON-OEDEMATOUS TISSUE TO SUSTAINED COMPRESSION *IN VIVO*.**

Gearóid P. Berry¹, Jeffrey C. Bamber^{1*}, Peter S. Mortimer², Nigel L. Bush¹, Naomi R. Miller², Paul E. Barbone³.

¹Institute of Cancer Research, Sutton, Surrey, England, UK; ²Royal Marsden NHS Foundation Trust, Sutton, Surrey, England, UK; ³Boston University, Boston, MA, USA.

Background: Breast cancer related lymphoedema is a chronic swelling of the arm caused by an accumulation of excess interstitial fluid. The condition is often accompanied by a change in the time-dependent mechanical behaviour of the affected tissue under sustained compression [1–3]. However, non-imaging data acquisition techniques were used in previous investigations of this behaviour, and thus the nature of the spatio-temporal variation of the mechanical response is currently unknown. Such local knowledge may eventually help to identify which tissue layers have been worst-affected and thus help to explore the pathophysiology of this poorly understood condition.

Aims: Previously, we developed elastographic strain imaging techniques for imaging the time-evolution of the strain in fluid-rich poroelastic phantom materials under sustained compression [4,5]. In this current work, we investigate the extent to which these methods can be used to image the time-varying mechanical response of oedematous and non-oedematous tissue under sustained compression *in vivo*.

Methods: The ipsilateral (affected) and contralateral (apparently normal) forearm tissue of 6 patients presenting with unilateral lymphoedema was compressed and, once applied, the compression was sustained for at least 500 s while the axial strain (along the direction of sound propagation) was imaged as a function of time.

Results: Figure 1 displays the axial strain distribution in both arms of a typical patient at the end of the ramped compression and also displays the cumulative change in that axial strain distribution as a function of time since the instant at which the compression was fully applied. On both limbs, immediately after the compression was fully applied, Figure 1(b) shows that the axial strain was not uniformly distributed. Furthermore, post-compression, a redistribution of this axial strain occurred with time, some regions expanded in the axial direction while others contracted. The observed time-dependent behaviour is consistent with that of a layered poroelastic material. In all six patients, this time-dependent spatially-varying behaviour was seen in both arms, although in 5/6 it was more easily observed in the ipsilateral arm than the contralateral arm.

Conclusions: We conclude that, despite the presence of patient motion, it is possible to image the time-evolution of the compression-induced axial strain in soft biological tissue *in vivo* provided that a sufficiently-high echo-frame acquisition rate is used. The future development of a volumetric strain imaging capability should greatly facilitate the use of strain imaging as a clinical tool for the assessment of lymphoedema.

Acknowledgements: We thank the patients for participating in the trial, and EPSRC and ICR for funding this research. PE Barbone gratefully acknowledges support from NSF.

References:

- [1] Bates DO, Levick JR, Mortimer PS. Quantification of rate and depth of pitting in human edema using an electronic tonometer. *Lymphology* 1994;27:159–172.
- [2] Lindahl OA. The evaluation of a biexponential model for description of intercompartmental fluid shifts in compressed oedematous tissue. *Physiol Meas* 1995;16:17–28.
- [3] Mridha M and Odman S. Noninvasive method for the assessment of subcutaneous oedema. *Med & Biol Eng & Comput.* 1986;24:393–398.
- [4] Berry GP, Bamber JC, Armstrong CG, Miller NR, Barbone PE. Towards an acoustic model-based poroelastic imaging method: I. Theoretical Foundation. *Ultrasound Med Biol* 2006a;32:547–567.
- [5] Berry GP, Bamber JC, Miller NR, Barbone PE, Bush NL, Armstrong CG. Towards an acoustic model-based poroelastic imaging method: II. Experimental Investigation. *Ultrasound Med Biol* 2006b;32:1869–1885.

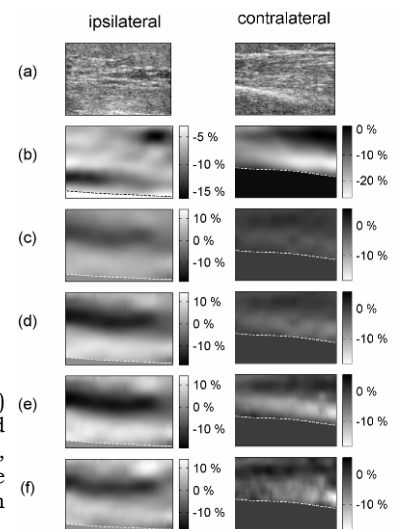


Figure 1: The spatio-temporal behaviour of the axial strain for both arms of a typical patient. (a) B-Mode images; (b) Axial strain immediately after the compression was fully applied (c-f) the change in axial strain since the compression was fully applied at times 50s, 150s, 275s, 400s respectively. All images for a given arm are co-registered and have dimensions 24mm (vertical) x35mm (horizontal). The top of each image is 3.3 mm below the surface of the skin. The tissue-bone interface is identified by the dashed line.

Background: In tissue engineering, biodegradable polymer scaffolds are used to support cells and growing blood vessels until they are replaced by the body's own extracellular matrix [1]. The mechanical and degradation property of the scaffold is one of the key design factors. Non-invasive feedback as a function of time will improve scaffold design and tissue culture methods [2]. Cell histology and direct mechanical measurements are invasive, and high growth deviation between specimens makes analysis difficult. Ultrasound elasticity imaging (UEI) based on phase sensitive speckle tracking can assess the internal mechanical, structural and compositional change at high resolution. *In-vitro* and *in-vivo* animal experiments are presented.

Aims: To quantitatively assess the degradation process of biomaterial scaffolds, *in-vitro* and *in-vivo* UEI and elastic modulus reconstruction were performed and compared with direct mechanical measurements and weight loss.

Methods: 6 Poly (1, 8 Octanediol-co-Citrate) (POC) scaffolds (D=6.0mm H=4.0mm, porosity=50%) were fabricated. Three scaffolds were degraded to about 40% by weight by agitating them in phosphate buffer solution at 25°C. UEI was performed on the scaffolds embedded in a gelatin phantom with ultrasound (US) scatterers before and after degradation. Under a local animal protocol, the other three scaffolds were implanted in pockets created in the back of an anesthetized immuno-compromised NIH-III mouse. A commercial US scanner (iU22, Philips) was used to collect RF data frames during a continuous deformation by a linear ultrasound probe. Phase-sensitive correlation-based 2D speckle tracking was performed to determine the strain. Strains developed in the scaffold were normalized to the average strain (about 10%) applied to the phantom and mouse. Elastic modulus was also reconstructed from measured displacement by using an appropriate mathematical model and solving an inverse problem. The compression test on the scaffold was also performed using a mechanical measurement device built in house [3].

Results: The average strain inside the scaffold was significantly increased after degradation both *in-vitro* and *in-vivo* (Figure 1). The elastic modulus change after degradation estimated from the stress-strain curve from the direct compression measurements matched well to the strain estimates. These measurements also correlate well with the percent weight loss. The strain map clearly illustrates the internal mechanical property change of the scaffolds both *in-vitro* and *in-vivo*. The strongly increased inhomogeneity in the strain map also reflects the local variability of internal structural decomposition of the scaffold. The reconstructed average elastic modulus compared well with the direct mechanical measurements.

Conclusions: Preliminary *in-vitro* and *in-vivo* results support the feasibility of UEI as a non-invasive monitoring tool of tissue scaffold degradation. This technique can be easily integrated into a commercial ultrasound scanner for real-time *in-vivo* animal study, possibly for a clinical tool to monitor the soft tissue growth and scaffold degradation.

Acknowledgements: Work supported in part by NIH grants EB-003451, HL-67647, HL-68658, HL-082640, and CA-109440. Thank Philips Ultrasound, Bothell, WA, USA for their system support.

References:

- [1] Gao J et al. Macroporous elastomeric scaffolds with extensive micropores for soft tissue engineering. *Tissue Eng*, 2006, 12:917-925.
- [2] Cohn N.A. et al., High Resolution, Elasticity Imaging for Tissue Engineering, IEEE Transactions on Ultrasonics, Ferroelectrics and Frequency Control UFFC, 2000, (47)956-966.
- [3] Erkamp RQ et al, Measuring the Elastic Modulus of Small Tissue Samples, Ultrasonic Imaging, 1998, 20:17-28.

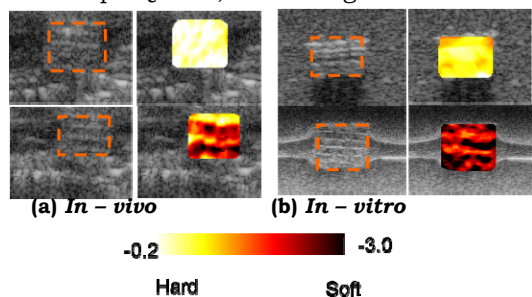


Figure1: Strain maps of POC scaffolds *in-vitro* (a) and *in-vivo* (b). The images in the top row are before degradation and those in the bottom row are after degradation. The dotted boxes represent the embedded scaffolds. The average strain after degradation was significantly increased. The strongly increased inhomogeneity in the strain map also reflects the local variability of internal structural decomposition of the scaffold. Note that the strain was normalized to the average applied strain estimated by the displacement of the bottom of the phantom and mouse during each deformation.

109 **BREAST ELASTICITY IMAGING AIDS PATIENT MANAGEMENT IN THE ONE STOP BREAST CLINIC.**

William E Svensson^{1*}, Nilofer Zaman¹, Nigel K Barrett¹, Gita Ralleigh¹, Keshthra Satchithananda¹, Stella Comitis¹, Vaishali Gada¹, Nik R Wakeham¹.

¹Breast Imaging and Radiology Department, Charing Cross Hospital, London, England, UK.

Aims: To demonstrate how real time freehand elasticity imaging aids management of patients in a one stop combined surgical and imaging breast clinic.

Background: The authors have been using real time elasticity breast imaging for over five years in a one stop breast clinic. The first four years (February, 2002 to February, 2006) were spent evaluating the potential of elasticity imaging as an adjunct to routine breast ultrasound as an addition to routine imaging assessment of breast problems for which ultrasound imaging was clinically indicated. Since February 2006, several versions of pre-release then release software have been evaluated while auditing the use of elasticity imaging.

Methods: The first four years work was done using Real Time Elasticity Imaging (Software from Hall & Zhu of KUMC) implemented on a Siemens Elegra (SE). Since February 2006, the work has been done on a Siemens Antares (SA) ultrasound scanner with updated and improved versions of the earlier software. All breast imaging was performed with a VFX 13–5 linear array transducer.

Patients, attending for routine breast ultrasound of focal breast abnormalities during the first four year research period, were invited to have breast strain imaging at the end of their ultrasound. The results of those initial studies led to the gradual adoption of strain imaging into routine clinical practice to improve diagnostic certainty. Current guidance for the use of elasticity imaging can be summarised as:

- 1) Clinical decisions must be based on current ultrasound practice.
- 2) Strain Imaging results may only be used to alter management if it results in the same or a more cautious approach to dealing with an abnormality.
- 3) The strain images recorded during the clinic are correlated with subsequent histology or follow up.
- 4) Situations include: identification of echogenic lesions as cysts, defining the extent carcinoma when significantly greater than demonstrated by B-mode, differentiating fat islands from pathology masquerading as a fat island.

Results: 930 strain imaging cases have been assessed so far (SE 334, SA 596). 237 Cancers (SE 116, SA 121), 35 intermediate grade lesions (SE 9, SA 26), 584 benign pathologies (SE 206, SA 378) 233 fibroadenomas, 104 cysts, 40 male gynaecomastias, 27 inflammation, 27 lymph nodes, 85 other benign conditions, and 91 areas of B-mode normal breast tissue. 51 cases currently have incomplete data.

Excluding cysts, lymph nodes and normal breast tissue, using an elasticity to B-mode ratio > 0.75 as an indicator for cancers and intermediate lesions, an audit of the Antares examined lesions over the last eighteen months shows: sensitivity = 97.5%, specificity = 48%. This compares with the earlier research on the Elegra with sensitivity = 96.3%, specificity = 53.3%. False negatives include two cases each of ADH and DCIS and one radial scar. Four phylloides, six mucinous cancers and 4 pure DCIS were true positives. During the last 18 months (Antares), the number of cancers with an elasticity to B-mode ratio between 1 and 0.75 dropped from 16% to 3.8%.

Audit of the Antares data showed in 45% of cases, strain imaging increases diagnostic confidence of the operator. In 2% of cases strain imaging effected management Cysts with echogenic contents were identified more easily, ensuring fine needle aspiration rather than core biopsy. Fibroadenomas, isoechoic with surrounding fat, were identified because of their stiffness allowing biopsy under ultrasound rather than stereotactic guidance.

Cancers with a smaller strain than B-mode footprint, all had either a worrying B-mode or colour Doppler vascular appearance. Ductal carcinoma *in situ* and invasive lobular cancers, causing minimal B-mode change, have larger areas of stiffness. Phylloides tumours, cellular fibroadenomas and all papillomas have similar sized B-mode and strain footprints. Inflammation and trauma tend to have smaller strain than B-mode footprints. No abnormal stiffness has been seen in B-mode normal breast tissue in cases with a low clinical index of suspicion. No focal stiffness has been seen in gynaecomastias, but other male breast pathology (Cancer 1, focal inflammation 2) has demonstrated increased stiffness.

Conclusions: Our experience is that real time elasticity imaging is a useful addition to routine breast ultrasound imaging.

Acknowledgement: Siemens have provided support for this work.

017 ON THE IMPACT OF VARYING VISCOELASTIC PARAMETERS ON IMPULSIVE ACOUSTIC RADIATION FORCE GENERATED SHEAR WAVES IN LIVER.

ML Palmeri^{1*}, MH Wang¹, SJ Rosenzweig¹, KR Nightingale¹.

¹Duke University, Durham, NC, USA.

Background: There are several imaging modalities that monitor shear wave propagation *in vivo* to characterize tissue, including Shear Wave Elasticity Imaging (SWEI), supersonic imaging (SSI), FibroScan, and Acoustic Radiation Force Impulse (ARFI) imaging [1-4]. The ways in which shear waves are tracked can vary, including using inversion of the Helmholtz equation [2], correlation-based “time-of-flight” estimates [5], and time-to-peak (TTP) displacement estimates [4]. While the Helmholtz algorithm is not dependent on *a priori* knowledge of shear wave shape or propagation, it relies on second-order differentiation of displacements that amplify jitter. Time-of-flight based methods do not require such differentiation, but are dependent on the stability of the shear wave morphology as it propagates.

Aims: The goals of this work are to characterize the tissue properties that affect the spatial and temporal stability of propagating shear waves in tissue, including elastic shear modulus, density, and viscosity, and to evaluate how changes in shear wave morphology impact the accuracy and precision of time-of-flight based shear wave speed estimation algorithms.

Methods: A parametric analysis of Gaussian excitation geometries, both symmetric and asymmetric with varying widths and temporal durations, was performed using finite element method (FEM) models of linear elastic and viscoelastic materials. A three-dimensional mesh with solid cubic elements with a 0.1 mm node spacing was solved using a time-domain, explicit algorithm using single-point quadrature (LS-DYNA3D, LSTC). Shear relaxation behavior for the viscoelastic materials was modeled using a Jaumann rate formulation. Simulation results were validated using calibrated phantom experiments and *in vivo* liver datasets acquired with a Siemens SONOLINE™ Antares scanner and a PH4-1 linear array (Siemens Medical Solutions USA, Ultrasound Division). 4:1 parallel receive tracking was utilized, and displacements were tracked using Loupas’ algorithm on IQ data.

Results: Simulation results of asymmetric Gaussian excitations demonstrate that the spatial extent of the region of excitation (ROE) in the plane of shear wave tracking is the dominant factor in determining the shear wave’s spatial morphology, as validated in calibrated tissue-mimicking phantoms. Duration (10–500 μ s) of the “impulsive” excitation does not influence the spatial extent of propagating shear waves. As expected in linear elastic materials, the mean energy of the shear wave travels with a linear shear wave speed once outside the ROE. When characterizing shear moduli in viscoelastic media, shear relaxations > 1 kPa over a range of 150 – 4000 Hz can introduce nonlinear temporal propagation of the mean energy of the shear wave, but the spatial morphology of the shear wave is maintained. Nonlinear trends have not been observed in healthy *in vivo* human liver data, with reconstructed shear moduli ranging from 1.4 – 3.0 kPa with a mean precision < 1.0 kPa.

Conclusions: As demonstrated in simulation and experiment, the spatial frequency of shear waves generated by focused, impulsive acoustic radiation force is dependent on the spatial extent of the region of excitation and is independent of the duration of the excitation (10 – 500 μ s). The temporal frequency content of the shear wave is dependent of the shear wave speed / shear modulus of the medium being characterized. To date, *in vivo* liver shear wave data generated with impulsive acoustic radiation force in healthy human volunteers do not demonstrate nonlinear viscous behavior when reconstructing shear wave propagation speeds using time-of-flight methods, specifically using the TTP displacement method.

Acknowledgements: The authors would like to thank Siemens Medical Solutions, Ultrasound Division for their technical support and Dr. Gregg Trahey for his insights. Funding: NIH R01-EB002132.

References:

- [1] Sarvazyan et al. “Shear Wave Elasticity Imaging: A new ultrasonic technology of medical diagnostics,” *UMB*, 24(9):1419–1435, 1998.
- [2] Bercoff et al. “Supersonic Shear Imaging: A new technique for soft tissue elasticity mapping,” *IEEE UFFC*, 51(4):396–409, 2004.
- [3] Sandrin et al. “Transient elastography: a new noninvasive method for assessment of hepatic fibrosis,” *UMB*, 29(12): 1705–1713, 2003.
- [4] Palmeri et al. “Quantifying hepatic shear modulus *in vivo* using acoustic radiation force,” *UMB*, in review.
- [5] McLaughlin et al. “Shear wave speed recovery in transient elastography and supersonic imaging using propagating wave fronts,” *Inverse Problems*, 22: 681–706, 2006.

018 **ACOUSTIC ENERGY BALANCE DURING DIAGNOSTIC AND THERAPEUTIC ULTRASOUND IMAGING.**

ML Palmeri^{1*}, RW Nightingale¹, KD Frinkley¹, GE Trahey¹, KR Nightingale¹.

¹Duke University, Durham, NC, USA.

Background: Ultrasonic acoustic energy interacts with tissue through both thermal and mechanical mechanisms. High Intensity Focused Ultrasound (HIFU) systems take advantage of these thermal mechanisms to provide therapeutic/ablative hyperthermia capabilities, while acoustic radiation force-based imaging modalities that have been developed over the past decade allow the mechanical properties of fluids and tissues to be characterized.

Aims: The goals of this work are to quantify the acoustic energy balance between thermal and mechanical energies for typical ultrasound configurations used during diagnostic and therapeutic soft tissue insonification and to determine how those energies dynamically change after being absorbed by tissue.

Methods: Finite element method (FEM) models of tissue heating and models of the dynamic response of elastic media to focused, impulsive acoustic radiation force excitations were used to characterize the thermal and mechanical energies associated with insonifications using a VF10-5 linear array on a Siemens SONOLINE™ Antares scanner. Field II [1] was used to characterize the three-dimensional acoustic intensity fields associated with these linear arrays. Acoustic attenuations ranging from 0.3 – 2.0 dB/cm/MHz were characterized, with fixed thermal material properties ($c_v = 4.2 \text{ J/cm}^3/\text{°C}$, $\kappa = 0.00143 \text{ cm}^2/\text{s}$). A mechanical parametric analysis with Young's moduli ranging from 1 – 30 kPa and Poisson's ratios ranging from 0.48-0.5 was performed. The FEM models were solved using LS-DYNA3D (LSTC) [3]. Thermal, strain, and kinetic energies were summed over all elements in the mesh; energies were quantified using LS-PREPOST2 (LSTC) in 10 μs time steps. Temperature fields were experimentally validated using Type T thermocouples (Omega) and thin film thermocouples (TFT) after insonifications with a VF10-5 linear array; dynamic displacement fields were validated experimentally using calibrated tissue-mimicking phantoms.

Results: In a 0.5 dB/cm/MHz attenuating medium where 2% of the attenuated acoustic energy is assumed to scatter [4], 55% of the total transmitted energy is absorbed within the region of excitation (ROE), with >54.9% of the total transmitted energy leading to tissue heating (10^{-3} J). For increasing acoustic attenuation, peak temperatures generated during tissue heating decrease, but total thermal energy generated increases. The distribution of mechanical energy (10^{-9} J) associated with acoustic radiation force-induced deformation of an elastic solid varies relative to the excitation. Initially, after an "impulsive" ($\sim 45 \mu\text{s}$) excitation, > 90% of the energy is accounted for by the kinetic energy fields, while after the material achieves peak displacement in the ROE, the kinetic energy accounts for $\sim 2/3$ of the total energy, with the remaining energy present in the shear strain fields that propagate away from the ROE. Strain and kinetic energy fields decrease as an elastic material becomes more incompressible ($\nu \rightarrow 0.5$). While the mechanical energies associated with an insonification persist at appreciable levels for several milliseconds, the thermal energies can persist for tens of seconds. The heat generated during acoustic absorption can also lead to thermal expansion of tissue and thermoacoustic emissions; these energies are currently being characterized.

Conclusions: Insonification of tissue with ultrasonic frequencies leads to a complex dynamic balance between thermal and mechanical energies that persist on different time domains (10^1 vs. 10^{-3} s) and vary appreciably in magnitude (10^{-3} vs. 10^{-9} J). Acoustic radiation force-based imaging modalities are able to take advantage of very small amounts of absorbed acoustic energy, compared with thermal energy, to generate strain fields in tissue. While the dynamic displacement behavior of focused, impulsive acoustic radiation force excitations are shear mediated, material properties such as Poisson's ratio can have a significant effect on the amount of mechanical energy that is coupled into the material.

Acknowledgements: Siemens Medical Solutions, Ultrasound Division; NIH R01-EB002132.

References:

- [1] Jensen *et al.* "Calculation of pressure fields from arbitrarily shaped, apodized, and excited ultrasound transducers," IEEE UFFC, 39(2): 262-267, 1992.
 - [2] Palmeri *et al.* "On the thermal effects associated with radiation force imaging of soft tissue," IEEE UFFC, 51(5): 551-565, 2004.
 - [3] Palmeri *et al.* "A finite-element method model of soft tissue response to impulse acoustic radiation force," IEEE UFFC, 52(10): 1699-1712, 2005.
 - [4] Parker, K. "Ultrasonic attenuation and absorption in liver tissue," UMB, 9(4): 363-369, 1983.
-

Background: Dynamic elastography holds great promise for biological tissue characterization. Resulting from the radiation force induced by a focused ultrasound beam, plane shear waves are generated within the medium and imaged with an ultrafast ultrasound scanner. Known as Supersonic Shear Imaging (SSI) technique, this method allows computation of shear modulus (μ) maps from estimates of shear wave velocities. Additionally, in order to improve tissue evaluation, the estimation of the nonlinear elastic moduli could be of some interest. Recently a new formulation of the nonlinear equation describing the propagation of plane shear waves in isotropic soft incompressible solids has been developed using a new expression, up to the fourth order, of the strain energy density (e):

$$e = \mu I_2 + \frac{A}{3} I_3 + D I_2^2,$$

where in this case, I_2 , I_3 are invariants of the strain tensor and A , D the third and fourth order shear elastic constants. It has been shown that the nonlinearity parameter is only composed of three coefficients $\beta_s = \beta_s(\mu, A, D)$.

Aims: To date, no measurement of the parameter D has been carried out in incompressible media.

Methods: In order to estimate the nonlinear parameter A , this theoretical background on soft incompressible solids is applied to the acoustoelasticity theory. Such analysis gives the variations of shear wave speed as a function of the applied stress and leads to measure both the linear shear modulus (μ) and the third order shear modulus (A). Taking advantage of the SSI technique, an acoustoelasticity experiment is performed in different kinds of incompressible soft media (agar-gelatin phantoms, PVA phantoms). In addition, to create finite amplitude plane shear waves, the SSI technique is replaced by a vibrator applied at the surface of the phantoms. Thanks to the ultrasound ultrafast imaging system, shock shear wave formation is visualized. Then by comparing experiments and numerical simulations based on the discrete Burgers equation and, taking into account both viscosity and nonlinearity, the nonlinear parameter β_s is deduced. Finally, the combination of these experiments with results obtained in the acoustoelasticity experiments leads to the determination of the fourth order elastic modulus (D).

Results: First, measurements of the A modulus reveal that while the behavior of phantoms is quite close from a linear point of view, the corresponding nonlinear modulus A is quite different. Secondly, results from the complete procedure reveal a variation of the nonlinear behavior as a function of the increasing gelatin concentration. This set of experiments provides the characterization, up to the fourth order, of the nonlinear shear elastic moduli in incompressible soft media.

Conclusions: These combined techniques provide the first experimental measurement of the fourth order nonlinear shear modulus in incompressible media. Moreover, applied to acoustoelasticity, the SSI technique provides potential medical applications in conditions *in vivo* for characterization of the nonlinear shear properties of biological tissues.

079 **THE SUPERSONIC SHEAR IMAGING AS A QUANTITATIVE TOOL FOR IMAGING *IN VIVO* LIVER STIFFNESS.**

T. Deffieux¹, J.-L. Gennisson¹, M. Muller¹, M. Couade², J. Bercoff², M. Tanter^{1*}, M. Fink¹.

¹Laboratoire Ondes et Acoustique, ESPCI-CNRS UMR7587-INSERM-Université Paris VII, 10 rue Vauquelin 75231 Paris Cedex 5, FRANCE; ²Supersonic Imagine, Les Jardins de la Duranne, 510 rue René Descartes 13857 Aix-en-Provence Cedex, FRANCE.

Background: Recently, it has been clinically proven, that fibrosis staging can be assessed by a rough estimation of liver stiffness averaged along an ultrasonic A-line. Providing a complete 2D map of liver stiffness would thus be of great clinical interest for the diagnosis of hepatic fibrosis and help prevent impending cirrhosis. However, such measurement requires both a quantitative value of shear elasticity and great precision to discriminate between different fibrosis levels.

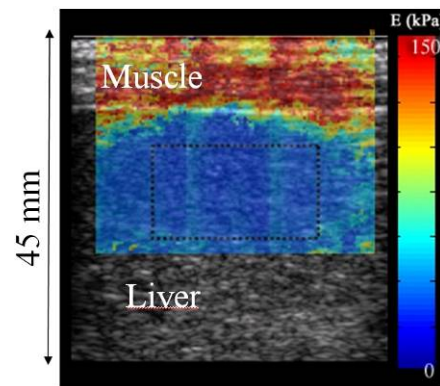
Aims: Beyond the scope of fibrosis quantification, it is also envisioned that quantitative elasticity imaging of liver will have potential interest for liver cancer diagnosis. In this work, the Supersonic Shear Imaging technique (SSI) is proposed to map the *in vivo* viscoelastic parameters of liver.

Methods: The SSI technique relies on the radiation force induced by a conventional ultrasonic probe to generate a planar shear wave deep into tissues. Thanks to an ultrafast ultrasound scanner (up to 5000 frames/s) the shear wave propagation throughout the medium is caught in real time. Using a reconstruction algorithm applied on these data, a map of the shear wave velocity of tissues is computed. A first feasibility study on 20 healthy volunteers has been conducted in order to investigate the reproducibility of the technique. Quantitative maps of liver elasticity were produced for each volunteer.

Results: The feasibility of inducing shear waves using the supersonic shear imaging technique is demonstrated in *in vivo* liver. The SSI approach is shown to be independent of the boundary conditions, e.g. the intercostal placement of the 1D linear array does not modify the ultrasound insonification and does not disrupt the “pushing” focused ultrasound beam. It is shown on 20 healthy volunteers that the assessment of quantitative elastic maps of the liver *in vivo* is feasible and reliable as shown in Figure 1. The good reproducibility and accuracy of the shear elasticity are discussed. Finally, the implementation of the technique on curved arrays is also proposed, discussed and validated. The improvement of the elasticity map using coded excitations (chirps) to image in deep zones of interest in liver is also experimentally quantified.

Conclusions: The SSI approach is of a great interest to non-invasively map the viscoelastic properties of liver *in vivo* and to assist physicians in liver diseases diagnosis.

Figure 1: *In vivo* assessment of Young’s modulus in a healthy volunteer.



References:

- [1] L. Sandrin, B. Fourquet, J.-M. Hasquenoph, S. Yon, C. Fournier, F. Mal, C. Christidis, M. Ziou, B. Poulet, F. Kazemi, M. Beaugrand and R. Palau. Transient Elastography: a new non invasive method for assessment of hepatic fibrosis, *Ultrasound in Med. & Biol.*, Vol. 29, No. 12, pp. 1705-1713, 2003.
- [2] J. Bercoff, M. Tanter, M. Fink. Supersonic shear imaging : a new technique for soft tissues elasticity mapping, *IEEE Trans. on Ultr., Ferr. And Freq. Ctrl.*, Vol 51(4), pp 396-409, April 2004.

080 **DIAGNOSTIC OF LIVER FIBROSIS IN RATS – COMPARISON BETWEEN SUPERSONIC SHEAR IMAGING AND MR ELASTOGRAPHY.**

N. Salameh¹, J.-L. Gennisson², B. Larrat¹, T. Deffieux², M. Tanter², R. Sinkus^{2*}, B. van Beers¹, M. Fink².
¹Diagnostic Radiology Unit, Hopital Saint Luc, Université Catholique de Louvain, 10 av Hippocrate, 1200 Brussels, BELGIUM; ²Laboratoire Ondes et Acoustique, ESPCI – CNRS UMR7587 – INSERM – Université Paris VII, 10 rue Vauquelin 75231 Paris Cedex 5, FRANCE.

Background: Elastography is a non invasive method to evaluate liver fibrosis by measuring the viscoelastic properties of the liver. The presence of fat in the liver can affect the viscoelastic properties of the tissues. Therefore, this may lead to misdiagnosis and, thus, to insufficient treatment of the patients.

Aims: The aim of this study is to diagnose *in vivo* liver fibrosis combined with hepatic steatosis using elastography. The effect of artificially induced steatosis is investigated within a longitudinal study on Sprague-Dawley rats fed with a choline deficient diet over 8 weeks. Results are obtained via two different elasticity imaging techniques: full 3D Magnetic Resonance Elastography (MRE) using a high field 7 Tesla system and Supersonic Shear Imaging (SSI) using a modified commercial ultrasound scanner (ATL HDI 1000).

Methods: MRE [1]: rats were placed under anesthesia in prone position on a piezoelectric based mechanical driver which generated mechanical waves at 300 Hz. The full 3D displacement field was imaged inside the liver (Figure 1a) in the stationary wave regime (Figure 1b) and used to calculate the shear modulus (Figure 1c) through a full inversion of the wave propagation problem.

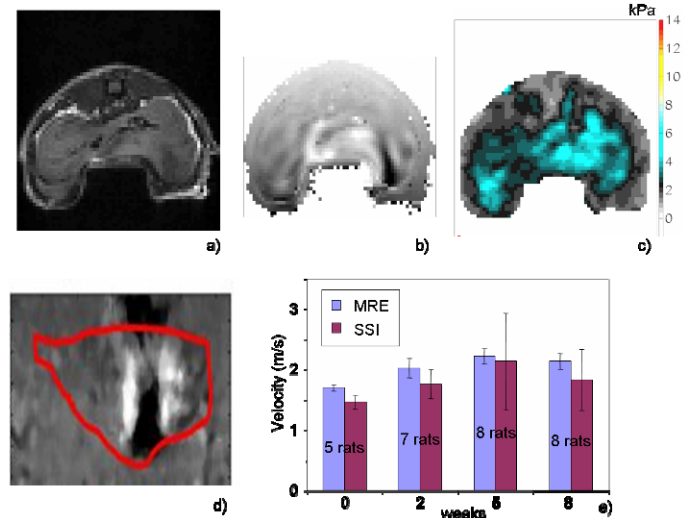
SSI [2]: Transient shear waves (with bandwidth frequency of 50–300 Hz) were generated inside the liver along a line using the SSI approach with the rats under anesthesia in the supine position. Using the same ultrasound transducer array, the shear wave propagation was imaged in real time (Figure 1d).

Results: Both techniques showed a clear increase of the shear velocity as a function of duration of the diet (Figure 1e) with a good quantitative agreement for the calculated values. Correlation with histology approach is also presented and explains the evolution of the shear wave’s velocity assessed with the two different techniques.

Conclusions: Considering MRE as the gold standard, due to its full 3D approach, this study demonstrates the validity of the SSI technique to assess the degree of the liver fibrosis in a much shorter scan time.

Figure 1:

- a) MR image of a rat liver;
- b) One component of the displacement obtained with MR–elastography;
- c) Elasticity map of the rat liver;
- d) Transient shear waves generated in the liver with the ultrafast ultrasound system;
- e) Shear wave velocity assessed in the rat livers with MRE or SSI as a function of the stage of fibrosis.



References:

[1] R. Sinkus, M. Tanter, T. Xydeas, S. Catheline, J. Bercoff and, M. Fink, “Viscoelastic shear properties of *in vivo* breast lesions measured by MR elastography”, Magn. Reson. Imaging, Vol.23 (2), pp. 159–165, 2005.
 [2] J. Bercoff, M. Tanter and, M. Fink, “Supersonic shear imaging: a new technique for soft tissues elasticity mapping”, IEEE Transactions on Ultrasonics, Ferroelectrics And Frequency Control., Vol. 51(4), pp 396–409, 2004.

* indicates Presenter

097 **HIGH RESOLUTION MR-ELASTOGRAPHY: A UNIQUE TOOL TO STUDY THE RHEOLOGICAL PROPERTIES OF TISSUE *IN VIVO* AND THE ORIGIN OF ITS MULTISCALE BEHAVIOUR.**

Benoît Larrat^{1*}, Najat Salameh², Mickael Tanter¹, Mathias Fink¹, Ralph Sinkus¹.

¹Laboratoire Ondes et Acoustique, ESPCI, CNRS UMR 7587, INSERM, Université Paris VII, 10 rue Vauquelin, 75231 Paris, FRANCE; ²Unite RDGN, Clinique Universitaire Saint Luc, Imagerie par Résonance Magnétique, 10 av Hippocrate, 1200 Brussels, BELGIUM.

Background: Although the rheology of soft tissue samples is subject to extensive studies, mainly via rheometer measurements, only a few papers discuss the mechanical behaviour of living biological tissues [1,2]. This is mainly due to the lack of a reliable and accurate technique to quantitatively assess the stress-strain relationship *in vivo*.

Aims: In this study, we show that MR-Elastography with its full 3D potential gives unique access to the frequency dependency of the complex shear modulus. Multi-frequent experiments were conducted in rat brain tissue, fibrotic rat liver and human breast tissue. Additionally, a full physically-motivated model, in agreement with the causality principle, has been developed to explain the observed dispersion properties. Finally, finite element simulations were conducted to explain the observed frequency dependence and to understand its microscopic origin.

Methods: For animal studies, experiments were conducted on a high-field MR-scanner (Bruker Pharmascan 7 Tesla). Piezoelectric plates were used to generate steady state shear waves inside the organ of interest. Monochromatic acquisitions were repeated between 200 and 1000 Hz in rat brains. A longitudinal preliminary study was performed within the liver of rats developing fibrosis artificially induced by a choline deficient diet over several weeks. For human breast experiments, a full body MR-scanner was used (Philips Intera Achieva 1.5 Tesla) with a dedicated mechanical driver for breast elastography. Data were acquired between 65 and 100 Hz on healthy volunteers. All experiments were performed using a motion-sensitized MR sequence phase-locked to the mechanical excitation. This allowed recording all 3 components of the entire displacement field for each frequency. A local inversion algorithm was used to reconstruct the 3D maps of the complex shear modulus removing remnants of the compressional wave via the application of the curl operator.

Results: In all experiments, both real and imaginary parts of the complex shear modulus were found to rise with frequency according to a power-law. In addition, the ratio between those 2 quantities appeared to be constant with frequency and directly linked to the exponent of the power law. Based on the hypothesis of a power-law damping, a full physical model was derived to fit the data taking into account the causality principle (Kramers-Kronig relations) [3]. This leads to a new interpretation of the viscoelastic properties in terms of intrinsic properties and architecture.

Conclusions: MR-Elastography can be efficiently used to study rheology *in vivo*. The frequency behaviour of the macroscopic viscoelastic parameters gives additional information about the microscopic structure of the material. The observed power-law leads to the hypothesis that an underlying self-similar network is responsible for it [4]. Simulations show that the vascular network is a potential candidate. If proven, this could lead to a contrast provided on a macroscopic scale sensitive to changes on the level of the microscopic vascular architecture [5]. Furthermore, at low frequency, the apparent loss modulus seems to originate more from the multiple scattering at the micro level than from the intrinsic viscosity. Further work is needed to validate this hypothesis.

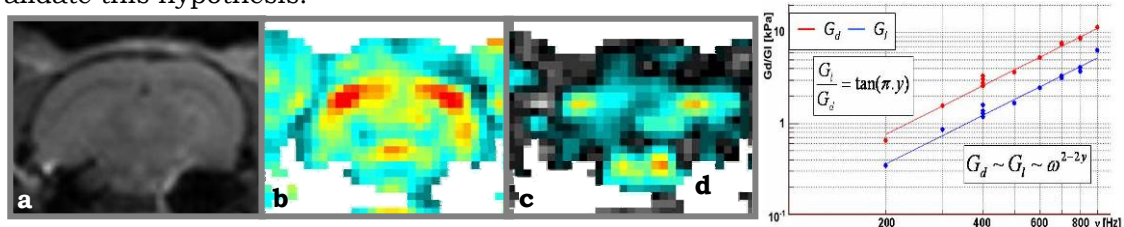


Figure 1: High resolution magnitude MR image in the rat brain (a) and the corresponding dynamic modulus (b) and loss modulus (c) at 400Hz. Dispersion curves for both moduli between 200 and 900 Hz (d).

References:

- [1] Kiss MZ, et al. Phys Med Biol. 2004;49(18):4207-4218.
- [2] Fabry B, et al. Phys Rev E. 2003;68:041914.
- [3] Pritz T. J of Sound and Vibration. 1999; 228(5):1145-1165.
- [4] Oshmyan VG, et al. Phys Rev E. 2001;64:056108.
- [5] Gazit Y, et al. Microcirculation. 1997 Dec;4(4):395-402.

B. Larrat^{1*}, Q. C. Chan^{2,3}, X. F. Yang³, G. Li³, E. S. Yang^{2,3}, M. Fink¹, R. Sinkus¹.

¹Laboratoire Ondes et Acoustique, ESPCI, CNRS UMR 7587, INSERM, Université Paris VII, 10 rue Vauquelin, 75231 Paris, FRANCE; ²Electrical and Electronic Engineering Department, The University of Hong Kong, Pokfulam, Hong Kong, CHINA; ³Jockey Club MRI Centre, The University of Hong Kong, Pokfulam, Hong Kong, CHINA.

Background: Alzheimer’s disease (AD) is characterized by progressive cognitive deterioration with declining activities of daily living and neuropsychiatric symptoms. It is the most common cause of dementia. It is recognized that the production and maintenance of myelin is essential for normal brain function. Age-related breakdown of myelin negatively impacts cognitive performance with the neurofibrillary tangles and amyloid plaques being the hallmarks of the disease [1,2]. Currently, the only definite way to diagnose AD is to determine whether there are plaques and tangles in brain tissue. This requires histopathological examination of brain tissue. Previous research on AD using MRI focuses mainly on direct amyloid plaque imaging.

Aims: This study aims to validate the hypothesis that AD alters the mechanical properties of the axons in the region between hippocampus and cortex, i.e. within the corpus callosum (CC), which is the area most strongly affected by demyelination.

Methods: As a unique tool to study those properties non-invasively, we use 3D MR-elasticity (MRE) operating at 1000Hz mechanical excitation frequency with a high-field MRI system (Bruker Pharmascan 7T). Post-processing of the mechanical wave (as measured by MRE) provides the shear modulus perpendicular (μ_{Perp}) and parallel (μ_{Para}) to the local fiber direction within the brain at 300 μ m isotropic resolution. Transgenic mice expressing mutant human PS1–Leu235Pro and APP^{sw} were established at the National Institute of Environmental Health Science, NC3. Seven 16 to 18-month old male (25–40g) APP/PS1 (n=3) and wild-type (WT) mice (n=4) were studied.

Results: As expected from normal anatomy, we observe locally enhanced values for the anisotropy ($A=\mu_{Para}/\mu_{Perp}$) between the cortex and hippocampus characterizing the transversal isotropic mechanical properties of the axons. The AD group shows a decrease of about 8% in fractional anisotropy (FA, definition identical to Diffusion Tensor MR-Imaging-DTI) compared to the WT group. The FA within the region of the thalamus remains unchanged. The decrease of FA is similar to previous DTI study findings.

Conclusions: These preliminary results indicate that AD influences the mechanical properties of the axons. Longitudinal studies are currently being prepared to follow the temporal evolution for the mechanical properties for each mouse individually.

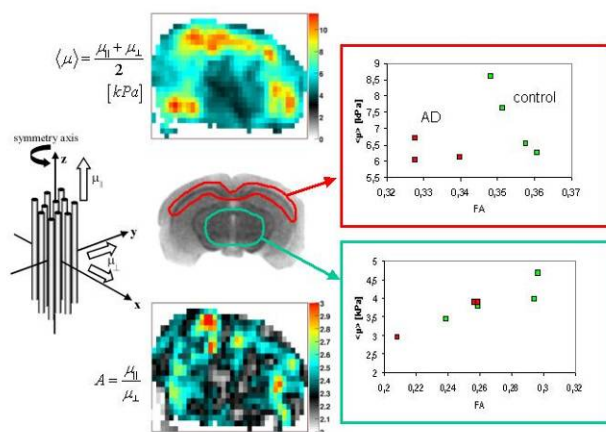


Figure 1: Mean elasticity map and anisotropy map in an AD mouse brain. Average values of those parameters in the corpus callosum (red/top) and in the thalamus (green/bottom) for both control group and AD group.

References:

[1] Bilgen M., Elshafiey I. and Narayana P.A.: Mohr Diagram representation of anisotropic diffusion tensor in MRI. Magn. Reson. Med. 47: 823–827, 2002.
 [2] Sinkus R., Tanter M., Catheline S., Lorenzen J., Kuhl C., Sondermann E. and Fink M.: Imaging anisotropic and viscous properties of breast tissue by magnetic resonance-elasticity. Magn. Reson. Med. 53: 372–387, 2005.

072 **A NOVEL *IN VIVO* QUANTITATIVE SONOELASTOGRAPHIC TECHNIQUE FOR INVESTIGATING THE ELASTICITY OF SKELETAL MUSCLE TISSUE.**

K Hoyt^{1*}, B Castañeda¹, T Kneezel¹, KJ Parker¹.

¹University of Rochester, Rochester, NY, USA.

Background: Elasticity imaging modalities have considerable potential for assessing the biomechanical state of tissues and organs. Based on shear wave interference patterns (termed crawling waves), a novel two-dimensional (2D) quantitative sonoelastographic technique was developed utilizing a dual mechanical source configuration which vibrates normal to the tissue surface. Since crawling wave patterns depend on the elastic properties of the supporting medium [1], analysis of such allows for the non-invasive characterization of soft tissue elasticity.

Aims: To develop and evaluate a novel quantitative sonoelastographic technique for characterizing the elastic properties of human skeletal muscle *in vivo*.

Methods: To evaluate our novel sonoelastographic shear velocity estimation technique, a simulation program was developed in Matlab. Specifically, crawling waves produced using two parallel strip loads vibrating in a direction normal to the free surface of semi-infinite isotropic elastic solid were modeled using the displacement equations presented by Miller and Pursey [2]. Experimental results were obtained using a GE Logiq 9 ultrasound scanner with demodulated color flow data saved for processing. Shear velocity sonoelastograms were produced offline from the reconstructed crawling wave images using a 2D autocorrelation-based estimation technique. Statistics were computed from shear velocity sonoelastogram sequences (equating to one spatial wavelength of crawling wave propagation). Using a homogeneous gelatin-based elasticity phantom, shear velocity results were obtained (for vibration frequencies of 75 to 200 Hz in 25 Hz increments) and compared to theoretical crawling wave results. Clinical data were obtained from the relaxed quadriceps femoris muscles in two healthy male volunteers to demonstrate clinical utility. For the *in vivo* scans, the mechanical source setup was oriented under B-mode guidance to produce shear wave propagation parallel to the muscle fibers to minimize anisotropic effects. Note for all experimental results, the source pair (separated by 11 or 15 cm about the lateral axis of the US transducer) was vibrated at slightly offset frequencies (0.2%) in order to produce slowly propagating shear wave interference patterns.

Results: Simulation results describe an effective region-of-interest (ROI) where shear velocity reconstructions can be assumed valid. Within this ROI, simulation and experimental results (in homogeneous elastic material) are in good agreement. Regarding *in vivo* experiments, a representative set of images obtained from the relaxed quadriceps femoris muscle (with shear wave propagation parallel to muscle fibers) is depicted in Figure 1. Comparison of frequency-dependent shear velocity data from contralateral muscles and between subjects was not statistically different ($p > 0.74$ and $p > 0.91$, respectively), which demonstrates reproducibility albeit based on limited data. Furthermore, a systemic dependence of shear velocity estimates on shear rate confirms that skeletal muscle tissue is viscoelastic.

Conclusions: A novel quantitative sonoelastographic technique was developed and analyzed. Results indicate this method may be feasible for characterizing the elastic properties of skeletal muscle tissue.

Acknowledgements: This work was supported by NIH Grant 5 R01 AG16317-05.

References:

- [1] Hoyt K, Parker DJ, Rubens DJ. Sonoelastographic shear velocity imaging: An application of crawling waves. Proceedings of 5th International Conference on the Ultrasonic Measurement and Imaging of Tissue Elasticity, 2006.
- [2] Miller GF, Pursey H. The field and radiation impedance of mechanical radiators on the free surface of a semi-infinite isotropic solid. Proceedings of the Royal Society of London A, 223: 521-541, 1954.

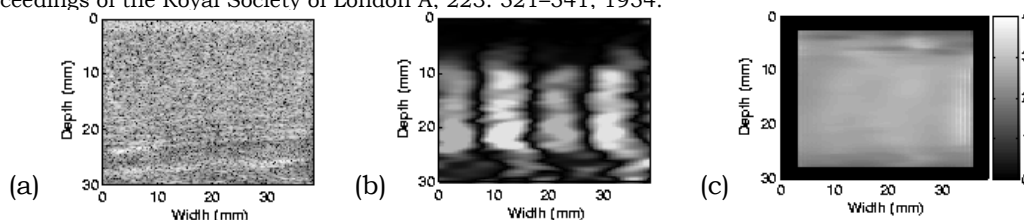


Figure 1: Matched (a) B-mode US, (b) crawling wave sonoelastogram and (c) shear velocity sonoelastogram (averaged over one spatial wavelength of crawling wave propagation) obtained from a healthy volunteer in the relaxed quadriceps femoris muscle. Note that crawling waves were induced using a dual source configuration vibrating at frequencies of 75 and 75.15 Hz.

Hassan Rivaz^{1*}, Pezhman Ferooghi¹, Emad Boctor², Richard Zellars³, Gabor Fichtinger^{1,2,4}, Gregory Hager¹.

¹Computer Science Department, Johns Hopkins University, 3400 N. Charles St, 224 NEB, Baltimore, MD 21218, USA; ²Radiology Department, Johns Hopkins Medical Institute, 600 North Wolfe Street, Baltimore, MD 21287, USA; ³Radiation Oncology & Molecular Radiation Sciences Department, Johns Hopkins Medical Institute, 401 North Broadway, Suite 1440, Baltimore, MD 21231, USA; ⁴Mechanical Engineering Department, Johns Hopkins University, 3400 N. Charles St, 223 Latrobe Hall, Baltimore, MD, 21218, USA.

Background: Most ultrasound elastography [1] techniques estimate the tissue displacement map using correlation analysis of echoes. Cross-correlation is robust to noise and is very accurate even when tracking very small tissue deformations. However, speckle decorrelation (caused by out-of-plane motion, high compression and biological motions) leads to displacement estimation error. Robust methods to decorrelate noise have been proposed before [2,3], but at a high computational cost.

Aims: This presentation describes a 2D elastography technique that finds displacement by using dynamic programming (DP) for global optimization of a regularized displacement field in potentially real-time. DP is an efficient method of global optimization and has been extensively used in computer vision for finding correspondences between two images acquired from two cameras in stereo, matching deformable contours and word recognition.

Methods: Consider two echo signals $g(i)$ and $g'(i)$ corresponding to two A-lines acquired before and after compression, each signal sampled at $i=1 \dots m$. In 1D elastography, the distance between the two signals is calculated as $\Delta(i,d) = |g(i)-g'(i+d)|$, where d is the displacement at the sample i . The smoothness of the displacement is quantified as $S(d_i,d_{i-1}) = (d_i-d_{i-1})^2$, where d_i and d_{i-1} are the displacements at the samples i and $i-1$ respectively. The cost function at each point, i , and its associated displacement, d_i , is defined as a recursive cost function $C = \min \{C(i-1,d_{i-1}) + w S(d_i,d_{i-1})\} + \Delta(i,d_i)$ where w is the smoothness weight and minimization is performed over d_{i-1} . A dynamic programming algorithm is used to find the displacement map that minimizes the cost function. Further, we refine hierarchically the displacement map to the subpixel level by using the same DP algorithm. In 2D elastography, a 2D displacement map is calculated by imposing a 2D smoothness regularization. We do not present the formulation here because of space limitation.

Results: Radiofrequency (RF) data were acquired from an Antares Siemens system (Issaquah, WA, USA) with a 7.27MHz linear array at a sampling rate of 40MHz. Freehand palpation experiment results of a CIRS breast elastography phantom are shown in Figure 1. A high level of lateral motion at the top-left corner of the image makes the 1D DP elastogram (Figure 1b) noisy in this region, while 2D DP (Figure 1c) successfully tracks this motion. Figure 1d shows the elastogram obtained only from B-mode data, which is accessible from all ultrasound machines without modification, using our 1D DP algorithm. The CNR at the specified windows are 1.78, 3.14 and 1.02 for the three elastograms from left to right. On our first non-optimized implementation of the algorithm, an elastogram of 1000x100 pixels with maximum axial displacement of 10 samples (1% strain) and maximum lateral displacement 1 A-line takes 1.4sec to generate (on a 3.8GHz P4 CPU).

References:

- [1] Ophir, J., et al., "Elastography: a quantitative method for imaging the elasticity of biological tissues", *Ultrason. Imag.* v. 13, pp 111-34, 1991.
- [2] Alam, S., Ophir, J., Konofagou, E., "An adaptive strain estimator for elastography", *IEEE UFFC*, 4, 461-472, 1998.
- [3] Pellot-Barakat, C., et al, "Ultrasound elastography based on multiscale estimations of regularized displacement fields, *IEEE TMI*, v. 23, pp 153-163, 2004.

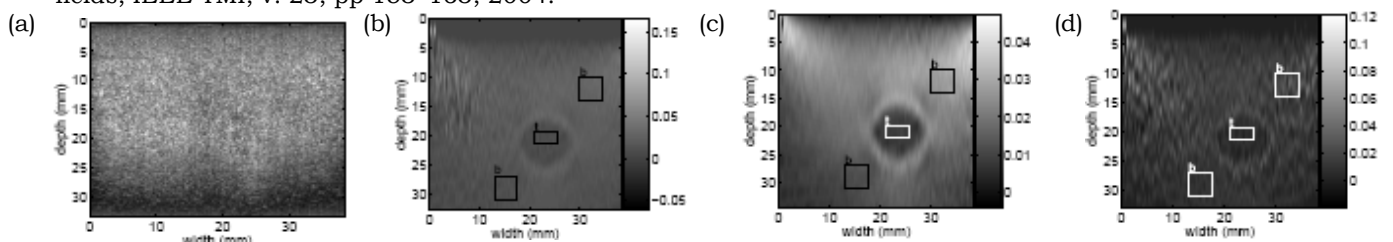


Figure 1: (a) B-mode image, (b) 1D DP elastogram, (c) 2D DP elastogram and (d) 1D DP elastogram obtained using only B-mode data. The rectangles show CNR calculation windows (t and b refer to target and background).

031 REAL-TIME POROELASTOGRAPHY: A FEASIBILITY STUDY.

R. Zahiri-Azar ^{1*}, R. Righetti ², J. Ophir ², S.E. Salcudean ¹.

¹The University of British Columbia, Vancouver, BC, CANADA; ²The University of Texas Health Science Center Houston, Houston, TX, USA.

Background: The Poisson's ratio describes the coupling between orthogonal strain components and is related to the ability of a material to change volume under compressive or tensile loading. Generally, the time-dependent mechanical behavior of poroelastic materials is studied using different compression techniques. Typically in the field of elastography, the effective Poisson's ratio elastograms are computed as the ratios between lateral and axial strain elastograms acquired from a poroelastic material undergoing stress relaxation [1].

Aims: We report implementation of a real-time Poisson's ratio imaging system that is clinically desired.

Method: Real-time effective Poisson's ratio imaging was implemented on a SonixRP US machine (Ultrasonix Medical Corp., Richmond, Canada) as a client-software. The software connects to the US machine and captures RF frames and B-mode images continuously. The relative/absolute displacements are then estimated from the set of RF signals. Time Domain Cross Correlation with Prior Estimates (TDPE) [2] and cosine interpolation for sub-sample resolution was used to estimate both axial and lateral components of the displacement. The Least Squares Strain Estimator (LSE) with adjustable kernel size was used as a strain estimation algorithm [3]. The effective Poisson's ratios were estimated as the ratios between the lateral strains and the axial strains. The estimated Poisson's ratios are then scan-converted, color coded and displayed on the screen alongside the corresponding B-mode images in real-time.

Results: For qualitative validation, experiments were run using several different types of tofu phantoms [1]. The phantoms were imaged to a depth of 70 mm with a linear array of 128 transducer elements with 3.3 lines per millimeter in the lateral direction with a 6.6 MHz center frequency digitized at 40 MHz. One RF frame was acquired and stored as a pre-compression signal. Using a mechanical compressor, the phantoms were then slightly compressed (<1%) axially and sustained under a fixed axial strain. Immediately after applying the compression, post-compression RF frames were captured continuously. Both axial and lateral displacements between the pre- and post-compression RF signals were estimated using 1 mm windows with 50% window overlap. Both axial and lateral strains were estimated using a LSE with a kernel size of 6. Instantaneous Poisson's ratio elastograms were then estimated from the ratio between lateral strain and axial strain at every time slot. Screen shots of effective Poisson's ratio elastograms for a tofu phantom at different times after the initial applied load are shown in Figure 1.

Conclusion: The results confirm that elastography may be used to image the effective Poisson's ratio in porous media in real-time. Furthermore, the feasibility of studying the time-dependent mechanical behavior of poroelastic materials in real-time is shown which may be useful in clinical applications.

Acknowledgements: This work is a collaborative effort between the University of British Columbia and the University of Texas (UT) Health Science Center Houston Medical School. The work at UT was supported by NIH Program Project P01-CA64597-13 and by the John S. Dunn Foundation.

References:

- [1] R. Righetti, J. Ophir, S. Srinivasan, TA. Krouskop, The feasibility of using elastography for imaging the Poisson's ratio in porous media, *Ultrasound in Medicine and Biology*, 30(2), 215-228 (2004).
- [2] R. Zahiri-Azar and S. Salcudean, Real-Time Estimation of Lateral Motion using Time Domain Cross Correlation with Prior Estimates, *IEEE Ultrasonics Symposium*, Vancouver, Pages: 1209-1212 (2006).
- [3] R. Zahiri-Azar and S. Salcudean, Real-Time Least Squares Strain Estimator for Elastography, Proc. Fifth Intl. Conf. on Ultrasonic Measurement and Imaging of Tissue Elasticity, Snowbird, UT, USA, Page: 109 [2006].

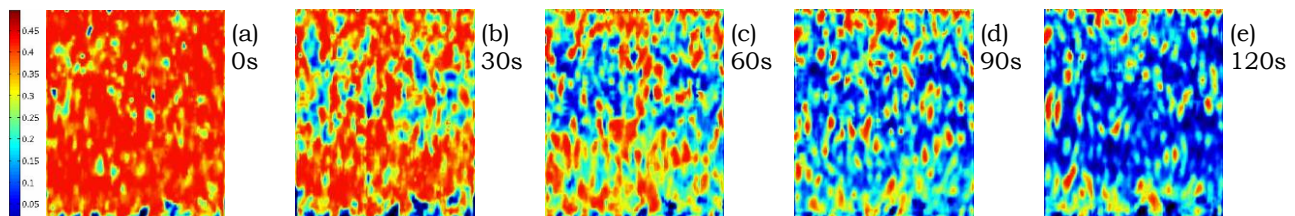


Figure 1: Screen shots of sequential poroelastograms demonstrating real-time changes in the local Poisson's ratios during the relaxation phase following a step compression: Initial poroelastogram immediately after compression (a), at 30 (b), at 60 (c), at 90 (d) and at 120 seconds (e). Using plates impervious to water on top and bottom explains the appearance of the poroelastograms over time.

086 **2D THEORETICAL ASSESSMENT OF THE AMPLITUDE-MODULATED HARMONIC MOTION IMAGING (AM-HMI) AND EXPERIMENTAL VALIDATION.**

C Maleke^{1}, J Luo¹, EE Konofagou¹.*

¹Columbia University, 622 W 168th St, New York, NY, 10032, USA.

Background: In HMI, an acoustic radiation force is used as an oscillatory mechanical stimulus generated at the focus of the focused ultrasound (FUS) transducer for the detection of localized relative stiffness changes. Amplitude-modulated harmonic motion imaging (AM-HMI) [1] has the capability of imaging tissue mechanical properties during the application of the force. Since only displacement images are usually presented, the theory between tissue displacement and modulus in AM-HMI remains to be validated.

Aims: A finite-element method (FEM) is used to accurately model the dynamic response of homogeneous phantoms at different stiffnesses and evaluate the HMI performance. The FEM and experimental results from tissue mimicking phantoms with the same stiffness variations are compared to describe the mechanical behavior of phantoms using similar boundary conditions.

Methods: A 4.68 MHz single-element focused ultrasound (FUS) transducer generated a localized oscillatory force. The resulting motion was imaged simultaneously using a diagnostic (pulse-echo) transducer operating at a center frequency of 7.5 MHz. Radiofrequency (RF) signals were acquired using a standard pulse-echo technique with a PRF of 5.4 kHz. 1D cross-correlation technique was performed to estimate and image the resulting axial displacement with a window size equal to 0.47 mm and 90% overlap.

In the FEM simulation, a rectangular mesh, with dimensions of 35 mm in the axial and 30 mm in the lateral directions, was generated. There were a total of 2771 nodes and 5424 triangular elements used in the mesh. For simplicity, the mesh was assumed to be a purely elastic medium with different assigned Young's moduli. The acoustic pressure field was simulated in Field II using the same FUS transducer parameters used in the experiment. This pressure field was used as the excitation force to generate displacements. The imaging field was simulated in Matlab 7.2 using a linear scattering model with 64 acoustic elements, a center frequency of 7.5 MHz and a 40 MHz sampling frequency. The displacement estimation at the center RF lines only was considered in the validation with the single-element (pulse-echo) transducer used in experiments.

Results: The results from the FEM and phantom experiments for the 20, 40 and 60 kPa phantoms were in excellent agreement. The differences between experimental and simulated displacements were 8.45 ± 1.49 , 4.56 ± 0.233 and 3.78 ± 1.86 microns respectively. The measured displacements obtained experimentally were smaller by about 9.8% compared to the FEM equivalents. This is most likely because the effect of viscosity was ignored in the FEM simulations. However, the experimental results also show that the phase shift between the stimulated force and HMI displacement increased with the stiffness of the tissue phantom. This information will be considered for viscosity estimation in the future.

Conclusions: Although there is a small discrepancy between the FEM and experimental results, the relationship between HMI-estimated displacement and the phantom Young's modulus was validated successfully both in simulations and experiments.

Acknowledgements: The authors wish to thank Wei-Ning Lee, MS for valuable discussions.

References:

[1] Maleke C et al. *Ultrason Imaging* 2006; 28:144-158.

089 **DIGITAL IMAGE ELASTO-TOMOGRAPHY: IMAGING INTERNAL ELASTICITY THROUGH EXTERNAL SURFACE MOTION MEASUREMENTS.**

A Peters¹, JG Chase¹, EEW Van Houten^{1*}.

¹University of Canterbury, Private Bag 4800, Christchurch, 8140, Canterbury, NEW ZEALAND.

Background: To date, elastic property imaging has been investigated primarily using motion data obtained by traditional medical imaging technologies such as ultrasound and MR. While these methods have shown great success in generating elasticity images of various types, alternative, potentially less expensive, approaches for imaging motion do exist and may be viable as elastographic methods.

Aims: This work investigates the use of a calibrated 3D imaging system generating high-resolution surface motion measurements as an elastography method. Reconstruction of the internal elasticity distribution based solely on these external measurements is accomplished through the use of a hybrid reconstruction algorithm coupling traditional gradient decent methods with modern combinatorial optimization approaches.

Methods: 3D photogrammetry techniques are used to capture the surface motions of a vibrating phantom as it cycles through its steady-state motion pattern. Careful strobing is used to accurately characterize the relatively high-frequency (~100 Hz) movement at a set of measurement points along the phantom's surface [1,2]. The resulting time-harmonic amplitude and phase data is then passed to a hybrid reconstruction algorithm which makes use of combinatorial optimization techniques to avoid local minima as well as gradient decent methods to gain computational efficiency in generating the internal stiffness distribution of the phantom.

Results: Successful elasticity reconstructions of heterogeneous silicon phantoms have been achieved, along with corresponding tests against homogeneous phantoms. The hybrid reconstruction algorithm has proven successful in overcoming local minima while still maintaining reasonable efficiency. Optimization of both the imaging system as well as the reconstruction technique has been performed with significant improvements in performance.

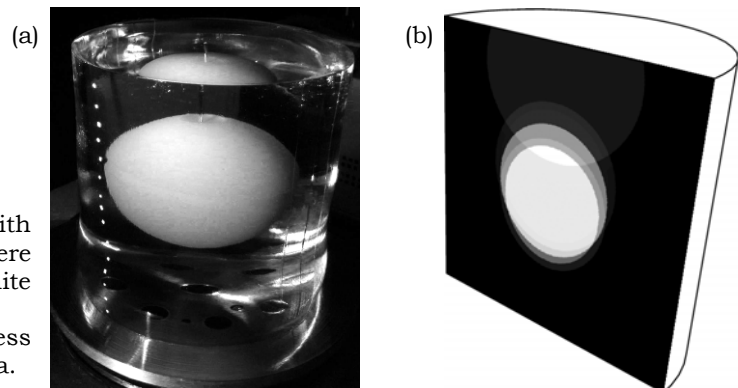


Figure 1: (a) shows a soft silicon phantom with a hard spherical inclusion where motion data was taken at the white markers. (b) shows the resulting stiffness reconstruction for the phantom data.

Conclusions: Elastic property reconstruction based on surface motion is possible, requiring only an array of digital cameras for data capture. Successful phantom experiments have been conducted with very encouraging results. Challenges in the method involve the imaging of the relatively high-frequency vibrations as well as the presence of local minima in the poorly conditioned elastic property reconstruction problem.

References:

- [1] A Peters *et al*, "Digital Image-Based Elasto-Tomography: First Experiments in Surface based Mechanical Property Estimation of Gelatine Phantoms." JSME Series C, 48:562-569, 2005.
- [2] A Peters *et al*, "Digital Image-Based Elasto-Tomography: Non-Linear Mechanical Property Reconstruction of Homogeneous Gelatine Phantoms." INT. J. Info. Sys. Sc. 2:512-521, 2006.

Michael S. Richards^{1*}, Jonathan M. Rubin¹, Paul E. Barbone², Assad A. Oberai³.

¹Radiology Department, University of Michigan Health System, 200 Zina Pitcher Place, Ann Arbor, MI, USA; ²Aerospace and Mechanical Engineering Department, Boston University, 110 Cummington St, Boston, MA, USA; ³Mechanical, Aerospace and Nuclear Engineering Department, Rensselaer Polytechnic Institute, 110 8th Street, Troy, NY 12180 USA.

Background: Elasticity Imaging (EI) techniques have been investigated for a wide range of applications. One common application is the use of EI for breast lesion characterization, typically using free hand elastography methods [1]. The physical integration of an EI technique, using ultrasound (US), with an X-ray mammographic system can offer images which are inherently registered with the X-ray images. Additionally, the compression paddles of mammography units offer a means for stabilizing the transducer and imposing a controlled compression. Furthermore, acquiring three dimensional (3D) US images allows for the possibility of measuring a full 3D displacement vector field. Shear modulus can then be recovered from the measured deformation by using an appropriate mathematical model and solving an inverse problem. The combination of 3D US and modulus imaging as an adjunct to an X-ray tomosynthesis mammography system is expected to improve the specificity of standard mammographic practices.

Aims: The aim of our work is to develop and evaluate an US technique to quantitatively measure and image the shear modulus of soft tissues in 3D. Specifically, to design and evaluate algorithms which accurately measure 3D displacement vector field from sets of US images and then use these displacements to accurately and efficiently measure the shear modulus of the imaged material. To that end, we designed a phantom study to test the accuracy and resolution of our algorithms.

Methods: Ultrasound tissue mimicking phantoms were created, using gelatin of differing concentrations, with cylindrical lesions of various sizes and stiffness within the range of diagnostically relevant tumors. These phantoms were imaged with a linear array (Analogic AN2300, 12 MHz), which was scanned elevationally to create 3D images. Typically, the tissue material is imaged before and after a slight axial compression (~1.5%). A novel image registration based algorithm was developed to noninvasively measure the 3D displacement field from sets of US images of the deforming material. This problem is posed as an optimization which minimizes US radiofrequency (RF) image intensities of a pre- and a post-deformation image, as the pre-deformation image is artificially deformed by the desired displacement. The novel features of this algorithm include Gauss-Newton minimization, finite element (FE) interpolation of the displacement field, inclusion of prior information and the ability to enforce physical constraints. A second algorithm was created to recover the shear elastic modulus distribution of the deforming material by efficiently solving the 3D inverse problem as an optimization problem. It is solved by minimizing the difference in the measured displacement and that predicted by an incompressible, isotropic, single phased, linear elastic model [2,3]. This method utilizes FE interpolations, the adjoint method to evaluate the gradient and a quasi-Newton method for optimization.

Results: Inclusions as small as 5mm in diameter, some with contrasts marginally above unity, were successfully and clearly reconstructed. The accuracy of the reconstructed modulus contrast, in each case, is within 35% of independent validation measurements and varies depending on the actual modulus distribution. The effect of the boundary conditions and regularization methods on the reconstructed modulus images and the uniqueness of the solution are discussed.

Conclusions: These EI algorithms may improve the detection and diagnostic power of standard mammography practices. The resulting modulus images are quantitative and can provide an accurate representation of the mechanical properties and spatial distributions of soft tissue. Additionally, initial clinical results are presented to show feasibility of algorithm implementation for breast tissue.

Acknowledgements: This work was supported in part by NSF Award No. EEC-9986821, DOD Breast Cancer Research Program Award No. W81XWh-04-1-0763, and NIH Grants RO1-CA91713 and R21-CA109440.

References:

- [1] Doyley MM, Bamber JC, Fuechsel F, Bush N. "A freehand elastographic imaging approach for clinical breast imaging: system development and performance evaluation." *Ultras Med Biol*, 2001; 27: 1347-1357.
- [2] A.A. Oberai, N.H. Gokhale, and G.R. Feijoo. "Solution of inverse problems in elasticity imaging using the adjoint method". *Inverse Problems*, 19:297-313, 2003.
- [3] A.A. Oberai, N.H. Gokhale, M.M. Doyley, and J.C. Bamber. "Evaluation of the adjoint equation based algorithm for elasticity imaging". *Physics in Medicine and Biology*, 49:2955-2974, 2004.

063 **PERFORMANCE OF 3D DISPLACEMENT ESTIMATION USING A CURVILINEAR PROBE.**

NR Miller¹, EJ Harris¹, PM Evans¹, RN Symonds-Taylor¹, JC Bamber^{1*}.

¹Joint Department of Physics, Institute of Cancer Research and Royal Marsden NHS Foundation Trust, Downs Road, Sutton, Surrey, SM2 5PT, England, UK.

Background: 3D soft tissue tracking is of interest for monitoring organ motion during radiotherapy and HIFU. The goal of this work is to assess the feasibility and best-case performance of using volumetric envelope-detected echo data from a commercially available curvilinear 3D ultrasound probe (3D4-7EK, Medison Co., S. Korea) for 4D tracking of abdominal organs.

Aims: To identify the depths of tissue for which this technique is useful, we examined how the performance of the displacement estimation algorithm varied with ultrasound imaging depth. The maximum organ speed that can be tracked will depend on the temporal resolution of the ultrasound probe. There is a trade off between temporal resolution and spatial sampling, and, therefore, we also investigated how tracking performance varied as a function of spatial sampling.

Methods: Volume images of a phantom were acquired before and after the probe had been moved by a known displacement (1, 2 or 8mm). 3D tracking was performed on B-mode data using 3D cross-correlation, and displacements were estimated as a function of depth (up to 20cm), spatial sampling frequency (0.18mm⁻¹, 0.25mm⁻¹ and 0.3mm⁻¹ at 15cm depth) and direction of displacement. In a second experiment, *in-vivo* 3D tracking of liver was performed. A healthy volunteer was asked to first hold his/her breath and then to breathe deeply and regularly whilst a sequence of 3D images of the liver was acquired. Liver tissue motion was tracked in 3D as a function of time.

Results: For 2mm displacements, good accuracy and precision (<+/-0.4mm) were observed up to an imaging depth of 15cm and for all directions of displacement. For 8mm displacements, good accuracy and precision (<+/-0.5mm) were observed up to a depth of 10cm. These results were achieved for the highest spatial sampling frequency investigated (0.3mm⁻¹ at 15cm depth). For abdominal treatments, imaging depths greater than 10cm may be required and, therefore, we may need to ensure that the distance between volume image acquisitions is no greater than a certain value (e.g., 2mm). Depending on the speed of the organ motion, this may require the temporal resolution to be increased, for example, by reducing the size of the field of view. The relationship between field of view, depth and the maximum trackable organ speed will be discussed. Analysis of *in-vivo* 3D data showed that liver motion can be tracked in all three orthogonal directions, and that the orthogonal motions are correlated.

Conclusions: Using high spatial sampling, 3D tracking performance was shown to be sufficient to be useful for monitoring organ motion. Provided the displacement between volume images is not too large, good tracking performance can be achieved for depths of up to 15cm. Initial results from *in-vivo* measurements show that 3D tracking of respiratory motion of liver tissue is feasible with this system.

Acknowledgements: Work supported by Cancer Research UK. The authors acknowledge Paul Barbone and Michael Scott Richards at Boston University for their modifications to the tracking code.

Background: It is well known that the mechanical properties of soft tissue can change with tissue pathology. For example, it is observed that the elastic (shear) modulus of malignant breast masses is typically an order of magnitude higher than the background. In addition, there is recent evidence that with increasing applied strain the stiffness of malignant breast lesions increases more rapidly than non-malignant lesions [1,2]. While many attempts have been made to image and map the linear elastic properties of soft tissue (c.f. [3]), relatively few attempts have been made to account for both large deformation and material nonlinearity in reconstructing the elastic properties of soft tissue. One notable exception is the work of Skovoroda [4], which accounts for large deformations but uses a linear constitutive model.

Aims: In our previous work, we have developed, implemented and tested the performance of an efficient algorithm to reconstruct the material properties of a nonlinear hyperelastic solid undergoing finite deformations. In this presentation, we consider its application in reconstructing the nonlinear material properties of breast tissue. We also wish to compare the utility of linear measures of modulus like the secant modulus at different levels of strain with true nonlinear measures.

Methods: The overall problem of determining the nonlinear elastic parameters was formulated as a constrained minimization problem. The constraint takes the form of a finite element (FEM) model for the hyperelastic tissue response. The optimization problem was solved efficiently using a quasi-Newton method and the adjoint method. A novel continuation technique was used to further accelerate the inverse problem solution. Remarkably, the overall cost of solving the nonlinear inverse problem was only about two times that of solving the nonlinear forward problem.

The new nonlinear inverse algorithm was applied to displacement data obtained from one benign (fibroadenoma) and one malignant (invasive ductal carcinoma) breast lesion. The displacement fields were acquired at small (about 2%) and large (about 12%) levels of overall strain in order to highlight the nonlinear behavior of the tissue. In each case, displacements were referred back to the frame with the smallest deformation, which was treated as the reference configuration. In the inverse algorithm, two elastic parameters were evaluated. These included the shear modulus at zero strain and the nonlinear parameter in an exponential stress–strain law (Veronda–Westman model). In addition, using the same displacement fields in a linear inverse problem, secant shear modulus at the two levels of overall strain were also evaluated.

Results: Both lesions (benign and malignant) were clearly seen in shear modulus images. The secant modulus for the benign lesion was observed to reduce with increasing overall strain, while that of the malignant lesion was found to increase with increasing overall strain. This trend was consistent with value of the nonlinear parameter, which was elevated (when compared with the background) only for the malignant lesion.

Conclusions: We have applied a new inverse algorithm to determine the nonlinear elasticity parameters of breast tissue. In our preliminary study, we have considered one benign and one malignant lesion. We conclude that both lesions are clearly seen in images of shear modulus and that they exhibit distinct nonlinear behavior that is captured in images of the nonlinear parameter.

Acknowledgements: PEB acknowledges NSF support and TJH acknowledges the support of NIH grant NIH R01CA100373.

References:

- [1] Krouskop TA, Wheeler TM, Kallel F, Garra BS and Hall T. Elastic moduli of breast and prostate tissues under compression *Ultrasonic Imaging* 20:260–274, 1998.
- [2] Wellman P, Howe RH, Dalton E and Kern KA. Breast tissue stiffness in compression is correlated to histological diagnosis Technical Report, Harvard Biorobotics Laboratory, 1999.
- [3] Oberai AA, Gokhale NH, Feijoo GR. Solution of inverse problems in elasticity imaging using the adjoint method *Inverse Problems* 19:297–313 2003.
- [4] Skovoroda AR, Lubinski MA, Emelianov SY and O'Donnell M. Reconstructive elasticity imaging for large deformations. *IEEE Transactions of Ultrasonics, Ferroelectrics and Frequency Control*, 46:523, 1999.

029 **2D LOCALLY REGULARIZED DEFORMATION IMAGING DURING FREEHAND EXAMINATION: INITIAL RESULTS.**

E. Brusseau^{1*}, J.F. Déprez¹, F. Duboeuf¹, O. Basset¹.

¹CREATIS UMR CNRS 5220 – INSERM U630, Villeurbanne, FRANCE.

Background: Ultrasound elastography is now recognized as a relevant technique for tissue characterization.

Aims: Recently, we have developed a 2D locally regularized strain estimation method [1]; its performance was demonstrated with simulations and freshly excised cut specimens of bovine livers, with the media deformed under well-controlled conditions. In this presentation, we investigate the ability of our algorithm to provide good quality elastograms during freehand examination.

Methods: Contrary to most 2D techniques that model the compression-induced local displacement as a 2D shift, the model of tissue motion and deformation we use is direction-dependent, linked to the highly anisotropic character of RF ultrasound image resolution. In addition to the 2D shift, an axial scaling factor is also considered. Parameters are estimated by maximizing a similarity criterion defined as the normalized correlation coefficient (NCC) between an initial region and its corresponding deformed version, when the latter is compensated for according to these parameters. This optimization problem is solved with the sequential quadratic programming methodology [2]. Finally, the resulting strain maps are locally regularized to correct potentially incorrect estimates, identified by an insufficiently high NCC (NCC<0.8) in the solution. When such an estimate is detected, its value is computed anew, by adding a smoothness constraint, ensuring continuity with surrounding reliable estimates.

Results: The developed method was tested with the dedicated elastography QA phantom, CIRS, model 049, as well as on cut specimens of bovine livers containing hard inclusions of agar gel. While the operator was slowly compressing the medium, ultrasound RF images were acquired in real-time, with the Ultrasonix - Sonix RP scanner, using a 7 MHz probe and a fixed sampling frequency of 40 MHz.

This elasticity QA phantom consists of a parallelepipedic medium, whose dimensions are 15x10x8 cm³ and containing several targets of known hardness. We investigated the deformation of two 10 mm spheres located at 15 mm depth, one softer, the other harder than the surrounding material. Their Young's modulus, provided by the manufacturer, is 6KPa for the softer and 62 KPa for the harder lesion, respectively, whereas the background has an elasticity of 29 KPa. Figure 1 shows 5 elastograms extracted from the sequence of estimated strain maps at 5 different time points, for the soft lesion case. Results with the hard lesion as well as with *in vitro* bovine liver samples will be also presented.

Conclusions: In this presentation, a 2D strain estimation technique has been introduced and initial results on a dedicated elastography phantom and *in vitro* bovine liver during freehand scanning are promising. Future work will focus on continuing the assessment of the algorithm with additional biological tissues. However, as implemented, the algorithm needs several minutes to compute one elastogram, and decreasing the computational time will be essential to converge towards medical application.

Acknowledgements: This work was partly supported by the Cancéropôle Grand Ouest.

References:

- [1] E. Brusseau, J. Kybic, J.F. Deprez and O. Basset, "2D locally regularized strain estimation from radiofrequency ultrasound images: Theoretical developments and results on experimental data", *IEEE Trans. Med. Imag.*, 2007, in press.
- [2] P.T. Boggs and J.W. Tolle, "Sequential quadratic programming", *Acta Numerica*, vol.4, 1996.

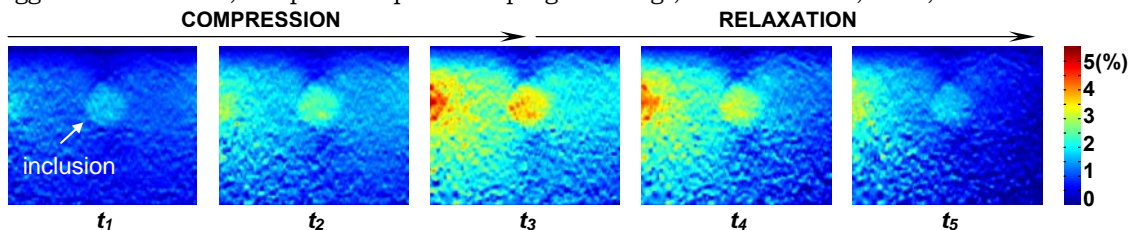


Figure 1: Deformation imaging of the elasticity phantom QA, CIRS, model 049. The 5 elastograms are extracted from the sequence of strain maps at 5 different time points. From $t=t_1$ to $t=t_3$, the experimenter was carefully compressing the phantom, while from $t=t_3$ to $t=t_5$ he was slowly relaxing the pressure. As expected, the soft inclusion deforms much more than the surrounding material. Moreover, we can observe that the experimenter tended to apply a stronger compression over the left part of the medium.

Background: Given the recent discussions about the clinical value and role of mammography screening, the availability of new and supporting methods is urgently needed. Ultrasonic strain imaging is a very promising method to help improve early breast tumor detection but is not yet routinely used in clinical practice. Medical doctors are hesitant to apply ultrasound–based methods if real–time imaging cannot be achieved and/or the methods are not robust enough.

Aims: With two–dimensional array transducers soon to be available, making possible rapid three–dimensional (3D) echo data acquisition and very robust 3D strain imaging, large data volumes must be processed meaning that very fast displacement and strain estimation methods are needed. As a first step towards 3D strain imaging in real–time, we introduce a new method to reduce the computation time of fast displacement estimators that are well–suited to strain imaging.

Methods: From earlier comparisons [1] of various fast displacement estimators for real–time strain imaging, we found that three methods are particularly well–suited for pulse and signal processing parameters that are typical when using commercial ultrasound scanners (mean frequency 7.5 MHz, relative FWHM–bandwidth 60%, sampling rate 30 MS/s, range gate length 16 samples): the well–known phase–root–seeking (PRS) algorithm [2], the 2D autocorrelator [3], an extension of the Kasai autocorrelator used in color flow imaging, and a method we call “imaginary part zero–crossing” (IPZC) [4]. In this presentation, we present a method to further reduce the computation times of the PRS and IPZC algorithms and also provide a detailed error analysis.

Results: Our results derived from simulations and tissue–mimicking phantom experiments show that the estimation errors of PRS and IPZC are virtually identical when a larger number k (8–10) of Newton iterations is used. Higher frame rates can be achieved with the IPZC since it only uses the imaginary part of the complex cross–correlation function of pre– and post–compressed echo signals and also avoids the phase calculation necessary for the PRS. Even if the mean frequency (MF) of the echo signals differs by 1.5 MHz from the MF of the transmission pulses, as commonly applied in practice for de– and re–modulation as well as time delay estimation using Newton’s method, both estimators only have a negligible displacement–dependent bias (zero at half and full–sample displacements, amplitude 0.03 μm) and a moderately increased (factor 1.7) standard deviation (maximal value of 0.075 μm at half sample displacements at $\text{SNR}=\infty$) as long as k is sufficiently large (~ 10). If, however, a smaller k is used (1–3) in an attempt to reduce the computation time, unacceptably large estimation errors result and render both estimators useless. We demonstrate that by modifying the PRS and IPZC, estimation errors can be largely decreased for a small number of iterations and a SNR larger than about 20 dB. For example, for $k=2$ the RMS error within the displacement range 0–1 sample (30 MS/s) is reduced with the modified IPZC by factors of 5.32 (SNR=20 dB) and 2.1 (SNR=40 dB), with the modified PRS by 14.7 (SNR=40 dB) and 2.1 (SNR=20 dB) which is virtually as low as with $k=10$ iterations. Processing times of 20–30% can thus be achieved without increasing estimation errors, even if significant echo signal frequency downshifts along the travel path in tissues with frequency–dependent attenuation occur when broadband pulses are applied for high axial resolution and low strain noise.

The estimator modifications need not be applied to each and every range gate. Our investigations show that it is possible to implement them for a group of adjacent range gates (axially and laterally) and update only every few millimeters which results in even shorter computation times.

Conclusions: The computation time of fast displacement estimators for real–time strain imaging can be reduced even further by modifying these estimators. From a signal processing point of view, strain frame rates can be increased by a factor of approximately 5 in practical situations with moderate SNR without increasing estimation errors when using this new method.

References:

- [1] Eder, A., and Kargel, Ch., “Fast displacement estimators for freehand ultrasonic strain imaging,” Intern. Conf. Sys. Sign. Img. Proc. (IWSSIP), Maribor, Slovenia, 2007.
- [2] Pesavento, A., Perrey, Ch., Krueger, M. and Ermert, H., “A time–efficient and accurate strain estimation concept for ultrasonic elastography using iterative phase zero estimation,” IEEE Trans. Ultrason. Ferroelect. Freq. Contr., vol 46, no. 5, pp. 1057–67, Sept. 1999.
- [3] Kargel, Ch., Plevnik, G., Trummer, B. and Insana, M.F., “Doppler ultrasound systems designed for tumor blood flow imaging,” IEEE Trans. Instr. Meas., vol 53, no. 3, pp. 524–536, April 2004.
- [4] Eder, A., Arnold, T., Elbischger, P., Käfer, M. and Kargel, Ch., “Displacement estimators for real–time ultrasonic strain and blood flow imaging with improved spatial resolution,” IEEE IMTC Proc., 2006.

066 CLUTTER REDUCTION METHODS FROM COMPRESSION OF TISSUE.

Jeremy J. Dahl^{1*}, Muujinatu Lediju¹, Michael J. Pihl¹, Stephen J. Hsu¹, Caterina M. Gallippi², Gregg E. Trahey¹.
¹Duke University, Durham, NC, USA; ²University of North Carolina, Chapel Hill, NC, USA.

Background: Clutter is a well-known phenomenon in ultrasonic imaging, presenting as a haze overlying tissues and organs of interest. The appearance of clutter varies from patient to patient, however, it is more prevalent in those patients that are overweight or obese. In fetal imaging, for example, clutter can obscure important anatomical details of the fetus such as the heart or umbilical cord insertion. Clutter is caused by two particular sources, namely reverberation between tissue layers and off-axis scattering due to side and grating lobes. Reducing clutter will greatly improve image quality.

Aims: We hypothesize that clutter generated by scattering in the nearfield tissue layers will remain coherent under axial compression of tissue. Using its coherent property, the clutter can be removed from the signals of interest using finite impulse response and blind source separation motion filters. We have applied these techniques to *in vivo* human bladder to quantify the clutter reduction using these methods. The human bladder is an ideal location to observe and quantify this clutter because, when full, it contains a large anechoic void. The techniques used in this clutter reduction method rely on similar techniques used in elastographic imaging.

Methods: We collected 15 frames of RF data from the bladder of a human volunteer. During data acquisition, the transducer was used to apply mild compression over 15 frames, or approximately 1 second. Two-dimensional speckle tracking was applied to these data sets in efforts to characterize the source and extent of the clutter. Finite impulse response (FIR) and blind source separation (BSS) filters were implemented to remove clutter resulting from the abdominal wall. We demonstrate these techniques under ideal conditions using simulations in Field II.

Results: The results provide insight into the magnitude and sources of clutter and quantify clutter reduction between reference and filtered images. Speckle tracking indicated highly correlated clutter in the upper portion of the bladder cavity. Using the FIR filtered images, up to 18dB of this clutter was removed, concentrated in the regions just beneath the abdominal wall. In the BSS filtered images, up to 18dB of clutter was removed from the bladder cavity. The size of the region where clutter was removed was larger with BSS filtering than with FIR filtering. BSS filtering was found to be more sensitive to the coherent clutter, however was more likely to generate dropout artifacts. Figure 1 below shows the original image containing clutter in the bladder cavity, the FIR filtered image, and the amount of signal removed (in dB relative to the original image). The bladder and abdominal walls are outlined for clarity.

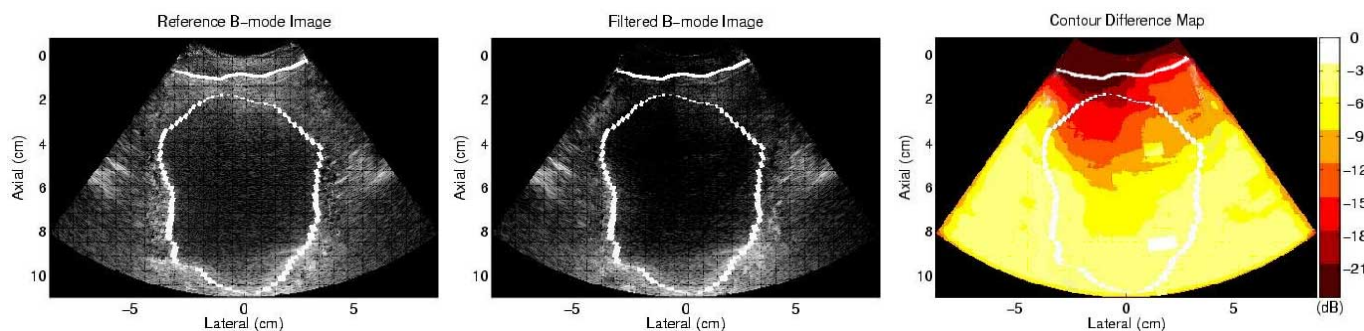


Figure 1: The reference B-mode image of a human bladder (a), FIR filtered B-mode image (b), and their relative difference in brightness (c). The bladder and abdominal wall are outlined for visualization.

Conclusions: We have proposed clutter rejection techniques based on axial compression of tissue. We have demonstrated this technique in the human bladder, achieving up to 18dB reduction in clutter. The bladder is an ideal location for such a technique due to the compressible nature of the bladder; however, we anticipate that such a technique will produce similar results in fetal imaging.

Acknowledgements: This work is supported by NIH grant R01-CA-114093. The authors would like to thank Siemens Medical Solutions USA, Inc. for their technical and in kind support.

Background: The performance of strain estimation in elastography is largely related to the quality of the displacement signal [1]. This signal has many sources of error, mainly the electronic noise, the signal decorrelation and the quantization errors due to the finite temporal sampling process [2,3]. A common solution to this issue is the use of a spatial filter on the strain elastograms, but it produces a non-negligible loss in resolution.

Aims: Our goal is to denoise elastograms with a fast and efficient process based on an image processing technique, the topological asymptotic analysis. The idea is to both preserve the spatial resolution of the elastograms and reduce noise within a real time restoration process.

Methods: The restoration technique is based on the resolution of a partial differential equation (PDE) that smoothes the image. A simple resolution of this PDE would degrade the edges of the image, just like common filters. The idea of the topological asymptotic analysis is to detect the edges by minimizing a cost function measuring the image energy outside the edges. The diffusion coefficient is then set to zero in the edge set in order to preserve it from smoothing and to keep a high resolution elastogram. The use of the adjoint differentiation allows us to compute the restored image in a very fast way [4].

Results: We first consider a simulated displacement field on a homogeneous phantom on which we apply our restoration technique. The axial strain fields derived from the original and restored displacement fields are presented in Figure 1. The mean to standard deviation ratios are 1.5 and 9.4 respectively. In comparison, a 5x5 median spatial filter produces a ratio equal to 6.6. We then consider simulated data from a phantom composed of two layers with axial displacement. Figure 2 shows the strain fields derived from the original and restored displacement fields. The mean to standard deviation ratios are 6.1 and 5.9 in the two layers before restoration and 26.4 and 25.5 after restoration. The mean slope of the interface between the two layers is 0.0022 before restoration and 0.0016 after. As the original spatial resolution is 1mm, the final resolution is 1.4mm.

Conclusions: Our algorithm provides an alternative to spatial filters for elastogram denoising. It is extremely fast (nearly in real time) and increases largely the mean to standard deviation ratio and, thus, the quality of the strain field. It also preserves quite well the spatial resolution in the restoration process. Some preliminary results on *in vivo* data confirm the qualities of our restoration technique.

References:

- [1] Ophir, J., Céspedes, I., Ponnekanti, H., Yazdi, Y. and Li, X: Elastography: a method for imaging the elasticity of biological tissues. *Ultrasonic Imaging*, 13 (2) (1991) 111–134.
- [2] Srinivasan, S., Righetti, R., and Ophir, J.: Tradeoffs between the axial resolution and the signal-to-noise ratio in elastography. *Ultrasound in Med. Biol.* 29 (6) (2003) 847–866.
- [3] Thitai Kumar, A., Krouskop, T. and Ophir, J.: Signal-to-noise ratio, contrast-to-noise ratio, and their tradeoffs with resolution in axial-shear strain elastography. *Phys. Med. Biol.* 52 (2007) 13–28.
- [4] Auroux, D., Masmoudi, M., and Belaid, L.: Image restoration and classification by topological asymptotic expansion, *Variational Formulations in Mechanics: Theory and Applications*, E. Taroco, E.A. de Souza Neto and A.A. Novotny (Eds), CIMNE, Spain, 2006.

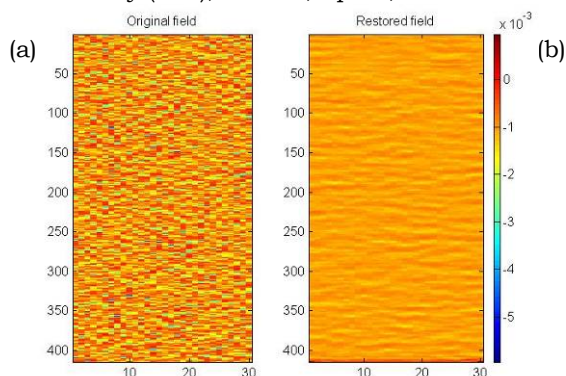


Figure 1: Original field (a); Restored field (b).

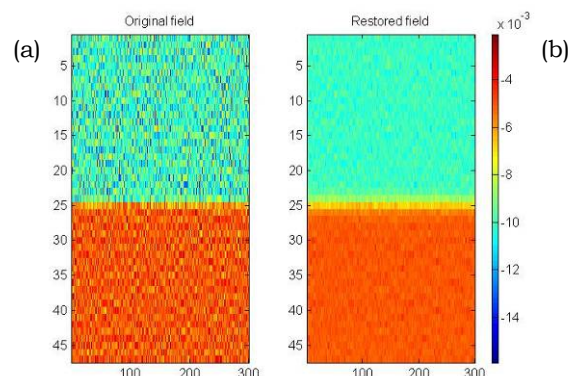


Figure 2: Original field (a); Restored field (b).

D Sosa-Cabrera^{1*}, J González-Fernández¹, L Gómez-Déniz¹, J Ruiz-Alzola^{1,2}.

¹University of Las Palmas de Gran Canaria, CTM Center for Technology in Medicine, Signals and Communications Department, Pabellón B Edif. Telecomunicaciones Lab. 203, Campus de Tafira s/n, 35017 Las Palmas de Gran Canaria, Canary Islands, SPAIN; ²Canary Islands Institute of Technology, Playa de Pozo Izquierdo, s/n 35119 Santa Lucía, Las Palmas de Gran Canaria, Canary Islands, SPAIN.

Aims: We propose a tensor analysis of elastography. The tensor strain field visualizes in one image the standard scalar parameters that are usually represented separately in elastography. By using strain tensor elastography (STE), physicians would have complementary information. To validate the method and the visualization scheme, ultrasound simulations based on FE software and an experiment on a commercial tissue-mimicking breast phantom were carried out. In this work, we present the theory and procedure to visualize the strain tensor field in an effort to better determine tumor infiltration, supported by a phantom study. This tensorial approach as well as its visualization can be extended to other elasticity imaging techniques.

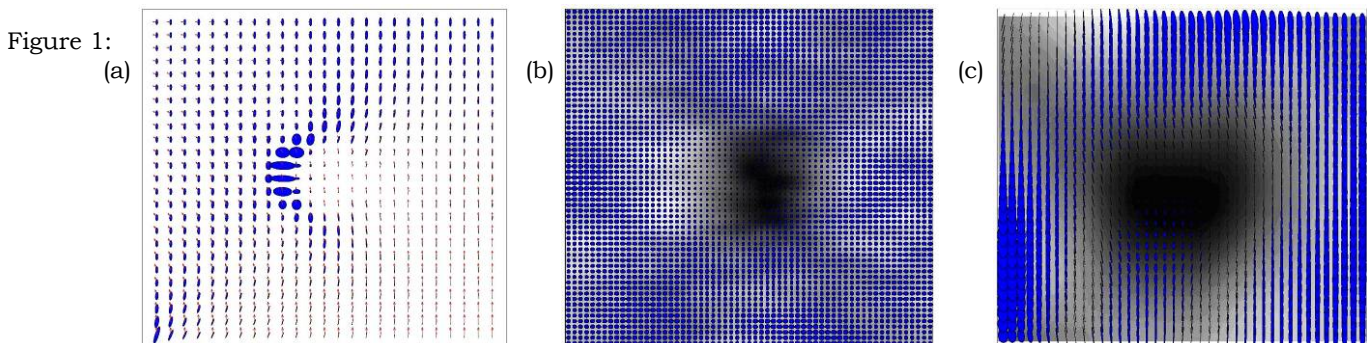
Methods: Two experimental phantoms were used: Computer-simulated ultrasound images (phantom A), using FIELD II after FE software modeling and a commercial breast elastography phantom (phantom B, Mod. 059, CIRS Inc.). To estimate the displacement vector field, we used a multi-scale variation method [1]. For gradient operations, a fast implementation least-squares strain estimator was utilised.

Results: DTI and cardiac strain-rate imaging are two examples that use tensor visualizations. Although DTI visualization techniques are quite well developed, its application to strain tensor fields is not obvious. The strain tensor is symmetric but does not satisfy the positive semi-definite condition. Hence, it is not possible to draw an ellipse with a negative value for one of its axes. However, for STE, that condition is not a barrier, because clinically the sign of the strain tensor eigenvalues, positive and negative, represents respectively material stretching or shortening in the direction of the corresponding eigenvector. This has been coded in color, blue for shortening and red for stretching. Representing the ellipses with the absolute values of the eigenvalues, it can be appreciated how much deformation from the total has been absorbed by the different tissues and, at the same time, giving idea of its anisotropy. As in the scalar elastograms, the darker is the stiffer; in STE, the smaller the ellipses are, the stiffer the area is. The experiments presented in this work show a homogeneous axially compressed target with symmetrical boundary conditions where the color coding of the ellipses seems to be trivial, but other settings, such as antisymmetric boundary conditions (Figure 1a), show its potential utility. The ellipses present the principal directions of deformation (i.e. direction in which the tissue is deformed the most at that point), their magnitude and the ratio between these magnitudes; while the scalar representations show the deformation in axial or lateral directions. Many applications in different elastographic modalities may be favored by STE. The results show that the OF method combined with the least-squares fitting algorithm, accurately estimate the strain tensor. Both scalar and tensorial elastograms clearly distinguish hard inclusions. In Figure 1b and c, the strain tensor elastograms are overlaid on the axial ones for phantom A and B respectively.

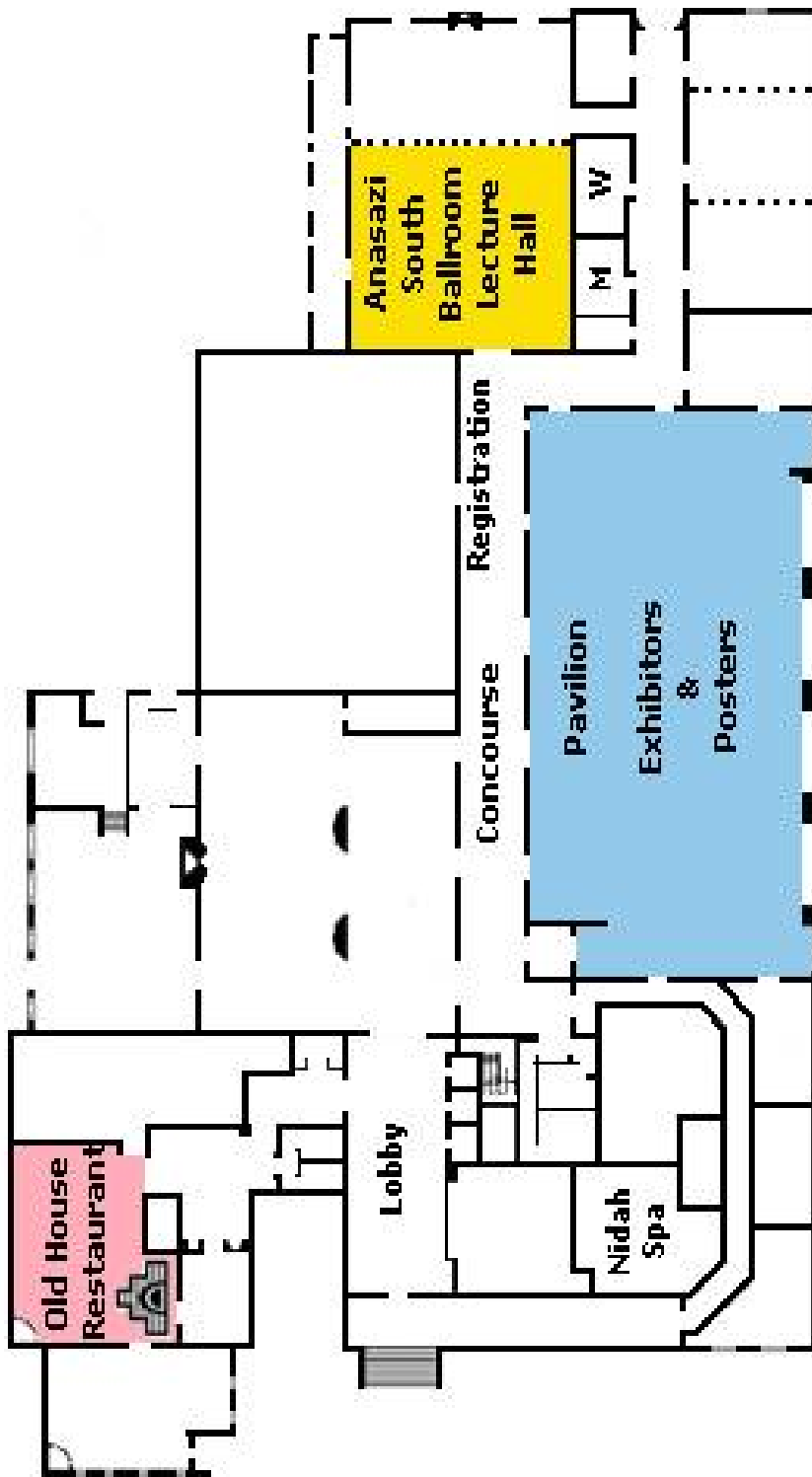
Acknowledgements: Spanish Gov. USIMAG grant (TEC2004-06647-C03-02) and CEE SIMILAR NoE (FP6-507609).

References:


- [1] D. Sosa-Cabrera, J. González-Fernández, C. Castano, L. Gómez-Déniz, L. Alvarez, and J Ruiz. A Multiscale Variational Optical Flow Method To Estimate Discontinuous Motion Fields For Ultrasound Elastography. Proc of Fifth International Conference on the Ultrasonic Measurement and Imaging of Tissue Elasticity, p 31, [2006](#).



Eldorado Conference Center Floor Plan



Downtown Santa Fe Map



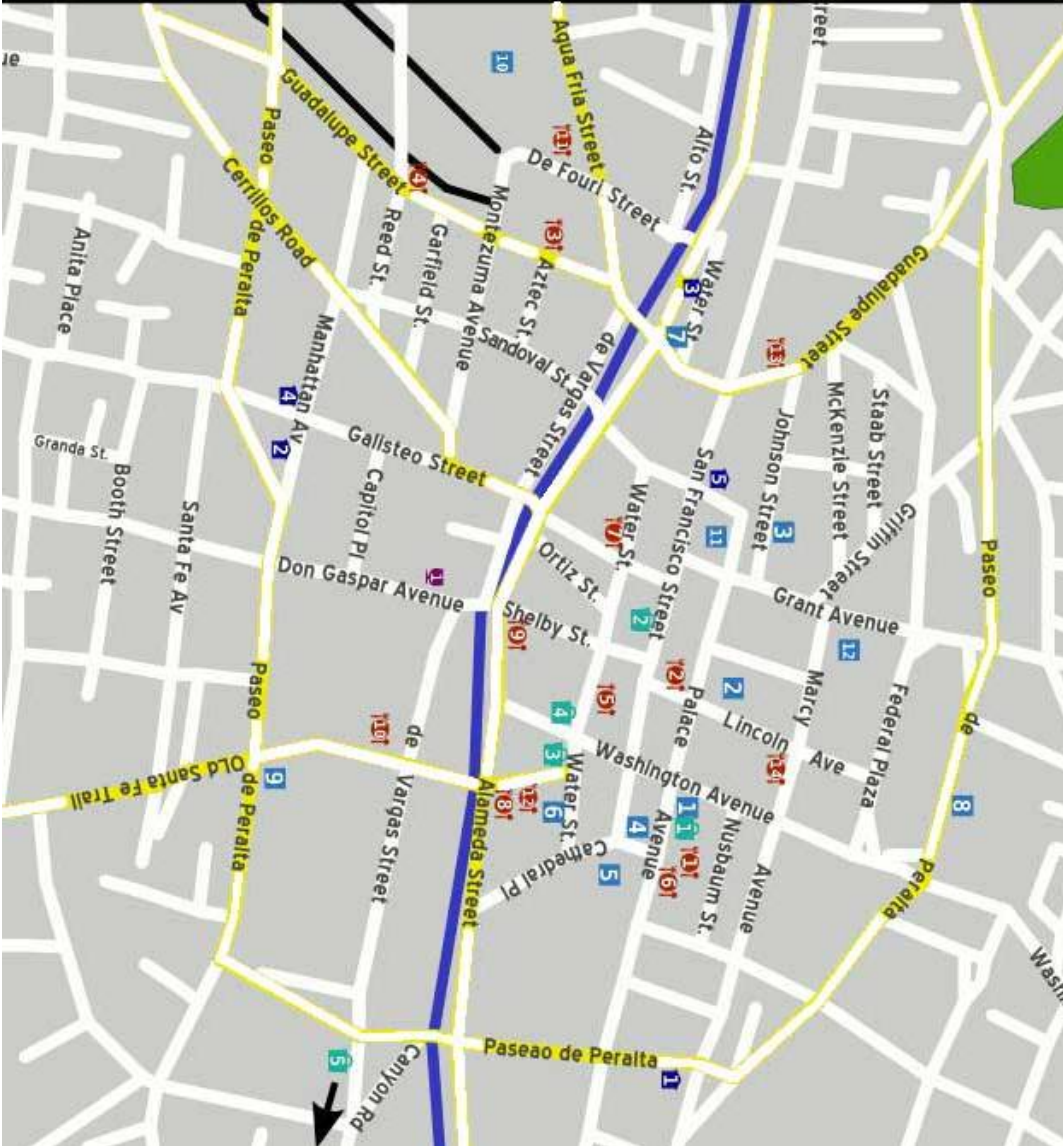
- See and Do**
- 1. Palace of the Governors
- 2. Museum of Fine Arts
- 3. Georgia O'Keefe Museum
- 4. Institute of American Indian Arts
- 5. St. Francis Cathedral
- 6. Loretto Chapel
- 7. Santuario de Guadalupe
- 8. Scottish Rite Temple
- 9. State Capitol
- 10. Sanbusco Center
- 11. Lensic Performing Arts Center
- 12. Sweeney Center

- Buy**
- 1. The Portal
- 2. Andrea Fisher Fine Pottery
- 3. Packard's
- 4. Price-Dewey Galleries
- 5. To the Canyon Road gallery district

- Eat**
- 1. The Shed
- 2. Plaza Cafe
- 3. Cafe Dominic
- 4. Tomasita's
- 5. Blue Corn Cafe
- 6. La Casa Sena
- 7. Coyote Cafe
- 8. Upper Crust Pizza
- 9. Indian House
- 10. Pink Adobe
- 11. Pranzo Italian Grill
- 12. 315
- 13. Tulips
- 14. Paul's

- Drink**
- 1. St. Francis Hotel Bar

- Sleep**
- 1. Dancing Ground of the Sun
- 2. Pueblo Bonto
- 3. Water Street Inn
- 4. El Favelito
- 5. Eldorado



Conference Evaluation and Questionnaire

OVERALL CONFERENCE

	Poor		Mid		Excellent
Overall Conference Evaluation	1	2	3	4	5
General comments:					

SCIENTIFIC PROGRAM

	Poor		Mid		Excellent
Quality of the Presentations	1	2	3	4	5
Relevance of Presentations to the Conference's Theme	1	2	3	4	5
Time Allotted for Presentations	1	2	3	4	5
Time Allotted for Discussion	1	2	3	4	5
Poster Session	1	2	3	4	5
Tutorials	1	2	3	4	5
Equipment Exhibit	1	2	3	4	5
Student Participation	1	2	3	4	5
Additional comments:					

CONFERENCE MATERIALS

	Poor		Mid		Excellent
Printed Proceedings Book	1	2	3	4	5
CD Proceedings	1	2	3	4	5
Other Registration Materials	1	2	3	4	5
Additional comments:					

CONFERENCE FACILITIES & SOCIAL PROGRAM

	Poor		Mid		Excellent
Lecture Hall	1	2	3	4	5
Registration Desk	1	2	3	4	5
Meals: Dining facilities	1	2	3	4	5
Conference Breakfasts and Lunches	1	2	3	4	5
Conference Dinner and Concert	1	2	3	4	5
Coffee Breaks	1	2	3	4	5
Opening Dinner Reception	1	2	3	4	5
Closing Pizza Party	1	2	3	4	5
Audio-Visual: Screen Visibility	1	2	3	4	5
Sound Level	1	2	3	4	5
Presentation Transistion	1	2	3	4	5
Wireless Internet Connectivity:	1	2	3	4	5
Additional comments:					

Conference Evaluation and Questionnaire

VENUE AND HOTEL

	Poor		Mid		Excellent
Venue – Santa Fe, New Mexico and Environs	1	2	3	4	5
Would you return to this city?	Yes		Perhaps		No
Area Attractions	1	2	3	4	5
Hotel: Overall	1	2	3	4	5
Reservations	1	2	3	4	5
Transportation and Accessibility	1	2	3	4	5
Reception and Check-In	1	2	3	4	5
Accommodations	1	2	3	4	5
Facilities	1	2	3	4	5
Parking	1	2	3	4	5
Would you return to this hotel?	Yes		Perhaps		No
Additional comments:					

CONFERENCE ADMINISTRATION

	Poor		Mid		Excellent
Website	1	2	3	4	5
Registration off-site	1	2	3	4	5
Registration on-site	1	2	3	4	5
Administrative staff	1	2	3	4	5
Correspondence	1	2	3	4	5
Additional comments:					

GENERAL INFORMATION

I am a Returning Delegate	Yes	No
I plan to attend the next conference	Yes	Perhaps
and present a paper(s) / poster(s)	Yes	Perhaps
Other(s) from my lab would attend the next conference	Yes	Perhaps
and he/she / they would present a paper(s) / poster(s)	Yes	Perhaps
How did you learn of this conference? (Check all that apply)	<input type="checkbox"/> Email Announcement	
<input type="checkbox"/> Internet	<input type="checkbox"/> Website	
<input type="checkbox"/> Other	<input type="checkbox"/> Colleague	
Tutorial Topic Suggestions for next year:		
Additional Comments:		

If you would be willing to host the Conference in your city, please give your name to the Conference Staff.

Questions or comments are welcome at any time at <elasticity.conference@uth.tmc.edu>

Thank You!